Characterisation and segmentation of basal ganglia mineralization in normal ageing with multimodal structural MRI

Andreas Glatz

Doctor of Philosophy

THE UNIVERSITY *of* EDINBURGH

2015

Declaration

I declare that I composed this thesis and that it is my own original work except where explicitly stated in the text. I have not submitted any part of this thesis for any other degree or professional qualification.

Andreas Glatz

24th June 2015

Abstract

Iron is the most abundant trace metal in the brain and is essential for many biological processes, such as neurotransmitter synthesis and myelin formation. This thesis investigates small, multifocal hypointensities that are apparent on T2*-weighted (T2*w) MRI in the basal ganglia, where presumably most iron enters the brain via the blood-brain-barrier along the penetrating arteries. These basal ganglia T2*w hypointensities are believed to arise from iron-rich microvascular mineral deposits, which are frequently found in community-dwelling elderly subjects and are associated with age-related cognitive decline.

This thesis documents the characteristic spatial distribution and morphology of basal ganglia T2*w hypointensities of 98 community-dwelling, elderly subjects in their seventies, as well as their imaging signatures on T1-weighted (T1w) and T2-weighted (T2w) MRI. A fully automated, novel method is introduced for the segmentation of basal ganglia T2*w hypointensities, which was developed to reduce the high intra- and inter-rater variability associated with current semi-automated segmentation methods and to facilitate the segmentation of these features in other single- and multi-centre studies. This thesis also presents a multi parametric quantitative MRI relaxometry methodology for conventional clinical MRI scanners that was developed and validated to improve the characterisation of brain iron. Lastly, this thesis describes the application of the developed methods in the segmentation of basal ganglia T2*w hypointensities of 243 community-dwelling participants of the Austrian Stroke Prevention Study Family (ASPS-Fam) and their analysis on R2* (=1/T2*) relaxation rate and Larmor frequency shift maps.

This work confirms that basal ganglia T2*w hypointensities, especially in the globus pallidus, are potentially MRI markers of microvascular mineralization. Furthermore, the ASPS-Fam results show that basal ganglia mineral deposits mainly consist of paramagnetic particles, which presumably arise from an imbalance in the brain iron homeostasis. Hence, basal ganglia T2*w hypointensities are possibly an indicator of age-related microvascular dysfunction with iron accumulation, which might help to explain the variability of cognitive decline in normal ageing.

Lay summary

Over the lifespan of humans iron in the brain is sequestrated and stored as part of a mechanism to protect the brain tissue from its toxic effects. In normal ageing brain iron often precipitates to form brain iron deposits, especially in the deep grey matter of the brain. These deposits are readily detectable on conventional magnetic resonance images (MRI) and were recently proposed as a novel biomarker for cognitive decline and small vessel disease. However, the mechanisms behind the formation of these iron deposits are poorly understood. In the first study we therefore established a baseline of their multi-modal MRI appearance with structural MRI data from a large-scale study of normal brain aging. These results were then used for fully automating the detection of these deposits on conventional MRI volumes. The developed method significantly reduced the time for detecting iron deposits, as well as reduced the dependence of the final results on a specific expert rater. Lastly, this iron deposit detection method was then validated with MRI data from an independent study of normal brain aging. The results from the latter research confirmed with quantitative MRI methods that the automatically detected features were indeed iron deposits, which grow in size with age and are independent of any iron deposition in the surrounding normal-appearing tissue. In summary, all results further confirm the initial assumptions that these iron deposits may be a novel marker of small brain vessel disease potentially linked with increased cognitive decline in normal ageing.

Acknowledgements

First and foremost I would like to thank my supervisors Mark E. Bastin, Maria C. Valdés Hernández and Joanna M. Wardlaw, the Director of the Brain Research Imaging Centre (BRIC) of the University of Edinburgh, for accepting me as a PhD student and their continuing support. At the same time I would like to acknowledge the "Scottish Imaging Network: A platform for scientific excellence" (SINAPSE) led by Dave Wyper, who funded my PhD through a SINAPSE/SPIRIT PhD scholarship in partnership with General Electric (GE). Many thanks also go to Scott Reid, who was my main GE contact and who sponsored me to attend the GE EPIC course in Pisa, Italy. I am grateful to the Scottish Funding Council for sponsoring my early career researcher exchange at the Neuroimaging Research Unit of the Medizinische Universität Graz, Austria, which was crucial for validating the methods that I developed. This exchange would not have been possible without the support of Stefan Ropele, Christian Langkammer, Lukas Pirpamer as well as the head of the Neurology department in Graz, Franz Fazekas, who also kindly offered me an internship at their department during the write-up phase of my PhD. Lastly, I also greatly appreciated the help from all the BRIC Radiographers led by Elaine Sandeman, my fellow PhD students of the Annex at the BRIC, and Michael Thrippleton and Dominic Job, who all helped to make my PhD life much easier and – let's be honest – more fun.

I am also very thankful for all the love, support and encouragement from my family and friends. I strongly believe that I had exceptional parents since they always supported my endeavours into engineering and science. It even went so far that my dad literally helped me to submit the first version of this thesis to the postgraduate office. I am indefinitely grateful for all their love and support, without which I would not have arrived where I am now. I also would like to acknowledge the kind support from my parents-in-law Felix and Coreen. I still remember the encouragement from Coreen, who replied vehemently to my doubts of leaving my working life behind me to become a PhD student with the words: "No worries, you do this!" I appreciate the help from my brothers Georg, Ming Jen, And Ming Wei, for making my wedding during the first year of my PhD a success. I would also like to thank my Uncle

Richard, Aunt Elfi, and cousins, Daniela and Jürgen, for their encouragement and support, which helped me a lot to shed any doubt that I could finish what I started. I am grateful to my godmother – "die kleine Gaby" – as well as Harald, Florian, my best man Helmut, Seppi the builder, Polly the teacher, Dr. Johannes the inventor, Thomas spelled Dr. Gmeda, and CEO Zoran with his out-of-the world Triumph for keeping me always grounded and true to my roots, which admittedly is not a very easy task partly due to the distance between us. Of course I must not forget to mention Omo, who sadly passed away in the last year of my PhD. Omo played an enormous part in my life and was exceptional in her own right. She gave me so much and wanted so little in return, for which I will always love and miss her. Lastly, I would like to thank my co-adventurer, best friend, moral compass and wife, Ming Sze, for always – and I mean always – being there for me, and by my side, although the oceans kept us apart for such a long time. Thank you.

Andreas Glatz

Edinburgh, Scotland

June, 2015

Table of Contents

List of Figures

Main text figures

Appendix figures

List of Tables

Main text tables

Appendix tables

List of Abbreviations

2D, 3D	Two, three dimensional
AChA	Anterior choroidal artery
ASPS-Fam	Austrian Stroke Prevention Study Family
ASSET	Array spatial sensitivity encoding technique
ATP	Adenosine triphosphate
BBB	Blood-brain barrier
BCB	Blood-cerebrospinal fluid barrier
BET	Brain extraction tool
BG	Basal ganglia
CaAlg	Calcium Alginate
CI	Confidence intervall
CMB	Cerebral microbleed
CMD	Cerebral mineral deposit
CNR	Contrast-to-noise ratio
CNS	Central nervous system
CPMG	Carr-Purcell-Meiboom-Gill
CSF	Cerebral spinal fluid
$CuSO_4$	Copper(II) sulfate
DESPOT1	Driven equilibrium single pulse observation of T1
dMRI	Diffusion MRI
DMT1	Divalent metal transporter 1
EPI	Echo planar imaging
Fe^{3+},Fe^{2+}	Ferric/ferrous iron
FID	Free induction decay
FLAIR	Fluid attenuated inversion recovery
fMRI	Functional MRI
FSE	Fast spin-echo
FSL	FMRIB Software Library
FAST	FMRIB's Automated Segmentation Tool

FIRST	FMRIB's Integrated Registration and Segmentation Tool
FMRIB	Functional MRI of the brain
FSPGR	Fast spoiled gradient-echo
GESFIDE	Gradient echo sampling of free induction decay
GESSE	Gradient echo sampled spin echo
GM	Grey matter
GRASS	Gradient recalled acquisition in the steady state
HA	Hydroxyapatite
ICV	Intracranial volume
IQR	Interquantile range
IRE	Iron responsive element
IR-prep	Inversion recovery prepared
IRP	Iron regulatory proteins
LBC1936	Lothian Birth Cohort 1936
LSA	Lenticulostriate arteries
MCD	Minimum covariance determinant
Mn^{2+}	Divalent manganese ion
$MnCl_2$	Manganese(II) chloride
MOLLI	Modified Look-Locker inversion recovery
MP-RAGE	Magnetization prepared rapid acquisition gradient-echo
MT	Magnetization Transfer
NaCl	Sodium chloride (Cooking salt)
ONS	Office for National Statistics
PD	Proton density
PDw	Proton density-weighted
PVS	Perivascular space
qMRI	Quantitative MRI
qSM	Quantitative susceptibility mapping
RF	Radio-frequency
RHA	Recurrent artieries of Heubner
ROI	Region of interest
ROS	Reactive oxidative species

SAR	Specific Absorption Rate
SD	Standard deviation
SNR	Signal-to-noise ratio
SWAN	Susceptibility weighted angiography
SWI	Susceptibility weighted imaging
T1w	T1-weighted
T2*w	T2*-weighted
T2w	T2-weighted
TE	Echo time
TFRC	Transferin receptor
TOF-MRA	Time of flight magnetic resonance angiography
UN	United Nations
WHO	World Health Organization
WM	White matter
WMH	White matter hyperintensity

List of Symbols

a, b	Coefficients
α	Level of significance
$\mathscr{b}$	Histogram bin index
B	Magnetic field [T]
c	Concentration [mol/m^3]
d	Diameter of sphere [m]
$\mathscr{d}$	Robust distance [m]
D	Diffusion coefficient [m^2/s]
e_x, e_y, e_z	Unit vectors of coordinate system
f	Frequency [Hz]
F_b	Fraction of bound water
$\mathscr{f}$	Gel bead replicate index
g	g-factor
$\mathscr{g}$	Gel bead index
γ	Gyromagnetic ratio [s^{-1}T^{-1}]
G	Cummulative distribution function
h	Connected component index
$\hbar$	Reduced Plank's constant
$\mathcal{H}$	Set of connected component indices
i	Voxel index
$\mathscr{i}$	Nuclear spin quantum number
I	Nuclear angular momentum [Js]
j	MRI volume type
J	Jaccard index
$\mathcal{J}$	Spectral density function [s]
k_x, k_y, k_z	Unit vectors of k-space
$\mathscr{k}$	Subject index
l	Structure label
L	Set of structure labels

m	Method type
μ	Magnetic moment [Am^2]
M	Magnetization [A/m]
$\mathcal{M}$	Mask (set of voxel indices)
n	Number of voxels
v	Volume fraction
N	Number of samples
ξ	Mixture ratio
p	Probablility
q	T2*w intensity variance threshold
Q	Quantile
r	Relaxivity [$s^{-1}/mol/m^3$]
r	Pearson's correlation coefficient
R	Relaxation rate
s	Signal intensity
S	Set of voxel signal intensities
t	Time [s]
τ	Correlation time [s]
ψ	Flip angle [°]
χ	Magnetic susceptibility
ω	Angular frequency [1/s]

Chapter 1 Introduction

1.1. Human population ageing trends and prospects

At the turn of this century, for the first time in human history, the number of people above 60 years of age living in Europe rose above the number of people below 15 years of age (UN, 2014). This landmark shift in the demography of the human population is predicted to continue around the world with North America and Asia to follow Europe by 2030 and 2040. Overall, the World Health Organization (WHO) predicts that for the first time the population older than 65 years will outnumber the population younger than 5 years before 2020 (WHO/US-NIA, 2011). In every country around the world there is a continuous upward trend in the median population age, which is either due to an increase in the number of elderly, their proportion in the population of a country or both. In the UK, for example, the median age rose from 35 to 40 years between 1985 and 2010 (ONS, 2014), which is an average increase of 0.3 median age years per calendar years. This median age is projected to rise to 42 years by 2035, a further average increase of 0.08 median age years per calendar years. In the UK, one in six people are older than 65 years and this population segment is projected to increase faster than the under 65 years group. Overall, the fastest growing population segment in the UK is the population older than 85 years, which increased from 1 to 2 % of the total population between 1985 and 2010, i.e. by 100 %. Figure 1-1 shows the measured and estimated population pyramids for Scotland as an example of a developed nation. This figure illustrates that the population above 40 years is projected to increase relative to the one below 40 years. Here 40 years represent the middle working life age, assuming that the working life starts at 20 and ends at 60.

Human population ageing is caused by falling fertility and mortality rates, and an increase in longevity. However, it is widely accepted that the main driver behind population ageing are the falling fertility and mortality rates (Harper, 2014). While the falling fertility rates might be due to changes in the general lifestyle of younger individuals, the falling mortality rate is explained by healthy living, disease prevention and cure, senescence prevention and regenerative medicine. The results of

these changes are a declining and ageing population, which poses new challenges for the economies of developed countries. One of these challenges is the rising social and health care cost for the increasing number of elderly. A promising strategy to address this challenge is the postponement of frailty and disability, which would allow older individual to sustain themselves independently for longer. Ageing without major disabilities is often termed 'healthy' or 'successful' ageing (Rowe & Kahn, 1998), which is the theme of current research aiming to identify factors for increasing the quality of ageing (WHO/Europe, 2012).

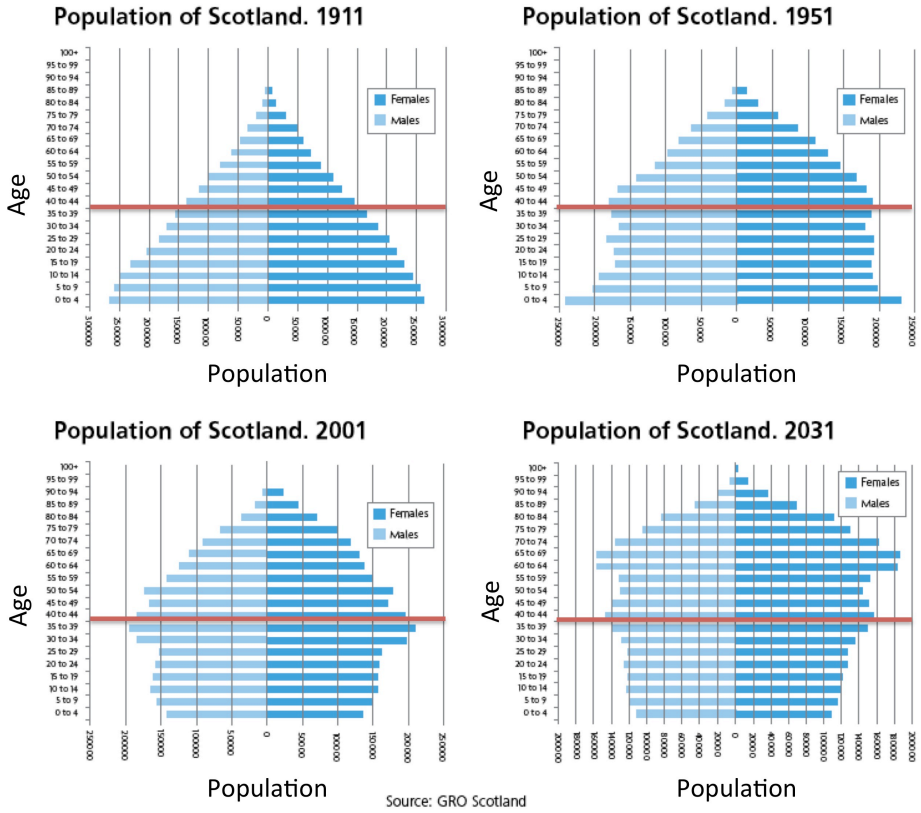

Figure 1-1: Measured and projected demography shift in Scotland. These population pyramids were calculated from General Register Office Scotland data in 2005. The red horizontal line represents 40 years, the middle working life age.

Diseases of the brain, such as stroke and dementia, are diseases that disproportionally affect the elderly (Rechel *et al.*, 2013), and with a rising elderly population will increasingly burden the health care systems of predominantly, but not exclusively, developed countries. Therefore research into the early detection and prevention of neurological disorders in ageing is considered an important contribution for stabilizing and potentially decreasing health care costs (Fineberg *et*

al., 2013). An aspect of the research into disorders of the brain aims to identify physiological patterns of ageing and their differentiation from pathological patterns of age-related disease to increase the sensitivity of diagnosis of neurological diseases. High-resolution brain imaging techniques, such Magnetic Resonance Imaging (MRI), are highly valuable tools for characterising changes in brain structure due to age-related physiological and pathological conditions (Frisoni *et al.*, 2010; Lockhart & DeCarli, 2014). The principal focus of this thesis is the characterisation of presumably iron-rich brain mineral deposits in healthy ageing that can be visualized using routine structural MRI.

1.2. MRI features of ageing

Brain ageing in the absence of disease is a process that causes subtle changes at the microscopic (cellular) level that may lead or contribute to changes at the macroscopic (structural) level (Bishop *et al.*, 2010), such as atrophy, white matter degeneration, and microvascular stroke. Many of these macroscopic changes, such as iron, can be specifically detected and further classified with routine structural MRI sequences as summarized in the following sections. See Appendix A for an introduction to MRI and MRI sequences, and Appendix B for a summary of current ageing studies and their MRI protocols.

1.1.1 Atrophy

Atrophy is defined as the brain volume decrease over time that is not related to specific macroscopic focal tissue loss, such as that caused by trauma, inflammation or infarction (Wardlaw *et al.*, 2013). The general consensus of studies, e.g. as reviewed in (Raz, 2007), is that brain volume decreases with age. Atrophy typically manifests itself as shrinkage of grey and white matter structures, which is often paralleled by an increase in the volume of the ventricles and superficial sulci. Age-related atrophy can be especially marked in the frontal, parietal and temporal cortex, the hippocampus, the caudate and putamen, as well as the cerebellum. Longitudinal studies, as reviewed by Fjell *et al.* (2009), have shown that in normal ageing the brain shrinks by 0.2 % per year at age 30 – 50, which increases to 0.3 – 0.5 % per year at age 70 – 80. The volume of the hippocampus and entorhinal cortex, which are the brain regions observed to shrink the fastest, decrease by 0.8 – 2.0 % and 0.3 – 2.4

%, respectively. However, some researchers argue (Mora, 2013) that in normal ageing the effect of atrophy on brain function might be modest.

In vivo brain imaging techniques, such as MRI, have enabled the accurate quantification of how the volume of the brain and its substructures change with age (Fox & Schott, 2004). T1-weighted (T1w) MRI sequences, such as the magnetization prepared rapid acquisition gradient-echo (MP-RAGE) sequence (Deichmann *et al.*, 2000), are recommended for the volumetry of the brain, which ideally should be configured to generate T1w volumes with no slice gap and 1 mm isotropic voxels (Wardlaw *et al.*, 2013). As reviewed by Keller and Roberts (2009), many computational methods have been developed to facilitate the accurate segmentation of the ageing brain. These computational methods typically register brain images to a standard template. The brain is then either segmented semi-automatically, i.e. with manual intervention from a rater, or automatically using prior information. The drawbacks of semi-automatic methods compared with automatic techniques are that they are more time consuming and require a rater with a detailed knowledge of brain anatomy. However, semi-automated methods are currently preferred for volumetry of the aging brain since the anatomical variability of older brains is higher than that of younger brains, which makes the accurate segmentation of brain tissue more challenging (Wardlaw *et al.*, 2011). Current measurement standards also suggest that whole brain and brain sub-regional volume measurements should be adjusted for intracranial volume to normalise for head size (Wardlaw *et al.*, 2013).

1.1.2 T2w hyperintensities

In the ageing brain, T2-weighted (T2w) hyperintensities are commonly found in the white matter. However, T2w hyperintensities are also caused by subcortical infarcts and lacunes, as well as perivascular spaces, which are commonly found in the grey matter. These are imaging markers of small vessel disease (Pantoni, 2010; Thompson & Hakim, 2009), which is a systemic condition of ageing exacerbated by vascular risk factors.

White matter hyperintensities (WMH) of presumed vascular origin (Wardlaw *et al.*, 2013) appear as bilateral and mostly symmetrical regions of high signal intensity on T2w and fluid attenuated inversion recovery (FLAIR) MRI. WMH can be caused by focal demyelination to complete axonal disruption in case of neurodegenerative

diseases (Bolandzadeh *et al.*, 2012). Although WMHs are strongly associated with cerebrovascular disease and vascular risk factors, their pathogenesis is still poorly understood. WMH are often rated according to the Fazekas scale (Fazekas, 1989), which classifies them according to their severity on a scale from 0 (no WMH) to 4 (severe WMH), and their location (periventricular or subcortical). Perivascular and subcortical WMH are presumed to have differing pathogenesis, risk factors, and clinical consequences (Bolandzadeh *et al.*, 2012; Kim *et al.*, 2008).

Recent subcortical infarcts, formerly called lacunar infarcts (Fisher, 1982), account for about 25% of all ischemic strokes (Wardlaw *et al.*, 2013). These infarcts are typically small (up to 20 mm on a slice of an axial scan) and per definition must have occurred recently (< 3 weeks) in the vascular territories of the perforating arteries or arterioles in the internal part of the brain. Although such subcortical infarcts rarely lead to death in their acute phase, they increase the long-term risk of death, cognitive dysfunction, disability, as well as recurrence of stroke (Norrving, 2008). After the acute phase, 28 to 94 % of subcortical infarcts cavitate (Moreau *et al.*, 2012; Potter *et al.*, 2010), which leaves small cerebrospinal fluid (CSF) filled holes in the brain, so called lacunes of vascular origin (Wardlaw *et al.*, 2013). These lacunes appear as round or ovoid focal hypointensities on T2w MRI, where they have a diameter ranging between 3 and 15 mm. Conversely, on FLAIR MRI lacunes often appear as focal hypointensities, which are surrounded by a hyperintense rim. However, some lacunes appear without a hyperintense rim or are entirely hyperintense on FLAIR MRI, which makes their identification challenging.

Perivascular spaces (PVS) are an extension of the fluid filled subarachnoid space that accompanies the course of vessels into the brain, which are usually not visible on routine structural MRI. However, with increasing age PVS become larger in size (Heier *et al.*, 1989) and appear as focal hyperintensities on T2w MRI and focal hypointensities on FLAIR MRI (Wardlaw *et al.*, 2013). PVS have a linear shape if they are imaged along the course of a vessel or a round shape with a diameter of < 3mm if imaged perpendicular to the course of a vessel. To distinguish between lacunes and PVS, radiologists also consider the location, signal intensity and size of focal T2w hypointensities. Enlarged PVS are associated with other features of small

vessel disease (Doubal *et al.*, 2010; Zhu *et al.*, 2010), and potentially with cognitive function (Huijts *et al.*, 2014; Maclullich *et al.*, 2004).

1.1.3 T2w and T2*w hypointensities

Other frequently observed features of the ageing brain are T2w and T2*w hypointensities in the extrapyramidal system arising from age-related brain iron accumulation, and focal T2*w hypointensities arising from microvascular injury and mineralization. Small haemorrhagic stroke lesions also cause focal T2w and T2*w hypointensities, however, these are typically signs of an underlying pathology.

Spatz (1922) was one of the first researchers to systematically investigate brain iron and demonstrated that it predominantly accumulates in the extrapyramidal nuclei. Hallgren and Sourander (1958) further investigated the trajectories of iron accumulation in the ageing brain and quantified the extrapyramidal nuclei-specific rates of brain iron accumulation with age. Brain iron is typically stored as water-soluble ferritin, whereas in ageing it is increasingly stored as the water insoluble iron complex haemosiderin (Zecca *et al.*, 2004). Brain iron has a strong effect on the transverse relaxation of diffusing water protons (Gossuin *et al.*, 2009), which causes T2w and T2*w hypointensities that are especially prominent in the basal ganglia in elderly subjects (Drayer *et al.*, 1986; Milton *et al.*, 1991; Tsushima & Endo, 2006). Abnormal iron accumulation has been observed in ageing, where it was associated with cognitive decline (Ghadery *et al.*, 2014; Rodrigue *et al.*, 2013), as well as neurodegenerative diseases (Hare *et al.*, 2013), such as Alzheimer's disease.

Cerebral microbleeds (CMB; Charidimou *et al.*, 2012) are defined as small and rounded hypointense lesions on T2*w MRI, which appear otherwise isointense on other routine structural MRI sequences. Histopathological studies suggest that these lesions arise from structural abnormalities of small brain vessels, which cause microbleeds. Extravasated blood cells are digested by perivascular macrophages, which give rise to perivascular haemosiderin deposits that become apparent on T2*w MRI due to their strong effect on the main magnetic field of an MRI scanner (McAuley *et al.*, 2011). The prevalence of spontaneous CMB (Cordonnier *et al.*, 2007) in healthy adults is only around 5%, which increases to up to 11 % in community-dwelling elderly subjects. However, CMB are commonly found in hypertensive arteriopathy, cerebral amyloid angiopathy, ischemic and hemorrhagic

stroke, as well as small vessel disease, where they have been proposed as a biomarker of these conditions (Charidimou *et al.*, 2012; Cordonnier *et al.*, 2007). CMB are mostly rated according to the Microbleed Anatomic Rating Scale (Gregoire *et al.*, 2009) or Brain Observer Micro-Bleed Scale (Cordonnier *et al.*, 2009).

Cerebral mineral deposits (CMD; Valdés Hernández *et al.*, 2012) cause focal, often irregular shaped, hypointense lesions on T2*w MRI. Synonyms of CMD are, for example, calcification, ferrugination and siderocalcinosis (Cass *et al.*, 2007; Martínez *et al.*, 2012; Wadsworth *et al.*, 1995), where the specific term refers to the most abundant trace metal in the mineral deposits. CMD can have a very similar appearance to CMB, which makes their differentiation challenging (Charidimou *et al.*, 2012). However, CMD often appear symmetrically in both brain hemispheres and are typically limited to the pineal gland, choroid plexus, habenular, brain membranes (falx, tentorium), brain vasculature, and basal ganglia. CMD are often an incidental finding on MRI, as well as on computer tomography and are almost never clinically significant (Daghighi *et al.*, 2007) unless they occur at very young age or are very large. However, Penke *et al.* (2012) recently showed that CMD are associated with cognitive decline in ageing and has therefore proposed them as a novel biomarker for ageing and small vessel disease.

1.3. The role of iron in the brain

1.3.1. Brain iron entry and exit

Iron is the most abundant trace metal in the brain (Krebs *et al.*, 2014), it is tightly regulated (Rouault & Cooperman, 2006), and it is required for several essential functions, ranging from oxygen transport to mitochondrial respiration, which provide energy for cellular maintenance and metabolism. The amount of iron in the human body is in the range of 40 - 50 mg iron/kg and it is typically higher in men than women. Iron enters the human body through the duodenum, from where it is distributed to the organs (Figure 1-2; Crichton, 2009). In the body, most of the iron (30 mg iron/kg) is bound to haemoglobin, while most of the rest is stored in liver, spleen, bone marrow and muscles. In comparison the brain requires very small amounts of iron compared to other tissues in grown adults (Chen *et al.*, 2013).

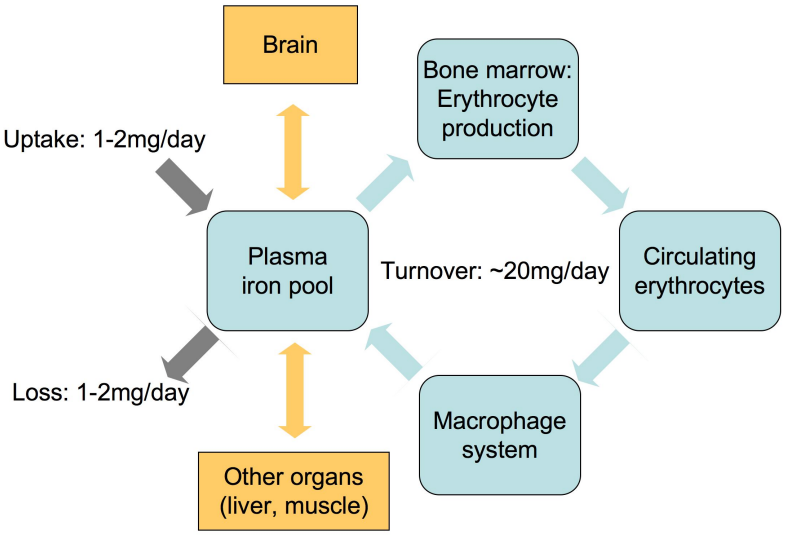

Figure 1-2: Iron distribution in the human body. This figure was adapted from Crichton (2009) and shows that the plasma iron pool represents the main source of brain iron in the human body.

Unlike other parts of the body, the entry of essential nutrients and trace metals, such as iron, into the central nervous system (CNS), as well as the efflux of waste products out of the CNS is tightly controlled by two barriers: the blood-brain-barrier around the penetrating arteries shown schematically in Figure 1-3 and the blood-CSF barrier around the capillaries of the choroid plexus and at the arachnoid membrane (Abbott *et al.*, 2006; Zheng *et al.*, 2003).

The blood-brain-barrier (BBB; Rouault & Cooperman, 2006) is formed by endothelial cells, which are connected by tight junctions. Astrocyte end-feet are connected to these endothelial cells and supply them with nutrients. Under normal physiological conditions the BBB has a low permeability for essential nutrients and trace metals therefore dedicated endothelial pathways exists to transport them across the BBB into the CNS. Iron in form of Fe^{3+} bound to holo-transferrin arrives through the penetrating arteries at the BBB, where the uptake on the luminal membrane of the endothelial cell is mediated by transferrin receptors. Transporters, such as ferroportin, are believed to facilitate the transport of iron in form of Fe^{2+} across the abluminal membrane of the endothelial cells and the entry into the interstitial fluid. Ferroxidase, such as Ceruloplasmin expressed by the astrocyte end-feets, reoxidise iron from Fe^{2+} to Fe^{3+}, which then can bind to interstitial apo-transferrin (transferrin without any Fe^{3+}) that is predominantly expressed by oligodendrocytes. Presumably

iron is then transported in form of holo-transferrin to the brain cells or returns to the systemic blood circulation through the venous drainage system.

Epithelial cells connected by tight junctions also form the blood-CSF barrier (BCB; Rouault *et al.*, 2009). The BCB is mainly found along capillaries of the choroid plexus that are fenestrated, which increases the permeability of the BCB with respect to the BBB. Notably, the choroid plexus is also one of the main sites, where transferrin is synthesised in the CNS.

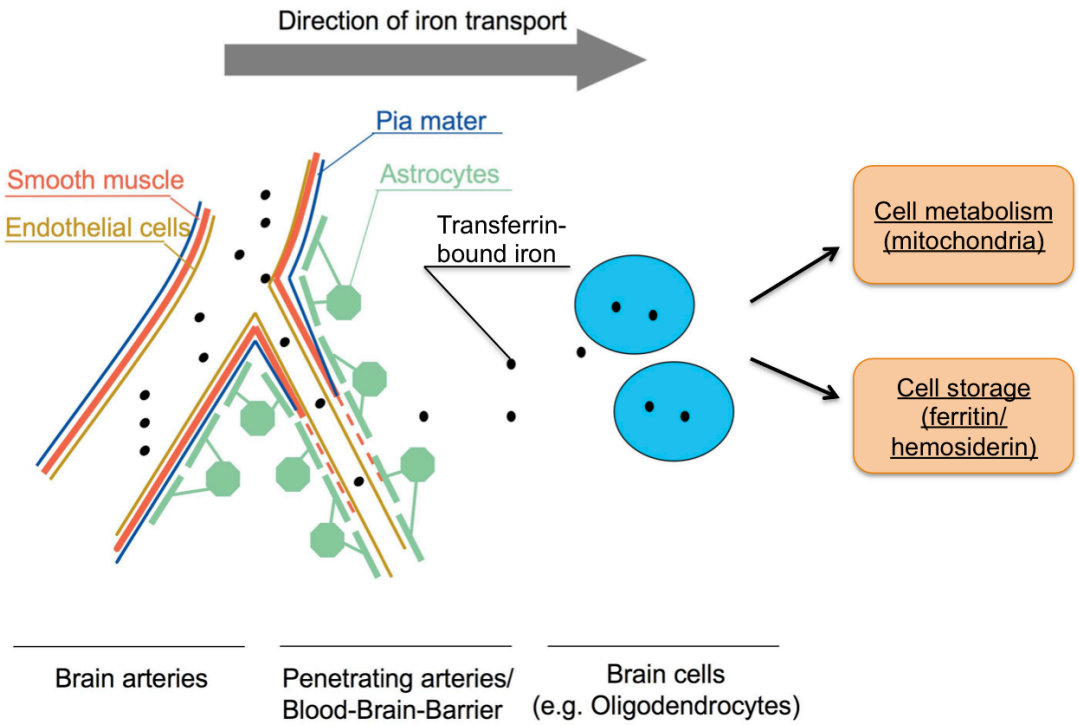

Figure 1-3: Iron transport in the brain. This figure is partly adapted from Iadecola and Nedergaard (2007). The black dots represent transferrin-bound iron that arrives through the penetrating arteries at the blood-brain-barrier, where it enters the CNS via specific pathways in a controlled manner. The iron is subsequently re-attached to transferrin, which transports it to brain cells, such as oligodendrocytes, where it is either metabolized or stored.

1.3.2. Brain iron storage

In the brain, as well as in other parts of the body, the water-soluble protein ferritin provides a very efficient means for iron storage (Chasteen & Harrison, 1999; Schenck & Zimmerman, 2004). Ferritin protects the tissue from the toxic effects of iron and can release iron in a controlled fashion in times of iron starvation and therefore it is believed to play an important role in protecting brain tissue and maintaining brain iron homeostasis. Brain ferritin may also contribute to the

formation of haemosiderin, a water-insoluble iron complex, which is found increasingly with age in the brain (Rouault, 2013; Zecca *et al.*, 2004).

Brain ferritin contains up to 4500 iron atoms in form of the mineral phase ferrihydrite that are encapsulated in a hollow protein shell. The protein shell of ferritin, so-called apo-ferritin, with approximate inner and outer diameters of 80 and 120 Å has a molecular weight of 450 kD and is assembled from 24 H- or L-polypeptite chains with 21 and 19 kD each. These H- and L-subunits of the ferritin shell have different functions: the H-subunits show ferroxidase activity and hence convert Fe^{2+} to Fe^{3+} before its storage, whereas the L-subunits do not show ferroxidase activity but are involved in the nucleation of the iron inside ferritin. The exact chemical formula of the contained ferrihydrite is not known but is often approximated as $Fe_5HO_8.4H_2O$ with a molecular weight of 480 D.

Ferritin protects brain tissue by storing free iron (Fe^{2+}, Fe^{3+}), which is highly reactive and can lead to cell death in combination with the formation of reactive oxidative species (ROS; Gutteridge, 1992). Under physiological conditions endogenous ROS are formed, for example, during the production of adenosine triphosphate (ATP) in the mitochondria, which are subsequently converted into water (H_2O). However, in an incomplete reaction not all ROS are converted into water, and the residual ROS can react with iron according to the Fenton reaction

$$Fe^{2+} + H_2O_2 \rightarrow Fe^{3+} + OH- + .OH. \qquad 1\text{-}1$$

This produces additional ROS, such as hydroxyl radicals (.OH), and hence can trigger a chain reaction. A sufficient amount of free radicals can trigger lipid peroxidation, which can destroy the cell membrane, and hence leads to cell death.

During the formation of the ferritin core iron in form of Fe^{2+} is taken up through hydrophilic channels (Chasteen & Harrison, 1999), which is then oxidised and crystallised. It is well known that extrapyramidal brain regions associated with motor function contain more brain iron than other brain regions and that brain iron accumulates with age at specific rates (Hallgren & Sourander, 1958). However, little is known about the driving factors, which give rise to this age-related and spatially diverse brain iron distribution in the brain. One possible hypothesis is that cells in the basal ganglia are genetically programmed to transcribe high amounts of ferritin proteins for creating CNS iron reservoirs (Rouault, 2013).

Lastly, lysosomes can extract the iron stored in ferritin by degrading it (autophagy) and releasing it into the cytosol for further utilisation (Asano *et al.*, 2011). Incomplete processing by lysosomes may lead to the production of the water-insoluble iron-storage complex haemosiderin (Cohen *et al.*, 2010), which is still poorly characterised. Recent research suggests that the release of iron from ferritin through lysosomal processing also happens even if iron is abundant in the cytosol, which might provide a further clue for explaining the increase in amount of haemosiderin in the ageing brain (Asano *et al.*, 2011; Zecca *et al.*, 2004).

1.3.3. Iron metabolism of brain cells

Dedicated pathways regulate the brain iron uptake into the cells. All cells, including brain cells, express transferrin receptors (TFRCs), as well as the divalent metal transporters (DMT1s) at their membrane (Zecca *et al.*, 2004). After binding of holo-transferrin to TFRCs endocytosis is initiated, which creates a compartment with the holo-transferrin TFRC complex and DMT1. Acidification of the compartment releases the iron molecules of the holo-transferrin, which are subsequently exported across the endosomal membrane into the cytosol by DMT1. The brain iron that is taken up in this manner is then either used for synthesis of haem and iron-sulphur clusters in the mitochondria or stored in form of cytosolic ferritin (Figure 1-3).

Brain iron levels in the cytosol (Rouault, 2006) are tightly regulated by means of iron absorption and storage in ferritin. This mechanism protects the cell in case of iron overload and releases iron in case of iron starvation. In particular, cytosol iron levels are regulated by the iron responsive element-binding proteins IRP1 and IRP2, which act as post-transcriptional factors since they can bind to iron-responsive elements (IREs) of the mRNA coding ferritin and transferrin. If an IRP is bound to the IRE of the ferritin-coding mRNA it suppresses the production of ferritin, and hence iron storage. Conversely, in high iron condition IRPs are either inhibited or degraded (Muckenthaler *et al.*, 2008), which leads to an increased production of ferritin and iron storage. Furthermore, IRPs bound to the IREs of the transferrin-coding region increases the transferrin production, and hence the number of TFRCs at the cell membrane, and hence the iron uptake by the cell.

As iron is required for the synthesis of haem and iron-sulphur clusters, iron that is not stored in the cytosol further migrates into the mitochondria, where iron levels

also have to be tightly regulated. So far, little is known (Gao & Chang, 2014) about the mechanisms by which mitochondrial iron levels are regulated and how iron is controlled at the systematic level in cells. Recently, a new ferritin like protein, i.e. mitochondrial ferritin, was implicated in this regulatory circuit (Nie *et al.*, 2005) since it modulates mitochondrial iron levels. At the systematic level, iron regulation involves the peptide 'hormone' hepticin (Ward *et al.*, 2014). Although it is mainly produced in the liver, hepticin is also expressed in the brain. Notably, hepticin seems to regulate the brain iron uptake mediated by ferroportin at the BCB at the choroid plexus (Marques *et al.*, 2009).

The expression of proteins, such as transferrin, ferritin and TFRC, varies between cell types of the brain and also depends on the iron status in their cytosol as mentioned before. Typically transferrin, ferritin and TFRC are expressed by oligodendrocytes, microglia and neurons, respectively. However, ferritin is also expressed by oligodendrocytes and neurons indicating that they also take up and store iron, whereas astrocytes express the least amount of ferritin indicating that they absorb and store only little amounts of iron.

1.3.4. Re-distribution of iron within the brain

Little is also known about the re-distribution of iron in the brain (Rouault & Cooperman, 2006). The current hypothesis is that iron enters the brain predominantly at the highly perfused basal ganglia via the BBB, from where it is distributed via axonal transport to other regions of the brain, such as the white matter (Dietrich & Bradley, 1988; Es *et al.*, 2008). The ageing brain requires less iron due to a slowing development, which in older age is presumably exacerbated by a loss of myelin, such as caused by WMH. However, as the brain continues to receive iron via the BBB, an iron demand-supply imbalance arises, which consequently might explain the increased age-related brain iron accumulation at the site of iron entry into the brain, such as in the basal ganglia.

1.4. Effect of brain iron on MRI

1.4.1. Modelling the effect of brain iron on the MRI signal

The effect of paramagnetic and diamagnetic particles, such as iron or calcium, on the brain MRI signal can be described by considering a simple tissue model

(Weisskoff *et al.*, 1994) as presented below. However, the interested reader is referred to Haacke *et al.* (1999) for a more in-depth introduction to this topic.

Here it is assumed that the magnetic particles are homogenous spheres with different diameters d_i and magnetic susceptibilities χ_i^p, where i is the particle index. These spherical particles are embedded in a homogenous medium with the bulk susceptibility χ^b, which is immersed in a homogenous, static magnetic field B_0. Due to the magnetic susceptibility differences $\Delta\chi = \chi_i^p - \chi^b$ each magnetic particle causes field inhomogeneities $\Delta \boldsymbol{B_i}(\boldsymbol{r})$, which influence the state of exited water protons in their vicinity. Consequently, this becomes apparent as a reduction of longitudinal and transverse relaxation rates R1 (=1/T1), R2 (=1/T2) and R2* (=1/T2*) that depends on the particle concentration, and hence can lead to hyperintensities on T1w MRI, and hypointensities on T2w and T2*w MRI.

Small magnetic particles, such as ions, with diameters in the few nm range typically cause microscopic magnetic field inhomogeneities. These inhomogeneities do not extend beyond the average diffusion lengths of water protons and are much smaller than the typical MRI voxel size ('free' water diffusion at 37° is about 0.34 mm/s according to Le Bihan (2003)). Conversely, larger magnetic particles, such as aggregated magnetic particles, with diameters in the µm range typically create mesoscopic field inhomogeneities that extent beyond the average diffusion length of water protons in tissue and are in the range of the typical MRI voxel size. Notably, the magnetic susceptibility and the water diffusion coefficient also determine the size length scales (Weisskoff *et al.*, 1994). Consequently, the magnetic field inhomogeneities in a medium can be formally classified as microscopic and mesoscopic field inhomogeneities $\Delta \boldsymbol{B}^{micro}(\boldsymbol{r})$ and $\Delta \boldsymbol{B}^{meso}(\boldsymbol{r})$ satisfying

$$\Delta \boldsymbol{B}(\boldsymbol{r}) = \boldsymbol{B}(\boldsymbol{r}) - B_0 \boldsymbol{e_z} = \Delta \boldsymbol{B}^{micro}(\boldsymbol{r}) + \Delta \boldsymbol{B}^{meso}(\boldsymbol{r}), \qquad 1\text{-}2$$

where $\Delta \boldsymbol{B}^{meso}(\boldsymbol{r})$ are the components of $\Delta \boldsymbol{B}(\boldsymbol{r})$ that only vary slowly along a path in the order of the average proton diffusion length of a MRI experiment.

In reality, macroscopic field inhomogeneities, such as caused by air-tissue boundaries in the brain, also contribute to the total field inhomogeneities in a medium. However, here these were neglected for simplicity.

In particular, microscopic and mesoscopic field inhomogeneities have a different effect on the transverse relaxation rates R2 and R2* due to two dephasing regimes,

the motional averaging regime and the static dephasing regime (Yung, 2003). In the motional averaging regime, the proton spins of a voxel loose their coherence by randomly diffusing through many different microscopic field inhomogeneities during an MRI experiment, which causes irreversible transversal dephasing. Irreversible dephasing increases the transverse relaxation rate R2=1/T2, as well as the effective transverse relaxation rate R2*=1/T2*=R2+R2' since R2'=0 s^{-1}, which leads to similar hypointensities on T2w and T2*w MRI. Conversely, in the static dephasing regime the water protons of a voxel loose their coherence by diffusing through ideally a single mesoscopic field gradient during an MRI experiment, which causes reversible transversal dephasing. In the latter case a 180° pulse of a spin-echo sequence can restore, at least partially, the coherence of these spins. The reversible dephasing only affects the effective transverse relaxation rate R2* since it only increases R2' (Yablonskiy & Haacke, 1994), which leads to hypointensities on T2*w MRI, whereas the T2w MRI signal remains largely unaffected.

1.4.2. Effect of microscopic field inhomogeneities on R1 and R2

Two theories are commonly used to estimate the R1 and R2 relaxation rates of liquids and tissues containing small paramagnetic particles: the Soloman-Bloembergen-Morgan theory (Bloembergen & Morgan, 1961), and the inner- and outer-sphere theory (Guéron, 1975).

Both theories are based on a mathematical description of the random movement of molecules, which increases with the temperature. The movement of a collection of molecules can be described by an autocorrelation function and its Fourier transform is the spectral density function

$$\mathcal{J}(\omega,\tau) = \frac{\tau}{1+\omega^2\tau^2}, \qquad 1\text{-}3$$

where τ is the characteristic time that a proton remains on average in a particular orientation, and ω describes the frequency of the random motion. The spectral density function has a low-pass filter characteristic with a 'cut-off' frequency $\omega_c = \tau^{-1}$. In case of a collection of bound molecules the molecules remain in a particular orientation for a long time, hence the characteristic time is high and the 'cut-off' frequency is low. Conversely, in case of a collection of liquid molecules

that can freely move around, the characteristic is time low, and the 'cut-off' frequency high (McRobbie *et al.*, 2003).

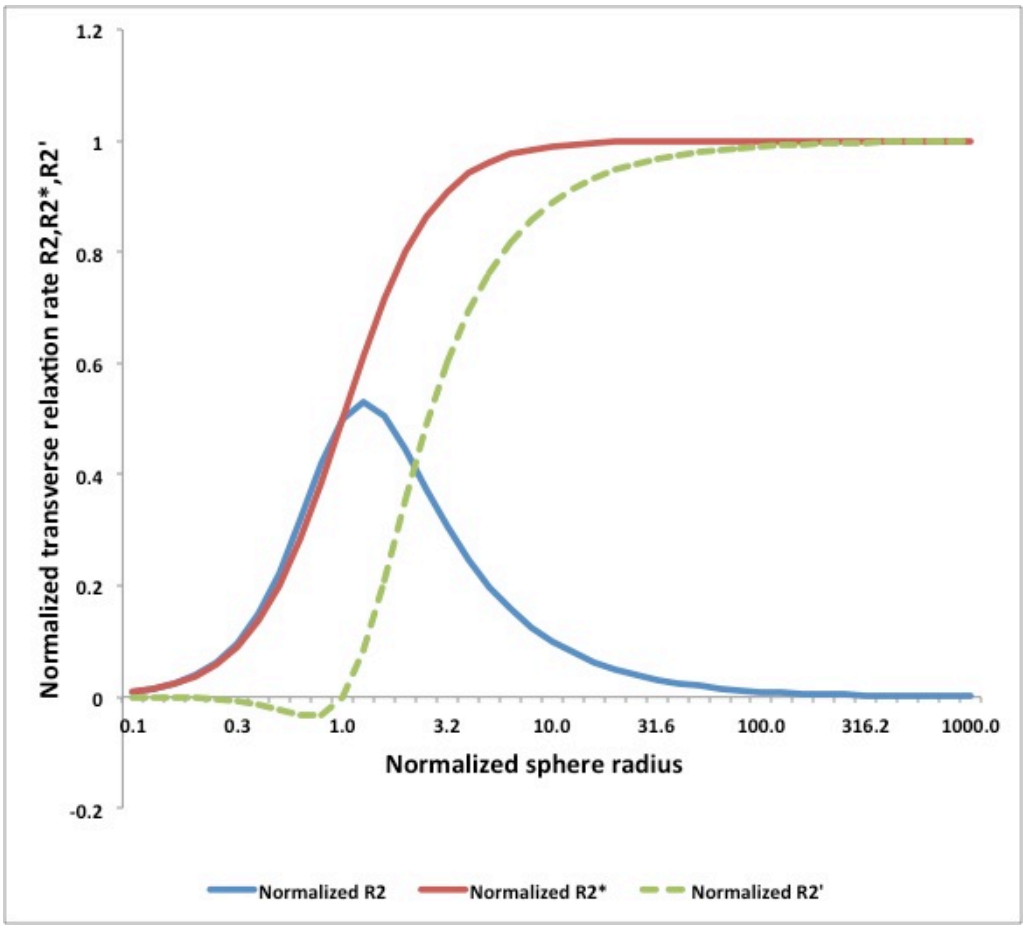

Figure 1-4: Dependence of the transversal relaxation rate on the magnetic particle size. The red and blue curves show the dependence of the relaxation rates R2, R2* on the size of magnetic spheres, which were calculated with the empirical relaxation rate model described by Equations 18 and 19 in Yung (2003). In the motional averaging regime (normalized sphere radius << 1) both relaxation rates are approximately the same, whereas in the static dephasing regime (normalized sphere radius >> 1) the normalized relaxation rate R2 decreases towards 0.

The Soloman, Bloembergen and Morgan theory was originally developed for estimating the relaxation rates R1 and R2 of liquids with small paramagnetic particles, such as Mn^{2+} ions (Bloembergen & Morgan, 1961). This theory is based on the observation that in such liquids the relaxation rates are mainly influenced by the interaction between the electronic spins of the dissolved ions and the spins of the neighbouring protons, which is called proton-electron dipole-dipole interaction. This theory estimates the longitudinal and transverse relaxation rates

$$\begin{aligned} R1 &= a\big(3\tau_c + 7\mathcal{J}(\omega_s,\tau_c)\big) + b\mathcal{J}(\omega_s,\tau_e) \\ R2 &= \frac{a}{2}\big(7\tau_c + 13\mathcal{J}(\omega_s,\tau_c)\big) + \frac{b}{2}\big(\tau_e + \mathcal{J}(\omega_s,\tau_e)\big)\end{aligned}, \qquad 1\text{-}4$$

where a, b are constants, τ_c, τ_e are the correlation times for spin- and dipole-exchange, and ω_s is the angular Larmor frequencies of electrons. These results are valid for $\omega_s\tau_c \ll 1$, which is the case for fast moving molecules in liquids. The temperature and the main magnetic field strength influence the relaxation rates since the correlation times depend on the temperature and the Larmor frequency depends on the field strength.

The inner- and outer-sphere theory takes its name from the fact that the regions around magnetic particles are partitioned into the inner and outer spheres of influence of the susceptibility-induced microscopic magnetic field gradients caused by the magnetic particles (Gillis *et al.*, 1999; Guéron, 1975). Although this interaction increases both transverse and longitudinal relaxation rates it predominantly affects the transverse relaxation rate R2, especially in case of paramagnetic particles. This theory estimates under simplifying assumptions as detailed in Brooks *et al.* (2001) the inner sphere transverse relaxation rate

$$R2_{IS} = F_b t_{ex} (\Delta\omega_{rms})^2 \qquad 1\text{-}5$$

and the outer sphere relaxation rate

$$R2_{OS} = \frac{4}{9}\nu\tau_D (\Delta\omega_{rms})^2, \qquad 1\text{-}6$$

where F_b is the fraction of bound water molecules, $\Delta\omega_{rms}$ is the root-mean-square angular frequency shift at a distance d from the magnetic particle, t_{ex} is the average exchange time, ν is the volume fraction of magnetic particles in the medium, and τ_D is the diffusive correlation time of water molecules in the medium. In the inner sphere the molecules bind to the magnetic particles, whereas in the outer sphere the water molecules just diffuse past the magnetic particles. The inner sphere effect is therefore larger than the outer sphere effect since in the inner sphere the water molecules experience higher magnetic field gradients and the interaction times are longer. However, for magnetic particles that are separated from water e.g. by a dextran or protein shell the outer-sphere effect predominantly causes the increase of the transverse relaxation rate R2 (Schenck & Zimmerman, 2004).

1.4.3. Effect of mesoscopic field inhomogeneities on R2' and Δf

The mesoscopic magnetic inhomogeneities caused by magnetic particles in a homogenous magnetic field

$$\Delta B_i \propto \left(\chi_i^p - \chi^b\right) B_0 \qquad 1\text{-}7$$

mainly depend on the differences between the magnetic susceptibilities of the magnetic particles and the surrounding medium χ_i^p and χ^b (Yablonskiy & Haacke, 1994). In case of para- or diamagnetism with $\left|\chi_i^p\right|, |\chi^b| \ll 1$ and $|\Delta B_z| \ll B_0$ it can be shown that the corresponding magnetization ΔM_z is a linear function of the magnetic susceptibility difference between the particles and the surrounding medium (Sharp & Saunders, 1995)

$$\Delta M_z \propto \left(\chi_i^p - \chi^b\right) \frac{B_0}{\mu_0}, \qquad 1\text{-}8$$

which simplifies further calculations as it allows analysis of the problem with Maxwell's equations for magnetostatics (Vanderlinde, 2004). The mesoscopic magnetic inhomogeneities caused by para- or diamagnetic particles with very simple geometries can be calculated analytically (Bhagwandien *et al.*, 1992; Lüdeke *et al.*, 1985; Sharp & Saunders, 1995), whereas for arbitrarily shaped magnetic particles and particle distributions they are typically calculated numerically using e.g. finite element methods (Silvester & Ferrari, 1996).

For example, the mesoscopic magnetic field inhomogeneities of a homogenous magnetic sphere with diameter d^p in the range of a typical MRI voxel size and the magnetic volume susceptibility χ^p, which is embedded in a homogenous medium with the magnetic volume susceptibility χ^b that extents into infinity, can be calculated analytically with Maxwell's equations of electrostatics in a polar coordinate system (r, θ, ϕ) (Lüdeke *et al.*, 1985; Sharp & Saunders, 1995). Assuming that the sphere and the medium are immersed in a homogenous magnetic field B_0 then field inhomogeneities that are experienced by the water protons are

$$\begin{aligned} \Delta B_z^{in} &= -B^{\infty} && 0 \le |r| < d^p/2 \\ \Delta B_z^{out} &= -B_0 \frac{\chi^b - \chi^p}{3} \frac{(d^p/2)^3}{r^3} (3\cos^2\theta - 1) - B^{\infty} && |r| > d^p/2 \end{aligned} \qquad 1\text{-}9$$

with $B^{\infty} = B_0 2/3 \chi^b$, which are visualised in Figure 1-5 for a diamagnetic sphere.

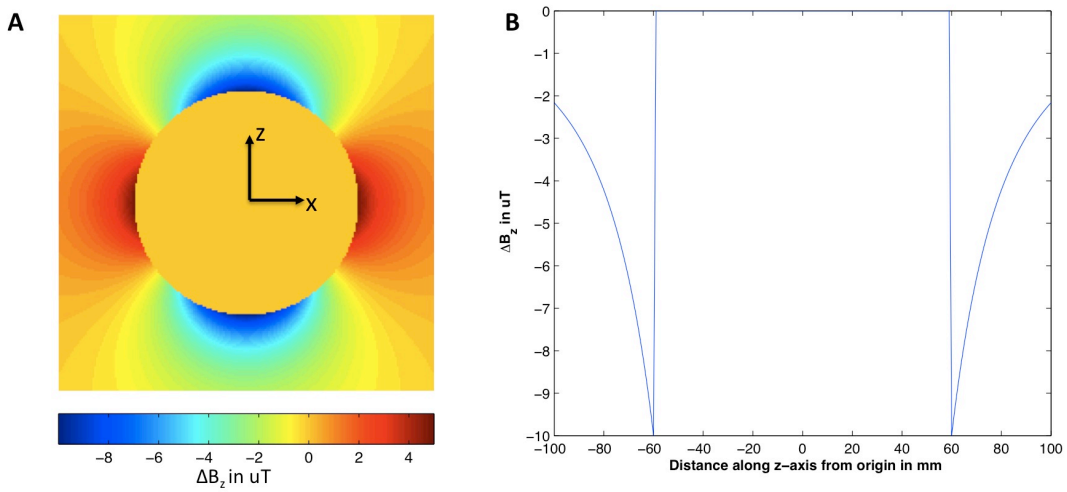

Figure 1-5: Mesoscopic field inhomogeneities around a diamagnetic sphere. Figure (**A**) shows the mesoscopic field inhomogeneities $\boldsymbol{\Delta B_z(r)}$ around a homogenous sphere with $\boldsymbol{\chi^p = -10ppm}$ embedded in a homogenous medium with $\boldsymbol{\chi^b = 0ppm}$, which were calculated with Equation **1-9**. Figure (**B**) shows $\boldsymbol{\Delta B_z(r)}$ along the z-axis indicating that large field inhomogeneities at the top and the bottom of the sphere are caused by the discontinuity in $\boldsymbol{\chi(r)}$ at the sphere edges. The latter result is equal to the analytical result shown in Figure 2 in De Munck *et al.* (1996).

These results differ from the analytical results obtained directly from Maxwell's equations by the sphere of Lorenz correction (Sharp & Saunders, 1995), which accounts for the fact that the magnetic field experienced by the water protons is different from the one present in a homogenous medium. Furthermore the magnetic field at the centre of the sphere and far away from the sphere is $\Delta B_z = -B^{\infty} = -B_0\, 2/3\chi^b$ indicating that both fields are homogenous and only depend on the susceptibility of the surrounding medium.

Given the mesoscopic magnetic field inhomogeneities the Larmor frequency shift caused by para- and diamagnetic particles in a homogenous magnetic field is

$$\Delta f(\boldsymbol{r}) = \frac{\gamma}{2\pi}\Delta B_z(\boldsymbol{r}), \qquad 1\text{-}10$$

where γ is the gyromagnetic ratio, which is $\gamma \approx 2\pi\, 42.576\, 10^6 s^{-1}T^{-1}$ or $\gamma/(2\pi) \approx 42.576\, MHz/T$ for water protons. The gradient-echo MRI signal of a voxel with volume V after quadrature demodulation is (Yablonskiy & Haacke, 1994)

$$s(t) \propto \frac{1}{V}\int_V \exp(-i2\pi\Delta f(\boldsymbol{r})t)\, d\boldsymbol{r} = \exp\,(-R2't - i2\pi\Delta f t), \qquad 1\text{-}11$$

which shows that the measured reversible relaxation rate R2', as well as the Larmor frequency shift Δf of a voxel in an MRI experiment are caused by integrating the magnetic field inhomogeneities over a voxel volume. If $\Delta f(\boldsymbol{r})$ can be expanded as a

Taylor series, it can be shown that the zero-order Taylor series component $\boldsymbol{r}^0$ only affects Δf and not $R2'$. Furthermore, higher order Taylor series components, i.e. microscopic field variations, have less effect on $R2'$ and Δf than lower order Taylor series components, i.e. mesoscopic field variations.

Yablonskiy and Haacke (1994) used this theory to derived a closed solution for the integral in Equation 1-11 for calculating R2' caused by MRI contrast agents and microvessels in tissue, which were modelled as randomly distributed magnetic spheres and cylinders. Kiselev and Posse (1999) extended this theory to include diffusion effects. A computational method for solving Equation 1-11 in case of randomly distributed particles is presented in Müller-Bierl *et al.* (2006).

1.4.4. MRI of ferritin

Brain ferritin contains up to 4500 Fe^{3+} ions in form of the mineral phase ferrihydrite that are encapsulated in a hollow protein shell (Schenck & Zimmerman, 2004). The ferrihydrite core of ferritin is antiferromagnetic, however, at body temperature it shows characteristics of para- and superparamagnetic particles Gossuin *et al.* (2009). Further biological and chemical properties of ferritin were summarized in Section 1.3.2.

Ferritin was first recognized on MRI as hypointensities on T2w MRI that was later explained by its strong effect on the transversal relaxation rate R2 and much weaker effect on the longitudinal relaxation rate R1 (Brooks *et al.*, 1998; Drayer *et al.*, 1986). A theoretical model for estimating the transverse relaxation rate R2 of ferritin was based on the outer sphere model (Section 1.4.2) as described in Gossuin *et al.* (2009). In particular, Gossuin *et al.* (2000) showed that the transverse relaxation rate R2 of ferritin in solution increases linearly with the magnetic field strength, which was unexpected for a nanoparticle solution. Vymazal *et al.* (1996) showed that the transversal relaxation rate R2 not only depends on the concentration of ferritin solutions but also the amount of iron per ferritin molecule indicating that R2 correlates with the iron concentration and not just ferritin concentration. The R2 relaxation rates of ferritin are 2 to 3 times larger *in vivo* than *in vitro* due to the formation of ferritin clusters (Gossuin *et al.*, 2007), which causes a shift from the motional averaging regime towards the static dephasing regime (Section 1.4.1).

1.5. Methods for assessing iron stores with MRI

In brain tissue iron not only occurs in form of ferritin but also in other forms, such as haemosiderin (Zecca *et al.*, 2004). Methods based on routine structural and quantitative MRI sequences were developed to increase the sensitivity of MRI to brain iron and for differentiating specific brain iron storage proteins and complexes, such as ferritin and haemosiderin.

1.5.1. Routine structural MRI

Routine structural MRI sequences, such as T1w, T2w and T2*w sequences, are used in clinical practice due to their short acquisition times and low amount of post processing involved compared to quantitative sequences. Brain iron typically causes hypointensities on T2w and T2*w MRI and no apparent signal change on T1w MRI relative to tissue with a lower iron content (Brass *et al.*, 2006). However, iron in form of haemosiderin can also cause hypointensities on T1w MRI due to the fact that haemosiderin is less water-soluble than ferritin (Vymazal *et al.*, 2000). T2*w and T2w MRI were found to be more sensitive to larger and smaller iron particles (Haque *et al.*, 2003), respectively. The sensitivity of T2*w MRI to brain iron can be increased by shortening the flip angle, increasing the echo time, as well as the repetition time in case of an unspoiled gradient-echo sequence (Chavhan *et al.*, 2009). T2*w MRI is predominantly used in the detection and classifications of microbleeds (Charidimou *et al.*, 2012; Cordonnier, 2010), stroke lesions (Wycliffe *et al.*, 2004), brain mineral deposits (Kruer *et al.*, 2012; Valdés Hernández *et al.*, 2012), as well as venous vascular malformations using deoxyhaemoglobin as an intrinsic MRI contrast agent (Mittal *et al.*, 2009; Reichenbach & Haacke, 2001).

Recently, two techniques were developed to further increase the contrast of brain iron on structural MRI; susceptibility weighted imaging (SWI; Haacke *et al.*, 2009) and susceptibility weighted angiography (SWAN; Annamraju *et al.*, 2008). The former method increases the brain iron contrast by combining the T2*w gradient-echo magnitude images with the corresponding high-pass filtered gradient-echo phase images. This improves the image contrast in case of a constant magnetic field inhomogeneities across a voxel (see Figure 7 in Haacke *et al.* (2009)), which would appear isointense on T2*w MRI (Equation 1-11). Conversely, the SWAN method

acquires T2*w gradient-echo magnitude images at up to 16 echo times that are subsequently used to calculate a weighted average MRI volume with a high signal-to-noise ratio and brain iron contrast (Annamraju *et al.*, 2008), where the latter comes from the increased susceptibility-weighted contrast obtained at later echo times. A recent review showed that both methods produce images with a similar contrast (Kunimatsu *et al.*, 2012). One of the advantages of SWAN over time of flight magnetic resonance angiography (TOF-MRA) is that this method can visualize both cerebral veins and arteries without MRI contrast (Boeckh-Behrens *et al.*, 2012).

Confounds in the detection of iron deposits on T2w and T2*w MRI are hypointensities caused by other magnetic particles, such as calcifications, vessels and susceptibility artefacts around the edges of the brain (Chavhan *et al.*, 2009). However, these artefacts are can be differentiated from iron deposits with additional information from other structural sequences, such as gradient echo phase images (Yamada *et al.*, 1996) or T1w MRI (Henkelman *et al.*, 1991; Wehrli, 2013).

1.5.2. Quantitative MRI relaxometry

Quantitative MRI relaxometry is used to estimate the water proton relaxation rates R1 (=1/T1), R2 (=1/T2) and R2* (=1/T2*). This is typically accomplished by acquiring an image series of a volume-of-interest with routine MRI sequences, where at least one sequence parameter is varied for each individual acquisition. Then the corresponding signal equation of the MRI sequence is fitted to the serial imaging data, which provides estimates of the relaxation rates (McRobbie *et al.*, 2003).

To date quantitative MRI (qMRI) relaxometry is still predominantly used in research although it already used in the clinic for the improved diagnosis and monitoring of several pathologies (Cheng *et al.*, 2012), such as Multiple Sclerosis (Ropele *et al.*, 2011), hepatic iron overload (St Pierre *et al.*, 2005), cartilage damage (Chan & Neu, 2013), as well as acute myocardial infarction (Zheng, 2013).

In research, qMRI relaxometry is widely used to visualize and quantify the iron content in the brain as reviewed in Haacke *et al.* (2005), Cheng *et al.* (2012) and Deoni (2010). Schenker *et al.* (1993) was one of the first studies that demonstrated that the transverse relaxation rates R2 of deep grey matter structures increase with age, which is caused by age-related brain iron deposition in the underlying tissue (Hallgren & Sourander, 1958). This finding was later confirmed by Aquino *et al.*

(2009) and Li *et al.* (2014), who estimated the trajectories of the effective transverse relaxation rates R2* of deep grey matter structures due to age-related iron deposition at magnetic field strengths of 1.5 T and 3 T. Lastly, Haacke *et al.* (2010) showed that the age-related increase of the transverse relaxation rates R2* can also be demonstrated with R2* values estimated from single-echo T2*w MRI. Although brain iron predominantly affects the R2 and R2* relaxation rates, Ogg and Steen (1998) demonstrated that the R1 relaxation rates of deep grey matter structures and the frontal white mater in normal ageing subjects also increase with age, and hence depend on the iron content of these structures. Recently, R1 maps were proposed as a complementary source of information for the improved characterisation of brain iron on MRI (Weiskopf *et al.*, 2013) since R1 is also influence by the chemical environment of the brain iron.

Several post-mortem studies were conducted for validating the effect of iron and confounding factors, such as the tissue susceptibility, on e.g. the R2 and R2* relaxation rates. Langkammer *et al.* (2010) measured the iron content in post-mortem grey and white matter samples with inductively coupled plasma mass spectrometry and showed that especially R2* correlates with those measurements, hence indicating that R2* is very sensitive to changes in brain iron. However, in white matter R2* provides less accurate estimates of the brain iron concentration than in grey matter since R2* in the white matter is additionally affected by the axonal fibre directions (Pasquale *et al.*, 2013) and the diamagnetic myelin sheets around the axons (Langkammer *et al.*, 2012), which both partly compensate the paramagnetic effect of brain iron. Recently, a post-mortem study (Birkl *et al.*, 2014) also investigated the temperature dependency of R1, R2 and R2* of brain tissue samples. This study found that R1 depends on temperature, whereas R2* only depends on temperature in case of paramagnetic grey matter tissue, where the temperature dependence is explained by the (Pierre) Currie law.

Lastly, efforts were also made to differentiate and estimate the amount of ferritin (dispersed iron) and haemosiderin (aggregated iron) in the brain. The aggregation state of iron theoretically can be estimated by quantifying the mesoscopic field inhomogeneities, since these correlate with the size of the magnetic particles as explained above. The mesoscopic field inhomogeneities can be quantified, for

example, with the gradient echo sampled spin echo (GESSE) sequence (Yablonskiy, 1998), as well as with the gradient echo sampling of free induction decay and echo (GESFIDE) sequence (Jin *et al.*, 2013; Ma & Wehrli, 1996). Recently, Sedlacik *et al.* (2014) developed a novel method that estimates mesoscopic field inhomogeneities from R2' maps, which are simply calculated by subtracting R2 from R2* maps. The latter method has the advantage over the former methods that it can be more easily implemented in a clinical setting since the former sequences are not available on most MRI scanners. Noticeably, the latter study showed that R2' of most deep grey matter structures increases with age indicating that brain iron becomes more aggregated. Other methods for differentiating ferritin from larger iron particles in tissue are based on the fact that aggregation leads to a non-exponential gradient-echo signal decay (Jensen & Chandra, 2002; Pintaske *et al.*, 2006), which results from the fact that mesoscopic field inhomogeneities of larger particels do not follow a Lorenzian distribution (Haacke *et al.*, 1999). Recently, Jensen *et al.* (2010) developed a method based on this observation, which, however, has to date only been applied in the liver.

1.5.3. Larmor frequency shift and quantitative susceptibility mapping

Both Larmor frequency shift mapping and quantitative susceptibility mapping are based on gradient-echo phase images, which are predominantly affected by mesoscopic, as well as macroscopic field inhomogeneities (Equation 1-11) whereas the contributions from microscopic field inhomogeneities are attenuated. During the post-processing of the acquired phase images the mesoscopic field inhomogeneities are separated from the macroscopic field inhomogeneities, since the former convey the information about the local iron distribution, whereas the latter mostly arise due to main field inhomogeneities and susceptibility artefacts. This separation is typically accomplished by unwrapping the acquired phase images and then high-pass filtering the obtained images. The reconstruction of quantitative susceptibility maps requires additional filtering to remove field inhomogeneities that arise due to discontinuities in the susceptibility distribution and do not reflect the underlying iron distribution.

Phase unwarping of the acquired phase images is necessary since the scanner typically maps phase values that lie outside the range $-\pi \ldots \pi$ to the corresponding values within this range, which causes so-called phase wraps. The original phase

value range can be restored and the phase wraps removed with phase unwrapping methods, such as presented in Bagher-Ebadian *et al.* (2008) based on Fourier transformation or in Witoszynskyj *et al.* (2009) based on region growing.

Larmor frequency shift maps are then obtained by scaling the unwrapped and high-pass filtered gradient-echo phase images by 2π (Equation 1-10). High-pass filtering is typically achieved with a homodyne filter (Deistung *et al.*, 2008) that is based on a low-pass Gauss filter (He & Yablonskiy, 2009). The contrast of the Larmor frequency shift maps is mainly influenced by the local magnetic susceptibility distribution $\Delta\chi(\boldsymbol{r})$ of the underlying tissue relative to the susceptibility of water (He & Yablonskiy, 2009). Therefore these maps can be used to differentiate paramagnetic tissue $\Delta\chi(\boldsymbol{r}) > 0$ and diamagnetic tissue $\Delta\chi(\boldsymbol{r}) < 0$, which are therefore associated with positive and negative Larmor frequency shifts. However, the limitation of Larmor frequency shift maps is that their contrast also depends on the high-pass filtering method, on field inhomogeneities that are caused by discontinuities in the magnetic susceptibility distribution of the underlying tissue (Figure 1-5), and orientation of the tissue relative to the main magnetic field B_0.

Quantitative susceptibility mapping (qSM) measures the absolute volume susceptibility of the underlying tissue and addresses the limitations of Larmor frequency shift mapping. QSM is based on the fact that the Larmor frequency shifts caused by mesoscopic field inhomogeneities (Equation 1-10) can be calculated for a given susceptibility distribution with the following convolution operation (Marques & Bowtell, 2005; Salomir *et al.*, 2003)

$$\Delta f(\boldsymbol{r}) = \frac{\gamma}{2\pi} B_0 \mathcal{F}^{-1}\left\{\frac{1}{3} - \frac{k_z^2}{\|\boldsymbol{k}\|^2}\right\} \otimes \chi(\boldsymbol{r}), \qquad 1\text{-}12$$

where $\mathcal{F}$ is the Fourier transformation operator, k_z is the component of the k-space vector $\boldsymbol{k}$ parallel to the main magnetic field. It can be shown that the inverse operation for calculating the susceptibility distribution from Larmor frequency shifts can be accomplished with

$$\chi(\boldsymbol{r}) = \mathcal{F}^{-1}\left\{\mathcal{F}\left\{\frac{2\pi\Delta f(\boldsymbol{r})}{-\gamma B_0}\right\}\left(\frac{1}{3} - \frac{k_z^2}{\|\boldsymbol{k}\|^2}\right)\right\}. \qquad 1\text{-}13$$

Quantitative susceptibility maps can therefore be calculated by deconvoluting the Larmor frequency shift maps (Shmueli *et al.*, 2009), which, however, introduces

stripe patterns in the reconstructed maps since the deconvolution operation becomes numerically unstable at certain k-space vector orientations. This limitation was addressed by subsequent methods (Bilgic *et al.*, 2012; De Rochefort *et al.*, 2010; Li *et al.*, 2014; Schweser *et al.*, 2010), which increased the quality of the quantitative susceptibility maps at the expense of the post-processing complexity. Recent post-mortem validations studies of qSM algorithms showed that quantitative susceptibly mapping provides accurate estimates of the tissue iron concentration, especially in grey matter (Langkammer *et al.*, 2012; Sun *et al.*, 2015; Zheng *et al.*, 2013).

1.6. Aims and outline of the thesis

The developed world faces the challenge of an ageing population, which is accompanied by rising social and health care costs. Many governments have realized that 'successful' ageing, which is ageing without any major disabilities, is an important factor for managing these rising costs. MRI plays an important role in the early detection and monitoring of age-related disease, such as stroke and dementia, as well as research into age-related decline.

This thesis investigates the role of iron in brain ageing, which represents an paramagnetic trace metal that is essential for the cell metabolism and can be detected with MRI. The primary focus of this thesis is the characterisation of age-related mineralization as an additional iron storage mechanism in the basal ganglia, where iron is believed to enter the brain. These basal ganglia mineral deposits appear as small, multifocal hypointensities on routine structural T2*w MRI, where they represent mimics of cerebral microbleeds, and possibly arise from mineralisation in and around the penetrating arteries. Basal ganglia T2*w hypointensities potentially represent an imaging biomarker of an age-related imbalance in brain iron homeostasis, which could therefore be useful for the detection and prevention of age-related diseases, such as small vessel disease.

The main aims of this thesis are: (i) the characterisation of focal basal ganglia hypointensities on routine T2*w, T1w, and T2w MRI of a representative sample of an ageing cohort; (ii) the development of a fully automated method for their segmentation on routine T2*w and T1w MRI; (iii) the development and validation of a iron-sensitive, quantitative MRI protocol for the improved characterisation of brain

iron; (iv) the validation of the developed segmentation method in an independent ageing cohort, as well as the confirmation with quantitative MRI that basal ganglia mineral deposits indeed represent brain iron stores.

This thesis consists of four chapters with results from original research, which is followed by the final chapter, which contains discussions and conclusions to this work. Chapter 2 describes the characteristic spatial distribution and morphology of basal ganglia T2*w hypointensities, as well as their characteristic appearance on T1w, T2w, and on T2*w MRI. Chapter 3 describes the developed automated method for the segmentation of basal ganglia T2*w hypointensities and its validation in a custom phantom with mineral deposit models and in a subject sample with a range of basal ganglia mineral deposits. Chapter 4 describes the developed multi-parameter MRI relaxometry protocol and its validation with a custom phantom and gold standard methods, as well as in ten healthy volunteers. Chapter 5 describes the validation of the automated method in a large sample of another ageing cohort as well as the additional findings obtained with R2* and Larmor frequency shift maps.

Chapter 2 Characterisation of multifocal T2*-weighted MRI hypointensities in the basal ganglia of elderly, community-dwelling subjects

This chapter was published as: Glatz A., Valdés Hernández M.C., Kiker A.J., Bastin M.E., Deary I.J., Wardlaw J.M. (2013). Characterisation of multifocal T2*-weighted MRI hypointensities in the basal ganglia of elderly, community-dwelling subjects. *NeuroImage* 82:470-80.

2.1. Abstract

Multifocal T2*-weighted (T2*w) hypointensities in the basal ganglia, which are believed to arise predominantly from mineralized small vessels and perivascular spaces, have been proposed as a biomarker for cerebral small vessel disease. This study provides baseline data on their appearance on conventional structural MRI for improving and automating current manual segmentation methods. Using a published thresholding method, multifocal T2*w hypointensities were manually segmented from whole brain T2*w volumes acquired from 98 community-dwelling subjects in their early 70s. Connected component analysis was used to derive the average T2*w hypointensity count and load per basal ganglia nucleus, as well as the morphology of their connected components, while nonlinear spatial probability mapping yielded their spatial distribution. T1-weighted (T1w), T2-weighted (T2w) and T2*w intensity distributions of basal ganglia T2*w hypointensities and their appearance on T1w and T2w MRI were investigated to gain further insights into the underlying tissue composition. In 75/98 subjects, on average, 3 T2*w hypointensities with a median total volume per intracranial volume of 50.3 ppm were located in and around the globus pallidus. Spatial probability maps suggested an association between T2*w hypointensities and the point of entry of lenticulostriate arterioles into the brain parenchyma. T1w and T2w and especially the T2*w intensity distributions of these hypointensities were generally not normally distributed indicating an underlying inhomogeneous tissue structure. In conclusion, these findings support that T2*w hypointensities may be caused by mineralized small vessels and perivascular spaces.

2.2. Introduction

The basal ganglia (Figure 2-1) are a collection of grey matter nuclei that are found at the centre of the brain. They contain neuronal networks that promote optimal motor and cognitive control (Graybiel, 2005). These structures are highly vascularized by small arteries, such as the lenticulostriate arteries, that branch of the middle cerebral and carotid artery (Feekes *et al.*, 2005).

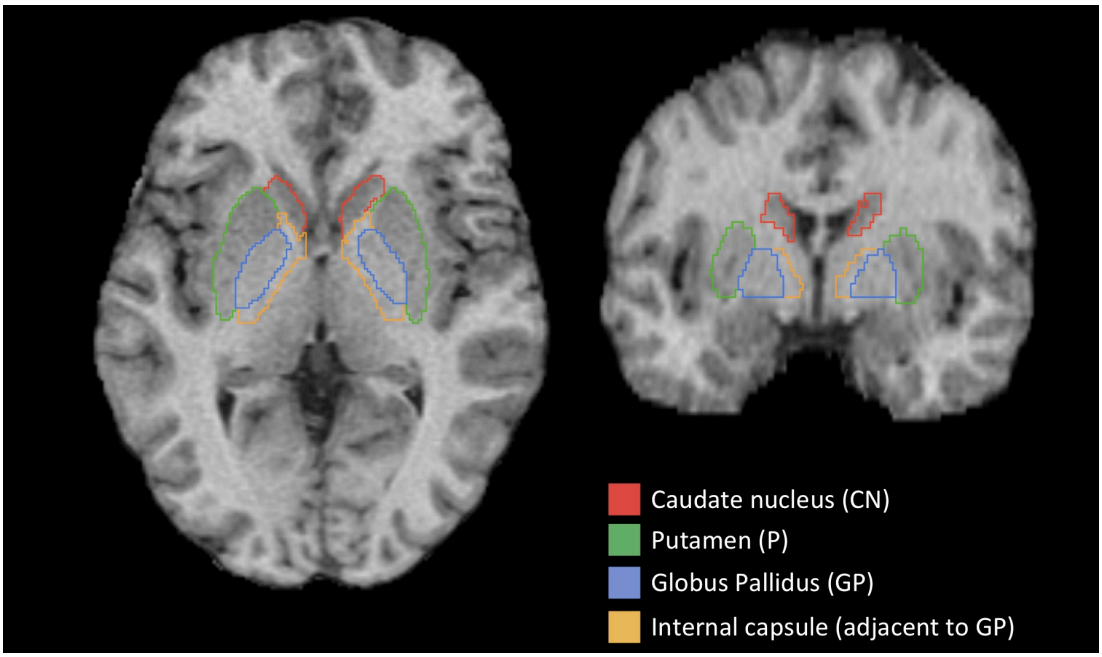

Figure 2-1: The anatomy of the basal ganglia. This figure shows the basal ganglia of a healthy volunteer on axial and coronal T1w MRI slices. The color masks indicate the perimeters of the individual basal ganglia structures, which were subsequently investigated in this study. The globus pallidus and the putamen form the lentiform nucleus, whereas the caudate, putamen and nucleus accumbens (not shown) form the striatum.

In the basal ganglia multifocal hypointensities are typically found on T2*-weighted (T2*w) structural MRI of elderly, otherwise healthy subjects (Penke *et al.*, 2012). They are believed to arise from mineralized tissue predominantly associated with iron encrustations (ferrunginations) and calcifications of lenticulostriate (perforating) arterioles and perivascular spaces (Casanova & Araque, 2003). T2*w hypointensities in the basal ganglia have generally been considered asymptomatic features of ageing and only a few studies have documented their chemical composition. Slager and Wagner (1956) analysed paraffin-embedded autopsy tissue from 200 brains and reported that iron is typically deposited in an organic matrix, which is then followed by the deposition of other trace metals, such as calcium.

Morris *et al.* (1992) visualized iron encrustations around the lenticulostriate arteries of the basal ganglia in frozen samples from 14 brains using Perl's staining method with diaminobenzidin intensification. They reported that iron encrustations did not seem to originate from leaking blood vessels, since they were mostly found in perivascular areas.

Histochemical and chemical methods are still considered the "gold standard" for assessing trace metals in tissue. Brain iron, for example, is commonly visualized with Perl's Prussian Blue tissue stain and can be quantified with the orthophenanthroline method combined with a colorimetrical technique (Hallgren & Sourander, 1958). However, MRI has become the *de facto* standard for non-invasively visualizing iron and mineral deposits in the brain (Drayer *et al.*, 1986; Schenck & Zimmerman, 2004; Valdés Hernández *et al.*, 2012). In this modality, endogenous magnetic particle deposits accelerate the realignment of water proton spins along the main magnetic field direction as well as their dephasing in the transverse plane. However, their predominant effect depends on their chemical environment (Brass *et al.*, 2006; Schenck & Zimmerman, 2004). This is characterized by a localized shortening of T1, T2 and T2* relaxation times and can lead to focal hyperintensities on T1-weighted (T1w), and hypointensities on T2-weighted (T2w) and T2*w MRI. As reviewed in Section 1.4, T1 and T2 shortening caused by microscopic magnetic particles is commonly explained by the inner and outer sphere theory. T2* shortening is always equal or higher than T2 shortening since 1/T2*=1/T2+1/T2' where the T2' relaxation time accounts for additional proton spin dephasing due to (i) mesoscopic field gradients caused by magnetic susceptibility differences among tissues and chemical shift effects, and (ii) macroscopic field gradients used for spatial encoding and caused by susceptibility artefacts. Notably, flow (Reichenbach *et al.*, 1997) can also cause focal hypointensities on T2*w MRI that mimic iron or mineral deposits. Local changes in tissue composition (Henkelman *et al.*, 1991; Kruer *et al.*, 2012; Valdés Hernández *et al.*, 2012; Vymazal *et al.*, 2000), such as a decrease in the water proton density, can cause hypointensities on T1w MRI.

MRI sequences and post-processing methods for identifying and quantifying iron and mineral stores in the brain were reviewed in Haacke *et al.* (2005), Ropele *et al.*

(2011) and Valdés Hernández *et al.* (2012), as well as in Section 1.5. Novel methods include susceptibility weighted imaging (SWI; Haacke *et al.*, 2009), and quantitative techniques that measure the T2 (Bartzokis *et al.*, 2007), T2* (Aquino *et al.*, 2009; Langkammer *et al.*, 2010) and magnetic susceptibility $\Delta\chi$ (De Rochefort *et al.*, 2010; Schweser *et al.*, 2010) parameters of brain tissue directly. However, daily clinical practice still relies mostly on conventional structural MRI sequences.

In this study, we characterize the appearance of basal ganglia T2*w hypointensities in a group of community-dwelling subjects in their early 70s. This study provides statistics of their count, load and morphological properties per basal ganglia nuclei and their spatial distribution, discusses potential difficulties in their segmentation, and derives their multimodal appearance as a first step towards their application as a possible biomarker for small vessel disease.

2.3. Materials and Methods

2.3.1. Subjects and MRI protocol

T1w, T2w and T2*w whole brain volumes were acquired from the Lothian Birth Cohort 1936 (LBC1936; Deary *et al.*, 2012; Deary *et al.*, 2007; Wardlaw *et al.*, 2011). All participants were imaged using a GE Signa HDxt 1.5 T clinical scanner (Milwaukee, WI, USA) equipped with a self-shielding gradient set (40 mT/m maximum gradient strength) and manufacturer supplied 8-channel phased-array head coil; relevant scan parameters are listed in Table 2-1.

The LBC1936 is a longitudinal study of cognitive ageing that originally recruited a group of 1091 community-dwelling individuals resident in the Edinburgh and Lothian areas of Scotland who were born in 1936. Approximately three years after they were first recruited into the study, 700 subjects underwent brain MRI at a mean age of 72.5 years (SD 0.7 years). The MRI scans of all participants were categorized according to the General and Putaminal Visual Rating Scale (Valdés Hernández *et al.*, 2011). For our study, a sample was generated containing 100 randomly selected subjects from each category of the General and Putaminal Visual Rating Scale. Two subjects of the sample were excluded due to missing MRI data, which left 98 subjects (45 females) for further analysis.

A representative LBC1936 subject, without major artefacts, significant white matter lesion load or any incidental findings on structural MRI, was chosen as a reference for spatial normalization and intensity standardization. This subject was selected based on head size, brain shape and spatial intensity distribution criteria using the Mahalanobis distance (De Maesschalck *et al.*, 2000).

Table 2-1: Relevant LBC1936 MRI sequences and their parameters. The complete LBC1936 MRI protocol is described in Wardlaw (2011).

Sequence	IR-prep FSPGR (3D)	FSE (2D)	GRASS (2D)
Contrast type	T1-weighted	T2-weighted	T2*-weighted
FOV in mm^2	256 x 256	256 x 256	256 x 256
Orientation	Coronal	Axial	Axial
Slice thickness in mm	1.3	2	2
Acquisition matrix	256 x 256 [a]	256 x 256	256 x 256 [a]
Flip angle in degrees	8	-	20
TI/TE/TR in ms	500/4/9.8	-/102/11320	-/15/940
Bandwidth in kHz	15.63	20.83	12.5

[a] After interpolation by the scanner software.

2.3.2. Semi-automated segmentation of focal T2*w hypointensities

A trained rater (AJK) used Analyze 10.0 (Mayo Clinic, Rochester, MN, USA) to semi-automatically segment focal hypointensities (Figure 2-2) in all brain regions on the T2*w volumes with a local thresholding method described in Valdés Hernández *et al.* (2011), which for each subject k were saved in form of basal ganglia T2*w hypointensity masks $\mathcal{M}_k^{Hypo}$. The rater also delineated regions within the T2*w hypointensities that appeared hypointense on T1w MRI, since they potentially relate to a change in the composition of the underlying tissue (Kruer *et al.*, 2012; Valdés Hernández *et al.*, 2012). The rater segmented 29 subjects twice to estimate the intra-rater variability. The similarity between the T2*w hypointensity masks of the first and second passes was measured using the Jaccard index (Shattuck *et al.*, 2009).

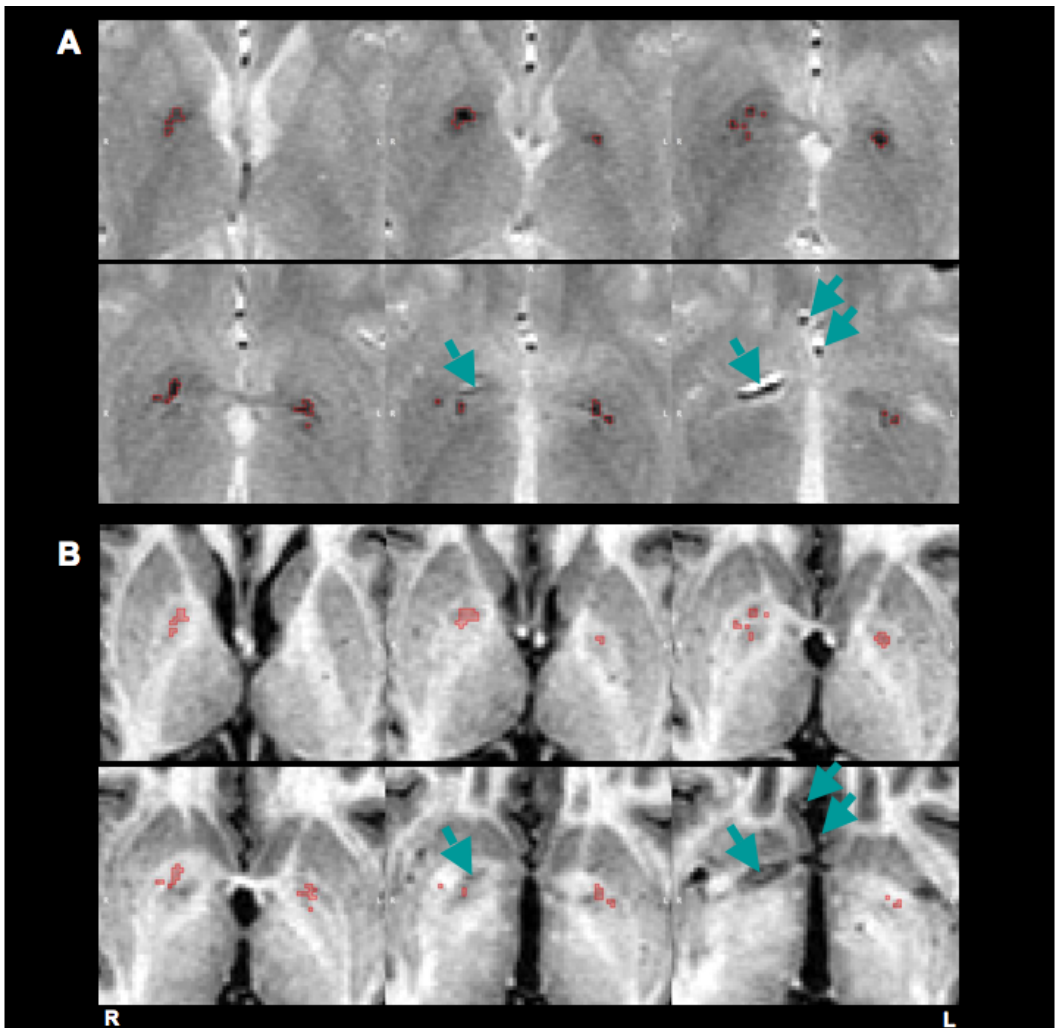

Figure 2-2: Focal T2*w hypointensities in the basal ganglia of a typical subject. The perimeters of the T2*w hypointensity masks from the rater are indicated by red lines on top of T2*w **(A)** and co-registered T1w axial slices **(B)**. This particular subject just exhibits multifocal T2*w hypointensities in the globus pallidus. In more severe cases, T2*w hypointensities are also found in the internal capsule, putamen and caudate. Arrows indicate arterial structures, which cause signal voids on T2*w MRI and mimic T2*w hypointensities These features were excluded by the rater based on their very linear appearance on T2*w and T1w MRI (the linearity can be apparent either within a slice or across adjacent slices) and their hypointense appearance on T1w MRI relative to the surrounding tissue.

2.3.3. Preprocessing

2.3.3.1. Co-registration of T1w, T2w and T2*w volumes

All T1w and T2w volumes were affine registered to the corresponding T2*w volumes using FSL FLIRT (Jenkinson *et al.*, 2002) from the FMRIB Software Library (http://fsl.fmrib.ox.ac.uk) with the correlation ratio as the optimization criteria and sinc interpolation with default parameters. In the T2*w volumes, non-brain structures were removed using FSL BET (Smith, 2002) and the obtained brain masks were used to estimate intracranial volume (ICV; Keihaninejad *et al.*, 2010).

All non-brain structures in the T1w and T2w volumes were then removed by linearly transforming the brain masks from T2*w to T1w and T2w space and applying them to the corresponding volumes. Non-anatomical intensity variations (bias fields) were finally removed from the brain-extracted T1w, T2w and T2*w volumes with N4 (Tustison *et al.*, 2010).

2.3.3.2. Automated segmentation of basal ganglia nuclei and internal capsule

The basal ganglia nuclei and the thalamus were segmented on the T1w volumes using FSL FIRST (Patenaude *et al.*, 2011) with default parameters. FSL FIRST is a model based brain structure segmentation tool that fits deformable shapes of brain structures to T1w volumes so that their spatial and T1w surface intensity distributions optimally coincides with those derived from training data. The so obtained basal ganglia and thalamus masks were then linearly transformed to T2*w space with the corresponding registration matrices (Section 2.3.3.1). Additional internal capsule masks were calculated by dilating the globus pallidus masks with a disk shaped 2D kernel with radius 6 mm and subtracting the corresponding thalamus, globus pallidus and caudate masks. The final set of masks required for the subsequent analysis consisted of caudate, putamen, globus pallidus and adjacent internal capsule masks.

2.3.3.3. Automated segmentation of grey/white matter and cerebrospinal fluid

Grey/white matter and cerebrospinal fluid (CSF), which were required for the subsequent intensity standardization, were segmented on co-registered T1w and T2*w volumes using FSL FAST (Zhang *et al.*, 2001) in multi-channel segmentation mode. The *a priori* tissue class number was set to four to obtain masks selecting grey/white matter, CSF and other voxels. As the volumes were already bias-field corrected, the bias-field correction method of FSL FAST was disabled. Partial volume estimation was enabled to estimate the location of voxels that contained a mixture of tissues (mixels), which were subsequently excluded from the grey/white matter and CSF masks to decrease the random variation of the corresponding intensity histograms. All automatically generated masks were visually checked for major segmentation artefacts, and corrected if necessary.

2.3.3.4. Intensity standardization of T1w, T2w and T2*w volumes

To compare signal intensities of structural T1w, T2w and T2*w volumes across subjects requires their intensities to be standardized (Jager & Hornegger, 2009). The method developed by Hellier (2003) was used for the intensity standardization of all subject volumes, and works by transforming the signal intensities of the subject volumes to maximise the similarity between intensity histograms of the transformed volumes and the histogram of a reference volume. Here, the signal intensities of all T1w, T2w and T2*w volumes were linearly transformed to equalize the robust grey/white matter and CSF intensity means of corresponding volumes from the representative and given subject.

Let $\mathcal{M} \subset \mathbb{Z}^3$ be a set that indexes a $n_x \times n_y \times n_z$ voxel lattice denoted by

$$\mathcal{M} = \{i = (x, y, z) | 1 < x \leq n_x, 1 < y < n_y, 1 < z \leq n_z\} \quad 2\text{-}1$$

then $s_{i,j}$ is the original signal intensity of voxel $i \in \mathcal{M}$ and volume $j \in \{T1w, T2w, T2^*w\}$ of a subject. The standardized signal intensities $s_{i,j}^{std}$ were obtained with the linear transformation

$$s_{i,j}^{std} = a_j s_{i,j} + b_j. \quad 2\text{-}2$$

The coefficients a_j and b_j were estimated by minimising

$$\sum\nolimits_{\forall t} (s_{j,ref}^{t,\mu} - (a_j \, s_j^{t,\mu} + b_j)) \rightarrow min, \quad 2\text{-}3$$

where $s_{j,ref}^{t,\mu}, s_j^{t,\mu}$ with $t \in \{GM, WM, CSF\}$ are the robust means of the grey/white matter and CSF signal intensities of a representative and given subject, which were selected by the corresponding masks $\mathcal{M}_{ref}^t \subset \mathcal{M}$ and $\mathcal{M}_k^t \subset \mathcal{M}$. These robust means were estimated with M-estimators of location with the psi-function (LIBRA toolbox; Verboven & Hubert, 2005).

For spatial normalization and intensity standardization a representative LBC1936 subject, without major artefacts, significant white matter lesion load or any incidental findings on structural MRI, was chosen as a reference. This subject was selected based on head size, brain shape and spatial intensity distribution criteria using the Mahalanobis distance (De Maesschalck *et al.*, 2000).

2.3.3.5. Connected component labelling of focal T2*w hypointensities

The locations of individual T2*w hypointensities, i.e. the connected components of the T2*w hypointensity masks from the rater (six-connected neighbourhood), that intersected at least 50% with the basal ganglia and internal capsule masks (Section 2.3.3.2) were labelled automatically. The remaining individual T2*w hypointensities were labelled manually and excluded from further processing. T2*w hypointensities that intersected with the internal capsule masks were not excluded because the border between globus pallidus and internal capsule was hard to define and the rater found a marked amount of T2*w hypointensities in this region. All labels were manually checked and corrected if necessary.

Mathematically, the labels of individual T2*w hypointensities were defined as follows. Let $\mathcal{H} = \{1,2,\dots,h^{max}\}$ be the set with the indices of all T2*w hypointensities from the basal ganglia and internal capsule of a subject, which were obtained with the Matlab function 'bwlabeln' and the basal ganglia T2*w hypointensity mask $\mathcal{M}^{Hypo}$ of a subject (Section 2.3.2). The label l_h of an individual T2*w hypointensity $h \in \mathcal{H}$ is then defined by the maximal intersection between its mask $\mathcal{M}_h^{Hypo} \subset \mathcal{M}^{Hypo}$ and the structural masks $\mathcal{M}_l^{BG} \subset \mathcal{M}$

$$l_h = \max_{l \in L} \left| \mathcal{M}_h^{Hypo} \cap \mathcal{M}_l^{BG} \right|, \qquad 2\text{-}4$$

where $L = \{11,12,13,14,50,51,52,55\}$ denoted the FSL FIRST labels for the left and right basal ganglia nuclei with two additional labels, 14 and 55, for the left and right internal capsule. In case of an ambiguous maximum, for example if exactly half of the T2*w hypointensity volume extended into two adjacent structures, the label l that corresponded to the most hypointense part of the T2*w hypointensity was chosen.

2.3.4. Analysis of basal ganglia T2*w hypointensity masks

T2*w hypointensity masks from the rater were analysed with a processing pipeline that was mainly implemented in Matlab 2011b (The MathWorks Inc., Natick, MA). The pipeline for generating the spatial distribution map of basal ganglia T2*w hypointensities was implemented in Bash (http://www.gnu.org).

2.3.4.1. Count and load of basal ganglia T2*w hypointensities

The count and load of basal ganglia T2*w hypointensities of a subject were derived automatically with the T2*w hypointensity labels (Section 2.3.3.5), and were

determined as follows. Let the set with all indices of T2*w hypointensities from a structure with label l be

$$\mathcal{H}_l = \{h | l_h = l\}. \quad 2\text{-}5$$

Then the T2*w hypointensity count per structure is

$$n_l = |\mathcal{H}_l|, \quad 2\text{-}6$$

and the total T2*w hypointensity load V_l^{norm} per structure is

$$V_l^{norm} = \frac{V_l}{V^{ICV}} = \frac{\left|\mathcal{M}_l^{Hypo}\right|}{V^{ICV}/V^{vox}}, \quad 2\text{-}7$$

where V_l is the total volume of T2*w hypointensities in a structure, V^{ICV} is the ICV, V^{vox} is the volume of a single voxel and

$$\mathcal{M}_l^{Hypo} = \bigcup_{h \in H_l} \mathcal{M}_h^{Hypo}, \quad 2\text{-}8$$

is the mask of all T2*w hypointensities from a structure. The volumes were normalized by ICV since this accounts for the variation of T2*w hypointensity volume with head size (Penke *et al.*, 2012). The two-sided Wilcoxon rank sum test was used to determine the significance of T2*w hypointensity count and load differences in left and right hemisphere structures.

2.3.4.2. Morphology of individual basal ganglia T2*w hypointensities

Morphological properties of individual T2*w hypointensities that were quantified included their volume, maximum in-plane extent (maximum area), and roundness and sphericity. Roundness and sphericity measures (Wadell, 1932) were originally developed for continuous 3D objects. Therefore similar measures, i.e. the compactness (Bribiesca, 2008) and relative anisotropy, were developed for characterizing discrete 3D objects, and have recently been used to characterize brain microbleeds (Barnes *et al.*, 2011). The compactness and relative anisotropy range from 0 to 1, with perfectly smooth and round discrete 3D objects having a compactness of 1 and relative anisotropy of 0. The morphological properties were calculated with the masks $\mathcal{M}_h^{Hypo}$ of all individual T2*w hypointensities of a subject after nearest neighbour interpolation to a 1 mm isotropic voxel lattice.

2.3.4.3. Spatial probability distribution of basal ganglia T2*w hypointensities

The spatial probability distribution of basal ganglia T2*w hypointensities was estimated by linearly aggregating the spatial probability maps $\boldsymbol{p}_{\mathbb{k}}^{spat}$ of all subjects $\mathbb{k} \in \{1,2,\dots,\mathbb{k}^{max}\}$ (Stone, 1961)

$$\boldsymbol{p}^{spat} = \sum_{\mathbb{k}=1}^{\mathbb{k}^{max}} w_{\mathbb{k}} \boldsymbol{p}_{\mathbb{k}}^{spat} \qquad 2\text{-}9$$

with equal weights $w_k = 1/\mathbb{k}^{max}$. The spatial probability maps are defined as $\boldsymbol{p}_{\mathbb{k}}^{spat} = \left(p_{1,\mathbb{k}}^{spat}, p_{2,\mathbb{k}}^{spat}, \dots, p_{i^{max},\mathbb{k}}^{spat}\right)^T$, where $p_{i,\mathbb{k}}^{spat}$ represent the estimated probability densities associated with a reference space voxel. These maps were obtained by non-linearly transforming the T2*w hypointensity mask of a subject $\mathcal{M}_{\mathbb{k}}^{Hypo}$ (Section 2.3.2) to the T1w reference space of the chosen representative subject (Section 2.3.1) and normalizing them. To obtain the warp fields for the non-linear transformation, the T1w volume from the representative subject was first rigidly registered to the MNI152 2 mm template using FSL FLIRT (Jenkinson *et al.*, 2002). Then the T2*w volumes were non-linearly registered to the T1w volume from the representative subject using FSL FNIRT (Andersson *et al.*, 2008).

2.3.5. Analysis of signal intensities selected by focal T2*w hypointensity masks

Segmentation thresholds of basal ganglia T2*w hypointensities were derived to identify factors influencing their segmentation. Then the average T1w, T2w and T2*w intensity probability distributions of these hypointensities and their appearance on T1w and T2w MRI relative to normal-appearing tissue were measured to infer further information about the underlying tissue structure and its composition. This part of the analysis pipeline was fully implemented in Matlab 2011b.

2.3.5.1. Segmentation thresholds of basal ganglia T2*w hypointensities

The segmentation thresholds of the rater s_l^{Thresh} were defined as the 97th-percentiles of the standardized T2*w hypointensities of a structure

$$S_{l,j}^{std,Hypo} = \{s_{i,j} | i \in \mathcal{M}_l^{Hypo}\} \qquad 2\text{-}10$$

with $j = T2^*w$, which were selected by the mask $\mathcal{M}_l^{Hypo}$ (Equation 2-8). The median T2*w intensity $s_{l,j}^{NABG}$ of the corresponding normal-appearing tissue intensities

$$S_{l,j}^{std,NABG} = \{s_{i,j} | i \in \mathcal{M}_l^{NABG}\} \quad 2\text{-}11$$

with $j = T2^*w$ were used as a reference. The normal-appearing tissue intensities were selected by the normal-appearing tissue mask $\mathcal{M}_l^{NABG} = \mathcal{M}_l^{BG} \cap \left(\mathcal{M}_l^{Hypo}\right)^c$, which was visually checked and manually corrected if segmentation artefacts were present to ensure a consistent reference across subjects.

2.3.5.2. Signal intensity distributions of basal ganglia T2*w hypointensities

The T1w, T2w and T2*w intensity distributions of basal ganglia T2*w hypointensities were estimated by linearly aggregating the intensity histograms of all subjects $\boldsymbol{p}_{j,\mathcal{k}}^{int}$ (Stone, 1961)

$$\boldsymbol{p}_j^{int} = \sum_{\mathcal{k}=1}^{\mathcal{k}^{max}} w_k \boldsymbol{p}_{j,\mathcal{k}}^{int}. \quad 2\text{-}12$$

The intensity histogram of a subject $\boldsymbol{p}_{j,\mathcal{k}}^{int} = \left(p_{1,j,\mathcal{k}}^{int}, p_{2,j,\mathcal{k}}^{int}, \dots, p_{\mathcal{b}^{max},j,\mathcal{k}}^{int}\right)^T$, where $p_{\mathcal{b},j,\mathcal{k}}^{int}$ represents the estimated probability density of a histogram bin $\mathcal{b}$, were calculated with the standardized signal intensities $S_{j,\mathcal{k}}^{std,Hypo} = \{s_{i,j,\mathcal{k}} | i \in \mathcal{M}_{\mathcal{k}}^{Hypo}\}$ and bin widths, which were optimized with all signal intensities $S_j^{std,Hypo} = \bigcup_{\forall k} S_{j,\mathcal{k}}^{std,Hypo}$ using the method from Shimazaki and Shinomoto (2007).

The estimated average distributions were characterized in terms of their modality and skewness. The skewness was quantified with the Bowley skewness coefficient $\left(Q_j^{int,1} - 2Q_j^{int,2} + Q_j^{int,3}\right)/IQR_j$, where the quartiles $Q_j^{int,q}$ with $q \in \{1,2,3,4\}$ and inter quartile ranges IQR_j were estimated from $\boldsymbol{p}_j^{int}$.

2.3.5.3. Appearance of basal ganglia T2*w hypointensities on T1w and T2w MRI

T2*w hypointensities of a structure with the masks $\mathcal{M}_l^{Hypo}$ (Equation 2-8) were considered hyper- or hypointense on the T1w and T2w volumes if (i) their signal intensities $S_{l,j}^{std,Hypo}$ (Equation 2-10) were significantly different from the signal intensities of normal tissue $S_{l,j}^{std,NABG}$ (Equation 2-11), and (ii) their median signal intensities $\left(S_{l,j}^{std,Hypo}\right)_{0.5}$ were brighter or darker than the median signal intensities of normal tissue intensities $\left(S_{l,j}^{std,NABG}\right)_{0.5}$. The Mann-Whitney U test was used to assess condition (i) at a significance level of $\alpha = 0.05$.

2.4. Results

2.4.1. Intra-rater variability and spatial distribution of T2*w hypointensities

The intra-rater variability between 29 T2*w hypointensity masks segmented on two separate occasions was 0.51 ± 0.20, as assessed by the Jaccard similarity index. As shown in detail in Table 2-2, the expert rater segmented 867 individual T2*w hypointensities in all subjects, 36% inside and 63% outside the region selected by the basal ganglia and internal capsule masks. Of the 549 individual T2*w hypointensities found outside the basal ganglia and internal capsule, 59% were in the choroid plexus, 10% in the pineal gland, 6% in the substantia nigra and the rest in other structures. Of the 318 individual T2*w hypointensities found inside the basal ganglia and internal capsule, 72% were in the globus pallidus, 18% in the internal capsule, 8% in the putamen and 2% in the caudate.

Table 2-2: Spatial distribution of focal T2*w hypointensities. This table shows the anatomical locations of the individual T2*w hypointensities, i.e. the connected components (six-connected neighbourhood) of the T2*w hypointensity masks from the rater. Additionally, it shows how many individual T2*w hypointensities were marked as partly or completely hypointense on T1w MRI. Regions within individual T2*w hypointensities that appeared hypointense on T1w might potentially indicate a change in the underlying tissue composition, such as calcification (Kruer *et al.*, 2012; Valdés Hernández *et al.*, 2012).

Anatomical structure	Total count	Partly hypointense on T1w MRI	Completely hypointense on T1w MRI
Basal ganglia and internal capsule			
Caudate	5	0	0
Putamen	26	0	1
Globus pallidus	229	46	5
Internal capsule	58	0	1
Total	318	46	7
Outside the basal ganglia and internal capsule			
Choroid plexus	325	4	317
Pineal gland	55	2	52
Substantia nigra	32	0	0
Other structures	137	3	9
Total	549	9	378

2.4.2. Count and load of basal ganglia T2*w hypointensities

As shown in Figure 2-3, each subject with basal ganglia T2*w hypointensities had on average one hypointensity in each globus pallidus, two hypointensities in the left and one in the right hemisphere structures, and 3 hypointensities in all structures. The average hypointensity loads in the left and right globus pallidus, in the left and right hemisphere structures, and in all structures was 21.1, 15.9, 28.9, 21.2 and 50.3 ppm, respectively. No significant ($p<0.05$) differences were found between the number of hypointensities and hypointensity loads in the left and right hemisphere structures, however, Figure 2-3 suggests that slightly more hypointensities were counted in the left than right hemisphere structures.

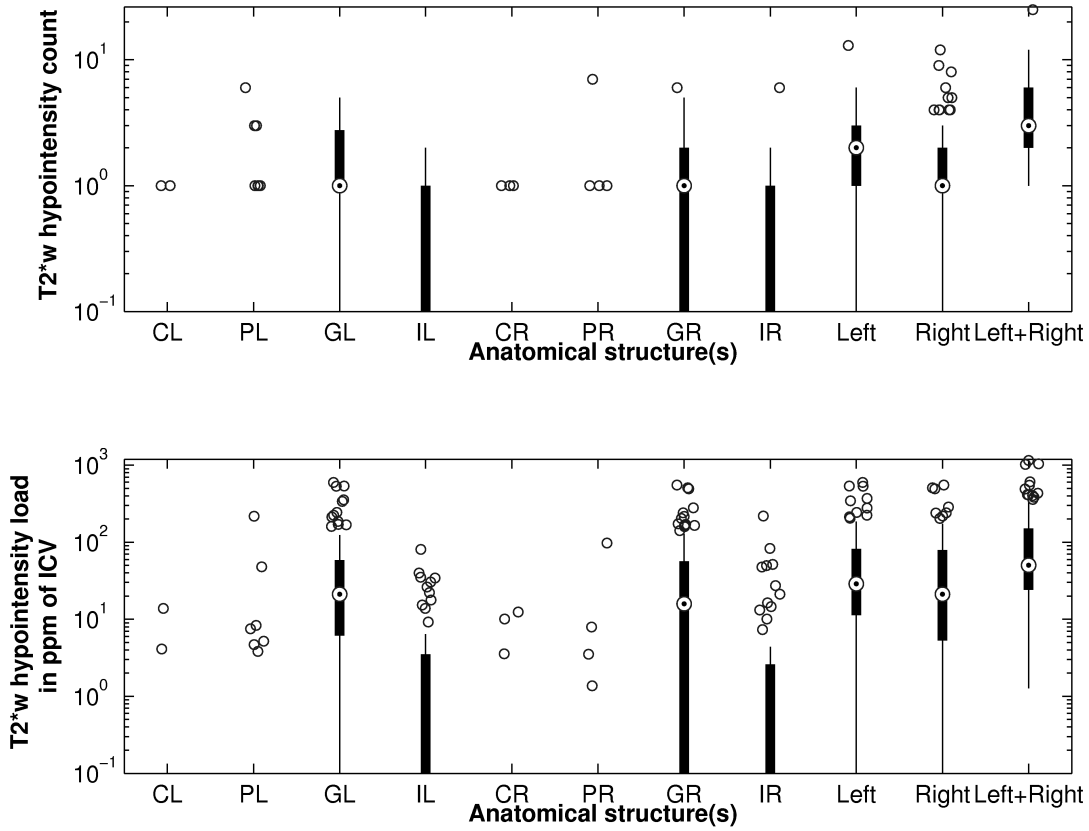

Figure 2-3: Average count and load of basal ganglia T2*w hypointensities. The anatomical structures include the left caudate (CL), left putamen (PL), left globus pallidus (GL), left internal capsule (IL), right caudate (CR), right putamen (PR), right globus pallidus (GR) and right internal capsule (IR). Additionally, the boxplots show the T2*w hypointensity count in the left and right basal ganglia structures, and in all basal ganglia structures. T2*w hypointensity count and load were especially elevated in the globus pallidus. Although the upper plot suggests a difference between the T2*w hypointensity count in the left and right hemisphere structures, this difference was not significant at α=0.05.

2.4.3. Morphology of individual basal ganglia T2*w hypointensities

The volume, maximum in-plane area, compactness and relative anisotropy of individual basal ganglia T2*w hypointensities are shown in Table 2-3. These properties were significantly different for inter-slice hypointensities, which extend across more than one MRI slice, and intra-slice hypointensities, which are contained within one MRI slice. Generally, inter-slice hypointensities were very small, with a smooth surface and a round shape. Due to the limited resolution, intra-slice hypointensities appeared as squares, rectangles and L-shaped elements formed by 1 to 4 voxels.

Table 2-3: Morphological properties of individual basal ganglia T2*w hypointensities. The properties are significantly different ($p<0.05$) for inter- ($n_{slice}>1$) and intra-slice ($n_{slice}=1$) basal ganglia T2*w hypointensities.

Type	Inter-slice ($n_{slice}>1$)			Intra-slice ($n_{slice}=1$)			Both ($n_{slice}>=1$)		
Total count	148			170			318		
Percentile	25%	50%	75%	25%	50%	75%	25%	50%	75%
Volume in mm^3	18	30	106	2	6	8	4	12	30
Maximum area in mm^2	5	8.5	24.5	1	3	4	2	4	9
Compactness	0.85	0.88	0.91	0.92	0.93	0.95	0.88	0.92	0.93
Relative anisotropy	0.40	0.49	0.59	0.26	0.36	0.57	0.36	0.47	0.57

2.4.4. Spatial probability distribution of T2*w hypointensities

The spatial distribution map in Figure 2-4 indicates a high probability density of T2*w hypointensities within central regions of the globus pallidus in all MRI slices where this structure is evident. From this region the density decreases predominantly towards the posterior limb of the internal capsule and putamen, but also the anterior limb of the internal capsule and caudate. T2*w hypointensities also coincide with the posterior putamen. Anatomically, the region with the highest density of T2*w hypointensities coincides with the lenticulostriate arterioles that supply the globus pallidus (Donzelli *et al.*, 1998; Feekes *et al.*, 2005; Marinkovic *et al.*, 1985).

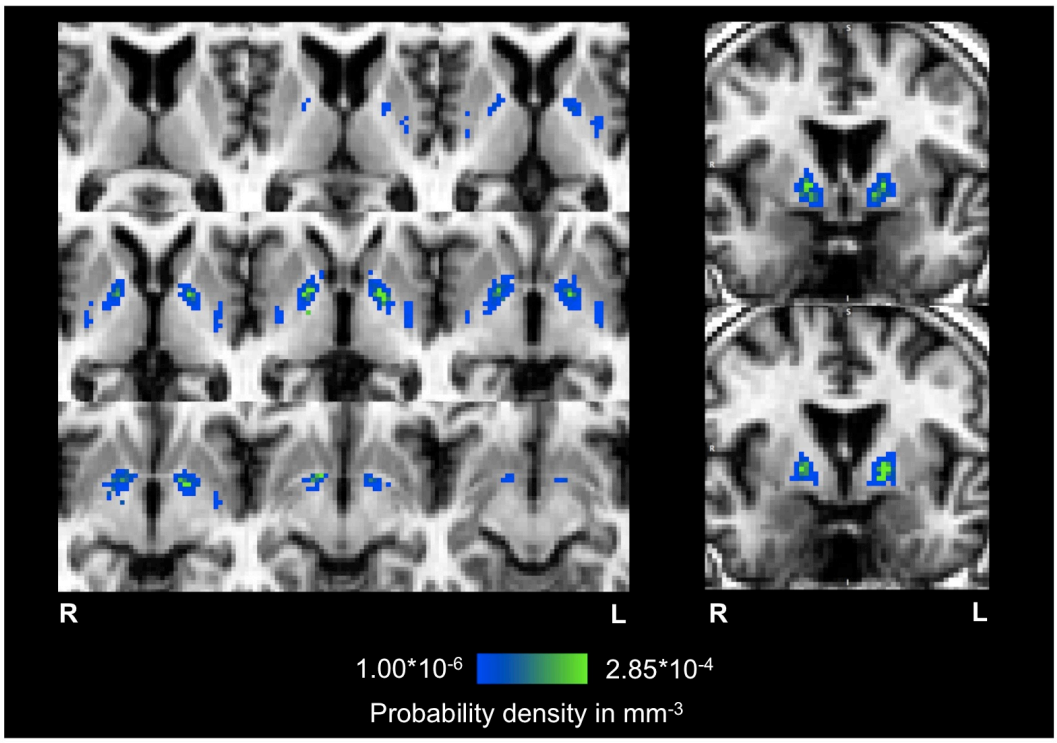

Figure 2-4: Spatial probability distribution of basal ganglia T2*w hypointensities. The generated spatial distribution maps of T2*w hypointensities are shown overlaid on axial and coronal slices of the 2 mm isotropic T1w reference volume of the representative subject used for non-linear registration. For comparison, the coronal slices approximately correspond to the coronal slices in Feekes *et al.* (2005), which show the vascular territories of the lenticulostriate arteries (LSA), recurrent arteries of Heubner (RHA), and anterior choroidal arteries (AChA). The spatial probability distribution of these focal T2*w hypointensities indicates a high density inside the globus pallidus (green region), which coincides with the point of entry of the lenticulostriate arterioles into the brain parenchyma; their density tends to decrease towards the internal capsule, putamen and caudate.

2.4.5. Segmentation thresholds of basal ganglia T2* hypointensities

The segmentation thresholds of T2*w hypointensities and the corresponding median signal intensities of normal-appearing tissue, which were similar for corresponding left and right hemisphere structures, are shown in Figure 2-5. The variation in the average segmentation threshold across the different brain structures indicates that the rater adjusted the threshold, which was initially the same for all structures, specifically for each structure. The segmentation thresholds of the caudate, putamen, globus pallidus and adjacent internal capsule were on average 27.3 ± 2.4, 30.0 ± 6.8, 16.5 ± 5.5 and 19.4 ± 5.8 % lower than the median signal intensities of normal-appearing tissue, respectively. These values suggest that the rater typically used two different thresholds, one for segmenting T2*w hypointensities in the caudate and putamen, and one for segmenting T2*w

hypointensities in the globus pallidus and internal capsule. The normal tissue intensities of the putamen, globus pallidus and adjacent internal capsule were 3.4 ± 2.1, 14.0 ± 2.3 and 15.6 ± 1.7 % lower than the normal tissue intensities of the caudate, respectively. These values confirm that the caudate appears brightest on T2*w MRI followed by the putamen, globus pallidus and internal capsule.

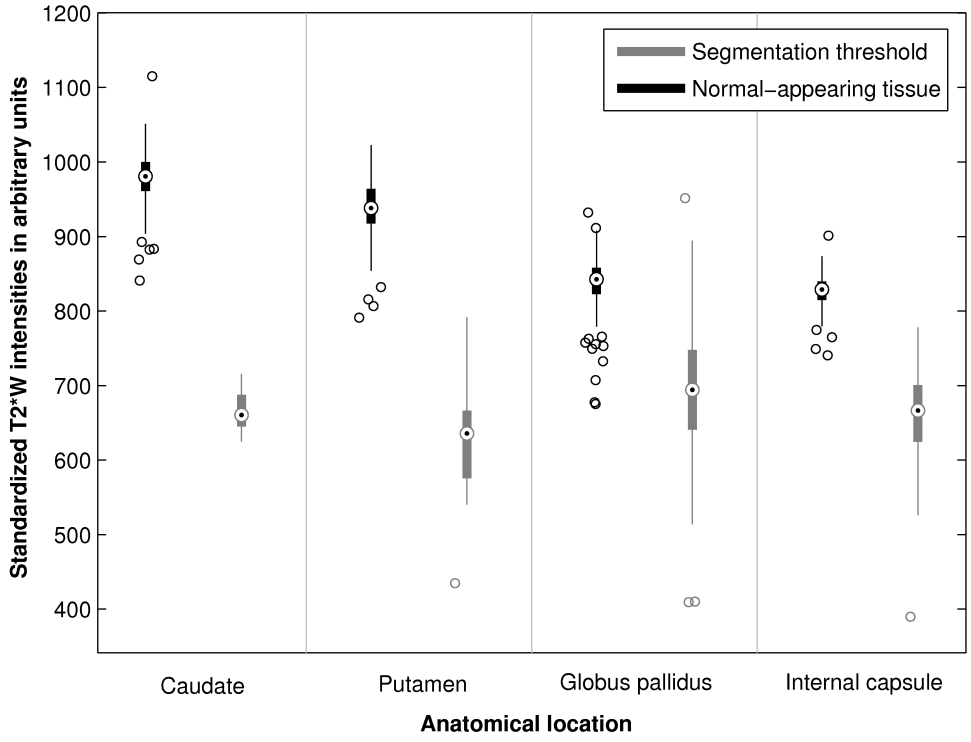

Figure 2-5: Segmentation thresholds of T2*w hypointensities and median T2*w intensities of corresponding normal-appearing basal ganglia tissue. This figure shows that the rater chose different segmentation thresholds for T2*w hypointensities from different anatomical structures. This systematic variation suggests that the manual segmentation of T2*w hypointensities was potentially influenced by a difference in appearance of T2*w hypointensities from different basal ganglia structures. An additional influence might be the difference in appearance of the normal-appearing tissue intensities of the caudate, putamen, globus pallidus and internal capsule which look increasingly dark on T2*w volumes.

2.4.6. Signal intensity distributions of basal ganglia T2*w hypointensities

Figure 2-6 shows the estimated average T1w, T2w and T2*w intensity distributions of basal ganglia T2*w hypointensities from the cohort. The T1w, T2w and T2*w intensity distributions are all unimodal with Bowley skewness coefficients of 0.044, 0.042 and -0.193. The skewness coefficients confirm that the T1w and T2w distributions are slightly positively skewed, whereas the T2*w distribution is negatively skewed. These average distribution shapes as well as their skewness

indicate that the T1w and T2w distributions, and especially the T2*w distributions are generally not normally distributed. The left tail of the T2*w distributions confirms the observation that there are smaller, darker hypointense regions within individual hypointensities, which are surrounded by larger, brighter hypointense regions.

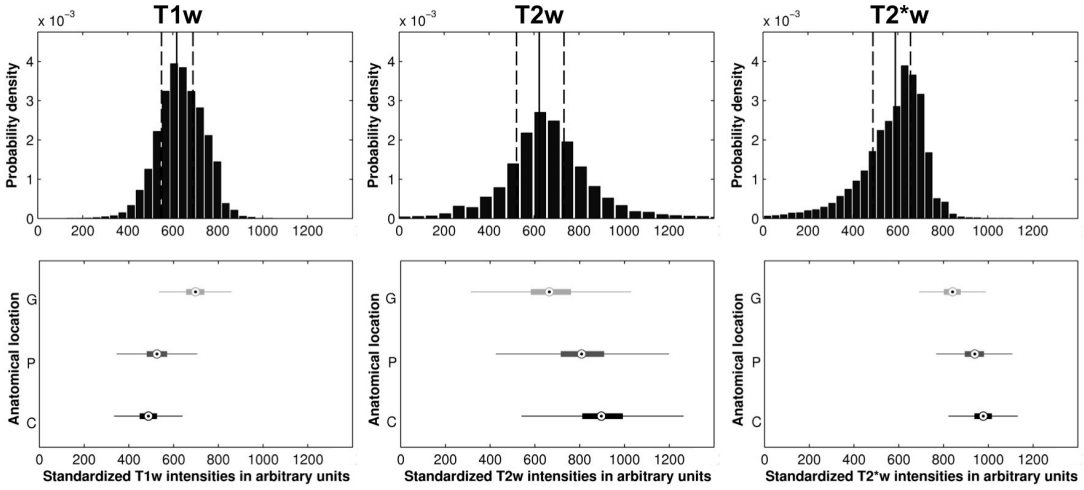

Figure 2-6: T1w, T2w and T2*w intensity distributions of basal ganglia T2*w hypointensities. The bin-width optimized histograms estimate the distributions of T2*w, T2w and T1w intensities of basal ganglia T2*w hypointensities. The solid vertical lines indicate median and the dashed vertical lines the 25th- and 75th- percentiles. The vertical boxplots of the bottom figures indicate the ranges of normal-appearing intensities of the globus pallidus (G), the putamen (P) and caudate (C). The histograms suggest that the T2*w, T2w and T1w intensity distributions of basal ganglia T2*w hypointensities are unimodal and that they generally do not resemble Normal distributions. The deviations of the T2w and T1w distributions from Normal distributions are potentially caused by inhomogeneous tissue. Conversly, the negatively skewed T2*w distribution is on the one hand caused by thresholding, which eliminates bright signal intensities, and on the other hand by signal voids due to the presumably high mineral concentrations at the centre of T2*w hypointensities.

2.4.7. Appearance of basal ganglia T2*w hypointensities on T1w and T2w MRI

Figure 2-7 shows that the appearance of T2*w hypointensities in the globus pallidus on T1w and T2w MRI differs from the appearance of T2*w hypointensities seen in other structures. In 77% of subjects with globus pallidus T2*w hypointensities, these features appeared hypointense on T1w MRI, whereas in 20% they appeared isointense and in 3% hyperintense. Conversely, in 51% of subjects, these globus pallidus T2*w hypointensities appeared isointense on T2w MRI, whereas in 22% they appeared hypointense and in 26% hyperintense. These results are in agreement with the rater (Table 2-2) who predominantly marked globus pallidus T2*w hypointensities as partly or completely hypointense on T1w MRI.

T2*w hypointensities in the internal capsule and putamen appeared isointense on T1w MRI in 61% and 55% of subjects, and hypointense on T2w volumes in 61% and 64% of subjects.

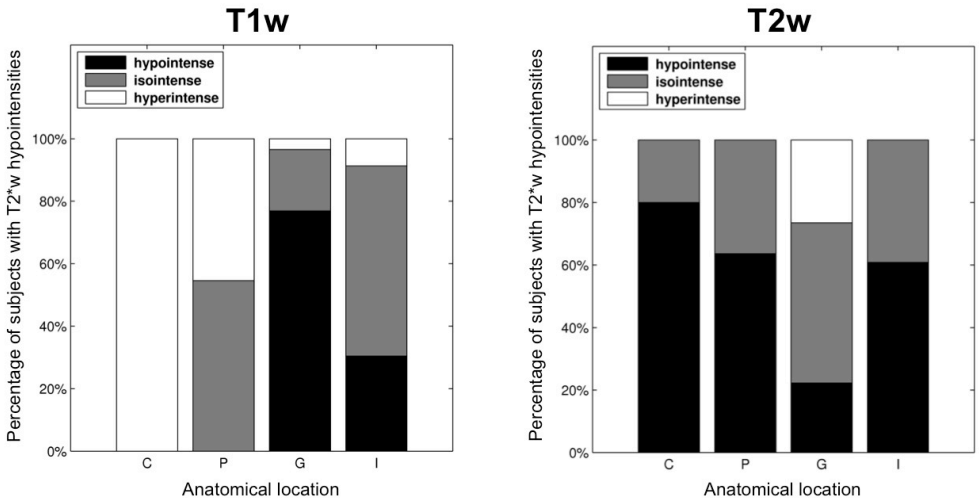

Figure 2-7: Appearance of basal ganglia T2*w hypointensities on T1w and T2w MRI. This figure shows the percentage of subjects with T2*w hypointensities in a specific basal ganglia or internal capsule region that appeared hypo-, iso- and hyperintense on T1w and T2w MRI. The anatomical structures include the caudate (C), putamen (P), globus pallidus (G) and internal capsule (I). There is a notable difference in appearance on T1w and T2w MRI between T2*w hypointensities in the globus pallidus and other structures. Globus pallidus T2*w hypointensities tend to appear hypo- and isointense on T1w and T2w MRI.

2.5. Discussion

T2*w hypointensities are frequently observed in the basal ganglia of healthy, older subjects, are associated with age-related cognitive decline, and may provide a useful biomarker of cerebral small vessel disease (Penke *et al.*, 2012). These features are believed to arise from mineralization in and around the small lenticulostriate arterioles in the inferior basal ganglia (Casanova & Araque, 2003; Morris *et al.*, 1992). In this study, we document their spatial and intensity distributions, morphology and appearances on T1w and T2w MRI in an older, community dwelling cohort with narrow age range with the aim of improving current manual segmentation methods.

Harder *et al.* (2008) analysed focal hypointensities in the globus pallidus and putamen of subjects with a wide age range and found that their SWI signal intensities decreased with age. A rating scheme for counting and classifying hypointensities in the putamen and globus pallidus was also proposed and an increase of the

hypointensity grade with age was reported. However, the suggested regularity of the hypointensity pattern and relation with age could not be confirmed in the current study. The former can be, at least partly, attributed to the higher sensitivity of the SWI sequence to iron compared to the T2*w sequence used here (Haacke *et al.*, 2009), and the latter to the very narrow age range of the participants in this study.

Van Es *et al.* (2008) investigated hypointensity patterns in the basal ganglia of non-demented elderly subjects and assessed associations between age-related changes in the brain. A method was developed for classifying the hypointensity of the whole caudate, putamen and globus pallidus on T2*w MRI. The study reported that hypointense caudate nuclei are a frequent finding in non-demented elderly subjects and that this change is significantly associated with more atrophy and increased white matter load. However, most of the focal T2*w hypointensities that were found in this study were located in the globus pallidus and far less were observed in the putamen and caudate. This can be attributed to the different analysis methods, variations in subject population as well as differences in imaging parameters, since the TE of the T2*w sequence employed in this study was lower and hence the T2*w volumes were less T2*-weighted (Conijn *et al.*, 2010) than those collected by van Es *et al.* (2008).

The spatial probability map of basal ganglia T2*w hypointensities (Figure 2-4) is consistent with observations in a larger sample of the LBC1936 (Penke *et al.*, 2012) and shows a high density of T2*w hypointensities at the centre of the globus pallidus coinciding with the point of entry of the lenticulostriate arterioles into the basal ganglia (Donzelli *et al.*, 1998; Feekes *et al.*, 2005; Marinkovic *et al.*, 1985). This finding is supported by histological studies (Morris *et al.*, 1992; Slager & Wagner, 1956), which report iron-encrusted vessels in the globus pallidus. Morris *et al.* (1992) speculated that encrustations make such vessels prone to rupture or cause constriction to the blood flow. Notably, mineralization with a similar spatial distribution pattern as that seen in the T2*w hypointensities studied here was found in the brains of cynomolgus monkeys (Wadsworth *et al.*, 1995). In that study, the authors confirmed that ferrunginations and calcifications were directly related to arterioles of the globus pallidus. Such a relationship could be confirmed in humans in further post-mortem studies where histological findings may be correlated with MRI

(Langkammer *et al.*, 2010), or MRI combined with MR angiography, which is able to visualize small vessels in the basal ganglia (Okuchi *et al.*, 2013; Seo *et al.*, 2012).

Brain microbleeds (Cordonnier, 2010) also appear as focal hypointensities on T2*w MRI with a prevalence of 9% in older, otherwise healthy subjects (Cordonnier *et al.*, 2007). Brain microbleeds have maximum diameter between 5 and 10 mm on T2*w volumes and are commonly assumed to be spherical in shape. Barnes *et al.* (2011) established statistics about their compactness and relative anisotropy. Comparing basal ganglia T2*w hypointensities and brain microbleeds with regard to volume ranges and values of compactness and relative anisotropy suggests that brain microbleeds and hypointensities have a similar appearance and morphology on T2*w MRI although they likely arise due to fundamentally different biological mechanisms and affect different parts of the brain (Charidimou *et al.*, 2012).

The rater typically used different thresholds for segmenting T2*w hypointensities from the caudate and putamen, and globus pallidus and internal capsule. This difference potentially arises from the manual refinement of the initial T2*w hypointensity masks from thresholding (Valdés Hernández *et al.*, 2011), where the rater was likely influence by the appearance of the T2*w hypointensities in the different structures. T2*w hypointensities from the globus pallidus and internal capsule tended to appear uniformly dark with sharper boundaries than T2*w hypointensities from the caudate and putamen, which often appeared more shaded with fuzzier boundaries. Harder *et al.* (2008) also accounted for this difference in appearance since they proposed alternative classification schemes for the putamen and globus pallidus.

The average T1w, T2w and T2*w intensity distributions of basal ganglia T2*w hypointensities do not resemble Normal distributions. In particular, T2*w intensity distributions resemble negatively skewed distributions, such as Beta or reversed Weibull distributions. The finding that T1w, T2w and T2*w signal intensities of MRI features, such as T2*w hypointensities, are not normally distributed is scarcely documented in the MRI literature. For example, current MRI segmentation methods, such as SPM (Statistical Parametric Mapping; http://www.fil.ion.ucl.ac.uk/spm) or FSL FAST, typically model lesions either as a finite mixture of Normal distributions (Seghier *et al.*, 2008) or as a uniform distribution (Zhang *et al.*, 2001). Both

approaches approximate the signal intensity distributions of hypointense lesions and the segmentation results can deviate significantly from manual segmentations. Alternative data models, such as the Gamma and Beta distribution, have been used by Ho *et al.* (2002), for example, to model and segment brain tumours on MRI and by (Rexilius & Peitgen, 2008) to develop a method for the accurate volumetry of small lesions. However, segmentation methods which do not model lesion intensities explicitly but treat them as outliers of the normal-appearing intensity distributions (García-Lorenzo *et al.*, 2011) might produce more accurate results.

The results of the analysis of T1w, T2w and T2*w signal intensities of focal basal ganglia T2*w hypointensities suggest that they might be associated with an inhomogeneous underlying tissue structure, which could be explained by increased mineral deposition. Signal intensities of normal-appearing brain tissue, such as grey and white matter, are generally assumed to be normally distributed (Ashburner & Friston, 2005; Zhang *et al.*, 2001). The fact that T1w, T2w, and especially, T2*w signal intensities of these T2*w hypointensities are generally not normally distributed might be due to irregular changes in tissue structure and composition, such as mineralization in form of aggregation of trace metals and calcification, as described by Slager and Wagner (1956). These changes can be detected with MRI and could lead to their hypointense appearance on T2*w and T1w MRI (Henkelman *et al.*, 1991; Valdés Hernández *et al.*, 2014), as found here in the globus pallidus. Globus pallidus T2*w hypointensities also tend to appear iso- and hypointense on T2w and T2*w MRI. This finding could also be explained by increased mineralization, which could entail increased aggregation of magnetic particles, increased magnetic susceptibility and decreased water proton diffusion around magnetic particles. All these changes lead to increased reversible water proton spin dephasing (static dephasing regime) and hence to a more isointense appearance on T2w MRI (Weisskoff *et al.*, 1994).

The subjects employed in this study were randomly selected from all participants of the LBC1936, a large longitudinal study of cognitive ageing. Because these subjects have a very narrow age range, this allows individual differences to be identified and analysed without the major confound of age. The experienced rater was not involved in the selection process and was presented only with the MRI data

required to segment T2*w hypointensities with the semi-automated segmentation method described in Section 2.3.2. The masks of the rater were then analysed independently with the automated methods described above. The study design was therefore chosen to minimize systematic bias, especially from the rating, identification and analysis of the T2*w hypointensities. The results of this study should therefore closely reflect the characteristic appearance of T2*w hypointensities across the whole cohort.

This study has several limitations. Firstly, the T2*w hypointensities were analysed on gradient-echo magnitude volumes, where the segmentation of T2*w hypointensities was not only complicated by partial volume effects but also blooming artefacts. Focal hypointensities on gradient-echo volumes caused by magnetic particles or complexes generally do not reflect the true particle size because the magnetic field gradients around magnetic particles also causes dephasing and hence hypointensities in voxels adjacent to the particle. For example, studies have shown that brain microbleeds typically appear approximately 1.57 and 2.5 to 5 times bigger *in vivo* than in post-mortem brains on standard SWI volumes collected from a 3T scanner and T2*w volumes from a 7 T scanner (De Reuck *et al.*, 2011; Schrag *et al.*, 2010). The apparent size increase of magnetic particles depends on the geometry and magnetic properties of the particle, as well as imaging parameters, such as the echo time (Pintaske *et al.*, 2006). In this study, the echo time of the T2*w sequence (Table 2-1) was chosen shorter than standard T2*w echo times, which are typically around 40 ms at 1.5 T, to reduced the blooming artefacts at the expense of a decreased sensitivity to magnetic particles (Conijn *et al.*, 2010). A better estimate of the true particle size could be derived from gradient echo phase volumes (McAuley *et al.*, 2011), which were not part of the LBC1936 imaging protocol.

The second limitation is that T2*w hypointensities were just segmented by a single rater, as their segmentation is very time consuming. Therefore no information is available about the exact values of the inter-rater variability. However, the inter-rater variability is expected to be similar to values reported in a previous study, which used the same data for comparing the performance of two manual segmentation methods (Valdés Hernández *et al.*, 2011).

A further limitation is that the bias field correction method N4 (Tustison *et al.*, 2010) was applied to the T1w, T2w and T2*w volumes with the default parameters. N4 is especially suited for bias-field correction on MRI data acquired from elderly subjects, as it does not require *a priori* information, such as the number of tissue classes. However, it has been suggested (Vovk *et al.*, 2007) that the performance of N4 can potentially be improved by optimizing the input parameters of the algorithm, such as the number of histogram bins.

2.6. Conclusion

This study finds that focal T2*w hypointensities in the basal ganglia have a characteristic spatial and signal intensity distribution. Their spatial distribution indicates that they appear to be associated with small vessels, especially those of the globus pallidus, while their signal intensities generally do not resemble Normal distributions. These findings as well as their difference in appearance on T1w and T2w MRI further supports the hypothesis that T2*w hypointensities are mainly caused by mineralized small vessels and perivascular spaces. The evaluation of basal ganglia T2*w hypointensities as a potential biomarker for cerebral small vessel or other vascular disease requires further study in different subject populations ideally with post mortem data, and is currently limited by a lack of an automated mineral deposit segmentation method. The following Chapter introduces such an automated method for segmenting T2*w hypointensities that addresses the limitations of the semi-automated segmentation method, which will be subsequently used in Chapter 5 for the segmentation of T2*w hypointensities in an ageing cohort with a wider age range than the LBC participants.

Chapter 3 Automated segmentation of multifocal basal ganglia T2*-weighted MRI hypointensities

This chapter was published as: Glatz A., Bastin M.E., Kiker A.J., Deary I.J., Wardlaw J.M., Valdés Hernández M.C. (2015) Automated segmentation of multifocal basal ganglia T2*-weighted MRI hypointensities. *NeuroImage* 105:332-46.

3.1. Abstract

Multifocal basal ganglia T2*-weighted (T2*w) hypointensities, which are believed to arise mainly from vascular mineralization, were recently proposed as a novel MRI biomarker for small vessel disease and ageing. These T2*w hypointensities are typically segmented semi-automatically, which is time consuming, associated with a high intra-rater variability and low inter-rater agreement. To address these limitations, we developed a fully automated, unsupervised segmentation method for basal ganglia T2*w hypointensities. This method requires conventional, co-registered T2*w and T1-weighted (T1w) volumes, as well as region-of-interest (ROI) masks for the basal ganglia and adjacent internal capsule generated automatically from T1w MRI. The basal ganglia T2*w hypointensities were then segmented with thresholds derived with an adaptive outlier detection method from respective bivariate T2*w/T1w intensity distributions in each ROI. Artefacts were reduced by filtering connected components in the initial masks based on their standardised T2*w intensity variance. The segmentation method was validated using a custom-built phantom containing mineral deposit models, i.e. gel beads doped with 3 different contrast agents in 7 different concentrations, as well as with MRI data from 98 community-dwelling older subjects in their seventies with a wide range of basal ganglia T2*w hypointensities. The method produced basal ganglia T2*w hypointensity masks that were in substantial volumetric and spatial agreement with those generated by an experienced rater (Jaccard index = 0.62 ± 0.40). These promising results suggest that this method may have use in automatic segmentation of basal ganglia T2*w hypointensities in studies of small vessel disease and ageing.

3.2. Introduction

Focal hypointensities appear as a frequent feature on T2*-weighted (T2*w) MRI in the basal ganglia of elderly, otherwise healthy, subjects (Chapter 2). These features are believed to arise from mineralisation in and around penetrating arteries and perivascular spaces (Casanova & Araque, 2003; Morris *et al.*, 1992; Slager & Wagner, 1956), which are possibly of ischemic origin (Janaway *et al.*, 2014). Harder *et al.* (2008), who studied focal basal ganglia hypointensities on susceptibility-weighted imaging (SWI), found that their degree and hypointensity increase with age, while Penke *et al.* (2012) demonstrated that their volume correlated negatively with cognitive ability in both youth and older age in a group of 143 community-dwelling subjects in their seventies. Other researchers such as Aquino *et al.* (2009) and Li *et al.* (2014) who have investigated the appearance of the basal ganglia in non-demented elderly subjects on gradient-echo MRI have found that this structure becomes more hypointense with age due to iron storage (Hallgren & Sourander, 1958). However, Es *et al.* (2008) reported that increased basal ganglia iron might also be associated with other age-related changes in the brain, such as white matter T2-weighted (T2w) hyperintensities.

Focal basal ganglia T2*w hypointensities appear predominantly iso- to slightly hypointense on T1w MRI and isointense on T2w MRI which indicates that the underlying mineral deposits are more water-insoluble than ferritin (Vymazal *et al.*, 2000), and consist of aggregated trace metals since this increases reversible dephasing of diffusing water protons (Sedlacik *et al.*, 2014; Weisskoff *et al.*, 1994). Subregions of basal ganglia T2*w hypointensities can also appear very hypointense on T1w MRI which has been linked to advanced mineralization of the underlying tissue, such as calcification (Henkelman *et al.*, 1991; Slager & Wagner, 1956; Valdés Hernández *et al.*, 2014).

Methods for analysing basal ganglia T2*w hypointensities either determine the hypointensity of the whole basal ganglia (Jasinschi *et al.*, 2006; Parsey & Krishnan, 1997; Es *et al.*, 2008) or the volume of focal T2*w hypointensities in individual structures (Valdés Hernández *et al.*, 2011). The former method first classifies all voxels as hypointense that fall below a T2*w threshold which is either derived from the T2*w signal intensities of the red nucleus or globus pallidus. The ratio of

hypointense to basal ganglia structure voxels quantifies the degree of hypointensity of each structure. The latest improvements in this method produce reliable results that are in good agreement with those generated by experienced raters (Jasinschi *et al.*, 2006). On the other hand, focal T2*w hypointensities in the basal ganglia are still typically segmented semi-automatically (Valdés Hernández *et al.*, 2011). An experienced rater first refines a T2*w threshold equal to the median T2*w signal intensity of the globus pallidus to exclude most artefacts. The rater then manually removes the remaining artefacts based on the visual appearance of focal T2*w hypointensities on T2*w and T1w MRI. An alternative method has also been developed that produces colour maps of the brain with minimum variance quantization of co-registered T2*w and fluid attenuated inversion recovery (FLAIR) volumes (Valdés Hernández *et al.*, 2010). Haemosiderin deposits, which appear green on these maps, are manually identified and included in the final masks. However, validation of these methods shows that both are very time-consuming and associated with high intra-rater variability and low inter-rater agreement (Valdés Hernández *et al.*, 2011).

In this study we therefore developed a fully automated method for segmenting basal ganglia T2*w hypointensities to address the limitations of the previously developed semi-automatic methods. We then investigated the effect of method parameters on the segmentation results in a custom-designed phantom employing several mineral deposit models. The method was also validated with MRI data from a group of community-dwelling subjects in their seventies with a wide range of basal ganglia T2*w hypointensities which have been manually and semi-automatically segmented by two experienced raters. The masks from the manual segmentation were then used to optimise the parameters of the fully automated method, and to assess and compare the accuracy and precision of the masks from the fully automated and semi-automated segmentation.

3.3. Methods

Figure 3-1 shows an overview of the fully automated method for segmenting basal ganglia T2*w hypointensities. This method generates basal ganglia T2*w hypointensity masks, which possibly indicate basal ganglia mineral deposits (Penke

et al., 2012), as well as T2*w/T1w hypointensity masks, which possibly indicate regions of advanced mineralisation, such as calcification (Valdés Hernández *et al.*, 2014). The method generates masks in three steps. Firstly, the structural T2*w and T1w input volumes are preprocessed, which produces co-registered T2*w and T1w volumes, as well as regions-of-interest (ROI) masks. Secondly, T2*w and T1w thresholds are derived for segmenting focal T2*w hypointensities. Lastly, initial output masks are created by applying these thresholds to the co-registered T2*w and T1w volumes, which are subsequently filtered to reduce thresholding artefacts.

The preprocessing pipeline was mainly implemented in GNU Bash (www.gnu.org) with tools from FSL 5.0 (www.fmrib.ox.ac.uk/fsl) and N4 (www.itk.org), whereas the main processing pipeline was implemented in Matlab 2011b (Natick, MA, USA) with the LIBRA (Verboven & Hubert, 2005) and NIFTI tools (Matlab Central, FileID#8797). This software is available at github.com/aglatz.

3.3.1. Preprocessing pipeline for structural T2*w and T1w MRI

A previously published preprocessing pipeline (Chapter 2) was used to obtain co-registered T1w and T2*w volumes, as well as caudate, putamen, globus pallidus and adjacent internal capsule masks, which were combined in a ROI mask set. In short, non-brain structures visible on T2*w volumes were automatically removed with FSL BET (Smith, 2002). Non-brain structures visible on T1w volumes were removed by transforming the brain masks created by FSL BET from T2*w to T1w space and by applying them to the corresponding T1w volumes. N4 was used for bias-field correction of all volumes and the T1w volumes were affine registered to the corresponding T2*w volumes using FSL FLIRT (Jenkinson *et al.*, 2002).

To generate the ROI mask set, the basal ganglia nuclei and the thalamus were automatically segmented on the original T1w volumes using FSL FIRST (Patenaude *et al.*, 2011). All structural masks were then linearly transformed from T1w to T2*w space with FSL FLIRT and the previously obtained transformation matrices. Additional internal capsule masks were created by dilating the globus pallidus masks towards the centre of the brain with half disk shaped structural elements of 6 mm radius and then removing regions of these masks that intersected with the union of caudate, putamen, thalamus and globus pallidus masks.

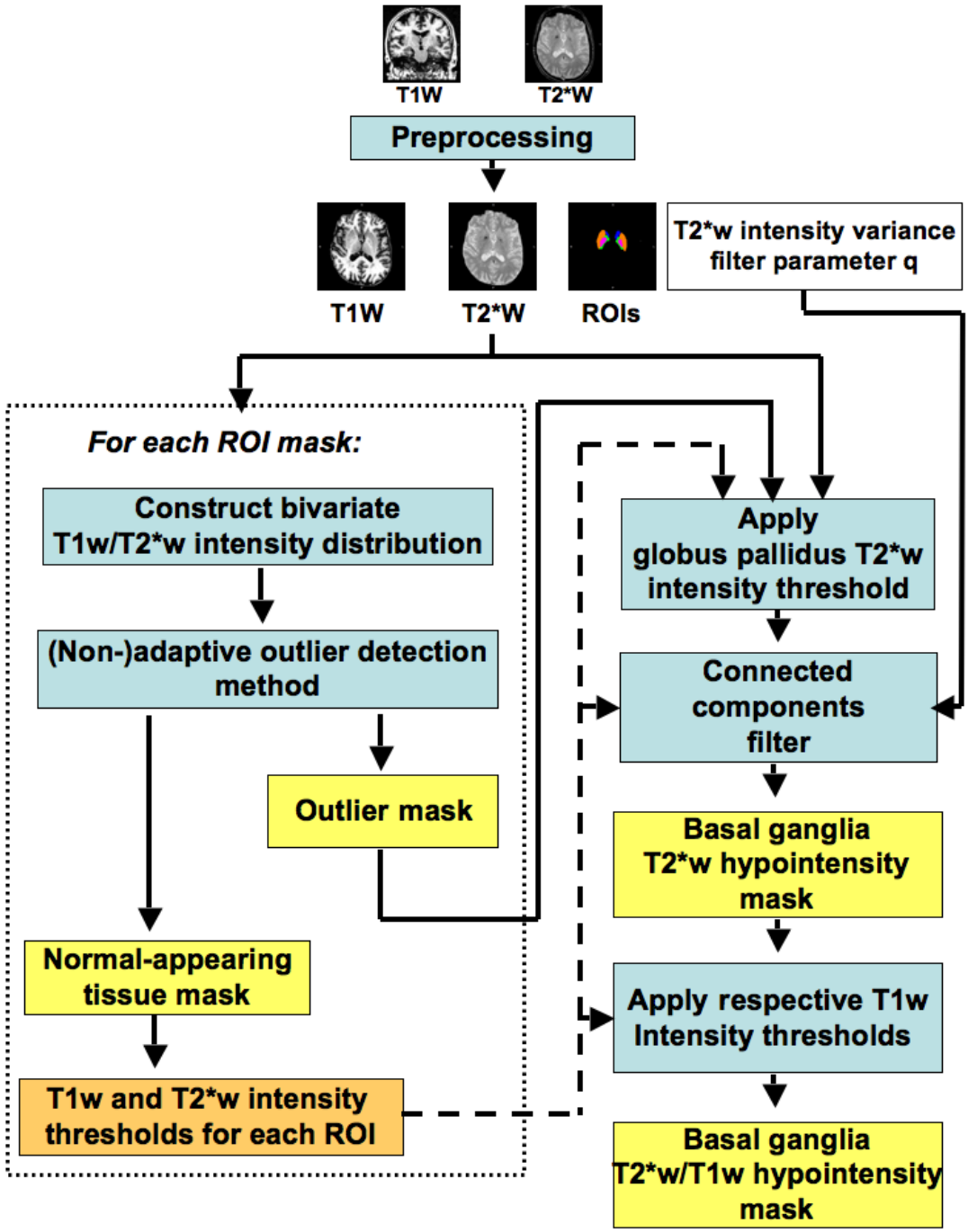

Figure 3-1: Overview of the fully automated method for segmenting basal ganglia T2*w hypointensities. The method requires structural T2*w and T1w volumes as input. The preprocessing step removes non-brain structures, reduces non-anatomical T2*w and T1w intensity variations (bias field) and automatically generates ROIs for the basal ganglia and adjacent internal capsule. Then T2*w and T1w thresholds are automatically derived with an unsupervised outlier detection method from the T2*w and T1w intensity distribution of each ROI. Initial T2*w hypointensity masks are obtained by applying the T2*w threshold to the T2*w volume. The connected components of these masks are identified and filtered according to their T2*w intensity variance, which yields the final T2*w hypointensity masks. Additionally, subregions of basal ganglia T2*w hypointensities that appear hypointense on T1w MRI are segmented since these possibly indicate advanced mineralization, such as calcification.

The final ROI mask set consisted of four ROI masks, $\mathcal{M}_l^{ROI} \subset \mathcal{M}$, with the structure labels $l \in \{cn, pu, gp, ic\}$ corresponding to the caudate nucleus (cn), putamen (pu), globus pallidus (gp) and adjacent internal capsule (ic), where $\mathcal{M} \subset \mathbb{Z}^3$ indexes the MRI volume voxel lattice.

3.3.2. Automated threshold selection for segmenting focal T2*w hypointensities

The T2*w intensities of tissue l with focal T2*w hypointensities are modelled as

$$G_l = (1 - \xi)G_l^{norm} + \xi G_l^{hypo}, \qquad 3\text{-}1$$

where the cumulative distribution function of the T2*w intensities G_l are a mixture of normal appearing T2*w tissue intensities and T2*w hypointensities with the cumulative distribution functions G_l^{norm} and G_l^{hypo}, and $0 \leq \xi \leq 1$ as the mixture weight. If both mixture components are normally distributed then methods, such as mixture discriminant analysis (Fraley & Raftery, 2002), can derive an optimal T2*w threshold for dividing the T2*w tissue intensities into normal appearing T2*w tissue intensities and T2*w hypointensities. However, as previously noted (Chapter 2), T2*w hypointensity distributions typically do not resemble normal distributions, their shapes are variable and their mixture weights are very small ($\xi \ll 1$), hence identifying their underlying parametric distributions is challenging. Therefore T2*w hypointensities were considered outliers of normal appearing T2*w tissue intensity distributions, which sufficiently well resemble normal distributions especially when the signal-to-noise ratio (SNR) is high (Gudbjartsson & Patz, 1995).

In this study a previously published robust multivariate outlier detection method (Filzmoser *et al.*, 2005) was adapted for co-registered T2*w and T1w MRI data as described in detail in Appendix C. This method automatically derives T2*w and T1w thresholds

$$\begin{aligned} s_{l,T2*w}^{thresh,m} &= s_{l,T2*w}^{\mu} - s_{l,T2*w}^{\sigma} \check{d}_l^{crit,m} \\ s_{l,T1w}^{thresh,m} &= s_{l,T1w}^{\mu} - s_{l,T1w}^{\sigma} \check{d}_l^{crit,m} \end{aligned} \qquad 3\text{-}2$$

in analogy to an experienced rater using a previously developed semi-automated thresholding method described in (Valdés Hernández *et al.*, 2011). These specific thresholds were optimised to segment focal T2*w hypointensities and their subregions that appear hypointense on T1w MRI that were of particular interest for experienced raters in previous studies (Penke *et al.*, 2012; Valdés Hernandéz *et al.*,

2012; Valdés Hernández *et al.*, 2011). The robust means $s^{\mu}_{l,T2*w}, s^{\mu}_{l,T1w}$ and standard deviations $s^{\sigma}_{l,T2*w}, s^{\sigma}_{l,T1w}$ of the normal appearing T2*w and T1w tissue intensity distributions were estimated with the minimum covariance determinant (MCD) method (Rousseeuw & Driessen, 1999). The z-score of the critical distance $\check{d}_l^{crit,m}$ was constant or variable in case of the non-adaptive or adaptive version of the outlier detection method $m \in \{na, ad\}$. A refinement of the constant z-score accounted for the sample size of the normal appearing T2*w and T1w tissue intensity distributions.

The contrast-to-noise ratio (CNR) of the thresholds (Equation 3-2) is

$$CNR_{l,j}^{thresh} = \frac{\left|s_{l,t}^{thresh} - s_{l,t}^{\mu}\right|}{s_{l,j}^{noise}} = \frac{\left|s_{l,t}^{\sigma}\right|}{s_{l,j}^{noise}} \check{d}_l^{crit,m} = CNR_{l,j}^{\sigma} \check{d}_l^{crit,m} \qquad 3\text{-}3$$

with $j \in \{T2^*w, T1w\}$. It depends on the CNR corresponding to the spread of the normal appearing T2*w and T1w tissue distributions as well as the z-score of the critical distance, hence it depends on the MRI sequence parameters influencing the image noise, the estimation method of the spread of the normal appearing T2*w and T1w tissue distributions, as well as the sample size of this distribution in the case of the adaptive outlier detection method. However, the CNR corresponding to the thresholds is independent of the mean T2*w and T1w tissue intensities, which both are known to decrease with age due to age-related tissue changes, such as iron accumulation (Aquino *et al.*, 2009).

3.3.3. Segmentation and filtering of focal T2*w hypointensities

The T2*w and T1w thresholds (Equation 3-2) were derived individually for each ROI. Similar to van Es *et al.* (2008) and Valdés Hernández *et al.* (2011), the T2*w hypointensities of all ROIs were then segmented with the respective T2*w threshold of the globus pallidus since it represents the lowest and hence most conservative T2*w threshold, which then created initial T2*w hypointensity masks. The thresholding artefacts of these masks were then eliminated with a connected components filter, which yielded the final T2*w hypointensity masks. This segmentation and connected components filtering step is summarized below and described in further detail in Appendix D.

The connected components filter is based on the observation that an experienced rater tends to inspect all segmented focal T2*w hypointensities of the initial T2*w

hypointensity masks, i.e. the connected components of the masks, and remove focal T2*w hypointensities that either appear too smooth, i.e. connected components with too similar T2*w intensities, or too small. The connected component filter of the developed method, whose principle is illustrated in Figure 3-2, identified connected components with 6-connected neighbourhood in three-dimensional (3D) T2*w hypointensity masks. The smoothness of the identified focal T2*w hypointensities was quantified with the standardised T2*w intensity variance, which represents the variance of the T2*w intensities of a focal T2*w hypointensity normalized by the variance of the T2*w intensities of the surrounding normal appearing tissue. Formally, the standardized T2*w intensity variance was defined as

$$q_{l,h} = \frac{\left(s_{h,T2*w}^{hypo,\sigma}\right)^2}{\left(s_{l,T2*w}^{norm,\sigma^{loc}}\right)^2}, \qquad 3\text{-}4$$

where $s_{h,T2*w}^{hypo,\sigma}$ is the standard deviation of the T2*w hypointensities of the connected component h and $s_{l,T2*w}^{norm,\sigma^{loc}}$ is the local standard deviation of the normal appearing T2*w tissue intensities of the structure where the connected component is located. The connected components filter then excluded connected components with a standardised T2*w intensity variance $q_{l,h}$ below a threshold q. Notably, a threshold $q > 0$ also implicitly removes connected components that have a size of a single voxel since their standardised T2*w intensity variance is 0.

Thresholding and connected component filtering yields the final T2*w hypointensity masks, which are furthermore denoted $\mathcal{M}_{l,T2*w}^{hypo}$. Lastly, hypointense subregions of co-registered T1w volumes selected by these masks were segmented with the T1w threshold of the basal ganglia structures where the T2*w hypointensity was located (Equation 3-2). The obtained T2*w/T1w hypointensity masks are denoted $\mathcal{M}_{l,T1w}^{hypo}$ and possibly indicate areas of advanced mineralization (Valdés Hernández *et al.*, 2014). As the T2*w/T1w hypointensities masks select subregions of the T2*w hypointensity masks $\mathcal{M}_{l,T1w}^{hypo} \subset \mathcal{M}_{l,T2*w}^{hypo}$ is always true.

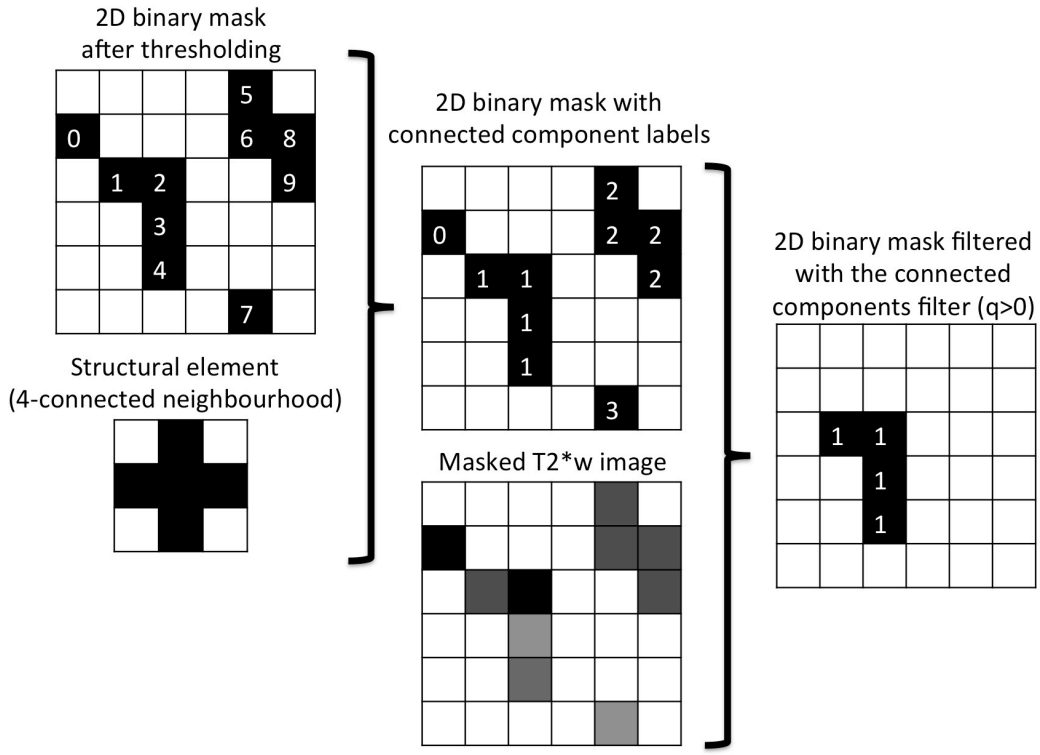

Figure 3-2: Principle of the connected components filter (2D example). Firstly the connected components with 4-connected neighourhood of a 2D binary mask are identified. In this example, a particular voxel is classified as part of a connected component if the convolution with the binary structural element shown on the left results in a value greater one. The identified connected components are then assigned unique labels as shown in the centre of this Figure, where in this particular case two connected components are single pixels, one is L-shaped and one is S-shaped. The connected component filter then calculates the standardised T2*w intensity variance (Equation **3-4**) for each connected component using the T2*w pixel values from the T2*w image and excludes connected components with a standardised T2*w intensity variance equal or below a threshold q. Here, three connected components are excluded since their T2*w pixels have the same intensity, which result in a standardised variance of 0 that is less than the threshold $q > 0$.

3.4. Validation

The presented automated method for segmenting focal T2*w hypointensities was validated with co-registered T1w and T2*w volumes acquired from (i) a custom-designed MRI phantom containing doped gel beads as models for basal ganglia mineralization and (ii) 98 community-dwelling subjects in their seventies recruited from the Lothian Birth Cohort 1936 (LBC1936; Deary *et al.*, 2007). In both cases the multifocal T2*w hypointensities were automatically segmented with the presented method. The automatically generated masks were compared with reference masks, which in the case of the subjects, were produced by an experienced rater. The purpose of the phantom was to analyse the appearance of the basal ganglia

mineralization models on T2*w MRI, as well as to investigate the effect of the adaptive outlier detection method and the connected components filter on the segmentation results. The validation of the software with subject data was carried out to identify the optimal connected components filter parameters for obtaining basal ganglia T2*w hypointensity masks that best resemble those from the rater, as well as to determine the accuracy and precision of the developed segmentation method.

3.4.1. Validation with a custom-built phantom

3.4.1.1. Phantom design

Three types of calcium alginate (CaAlg) gel beads (Figure 3-3A) containing the MRI contrast agents Nanomag-D 250nm (N/250nm), Nanomag-D 1200nm (N/1200nm) and Nanomag-D 1200nm mixed with hydroxyapatite (HA) nanocrystals (N/1200nm+HA) were produced as models for mineral deposits in the basal ganglia. Seven gel beads of the same type containing varying amounts of Nanomag-D 250nm or Nanomag-D 1200nm (Table 3-1) were suspended in 1.8% w/v agarose in a subcompartment of the phantom. The final phantom consisted of 9 such sub compartments, which were sealed 10 ml BD syringes (www.medisave.co.uk), so that each gel bead type with the same contrast agent concentration was replicated three times. To provide head coil loading and to reduce susceptibility artefacts, these sub compartments were placed in 1.25 g/l $CuSO_4$, 3.6 g/l NaCl solution and oriented parallel to the main magnetic field of the scanner.

Nanomag-D 250nm (micromod Partikeltechnologie, Rostock, Germany) is a MRI contrast agent, which consists of 5-15nm iron particles inside a dextran matrix with a diameter of 250 nm. Nanomag-D 1200nm particles are produced by carefully aggregating Nanomag-D 250nm with additional dextran as glue and have previously been used as a model of basal ganglia iron deposits (Sedlacik *et al.*, 2014). The protocol for producing the CaAlg gel beads was based on that described by (Xie *et al.*, 2010). In short, 2% (w/v) sodium alginate solutions were mixed either with N/250 nm, N/1200 nm, or N/1200 nm and a hydroxyapatite precursor, as summarized in Table 3-1, and were dripped with 10 ml BD syringes into 500 mM calcium chloride solutions. The droplets were transitioned in these solutions into

approximately spherical gel beads with a mean diameter of 3 mm containing iron and hydroxyapatite nanocrystals as shown in Figure 3-3A.

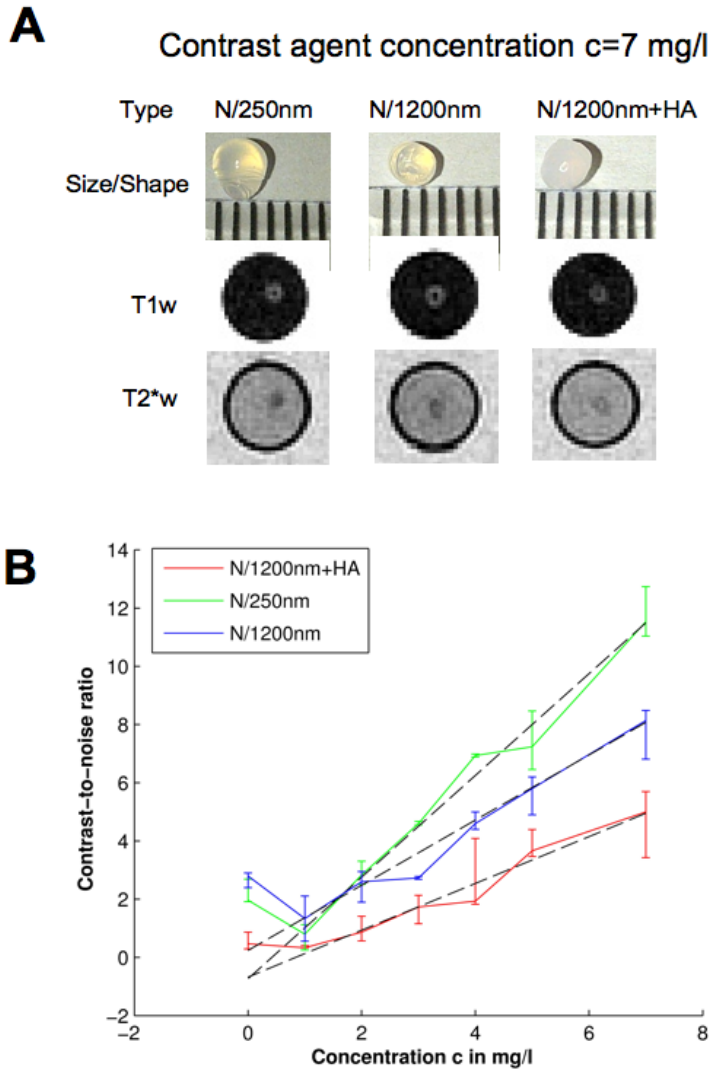

Figure 3-3: Phantom models of basal ganglia T2*w hypointensities and their appearance on T2*w MRI. Doped calcium alginate (CaAlg) gel beads were used as models for focal mineralizations in the basal ganglia (A). These gel beads were on average spherical with a diameter of 3 mm and either doped with the MRI contrast agent Nanomag-D 250nm (N/250nm), Nanomag-D 1200nm (N/1200nm), or Nanomag-D 1200nm and hydroxyapatite nanocrystals (N/1200nm+HA). These beads then appeared as focal hypo- and hyperintensities on T2*w and T1w MRI. The plot below (B) shows the median T2*w contrast-to-noise ratios (CNRs) of all three gel bead replicates (Equation 5) over the contrast agent concentrations, where the errorbars indicate the respective interquartile ranges. The CNR increase with the contrast agent concentration was modelled with robust linear regression lines (dashed).

Table 3-1: Composition of the sodium alginate solutions for creating the calcium alginate gel beads used as mineral deposit models. A 2% (w/v) sodium alginate solution was used as the base solution for creating all gel beads (Xie *et al.*, 2010). The MRI contrast agents Nanomag 250 and 1200 nm, as well as the hydroxyapatite precursor, were added in the following concentrations to the base solution to create gel beads containing iron and hydroxyapatite nanocrystals, which were then used as mineral deposit models.

Gel bead type	Sodium alginate solution additives	
	MRI contrast agent	Hydroxyapatite precursor
N/250nm	0, 1, 2, ..., 7 mg/l Nanomag 250 nm	None
N/1200nm	0, 1, 2, ..., 7 mg/l Nanomag 1200 nm	None
N/1200nm+HA	0, 1, 2, ..., 7 mg/l Nanomag 1200 nm	200 mmol/l Na_2HPO_4

3.4.1.2. MRI protocol

The phantom was scanned on a GE Signa HDxt 1.5 T clinical scanner (General Electric, Milwaukee, WI, USA) using a self-shielding gradient set with maximum gradient of 40 mT/m and an eight-channel phased-array receive/transmit head coil. Table 3-2 shows the MRI protocol for the phantom, which consisted of T2*w (GRASS) and T1w (IR-prep FSPGR) sequences. This protocol was the same as that used to image the subjects except that the field-of-view was smaller and the slices were thicker to reduce Gibbs ringing artefacts caused by the sub compartment walls of the phantom. T2*w and T1w sequences were prescribed to image exactly the same volume containing all the gel beads, which produced naturally co-registered T2*w and T1w volumes. The typical appearance of the gel beads on T2*w and T1w MRI is shown in Figure 3-3A. Unlike basal ganglia T2*w hypointensities (Chapter 2), all CaAlg gel beads were clearly visible on T1w MRI as focal hyperintensities, which had no impact on their automated segmentation and was exploited for creating the reference masks as described further below.

Table 3-2: MRI sequence parameters for scanning the phantom and LBC1936 subjects. The complete protocol for LBC1936 subjects is described in Wardlaw *et al.* (2011)**.**

Sequence	IR-prep FSPGR (3D)	GRASS (2D)
Contrast type	T1-weighted (T1w)	T2*-weighted (T2*w)
Flip angle in degrees	8	20
TI/TR in ms	500/9.8	-/940
Bandwidth in Hz/pixel	122	98
TE in ms	4	15
MRI phantom [a]		
FOV in mm^2	192 x 192	192 x 192
Orientation	Axial	Axial
Slice thickness in mm	1.2	2.4
Acquisition matrix (effective and final)	256 x 256	256 x 256
Subjects		
FOV in mm^2	256 x 256	256 x 256
Orientation	Coronal	Axial
Slice thickness in mm	1.3	2
Effective acquisition matrix	192 x 192	256 x 192
Final acquisition matrix [b]	256 x 256	256 x 256

[a] The T1w and T2*w sequences were configured to image the same phantom volume

[b] After interpolation by the scanner software

3.4.1.3. Image preprocessing and semi-automatic ROI segmentation

N4 was used for the bias field correction of the T2*w and T1w volumes (Tustison *et al.*, 2010). The T1w volume was then resampled using FSL FLIRT with sinc interpolation (Jenkinson *et al.*, 2002) to match the resolution of the T2*w volume. ROI masks were semi-automatically created with the T1w volume as described below and then resampled using FSL FLIRT with nearest neighbour interpolation (Jenkinson *et al.*, 2002).

Initial ROI masks were produced by thresholding the bias-field corrected T1w volume with a threshold equal to 80% of the mean T1w signal intensity of the $CuSO_4$/NaCl solution. The obtained mask was first dilated using a spherical kernel

with 6 mm diameter to close holes caused by the T1w hyperintensities of the gel beads and then eroded using a spherical kernel with 12 mm diameter to remove artefacts from the plastic walls of the sub compartments. The final ROI masks were obtained after manually removing remaining artefacts and assigning unique labels to the individual masks of each sub compartment.

3.4.1.4. Segmentation and quality control of the CaAlg gel beads on T2*w MRI

The CaAlg gel bead reference mask was obtained by automatically placing spherical shaped masks with the average diameter of the gel beads at the locations of the T1w hypointensities created by the gel beads. For the quality control of the CaAlg gel beads this mask was subsequently used to calculate the CNRs on T2*w MRI of all gel beads, which should increase approximately linearly per gel bead type with contrast agent concentration due to the short echo time and the low contrast agent concentrations.

The initial locations of these T1w hypointensities were estimated from masks which were created by logically inverting the initial ROI masks and combining them with the final ROI masks with a 'logical AND' operation. The connected components of the resulting masks then corresponded to most of the T1w hypointensities caused by the CaAlg gel beads. Missing connected components or connected components associated with artefacts were added or removed manually. Subsequently, the connected components were replaced by the spherical masks with a diameter of 3 mm, which were typically smaller than the hyperintensities visible on the original T1w volumes due to partial volume effects (Rexilius & Peitgen, 2008). Finally, the spherical masks $\mathcal{M}^{hypo,ref}_{g,f,l,T2*w}$, where $g \in \{1,2,\dots,7\}$ is the gel bead index, $f \in \{1,2,3\}$ is the replicate index, and $l \in \{1,2,3\}$ is the ROI index, were centred on the corresponding T1w hypointensities. The optimal position of a spherical mask was estimated by translating the masks along all coordinate system axes to find the position where the mean T1w intensities of selected mask voxels selected by this mask became a maximum.

The CNR of all CaAlg gel bead replicates on T2*w MRI then calculated with

$$CNR_{g,l,T2*w} = \left(\frac{1}{3}\sum_{f=1}^{3}\left|s^{hypo,\mu}_{g,f,l,T2*w} - s^{norm,\mu}_{f,l,T2*w}\right|\right)/s^{noise}_{T2*w}, \qquad 3\text{-}5$$

where $s^{hypo,\mu}_{g,f,l,T2*w}$ is the robust mean T2*w intensity of an individual CaAlg gel bead selected by the masks $\mathcal{M}^{hypo,ref}_{g,f,l,T2*w}$, $s^{norm,\mu}_{f,l,T2*w}$ is the robust mean intensity of the agarose in the respective sub compartment, and s^{noise}_{T2*w} is the T2*w image noise (Firbank *et al.*, 1999). The increase of the mean CNR per gel bead type with the contrast agent concentration was estimated with robust linear regression lines (Matlab function 'robustfit()').

3.4.1.5. Automated segmentation of focal T2*w hypointensities in the phantom

Focal T2*w hypointensities were segmented in each sub compartment of the phantom using the original and bias-field corrected T2*w and T1w volumes with the respective T2*w thresholds from the non-adaptive and adaptive version of the outlier detection method (Section 3.3.2). To investigate the effect of the connected components filter on the segmentation results, the initial masks were also filtered with the connected components filter parameters q = 0, 0.1, …, 1.5. To aid further analysis, the connected components (six-connected neighbourhood) of the generated masks $\mathcal{M}^{hypo}_{g,w,l,T2*w}(m^{bfc}, m, q)$, where $m^{bfc} \in \{None, N4\}$ created with the original or bias-field corrected T2*w and T1w volumes were also identified and labelled with the Matlab function 'bwlabeln()'.

3.4.1.6. Comparison of the non-adaptive and adaptive outlier detection methods

For the comparison of the non-adaptive and adaptive version of the outlier detection method the agreement between the CaAlg gel bead reference mask and the corresponding T2*w hypointensity masks, which were generated on the original and bias-field corrected volumes, were assessed. The number of segmented T2*w hypointensities that corresponded to gel beads, as well as those that represented thresholding artefacts were counted. A connected component of the generated masks was considered to be associated with a gel bead if its mask overlapped at least 50% with the corresponding reference mask, i.e. the regional sensitivity was greater than 0.5 (Shattuck *et al.*, 2009). The spatial agreement between the CaAlg gel bead reference and generated masks was quantified with the Jaccard index

$$J_l\,(m^{bfc}, m, q) = \left| \frac{\mathcal{M}^{hypo}_{l,T2*w}(m^{bfc}, m, q) \cap \mathcal{M}^{hypo,ref}_{l,T2*w}}{\mathcal{M}^{hypo}_{l,T2*w}(m^{bfc}, m, q) \cup \mathcal{M}^{hypo,ref}_{l,T2*w}} \right|, \qquad 3\text{-}6$$

which is 0 in situations where these masks are completely disjointed or 1 if they are identical (Shattuck *et al.*, 2009). Lastly, the minimum CNRs of the segmented CaAlg gel beads and the CNR of the respective T2*w thresholds (Equation 3-3) were calculated to investigate their agreement.

3.4.1.7. Analysis of the blooming artefacts around the CaAlg gel beads

To analyse how the blooming artefacts depend on the gel bead type and MRI contrast agent concentration, the apparent volume increase of the doped CaAlg gel beads on T2*w MRI was calculated and plotted over the MRI contrast agent concentration.

Firstly, the mean volumes of the connected components masks of all gel bead replicates containing the same amount and type of contrast agent were

$$V_{h,l}(m) = \frac{1}{3}\sum_{\mathfrak{f}=1}^{3} \left|\mathcal{M}^{hypo}_{h,\mathfrak{f},l,T2*w}(m^{bfc}, m, q)\right| V^{vox}, \qquad 3\text{-}7$$

where $\mathcal{M}^{hypo}_{l,T2*w}$ was created with $m^{bfc} = N4$ and $q = 0$, and V^{vox} as the voxel volume. As the connected components were on average spherical their diameter $d_{h,l}(m)$ could be estimated with the volume formula of a sphere. The apparent volume increase of the gel beads on T2*w MRI was then quantified with the relative gel bead diameter $d^{rel}_{h,l}(m) = d_{h,l}(m)/d^{bead}$ with $d^{bead} \approx 3mm$, which was then plotted over the contrast agent concentration.

3.4.1.8. Analysis of the connected components filter characteristics

The characteristic filter functions of the connected components filter indicate the change in the spatial agreement between the masks $\mathcal{M}^{hypo}_{l,T2*w}$, which were created with $m^{bfc} = N4$ and $m = ad$, and the CaAlg gel bead reference mask with the filter parameter q. To construct the characteristic filter functions of each ROI, the spatial agreement between each generated mask and the reference mask was quantified with the standardized Jaccard index

$$J^{std}_{l}(q) = \frac{J_l(q)}{J_l(q=0)}, \qquad 3\text{-}8$$

with $J_l(q) \coloneqq J_l(m^{bfc} = N4, m = ad, q)$ from Equation 3-6. The relative Jaccard index was evaluated at $q = 0{,}0.1, \ldots, 1.5$ and then plotted over the parameter q. The

FWHM of a characteristic filter function was the parameter q_l^{FWHM}, where $J_l^{std}(q_l^{FWHM}) = 0.5$.

3.4.2. Validation with subject data

3.4.2.1. Subject cohort and validation sample

The developed method was validated with 98 LBC1936 subjects, which were selected as described in Section 2.3.1. For comparison with the phantom MRI protocol the relevant LBC MRI protocol was also included in Table 3-2.

3.4.2.2. Automated and manual segmentation of basal ganglia T2*w hypointensities

For comparison the basal ganglia T2*w hypointensities of the subjects were segmented fully automatically and semi-automatically with the developed method, as well as manually with Analyze 10.0 (Mayo Clinic, Rochester, MN, USA) as described in Chapter 2.

The fully automated segmentation method was used to segmented basal ganglia T2*w hypointensities on the original, as well as bias-field corrected T2*w and T1w volumes with the adaptive outlier detection method since the latter yielded the most promising results *in vitro*. For the fully automated segmentation the optimal connected components filter parameters q were estimated with a 10-fold cross-validation method as described in Appendix E. This method optimized the connected components filter parameters to obtain basal ganglia T2*w hypointensity masks that are most similar to those created manually.

In the semi-automated segmentation of the basal ganglia T2*w hypointensities an experienced rater (MHV) used the developed method with the adaptive version of the outlier detection method to segment basal ganglia T2*w hypointensities in all subjects on bias-field corrected T2*w and T1w volumes. For each subject the rater manually adjusted the connected components filter parameters q, generated the T2*w hypointensity masks, and subsequently edited the generated masks with Analyze 10.0 to add missing T2*w hypointensities or remove thresholding artefacts.

3.4.2.3. Numerical analysis of the volumetric and spatial mask agreement

The volumetric agreement between the fully- and semi-automatically generated masks, and manually created reference masks was quantified with the intra class

correlation coefficient (ICC; agreement version), which was calculated with the R function 'icc()' (CRAN.R-project.org/package=psy). The spatial agreement between these masks was determined with the Jaccard index (Equation 3-6), which was also converted to the Dice coefficient as described in Shattuck *et al.* (2009). Furthermore, the Jaccard indices between the unfiltered basal ganglia T2*w hypointensity masks and the reference masks was quantified and related to the corresponding Jaccard indices obtained with the filtered masks to investigate the impact of the connected components filter on the spatial agreement between the generated and reference masks. The adjusted 95% confidence interval of all robust means was obtained from bootstrapping with the R function 'boot()' (CRAN.R-project.org/package=boot).

3.4.2.4. Bland-Altman analysis of the volumetric and spatial mask agreement

Modified Bland-Altman plots (Bland & Altman, 1986) were used to graphically assess the volumetric and spatial agreement between the generated and reference basal ganglia T2*w hypointensity masks. Quantile regression lines (Koenker & Hallock, 2001) were added to these plots to indicate the change of the average agreement (accuracy) and the variability of the agreement (precision) with the average mask volume, as well as to identify outliers. They were constructed by plotting the relative mask volume differences

$$\Delta V_{k}^{rel} = \left(V_{T2*w,k}^{hypo,opt} - V_{T2*w,k}^{hypo,ref}\right)/V_{k}^{\mu}, \qquad 3\text{-}9$$

and the Jaccard indices $J_{k}^{opt} = J_{k}(q^{opt})$ (Equation 3-6) over the logarithmised average mask volumes $V_{k}^{\mu} = \left(V_{T2*w,k}^{hypo,opt} + V_{T2*w,k}^{hypo,ref}\right)/2$, where $k \in \{1,2,\dots,k^{max}\}$ represents the subject index. The normalisation of the mask volume difference with the average masks volume and the logarithmic transformation of the average mask volume mapped the mask volume differences and the average mask volumes of very large and small basal ganglia T2*w hypointensities into a similar value range. The trend of the data in the modified Bland-Altman plots was estimated with quantile regression lines (Koenker & Hallock, 2001), which were estimated for the 5th, 25th, 50th, 75th and 95th percentiles. Subjects, where neither the method nor the rater segmented basal ganglia T2*w hypointensities masks, were excluded from the plots since Equation 3-9 is undefined in this case. The masks of subjects with corresponding relative volume differences or Jaccard indices outside the quantile

regression lines of the 5th and 95th percentiles, i.e. the 90% range, were considered as outliers and were visually inspected.

3.5. Results

3.5.1. Validation with a custom-built phantom

3.5.1.1. Quality control of the CaAlg gel beads on T2*w MRI

Figure 3-3B shows that the CNRs of all doped gel beads ($c > 0mg/l$) increase approximately linearly with the contrast agent concentration since the gel beads appear increasingly hypointense with respect to the surrounding agarose on T2*w MRI. As the gel beads with a contrast agent concentration $c = 0mg/l$ appear hyperintense with respect to the surrounding agarose on T2*w MRI their CNRs are higher than those of gel beads with $c = 1mg/l$, which appear predominantly isointense. The slopes of the robust regression lines associated with the gel bead types N/250nm, N/1200nm and N/120nm+HA were 1.75, 1.34 and 0.80 l/mg, whereas their intercepts were -0.73, 0.24 and -0.67. The differences in the slopes are caused by the differences in the mass magnetic susceptibility of the contrast agents. In the case of the N/1200nm and N/250nm gel beads the magnetic susceptibility difference comes from the fact that the N/1200nm particles were obtained by aggregating N/250nm particles with additional dextran with the result that the amount of iron per N/1200nm gel bead is slightly lower than that for the N/250nm gel bead. Conversely, the N/1200nm+HA gel beads have a lower magnetic susceptibility than N/1200nm gel beads since the magnetic susceptibility of N/1200nm and HA have opposite signs and therefore the HA crystals partly cancel the effect on the main magnetic field caused by the N/1200nm particles.

3.5.1.2. Comparison of the non-adaptive and adaptive outlier detection methods

Table 3-3 shows that the lowest CNRs, and hence the highest T2*w thresholds relative to the mean T2*w intensity of the agarose (Equation 3-3), were obtained with the non-adaptive outlier detection method on the bias-field corrected T2*w and T1w volumes. The focal T2*w hypointensity masks created with these thresholds selected the highest number of CaAlg gel beads, however, they were also affected by the highest number of thresholding artefacts. Conversely, the lowest T2*w thresholds

relative to the mean T2*w intensity of the agarose were obtained with the adaptive outlier detection method on the original T2*w and T1w volumes, which segmented the lowest number of CaAlg gel beads, as well as having the fewest thresholding artefacts. Overall, the T2*w thresholds obtained with the adaptive version of the outlier detection method on bias-field corrected T2*w and T1w volumes segmented, on average, 13% less CaAlg gel beads than the non-adaptive version, however, it also reduced the number of segmentation artefacts by, on average, 67%. In the case of the phantom this method therefore produced results that represented a trade-off in terms of the number of segmented gel beads, hence the segmentation sensitivity, and thresholding artefacts, which is also confirmed by the Jaccard indices in Table 3-3.

Table 3-3: Comparison of the outlier detection methods. The focal T2*w hypointensities of the phantom were segmented on the original and bias-field corrected T2*w and T1w volumes with the T2*w thresholds from the non-adaptive and adaptive version of the outlier detection method. This table shows the minimum CNR of the segmented gel beads and the CNRs of the T2*w thresholds (Equation 3), as well as the average Jaccard index, which quantifies the spatial agreement between the generated and reference masks of each ROI. Furthermore it includes the average number of segmented focal T2*w hypointensities per ROI that were associated with gel beads (total number of gel beads per ROI = 7) and thresholding artefacts.

Outlier detection method	Non-adaptive		Adaptive	
Bias-field correction	None	N4	None	N4
Minimum CNR of CaAlg gel beads	5.60 ± 0.80	4.58 ± 0.42	7.39 ± 1.45	5.19 ± 0.55
CNR of T2*w threshold	5.21 ± 0.40	4.51 ± 0.38	6.47 ± 0.87	5.02 ± 0.44
Jaccard index	0.16 ± 0.08	0.21 ± 0.07	0.12 ± 0.10	0.22 ± 0.09
Segmented gel beads	1.33 ± 0.87	2.56 ± 1.24	0.89 ± 0.93	2.22 ± 1.20
Thresholding artefacts	4.67 ± 2.96	20.44 ± 4.90	2.33 ± 1.41	6.67 ± 3.54

3.5.1.3. Analysis of the blooming artefacts around the CaAlg gel beads

Figure 3-4 shows that the relative diameter of the focal T2*w hypointensities $d_{h,l}^{rel}(m, q = 0)$ depends on the CaAlg gel bead type, as well as the contrast agent concentration, both factors that contribute to the volume magnetic susceptibility of the gel beads as described in Section 3.5.1.1. The apparent gel bead diameter increase on T2*w MRI can therefore be attributed to the volume of blooming artefacts around the gel beads, which are a function of the volume magnetic susceptibility (Pintaske *et al.*, 2006). Figure 3-4 also shows that the T2*w hypointensity masks of N/250 nm, N/1200 nm and N/1200 nm+HA gel beads, which were generated with T2*w thresholds from the adaptive outlier detection method, are (median [interquartile range] %) 5.4 [37.1], 10.6 [70.2], and 5.0 [5.3] % smaller than the respective masks created with T2*w thresholds from the non-adaptive outlier detection method. This approximately uniform decrease across all gel bead masks shows that the blooming artefacts cannot be selectively reduced with a subject specific threshold as was used here. The volumes of the basal ganglia T2*w hypointensity masks from the developed segmentation method are therefore influenced by the actual volume of the underlying mineralization, as well as its magnetic susceptibility.

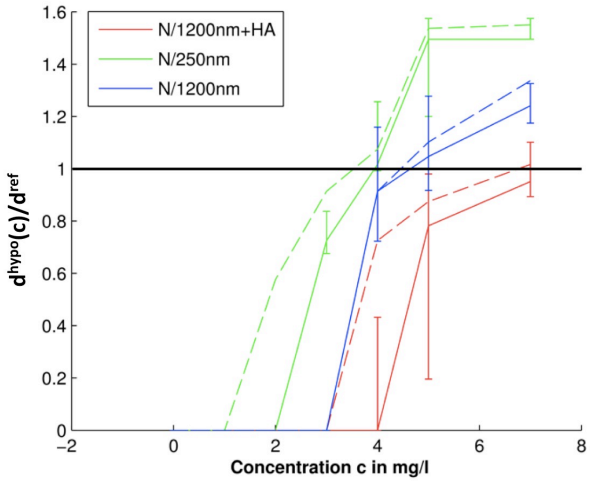

Figure 3-4: Apparent gel bead diameter increase on T2*w MRI due to blooming artefacts. The T2*w hypointensities of the doped CaAlg gel beads were segmented with the thresholds from the non-adaptive and adaptive outlier detection methods on bias-field corrected T2*w and T1w volumes. The T2*w hypointensities of the obtained masks that corresponds to gel beads were identified, their diameter measured and normalized by the average gel bead diameter $\boldsymbol{d^{bead} \approx 3mm}$. This plot shows the measured diameter $\boldsymbol{d_{h,l}^{rel}}$(m) over the contrast agent concentration. Dashed and solid lines refer to the results associated with the non-adaptive and adaptive outlier detection method.

3.5.1.4. Analysis of the connected components filter characteristics

Figure 3-5A shows the characteristic function of the developed connected components filter for each gel bead type. The FWHM of the characteristic filter functions associated with the N/250nm, N/1200nm and N/1200nm+HA gel beads were 1.39, 0.86, and 0.72. This indicates that this filter preferentially removed T2*w hypointensities associated with N/1200nm and N/1200nm+HA gel beads from the T2*w hypointensity masks obtained after thresholding, which is also illustrated in Figure 3-5B. The connected components filter also reduces thresholding artefacts, which can lead to maxima in the characteristic functions, as it was the case for the characteristic functions of the N/1200 gel beads. Overall these results confirm that the connected components filter preferentially retains features that appear more inhomogeneous on T2*w MRI, such as the N/250nm gel beads, which appear as focal T2*w hypointensities with dark core regions and bright shell regions.

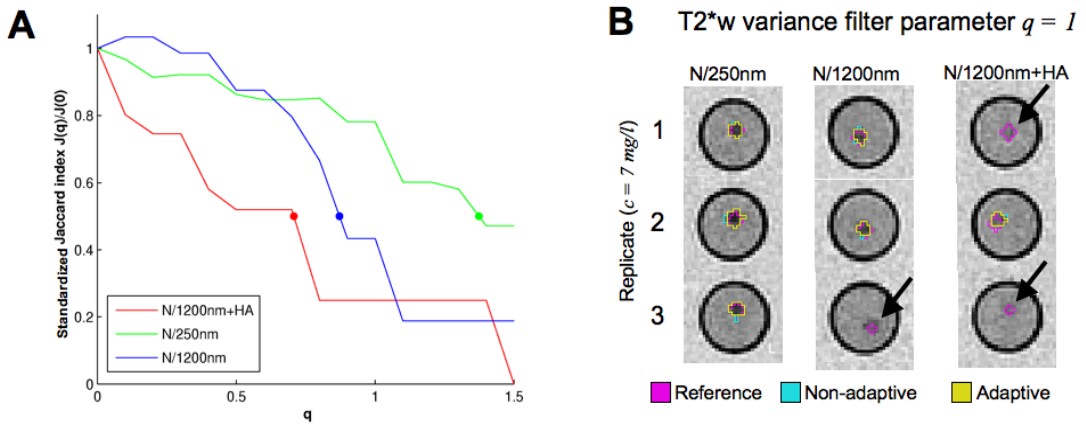

Figure 3-5: Characteristic functions of the connected components filter. The left Figure **(A)** shows the characteristic functions of the connected components filter for each gel bead type and the coloured dots represent the FWHM of the filter functions. These characteristic functions indicate that with increasing parameter *q* the filter predominantly rejects focal T2*w hypointensities associated with N/1200nm and N/1200nm+HA gel beads (black arrows) since these focal T2*w hypointensities appear more homogenous on T2*w MRI than those associated with N/250nm gel beads. The right Figure **(B)** illustrates these filter properties for the case *q = 1*.

3.5.2. Validation with subject data

3.5.2.1. Numerical analysis of the volumetric and spatial mask agreement

The steps by which the fully and semi-automated segmentation methods create basal ganglia T2*w hypointensity masks are illustrated in Figure 3-6.

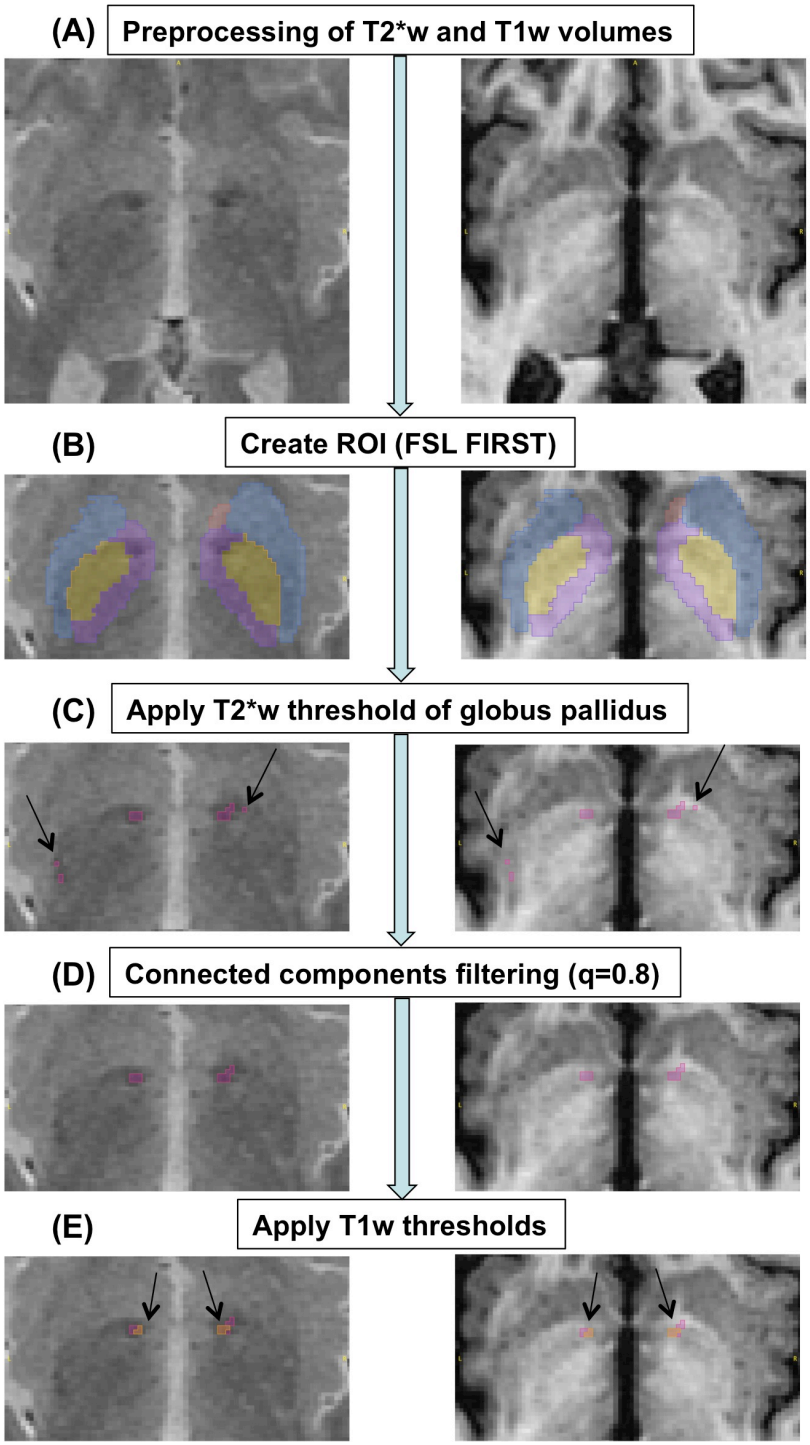

Figure 3-6: Intermediate and final masks created by the automated T2*w hypointensity segmentation method for an representative subject. Firstly, The preprocessed T2*w and T1w volumes (**A**) are used to generate ROI masks (**B**), which select most of the basal ganglia and the adjacent internal capsule. Applying the T2*w threshold of the globus pallidus creates initial T2*w hypointensity masks (**C**) that include several false positive features (arrows) according to the reference masks from the experienced rater. These thresholding artefacts are then removed by the connected components filter, which yields the final basal ganglia T2*w hypointensity mask (**D**). Applying the T1w thresholds to the segmented basal ganglia T2*w hypointensities creates basal ganglia T2*w/T1w hypointensity masks (**E**; yellow masks**)**, which possibly indicate regions of advanced mineralization.

The results of the numerical analysis of the volumetric and spatial agreement between the manually created basal ganglia T2*w hypointensity masks and the fully and semi-automatically created masks are summarized in Table 3-4. This table shows that the masks created with the thresholds from the adaptive outlier detection method on the original T2*w and T1w volumes were most similar to those created manually by the experienced rater as indicated by the corresponding Jaccard indices and Dice coefficients. In the semi-automated segmentation of the basal ganglia T2*w hypointensities the rater edited a total of 20 masks which, however, lead to a minimal change in the Jaccard index compared with that produced by the fully automated segmentation using the bias-field corrected volumes. The intraclass correlation coefficient associated with the semi-automated method, on the other hand, was higher than that of the fully automated method. This indicates that manual editing of the masks by the second rater had little effect on the spatial agreement between the generated and reference masks albeit it had a marked effect on their volumetric agreement. In all cases the CNR associated with the automatically estimated thresholds (Equation 3-3), as well as the connected components filter parameters, varied very little across the subjects. Lastly, Table 3-4 also shows that connected component filtering and manual editing of the unfiltered masks ($q = 0$) did not lead to a greater improvement in each subject's Jaccard index compared with connected component filtering only.

Table 3-4: Basal ganglia T2*w hypointensity segmentation statistics. Basal ganglia T2*w hypointensities were segmented with the fully- and semi-automated methods. In the former case the features were segmented on the original and bias-field corrected T2*w and T1w volumes, whereas in the latter case they were segmented on the bias-field corrected T2*w and T1w volumes. The T2*w and T1w thresholds were estimated with the adaptive outlier detection method and the connected components filter parameter q was either chosen with the 10-fold cross-validation method or manually by the rater. In the semi-automatic segmentation method, the rater also edited the generated masks to add basal ganglia T2*w hypointensities that were missed by the method and to remove thresholding artefacts. This table shows the robust mean, standard deviation (SD) and 95% confidence interval (CI) of the robust mean of the filter parameter q, the CNR associated with the T2*w threshold (Equation **3-3**), as well as measures that quantify the volumetric and spatial agreement between the generated and reference masks, which were manually created by a second experienced rater.

Method	Fully-automated				Semi-automated	
Bias-field correction	None		N4		N4	
Statistics	Mean ± SD	95% CI	Mean ± SD	95% CI	Mean ± SD	95% CI
q	0.90 ± 0.00	N/A	0.80 ± 0.00	N/A	0.80 ± 0.00	N/A
CNR	8.8 ± 1.3	8.6, 9.1	7.8 ± 1.4	7.7, 8.1	7.8 ± 1.4[a]	7.7, 8.1[a]
Jaccard	0.67 ± 0.40	0.51, 0.75	0.62 ± 0.40	0.53, 0.74	0.62 ± 0.41	0.48,0.70
ΔJaccard[b]	0.03 ± 0.34	0, 0.06	0.03 ± 0.23	0, 0.07	0.03 ± 0.30	0,0.05
Dice	0.80 ± 0.29	0.69, 0.83	0.77 ± 0.30	0.69, 0.86	0.77 ± 0.33	0.63,0.83
ICC	0.69	0.24, 0.91	0.70	0.23, 0.93	0.74	0.54,0.90

[a] Same as obtained with the automated method on bias-field corrected volumes.

[b] Relative to the corresponding Jaccard indices obtained at $q = 0$

3.5.2.2. Bland-Altman analysis of the volumetric and spatial mask agreement

The volumetric and spatial agreement between the basal ganglia T2*w hypointensity masks, which were automatically created on the bias-field corrected T2*w and T1w volumes, and the corresponding reference masks was assessed with the Bland-Altman plots in Figure 3-7. The plot in Figure 3-7A indicates that the average mask volume difference, as indicated by the median quantile regression line, is close to zero and slightly decreases with the average mask volume. This indicates that the generated and reference mask volumes were, on average, very similar. However, the masks for smaller and larger basal ganglia T2*w hypointensities were slightly too large and slightly too small. Conversely, Figure 3-7B shows that there was largely no spatial agreement between the generated and reference masks for very small basal ganglia T2*w hypointensities. However, the spatial agreement between generated and reference masks increased markedly with the average masks volume

to Jaccard indices above 0.7, corresponding to an 80 % overlap of these masks. Furthermore, both Figures show that the variability of the volumetric and spatial agreement decreased with the average mask volume. Overall, these results indicate that for subjects with large basal ganglia T2*w hypointensities there was substantial volumetric and spatial agreement between the automatically generated and the reference masks from the experienced rater.

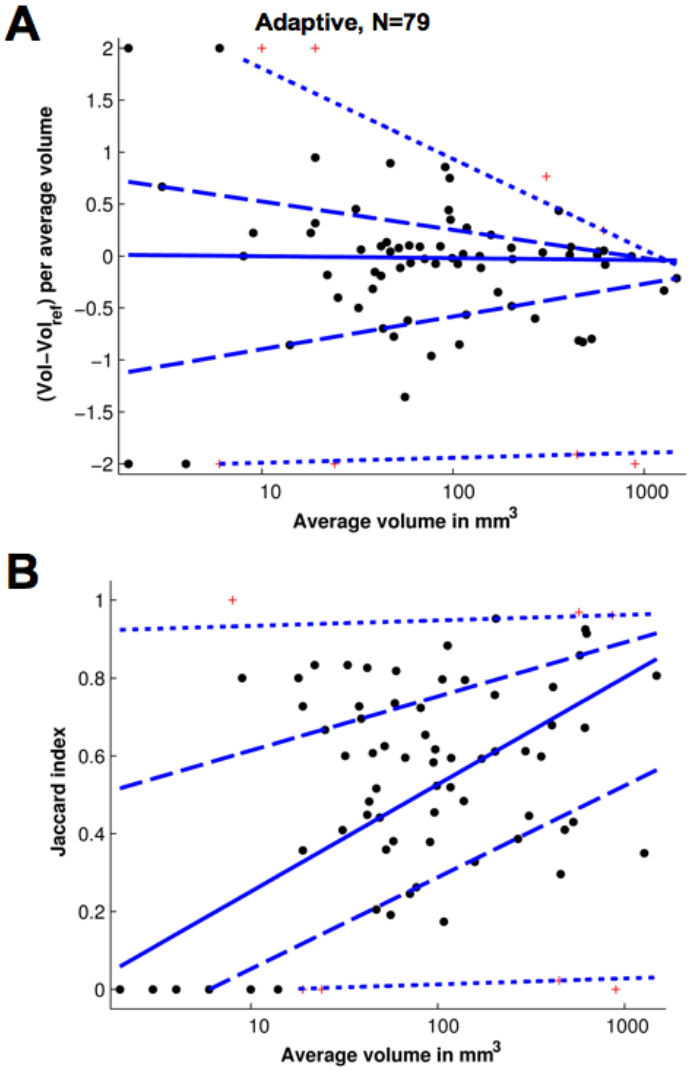

Figure 3-7: Volumetric and spatial agreement between basal ganglia T2*w hypointensity masks from the automated segmentation method and the rater. The upper plots (**A**) shows the mask volume differences over the average mask volumes and the lower plot (**B**) the Jaccard indices (Equation **3-6**) over the logarithmised average mask volumes. Subjects for which neither the rater nor the method generated basal ganglia T2*w hypointensity masks were excluded since the y-axis values were mathematically not defined. The trend in the data was estimated with quantile regression lines (Koenker & Hallock, 2001), which were calculated for the 50th percentile (solid line), 25th and 75th percentiles (dashed lines), and 5th and 95th percentiles (dotted lines). Data points outside the 90% range were considered outliers and are shown as red crosses. Quantile regression lines were censored if their y-axis values exceeded the valid y-axis value ranges.

Data points outside the 5th and 95th percentile quantile regression lines in Figure 3-7A and data points below the 5th percentile quantile regression line in Figure 3-7B represent subjects for which the method failed to produce masks. Visual inspection of the generated and reference masks of these subjects found that most of the T2*w hypointensities were very small, appeared isointense on T1w MRI, and were associated with a low CNR and fuzzy boundaries on T2*w MRI. In the case of one subject the T2*w MRI was heavily compromised by susceptibility artefacts, and in other two cases the T2*w and T1w intensity distributions of the normal-appearing basal ganglia tissue were either bimodal or did not resemble Normal distributions. The latter violated the main assumptions of the outlier detection methods and therefore there was a marked difference between the automatically estimated T2*w thresholds and those produced by the rater.

3.6. Discussion

In this study we developed and validated a novel method for the automatic segmentation of multifocal T2*w hypointensities in the basal ganglia and adjacent internal capsule which are believed to arise from mineral deposits in and around the penetrating arterioles and perivascular spaces. This method uses an adaptive outlier detection method to derive T2*w and T1w thresholds from bivariate T2*w and T1w intensity distributions of individual basal ganglia structures. The CNRs associated with these thresholds (Equation 3-3) are insensitive to a change in the mean T2*w and T1w intensity of a structure, as it is the case in ageing due to iron accumulation. These thresholds are then used to segment all focal T2*w hypointensities of a structure and a connected components filter subsequently removes focal T2*w hypointensities with standardised T2*w intensity variances below automatically derived thresholds to reduce thresholding artefacts. The output of this method are basal ganglia T2*w and T2*w/T1w hypointensity masks, where the latter presumably indicates regions of advanced mineralisation. The effects of the outlier detection method and the connected components filter on the segmentation results were investigated with a custom-built phantom containing different models of basal ganglia mineral deposits. The method was also validated with MRI data from 98

community-dwelling older subjects in their seventies to assess its ability to generate similar masks to those produced by an experienced rater.

The phantom experiments show that blooming artefacts around the CaAlg gel beads increase their apparent diameter on T2*w MRI by up to 1.6 times. The volume of the generated basal ganglia T2*w hypointensity masks therefore reflects not only the volume of the underlying mineral deposits but also their magnetic susceptibility (Bos *et al.*, 2003; Pintaske *et al.*, 2006). In previous studies (Penke *et al.*, 2012), the magnetic susceptibility therefore likely acted as an additional weight in the correlation analysis. Hence mineral deposits with the same volume, but different magnetic susceptibility, possibly have a different impact on the correlation result. As the magnetic susceptibility of mineral deposits can be determined with gradient-echo MRI it should be possible to develop a correction method for blooming artefacts (McAuley *et al.*, 2011). Such a method could help to clarify the specific impact of the chemical composition and extent of mineral deposits in the ageing brain.

The unsupervised multivariate outlier detection methods rely on the assumption that the co-registered T2*w and T1w signal intensities of normal-appearing tissue resemble bivariate normal distributions with robust distances which in turn resemble non-central χ^2 distributions (Hardin & Rocke, 2005). Although this assumption was not explicitly checked, it can be concluded that it was reasonably well satisfied since the automated method produced segmentation results that were in substantial agreement with the reference masks of the phantom and subjects. Furthermore, the T2*w sequence used in this study (GRASS) was chosen over spoiled gradient echo sequences since it can produce T2*w images with comparatively higher SNR (Bernstein *et al.*, 2004), which helps in assuring that the T2*w intensities of normal-appearing tissue are normally distributed (Gudbjartsson & Patz, 1995). Additionally, the non-anatomical intensity variations caused by the B1 field inhomogeneities (bias field) were corrected on T2*w and T1w MRI, which can also significantly distort the image intensities, and hence reduce the quality of the segmentation results as demonstrated with the phantom results. Recent performance studies also show that the adaptive variant of the unsupervised outlier detection method produces better results than the non-adaptive variant in the case of heavy tailed or skewed multivariate distributions (Filzmoser, 2005). However, further studies are required to

explore the impact on the segmentation results if the T2*w and T1w signal intensity distributions deviate from bivariate normal distributions and if other multivariate outlier detection methods, such as non-parametric methods (Ben-Gal, 2010), could improve the segmentation results.

The developed automated segmentation method for multifocal T2*w hypointensities employs a novel filter, which preferentially removes connected components that appear homogenous on T2*w MRI, i.e. are associated with a standardised T2*w intensity variance below a threshold q. The subject results show that this filter markedly improved the spatial agreement between the automatically generated and reference masks. These findings therefore suggest that the rater, after segmenting basal ganglia T2*w hypointensities with the semi-automated thresholding method (Valdés Hernández *et al.*, 2011), also tended to exclude homogenous T2*w hypointensities. Furthermore the phantom experiments showed that the filter preferentially removed T2*w hypointensities associated with gel beads that were doped with N/1200nm, and especially with N/1200nm and HA microcrystals. This suggests that the filter possibly excludes mineral deposits with a specific chemical composition, such as mineral deposits with calcification, since this makes them appear more homogenous on T2*w MRI. However, further work is required to explain the effects of the chemical composition of trace metal deposits on the T2*w intensity variance. So far, the local intensity variance has only been used as a quality measure for T1w MRI (Aja-Fernández *et al.*, 2006).

In this study the optimal connected components filter parameter for segmenting the basal ganglia T2*w hypointensities in the LBC1936 subjects was derived in a 10-fold cross validation with the reference masks of an experienced rater. However, as the optimal parameter depends on the outlier detecting method and potentially other factors, such as the T2*w sequence and main magnetic field strength, it might be different for subsequent studies. The optimal connected components filter parameter can then be estimated in two ways. As in this study, a representative and random subject subset can be constructed, where an experienced rater segments the basal ganglia T2*w hypointensities and the optimal filter parameter is estimated with cross-validation. If masks from an experienced rater are not available, a heuristic method could possibly be used to estimate the optimal connected components

parameter. A phantom with the same basal ganglia mineralization models as employed in the current study is needed to derive the characteristic connected components filter functions (Figure 3-5A). Here an optimal value of the filter parameter was identified as where the difference between the characteristic filter function of the gel beads with N/250 nm and the average filter function of the gel beads with N/1200 nm and N/1200 nm+HA was maximal. The additional advantage of this approach is that the detection sensitivity for focal mineralization, as well as the size of the blooming artefacts can also be quantified.

This study has several strengths. Firstly, our method was validated with standard structural T2*w and T1w volumes from both a custom-designed phantom and from a random sample of community-dwelling older subjects with a very narrow age range. Secondly, the subject sample was carefully chosen to include a wide range of basal ganglia T2*w hypointensities based on their appearance and morphology. Finally, the experienced rater who manually segmented these basal ganglia T2*w hypointensities was not involved in the selection process to ensure an unbiased reference. This study design therefore ensures that the developed automated segmentation method for T2*w hypointensities is largely unbiased and can therefore be readily evaluated in further studies of old age.

The presented automated method also has several limitations. Firstly, it requires co-registered T1w volumes to (i) automatically generate the ROI masks for all basal ganglia structures with FSL FIRST (Patenaude *et al.*, 2011), (ii) exclude artefacts, such as chronic haemorrhages, and (iii) segment subregions of basal ganglia T2*w hypointensities which might represent regions of advanced mineralization. High-resolution T1w volumes are typically part of clinical MRI protocols and a sufficiently accurate registration to corresponding T2*w volumes can often be achieved if the acquisition parameters are optimised. However, in situations where T1w volumes are missing or major registration artefacts are present the developed segmentation method cannot be used in its present form. Secondly, the volume of basal ganglia T2*w hypointensities, and hence the volume of the generated masks, is affected by the blooming artefact (Bos *et al.*, 2003; Pintaske *et al.*, 2006). As noted above, the blooming artefact depends on the magnetic susceptibility of the underlying tissue. However, it also depends on scanner and MRI sequence

parameters (Pintaske *et al.*, 2006), such as the main magnetic field strength B_0, the orientation of the plane of view relative to B_0, the echo time and the voxel size. Studies which acquire MRI data on different scanners, with different T2*w sequences or T2*w sequence parameters, therefore have to correct their results for these factors. Finally, the MCD method (Rousseeuw & Driessen, 1999), which is part of the unsupervised outer detection method for estimating the location and scatter of the bivariate T2*w and T1w distributions, enforces an upper size limit on the basal ganglia T2*w hypointensities, since it can only tolerate up to 50 % outliers. Therefore this method misclassifies basal ganglia T2*w hypointensities that are larger than half the volume of the surrounding normal-appearing tissue, as was the case for one subject in this study with very large bilateral basal ganglia T2*w hypointensities. However, very large basal ganglia T2*w hypointensities possibly have a non-ischemic aetiology (Janaway *et al.*, 2014; Morris *et al.*, 1992) and therefore should be analysed separately.

3.7. Conclusion

This Chapter presents a novel automated method for segmenting basal ganglia T2*w hypointensities which consists of an unsupervised outlier detection method and a connected components filter to reduce thresholding artefacts. Its validation with MRI data from a custom-built MRI phantom with mineral deposit models and a random sample of older subjects from the LBC1936 showed that this method was able to generate basal ganglia T2*w hypointensity masks that were in substantial agreement with manually created reference masks from an experienced rater. The developed method was subsequently used to facilitate the segmentation of T2*w hypointensities in 250 participants of a different ageing study as described in Chapter 5, where the MRI data was acquired with a scanner from a different manufacturer. The latter study aimed to demonstrate the cohort and scanner manufacturer independence of the developed method, as well as to explore the underlying tissue composition using quantitative MRI sequences, which will be introduced in the following Chapter. In further studies this method could be potentially useful for investigating relationships between basal ganglia T2*w hypointensities and other features of small vessel disease and the ageing brain, such as cognitive decline (Penke *et al.*, 2012).

Chapter 4 Combined R1, R2 and R2* relaxation rate mapping methodology to improve characterisation of brain iron using clinical MRI

This chapter was submitted as: Glatz A., Valdés Hernández M.C., Wardlaw J.M., Bastin M.E. (2014). Combined R1, R2 and R2* relaxation rate mapping methodology for the improved characterisation of brain iron on clinical MRI scanners. *J Magn Reson Im*.

4.1. Abstract

Purpose: To develop and validate longitudinal (R1) and transverse (R2, R2*) relaxation rate mapping methodology for investigating the distribution of brain iron *in vivo* using clinical fast spin-echo and spoiled gradient-echo MRI sequences.

Materials and Methods: R1, R2 and R2* maps were calibrated with a custom-built phantom containing 9 different $MnCl_2$ solutions, which was also used to assess the accuracy and precision of the measurements. The relaxometry methodology was further validated in 10 healthy subjects where it was used to assess brain iron distributions in the basal ganglia.

Results: The relaxivities of the $MnCl_2$ solutions ($r1$ = 7.2, $r2$ = 75.5 and $r2*$ = 76.2 s^{-1}/mmol/l) were in agreement with those reported from previous studies. The drift of the $MnCl_2$ relaxation rates over three months was not significantly different from 0 ms^{-1}/day indicating that these measurements were precise. *In vivo*, the estimated average relaxivities of basal ganglia brain iron were $r1$ = 2.6, $r2$ = 22.7 and $r2*$ = 52.0 s^{-1}/mg/(g fresh tissue weight). These findings agree with previous results and confirm that R2* is most sensitive to changes in brain iron.

Conclusion: The developed multi-parametric MRI relaxometry methodology could be potentially useful for the improved characterisation of brain iron in future multi-centre and longitudinal studies of ageing and neurodegenerative diseases

4.2. Introduction

The accurate and specific detection of brain iron is a prerequisite for further research into normal and abnormal brain iron accumulation. Current gold standard methods for assessing brain iron include histological methods, such as Prussian blue staining which demonstrates the presence of iron, as well as analytical techniques which quantify the amount of iron in a tissue sample (Becker *et al.*, 2010; Collingwood *et al.*, 2008; Hallgren & Sourander, 1958; Langkammer *et al.*, 2010). However, MRI has evolved to become the *de facto* standard for detecting brain iron *in vivo* (Haacke *et al.*, 2005). Although MRI signals can be affected by any magnetic particle, iron is the main contributor not only because of its high abundance, but also due to its high magnetic susceptibility compared to other trace metals present in the brain (Krebs *et al.*, 2014; Schenck & Zimmerman, 2004). Brain iron is typically separated from water by a protein shell, such as apoferritin, and hence has little effect on the exchange between coordinated shell water molecules and bulk water. Instead brain iron predominantly affects diffusing proton spins through its magnetic field gradients. Therefore brain iron predominantly increases the transverse relaxation rate R2 (=1/T2) as the increase in the longitudinal relaxation rate R1 (=1/T1) is approximately 10 times smaller (Ogg & Steen, 1998). Nevertheless, R1 can still provide complementary information about the type of brain iron and the environment where it accumulates (Weiskopf *et al.*, 2013). Recently, Langkammer *et al.* (2010) demonstrated that the effective transverse relaxation rate R2* (=1/T2*) provides a more sensitive and accurate measure of iron concentration in the deep grey matter than R2. R2* is always equal to or higher than R2 since it also measures the reversible transverse dephasing due to mesoscopic field inhomogeneities around magnetic particles (Rudko *et al.*, 2014). However, in white matter, R2* is confounded by the intrinsic R2 of water pools, myelin and the fibre orientation. Recently, the difference between R2* and R2, i.e. the reversible transverse relaxation rate R2′, was proposed as an alternative brain iron measure (Sedlacik *et al.*, 2014). This is because R2′ specifically depends on the volume magnetic susceptibility of brain iron and its particle size relative to the average proton diffusion length (Rudko *et al.*, 2014; Weisskoff *et al.*, 1994).

MRI relaxation rate mapping methods and their clinical applications have been extensively reviewed in Tofts (2004), Deoni (2010) and Cheng *et al.* (2012). These methods are typically based on repeatedly imaging an object with the same sequence, but different sequence parameters, and fitting a physical model to the serially acquired imaging data. Hence data acquisition and post-processing times of MRI relaxation rate mapping methods are usually much longer than those of conventional, clinical MRI. To shorten these times specialized sequences and post processing methods, such as MOLLI (Messroghli *et al.*, 2004) and GESFIDE (Jin *et al.*, 2013), have been developed. However, these methods have the disadvantage that they are not available on standard MRI scanners and require expert knowledge to set them up. More conventional, but slower MRI relaxometry methods are based on fast versions of standard spin-echo and spoiled gradient-echo sequences, which are readily available on most commercial MRI scanners (Deoni *et al.*, 2003; Graves *et al.*, 2008; Pell *et al.*, 2006). The MRI relaxation rate maps are either reconstructed on the scanner console or 'offline' with commercial and free software tools, such as those developed by Messroghli *et al.* (2010) and McAuliffe *et al.* (2001).

The aim of this study was to implement and validate R1, R2 and R2* relaxation rate mapping methodology using readily available fast spin-echo (FSE) and fast spoiled gradient-echo (FSPGR) MRI sequences. The relaxation rate maps were calibrated with a custom-built phantom that was also used to assess the accuracy and precision of the developed methods. Finally, the MRI relaxation rate mapping methodology was validated *in vivo* by assessing brain iron distributions in the basal ganglia and frontal white matter of 10 healthy volunteers.

4.3. Materials and methods

4.3.1. MRI phantom and subjects

The MRI phantom consisted of 9 sealed 10 ml BD syringes (http://www.bd.com) containing $MnCl_2$ solutions with linearly increasing amounts of manganese ions (Mn^{2+}) as a MRI contrast agent. These $MnCl_2$ solutions were prepared by diluting 1 mol/l $MnCl_2$ stock solution (Sigma Aldrich, Gillingham, UK) with distilled water (Baxter, Thetford, UK) into 0.05, 0.07, …, and 0.21 mmol/l $MnCl_2$ solutions which produced R1 and R2 relaxation rates in the range of normal appearing brain tissue

(Tofts, 2004). The sealed 10 ml BD syringes with the $MnCl_2$ solutions were then mounted in a spherical phantom container as shown in Figure 4-1. Lastly, the phantom container was filled with 1.5 g/l $CuSO_4$ and 3.6 g/l NaCl solution to simulate the coil loading of the human head. The phantom was then placed on the headrest of the scanner so that the syringes were oriented parallel to the main magnetic field. Before and between the experiments, the phantom was stored in the scanner room with a temperature of 20.0 ± 1.5 °C to reduce temperature-induced changes of the $MnCl_2$ solution relaxation rates (Tofts, 2004).

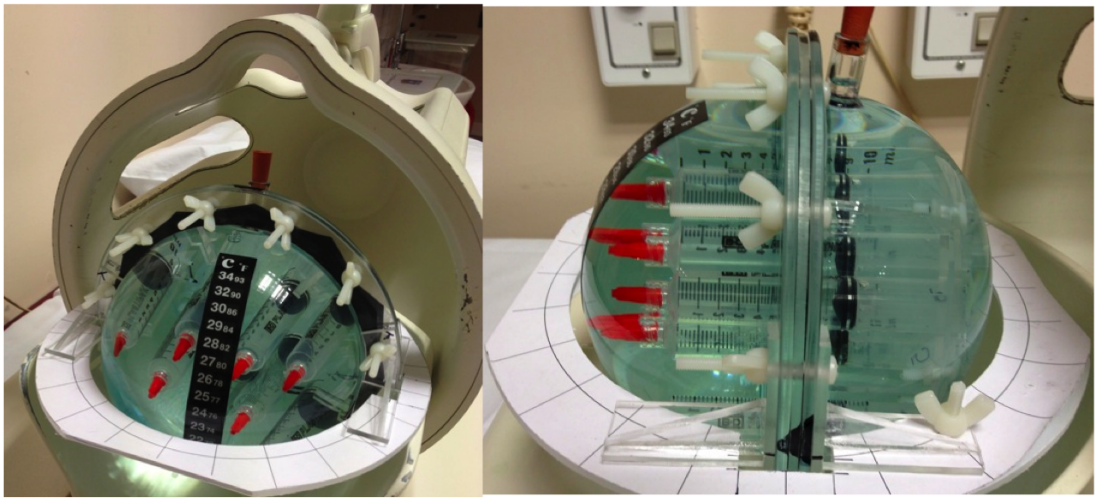

Figure 4-1: Calibration and validation phantom. The images show the custom-built phantom as well as the rest for stabilizing the phantom on the headrest of an 8-channel coil in a GE Signa 1.5T HDxt scanner. To reduce susceptibility artefacts, a spherically shaped phantom container was chosen.

The *in vivo* evaluation of the R1, R2 and R2* relaxation rate mapping methods was carried out in 3 female and 7 male volunteers (mean age 35.4 ± 6.4 years) without any history or signs of neurological disorders. Written informed consent was obtained from all subjects under protocols approved by the local UK National Health Service ethics committee.

4.3.2. MRI protocol

The MRI protocol (Table 4-1**)** was developed for a GE Signa 1.5 T HDxt (General Electric, Milwaukee, WI, USA) clinical scanner with an eight-channel head coil and 40 mT/m maximum gradient strength, and included a dual flip angle FSPGR sequence (Deoni *et al.*, 2003), a multi-echo FSE Carr-Purcell-Meiboom-Gill (CPMG) sequence and a multi-echo FSPGR sequence (Graves *et al.*, 2008). The

multi-echo FSE sequence was optimized using 160° refocusing pulses to reduce the Specific Absorption Rate (SAR) while the refocusing pulse slice selection gradients were scaled by 0.5 in the case of multi-slice acquisitions to reduce artefacts due to stimulated echoes (Pell *et al.*, 2006). This protocol also included an inversion recovery FSPGR (IR-prep FSPGR) sequence for acquiring structural T1-weighted (T1w) volumes which were used to configure the field-of-view as well as to determine the regions of interest (ROIs) in the phantom and the brains of the volunteers. In the phantom experiments serial imaging data were also acquired with inversion recovery spin-echo echo-planar imaging (IR-SE-EPI) and spin-echo (SE) sequences for reconstructing reference R1 and R2 maps.

The protocol was prescribed and run as follows. After running the localizer and Array Spatial Sensitivity Encoding Technique (ASSET) calibration sequences (Graves *et al.*, 2008), the T1w volume was acquired covering the parts of the syringes containing the $MnCl_2$ solution in the phantom and the basal ganglia in the volunteers. The acquisition volume of all the following sequences was set equal to that of the T1w sequence in order to facilitate co-registration of the different MRI volumes. The serial imaging data were then acquired with the dual flip angle FSPGR sequence; the sequence with the lower flip angle was acquired first with the radio-frequency (RF) transmitter and receiver gains held constant during both scans using the manual pre-scan option. Before running the multi-echo FSE and FSPGR sequences, ASSET was enabled and set to 1 since Graves *et al.* (2008) have shown that this improves the magnitude signal uniformity across the field of view and lowers the background noise. In the case of the phantom this sequence was followed by the IR-SE-EPI and SE sequences with the RF transmitter and receiver gains again held constant during the acquisition of serial imaging datasets using the manual pre-scan option. In case of the latter two sequences the acquisition volume was also copied from the T1w sequence, but was reduced to a single, 4 mm thick axial slice to shorten the acquisition times.

Table 4-1: MRI protocol. The MRI relaxation rate mapping protocol is based on fast multi-flip angle fast spoiled gradient-echo (FSPGR) and multi-echo fast spin-echo (FSE) Carr-Purcell-Meiboom-Gill (CPMG) sequences. An inversion recovery FSPGR (IR-prep FSPGR) sequence was used to acquire T1-weighted volumes. The phantom protocol also included inversion recovery spin-echo echo-planar imaging (IR-SE-EPI) and spin-echo (SE) sequences for calculating reference (ref) R1 and R2 relaxation rate maps.

Contrast/ Parameter	R1	R2	R2*	T1w	R1 (ref)	R2 (ref)
Sequence	FSPGR	FSE	FSPGR	IR-prep FSPGR	IR-SE-EPI	SE
TR [ms]	8.8	900	60	9.5	10000	1200
TE [ms]	3.4	25.1	5.4	4.1	25.4	30, 60, …, 180
# Echoes	1	4 (even)	8	1	1	1
ΔTE [ms]	N/A	25.1	9.2	N/A	N/A	N/A
TI [s]	N/A	N/A	N/A	0.5	0.3, 0.5, …, 1.3, 1.8, 2.3	N/A
Flip angle [degrees]	2, 12	N/A	20	8	N/A	N/A
Bandwidth [Hz/Pixel]	217	122	122	122	1950	122
FOV [mm]	307	307	307	307	307	307
Matrix	256x256	256x256	256x256	192x192	256x256	256x256
Slice [mm]	1.2	2.4	1.2	1.2	4.8	4.8

4.3.3. R1 mapping

R1 maps were calculated using the DESPOT1 method (Deoni *et al.*, 2003) with serial imaging data from the dual flip angle FSPGR sequence with flip angles of $\psi_1 = 2°$ and $\psi_2 = 12°$. To remove movement artefacts the serial imaging data was rigidly co-registered using FSL FLIRT with sinc interpolation (Jenkinson *et al.*, 2002). The R1 relaxation rate at each voxel was then determined from

$$R_1 = \frac{1}{TR} \ln \left(\frac{S(\psi_1)\sin\psi_2 cos\psi_1 - S(\psi_2) sin\psi_1 cos\psi_2}{S(\psi_1) sin\psi_2 - S(\psi_2) sin\psi_1} \right), \qquad 4\text{-}1$$

where TR is the repetition time, and $S(\psi_1)$ and $S(\psi_2)$ are the corresponding voxel signals of the co-registered FSPGR volumes.

The reference R1 map of the phantom was calculated with the image post-processing software MRMap (Messroghli *et al.*, 2010). This tool fitted a two-parameter inversion recovery signal model

$$S(TI) = S_0(1 - 2e^{-R1TI}) \qquad 4\text{-}2$$

voxel-wise to the corresponding signals of all volumes acquired with the IR-SE-EPI sequence. Here TI denotes the inversion recovery time and S_0 the signal immediately after the 180° pulse of the inversion recovery sequence.

4.3.4. R2 and R2* mapping

A two-parameter mono-exponential signal decay model (Graves *et al.*, 2008)

$$S(TE) = S_0 e^{-R\{2,2*\}TE}, \qquad 4\text{-}3$$

with TE being the echo time and S_0 the signal at $TE = 0s$, was fitted voxel-wise to the serial imaging data from the multi-echo FSE and FSPGR sequences in MATLAB (The MathWorks, Natick, MA, USA) using the Levenberg-Marquardt-Fletcher algorithm (MATLAB Central File ID: #16063). In the case of the R2 map the mono-exponential signal decay model was only fitted to the even echoes of the FSE CPMG sequence to reduce artefacts due to the 160° refocusing pulse angles (Section 4.3.2), whereas in case of R2* mapping it was fitted to all echoes.

The MRMap software was again used to calculate the reference R2 map of the phantom by fitting the signal decay model (Equation 4-3) to the MRI data from all single-echo spin-echo sequences. This reference map was also used to calibrate and validate the R2* maps of the phantom since the $MnCl_2$ solutions predominantly cause irreversible transverse dephasing (motional averaging regime; Weisskoff *et al.*, 1994) with the result that R2* is equal to R2.

4.3.5. ROI segmentation and transformation

The ROIs of the phantom and volunteers (Figure 4-2) were segmented on the corresponding T1w volumes. In the case of the phantom the ROIs were segmented semi-automatically with the following intensity thresholding method. Firstly, the $MnCl_2$ solutions, which appeared significantly darker on T1w MRI than the surrounding $CuSO_4$/NaCl solution, were segmented with two thresholds, which were

chosen to be 6 times higher than the mean background signal intensity and 0.8 times lower than the mean $CuSO_4$/NaCl solution signal intensity. The resulting masks were then eroded with a disk-shaped structural element with a diameter of 6 mm to reduce artefacts caused by the plastic components of the syringes. RF field inhomogeneities typically caused artefacts on the first and last three slices of the T1w volume, which also caused artefacts in the masks. Hence these slices were excluded from the final ROI masks. Finally, the masks of individual $MnCl_2$ solutions were identified and assigned unique labels with the MATLAB function 'bwlabeln()'. For the volunteers, a rater manually delineated the basal ganglia nuclei and frontal white matter on the T1w volumes with the image processing software Mango (http://ric.uthscsa.edu/mango).

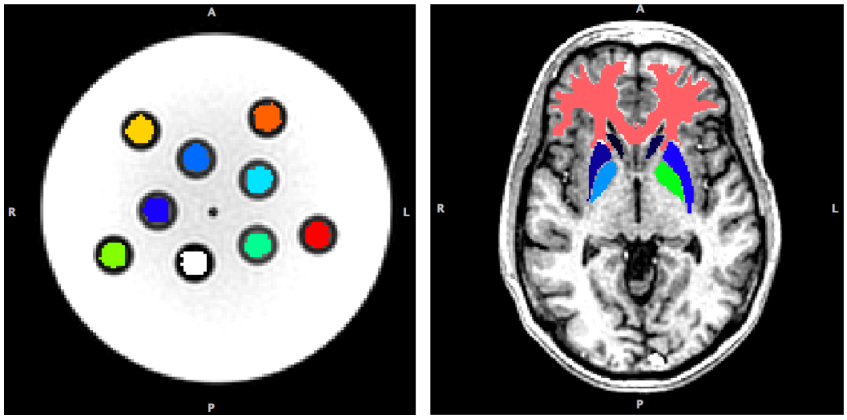

Figure 4-2: Regions of interest in the phantom and in the brain of a typical volunteer. These figures show the region of interest (ROI) masks of the phantom and a volunteer overlaid on T1-weighted volumes. In the phantom the ROI masks selected the $MnCl_2$ solutions, while in the volunteers the ROI masks selected the basal ganglia nuclei and the frontal white matter.

The resulting ROI masks were then linearly transformed into the space of the corresponding R1, R2 and R2* relaxation rate maps. Firstly, the volume of a serial imaging dataset with the sharpest contrast was linearly registered to the T1w volumes using FSL FLIRT (Jenkinson *et al.*, 2002) to obtain a linear transformation matrix. To improve registration, non-brain structures and non-anatomical signal variations (bias fields) were removed using FSL BET (Smith, 2002) and N4 (Tustison *et al.*, 2010) prior to registration. Finally, the ROI masks were linearly transformed into the space of the corresponding R1, R2 and R2* relaxation rate maps with FSL FLIRT using the inverse transformation matrices and nearest neighbour interpolation.

4.3.6. Statistical analysis

The systematic measurement errors associated with the R1, R2 and R2* mapping methods were estimated by comparing the mean R1, R2 and R2* relaxation rates of each $MnCl_2$ solution with corresponding reference values. These mean relaxation rates were calculated with the relaxation rates of the generated and reference R1, R2 and R2* maps selected by the corresponding ROI masks. The systematic measurement errors were then assessed graphically with line of equality and Bland-Altman plots (Bland & Altman, 1986). These were constructed by plotting the mean relaxation rates $R\{1,2,2*\}$ over the corresponding reference values $R_{ref}\{1,2,2*\}$, and by plotting the relaxation rate differences $R_{diff} = R - R_{ref}$ over the mean relaxation rates $R_{mean} = (R + R_{ref})/2$. Linear regression lines in the former and latter plots indicate the systematic measurement error (bias). Finally, the linear calibration functions for each relaxation rate map $R_{cal} = a + bR$ were given by the inverse of the linear regression lines from the line of equality plots.

The relaxivities $r\{1,2,2*\}$ in s^{-1}/mmol/l quantify the concentration-dependent increase of the calibrated mean $MnCl_2$ solution relaxation rates $R\{1,2,2*\}$. Here the relaxivities of $MnCl_2$ solution were estimated with the linear regression model

$$R_{est} = R_0 + rc, \qquad 4\text{-}4$$

where $R\{1,2,2*\}_{est}$, $R\{1,2,2*\}_0$ and c in mmol/l denote the estimated relaxation rate of the $MnCl_2$ solution, the relaxation rate of the solvent (distilled water) and the concentration of the $MnCl_2$ solution, respectively. The fit of the linear regression model was quantified with Pearson's correlation coefficient r, which also measures the linearity between the $MnCl_2$ solution concentrations and their relaxation rates.

Measurement precision describes how well the relaxation rate measurements can be reproduced in repeated experiments. This study assessed the short-term precision of the R1, R2 and R2* mapping methods by scanning the phantom an additional five times over three months with only the fast sequences of the above MRI protocol. The systematic error of all maps was then corrected with the calibration functions obtained in the first phantom experiment. After calculating the mean relaxation rates $R\{1,2,2*\}_l$ of each $MnCl_2$ solution l, their measurement precision was quantified with the coefficients of variation (CV)

$$CV_j = \frac{std(R_l)}{mean(R_l)}, \quad 4\text{-}5$$

while their drift over time $\delta R\{1,2,2*\}_l$ in ms^{-1}/day was estimated with the linear model

$$R_l = R_{l,0} + \left(\frac{\delta R_l}{1000}\right) t, \quad 4\text{-}6$$

where t is the time in days and $R\{1,2,2*\}_{l,0}$ is the relaxation rate in s^{-1} at day 0.

The developed MRI relaxation rate mapping methods were used to estimate the distribution and relaxivity of brain iron in the basal ganglia from the R1, R2 and R2* maps of 10 healthy volunteers. After scanning the volunteers with the fast sequences of the MRI protocol the relaxation rate maps were reconstructed and calibrated as in the phantom experiments. To estimate the average relaxivity of grey matter iron the mean relaxation rates $R\{1,2,2*\}$ of the investigated anatomical structures were subsequently calculated with the relaxation rate selected by the ROI masks. The characteristic functions presented in Hallgren and Sourander (1958), which describe the iron concentration increase with age in healthy subjects, were then used to estimate the grey matter iron concentration in the ROIs. The association between the mean relaxation rates of all grey matter structures of all subjects and their estimated iron content were then quantified by calculating Pearson's correlation coefficient $r = r(R, c)$ and fitting the linear regression model

$$R = R_0 + rc \quad 4\text{-}7$$

to the data. Here, c, $R\{1,2,2*\}$ and $r\{1,2,2*\}$ are the estimated iron concentration in mg/(g fresh tissue weight), the relaxation times in s^{-1} and the average relaxivities of brain iron in s^{-1}/mg/(g fresh tissue weight), respectively.

4.4. Results

4.4.1. Systematic measurement error and calibration functions

In the case of the R1 maps, Figure 4-3A shows that the estimated linear regression line is not parallel to the line of equality indicating the presence of a proportional measurement error. This proportional error is also confirmed in the corresponding Bland-Altman plot (Figure 4-3B) which shows that the difference between the measured and reference R1 values is close to 0 s^{-1} in the case of small R1 values

indicating that smaller R1 values are more accurate than larger ones. Conversely, in the case of the R2 and R2* maps, Figure 4-3C, E show that the estimated linear regression lines are approximately shifted parallel to the lines of equality indicating only the presence of a constant error. The corresponding Bland-Altman plots (Figure 4-3D, F) reveal that the R2 and R2* measurements are also affected by proportional errors and indicate that small R2 and large R2* values are more accurate. However, these proportional errors are small compared to the absolute R2 and R2* values and therefore hardly noticeable in the corresponding line of equality plots. The linear calibration functions were estimated as

$$\begin{matrix} R1_{cal} & = 1.30R1 - 0.09 \\ R2_{cal} & = 1.02R2 + 0.24\,, \\ R2*_{cal} & = 0.97R2* + 0.86 \end{matrix} \qquad 4\text{-}8$$

which mainly correct the proportional error associated with the uncalibrated R1 maps (slope >1) and the constant error associated with the uncalibrated R2 and R2* maps (slope ≈1). All R1, R2 and R2* maps generated in this study were subsequently calibrated with these functions.

4.4.2. Concentration-dependent increase of the $MnCl_2$ relaxation rates

Table 4-2 shows the $r\{1,2,2*\}$ relaxivities of the $MnCl_2$ solutions are in good agreement with those from previous studies (St Pierre *et al.*, 2005; Tofts, 2004). The corresponding intercepts of the regression lines, i.e. the relaxation rates of the distilled water at 20.0 ± 1.5 °C (Section 4.3.1), are 66, 30 and 13 % higher than the relaxation rates measured at 37°C in Rohrer *et al.* (2005). However, the obtained relaxation rates of distilled water are still acceptable since temperature differences, the amount of dissolved oxygen, as well as the oxidation of Mn^{2+} ions can all lead to disparity in the measured and reference water relaxation rates (Tofts, 2004). Table 4-2 also shows that the Pearson's correlation coefficients r are close to 1 confirming that the relaxation rates R{1,2,2*} of the $MnCl_2$ solutions increase linearly with their concentration.

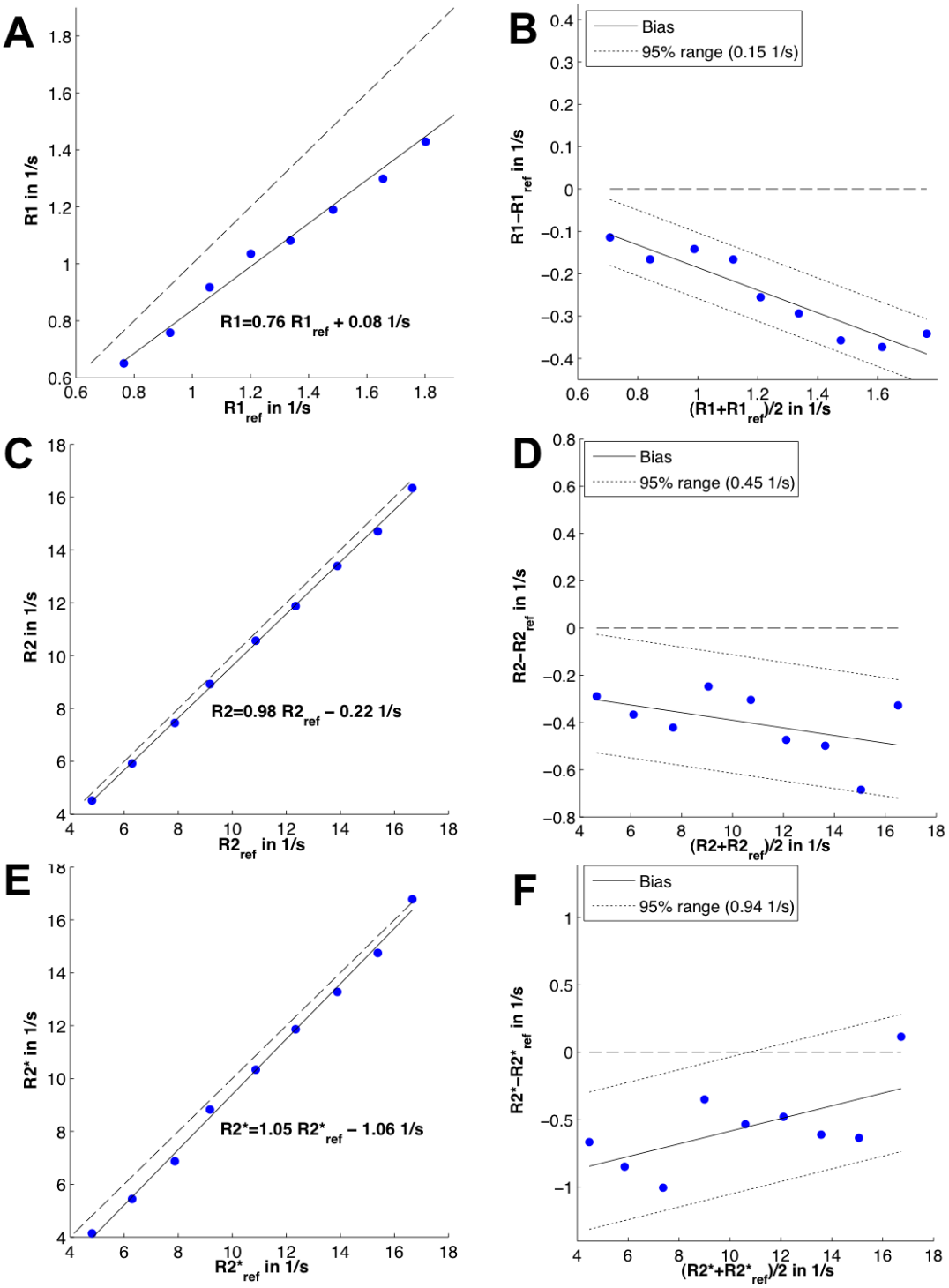

Figure 4-3: Line of equality and Bland-Altman plots for assessing the systematic error between the generated and reference R1, R2 and R2* maps. The line of equality plots (**A, C, E**) show the measured R1, R2, and R2* relaxation rates versus the corresponding reference values. Solid and dashed lines indicate the robust linear regression line and the line of equality. Bland-Altman plots (**B, D, F**) show the absolute difference between the measured and reference R1, R2 and R2* relaxation rates versus their averages. In these plots solid and dotted lines indicate the bias and the 95 % limits of agreement. The dashed line corresponds to the line of equality and serves as a reference for assessing the bias of the measurements.

Table 4-2: Association between the $MnCl_2$ solution relaxation rates and the $MnCl_2$ concentrations. The association between the $MnCl_2$ solution relaxation rates and the $MnCl_2$ concentrations was assessed with Pearson's correlation and linear regression lines. This table shows the Pearson's correlation coefficients r, the slopes of the linear regression lines, i.e. the $MnCl_2$ solution relaxivities $\boldsymbol{r}\{\mathbf{1},\mathbf{2},\mathbf{2}*\}$, the intercepts of the linear regression lines $\boldsymbol{R}\{\mathbf{1},\mathbf{2},\mathbf{2}*\}_{\mathbf{0}}$, i.e. the estimated relaxation rate of the solvent (distilled water), and the standard error of the estimated relaxation rates SEE. The temperature of the $MnCl_2$ solutions was 20.0 ± 1.5 °C.

Grey matter	Pearson's r	r [s^{-1}/(mmol/l)]	R_0 [s^{-1}]	SEE [s^{-1}]
R1	0.9952 [a]	7.25	0.40	0.04
R2	0.9998 [a]	75.53	1.04	0.09
R2*	0.9992 [a]	76.22	0.90	0.18

[a] significant at $\alpha = 10^{-7}$

4.4.3. Measurement precision

Table 4-3 shows the time drifts and CVs associated with the $MnCl_2$ solution relaxation rates R1, R2 and R2*. On average, the relaxation rates do not significantly drift over time indicating that the developed relaxation rate mapping methodology can produce precise measurements. Furthermore, the smallest CVs are associated with the R2 values, followed by R1 and R2*, which indicates that the R2 values are the most precise. However, Table 4-3 also shows that the R1 and R2* relaxation rates tend to decrease, whereas the R2 relaxation rates tend to increase over time.

Table 4-3: Precision measurement results. The R1, R2 and R2* relaxation rates of all $MnCl_2$ solutions in the phantom were measured on six occasions over the time span of three months at a temperature of 20.0 ± 1.5 °C. For each parameter and $MnCl_2$ solution the relaxation rate drift d and the coefficient of variation (CVs) of the measurements were calculated. This table shows the averages, standard deviations (SD) and 95 % confidence intervals (CI) across all $MnCl_2$ solution values. All drifts were not significant at $\alpha = 0.05$ since the respective confidence intervals included 0 ms^{-1}/day.

Precision statistics		Mean	SD	95 % CI
R1	δR [ms^{-1}/day]	-0.15	0.23	-0.32…0.01
	CV [%]	1.83 [a]	0.57	1.41…2.25
R2	δR [ms^{-1}/day]	0.53	1.66	-0.70…1.75
	CV [%]	1.68 [a]	0.78	1.10…2.26
R2*	δR [ms^{-1}/day]	-0.93	1.78	-2.24…0.38
	CV [%]	1.90 [a]	0.81	1.30…2.50

[a] significant at $\alpha = 0.05$

4.4.4. *In vivo* validation

The serial data for generating the R1, R2 and R2* maps covering the basal ganglia were acquired in 17 min, 45s indicating that subjects have to be able to lie in the scanner for at least 30 min to provide whole brain coverage.

Figure 4-4 shows the mean R1 relaxation rates versus age of the caudate, putamen, globus pallidus and frontal white matter in the volunteers. These R1 values generally fall within the 2-standard deviation range of those obtained in Vymazal *et al.* (1999) indicating a good agreement between the results of the two studies. However, Figure 4-5 indicates that the R2 and R2* relaxation rates of the investigated brain structures do not agree so well with previous studies since they are generally outside the 2-standard deviation range of values reported by Vymazal *et al.* (1999) and Aquino *et al.* (2009).

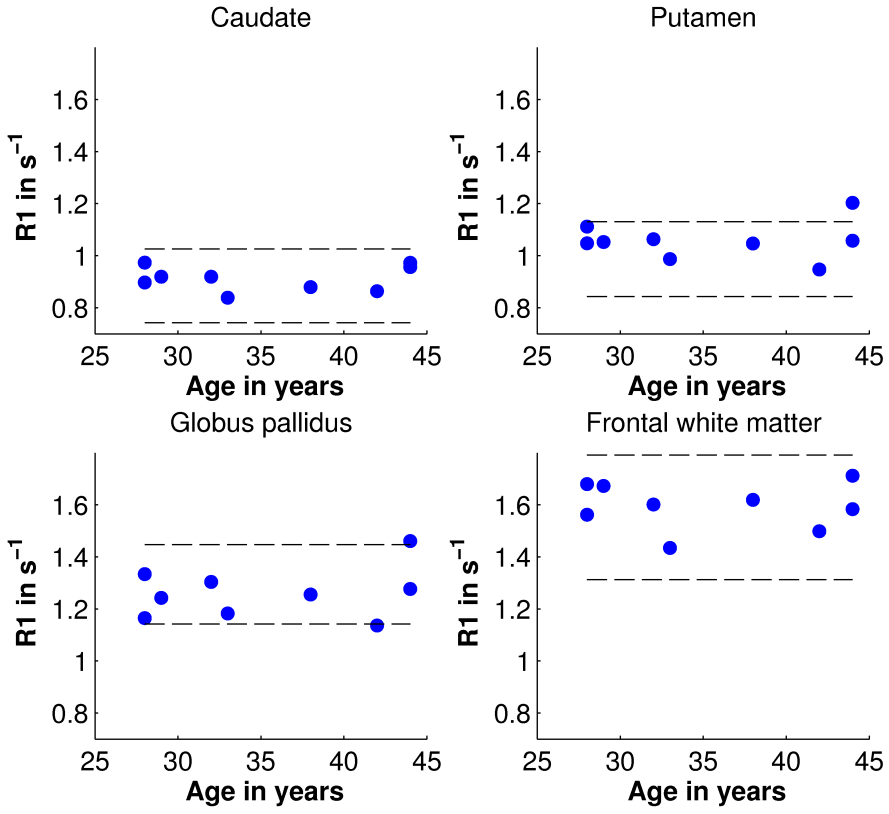

Figure 4-4: Longitudinal relaxation rates R1 of the globus pallidus and frontal white matter versus age in the volunteers. The blue dots represent the measured R1 relaxation rates. The dashed lines represent the 2-standard deviation (95 %) range of the R1 values reported by Vymazal *et al.* (1999) in the corresponding structures.

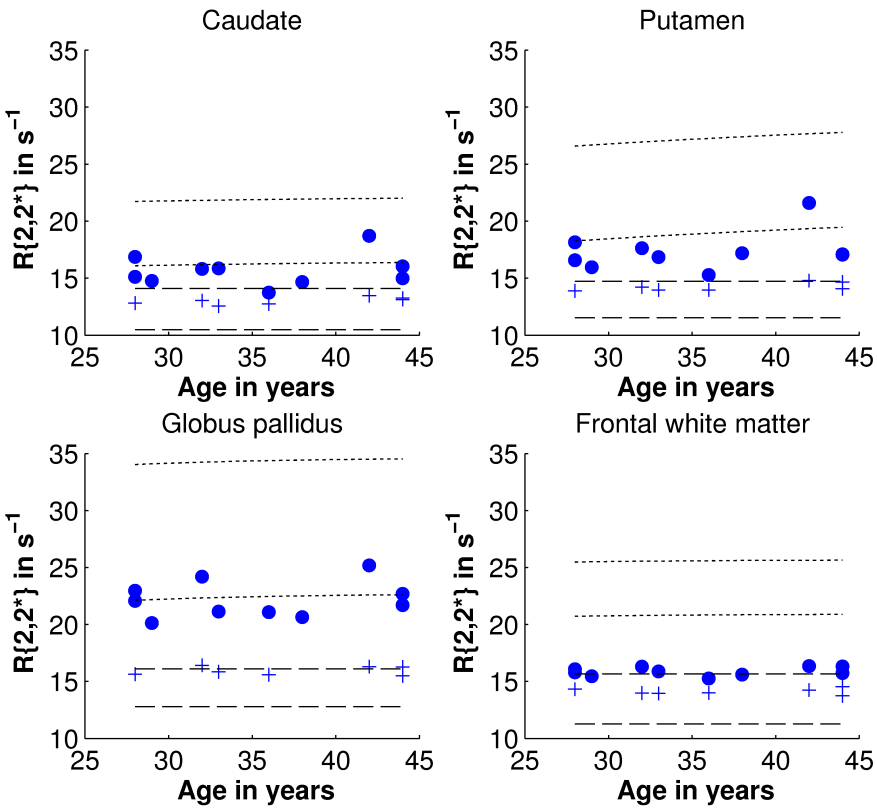

Figure 4-5: Transverse relaxation rates R2 and R2* of the globus pallidus and frontal white matter versus age in the volunteers. The blue crosses and dots represent the measured R2 and R2* relaxation rates. The dashed and dotted lines indicate the 2-standard deviation (95 %) ranges of the R2 and R2* relaxation rates reported by Vymazal *et al.* (1999) and Aquino *et al.* (2009) in the corresponding structures.

Nonetheless, the measured R1, R2 and R2* relaxation rates of the basal ganglia nuclei are significantly associated with their estimated iron content as shown in Table 4-4. Here, R2 correlates best with the tissue iron content, followed by R2* and R1. The relaxivities of grey matter iron shown in Table 4-4 are similar to those reported in previous studies (Haacke *et al.*, 2005; Li & Takahashi, 2004). The $r2^*$ relaxivity is highest followed by $r2$ and $r1$ confirming that R2* is most sensitive to changes in brain iron (Langkammer *et al.*, 2010), followed by R2 and R1. The intercepts of the linear regression lines that model the increase of R2 and R2* with brain iron content (R_0) are similar confirming that the differences between R2 and R2*, i.e. the reversible transverse relaxation rates R2′, also depend on brain iron concentration (Sedlacik *et al.*, 2014).

Table 4-4: Association between the basal ganglia relaxation rates and their estimated brain iron content. The brain iron content of the basal ganglia nuclei was estimated with the characteristic functions from Hallgren and Sourander (1958). The association between the relaxation rates and the estimated iron content of these brain structures was assessed with Pearson's correlation and linear regression lines. This table shows the Pearson's correlation coefficients r, the slopes of the linear regression lines, i.e. the estimated relaxivities of brain iron $\boldsymbol{r}\{\mathbf{1},\mathbf{2},\mathbf{2}*\}$, the intercepts of the linear regression lines $\boldsymbol{R}\{\mathbf{1},\mathbf{2},\mathbf{2}*\}_{\mathbf{0}}$, i.e. the estimated relaxation rate of the brain tissue without iron, and the standard error of the estimated relaxation rates (SEE).

Pooled grey matter	Pearson's r	r [s^{-1}/mg/g]	R_0 [s^{-1}]	SEE [s^{-1}]
R1	0.88 [a]	2.59	0.73	0.08
R2	0.96 [a]	22.7	11.3	0.37
R2*	0.91 [a]	52.0	11.5	1.41

[a] significant at $\alpha = 10^{-4}$

4.5. Discussion

In this study a R1, R2 and R2* relaxation rate mapping methodology was developed that is based on readily available FSE and FSPGR MRI sequences. The *in vitro* validation of the developed methodology showed that the $MnCl_2$ relaxivities derived from the calibrated phantom relaxation rate maps were in good agreement with those from previous studies and no significant drift of the $MnCl_2$ solution relaxation rates was noted over three month. The *in vivo* validation with 10 healthy volunteers showed that the measured R1, but not the R2 and R2* values, of the basal ganglia nuclei and frontal white matter values agreed with those from previous studies. However, the estimated $r\{1,2,2*\}$ relaxivities of grey matter iron agreed well with corresponding reference values from the literature.

The reference R1 and R2 relaxation rate maps for validating the developed relaxation rate mapping methods were obtained by acquiring serial imaging data with IR-SE-EPI and SE sequences (Pell *et al.*, 2006) and by reconstructing the resulting maps with MRMap (Messroghli *et al.*, 2010). Although lengthy, these sequences were deliberately chosen to reduce inaccuracies caused by imperfect slice selection and refocusing pulses associated with multi-echo FSE sequences (Pell *et al.*, 2006), and imperfect spoiling of the transverse magnetization associated with FSPGR sequences (Preibisch & Deichmann, 2009), which potentially lead to the constant errors in the R2 and R2* measurements (Equation 4-8). However, several factors can

still lead to inaccuracies in the reference R1 and R2 relaxation rate maps and these should be noted. Firstly, it was assumed that the IR-SE-EPI inversion pulse was exactly 180°, which allows for an estimation of the reference R1 values by fitting only a two-parameter model to the imaging data (Equation 4-2). More precise estimates of the R1 values can be obtained by fitting a three-parameter model to the imaging data, which accounts for imperfections in the inversion pulse (Rohrer *et al.*, 2005). Secondly, the two-parameter model for obtaining the R2 relaxation rates (Equation 3) did not include a constant offset, which might help to provide more precise R2 values when images are affected by noise (Rohrer *et al.*, 2005). Lastly, the SE volumes are not only affected by R2, but also the water diffusion coefficient, which might lead to an increase in the apparent R2 relaxation rates. Although water diffusion should have little influence on 2D SE sequences (Le Bihan & Turner, 1991), its influence can be minimised by acquiring the serial data for reconstructing the reference R2 maps with a single slice CPMG sequence (Tofts, 2004).

The phantom experiments revealed that the uncalibrated R1 maps were associated with a proportional measurement error that increased with the concentrations of the $MnCl_2$ solutions. As demonstrated by Preibisch and Deichmann (2009), the accuracy of the DESPOT1 method used above to obtain the R1 maps is not only influenced by the non-uniform flip angles across the imaging volume, which predominantly relates to an inhomogeneous RF (B1) field (Wang *et al.*, 2006), but also by the transverse magnetization spoiling method of the FSPGR sequence. Flip angle artefacts lead to a variation in R1 values across the volume of an otherwise uniform object, which becomes more apparent at higher field strengths (Deoni, 2007). In this study, flip angle artefacts potentially lead to a location-independent, $MnCl_2$ concentration proportional bias as well as a location-dependent error in the R1 measurements. The former was for example apparent as a deviation from the line of equality in Figure 4-3A, and the latter as a lower Pearson's r between the $MnCl_2$ solution concentration and R1 values (Table 4-2) than was found between the concentrations and R2 and R2* values. Both errors could be reduced by accounting for the deviation of the actual flip angle from the nominal flip angle entered at the scanner console during the reconstruction of the R1 map using methods such as those developed by Deoni (2007), and Dowell and Tofts (2007). The drawback of these methods is,

however, that they would increase the duration of the developed protocol which could be avoided with more sophisticated computational techniques such as presented in Cao *et al.* (2014). Another source of artefact of the DESPOT1 method is the imperfect spoiling of the transverse magnetisation during a TR cycle by the multi-flip angle FSPGR sequence. Preibisch and Deichmann (2009) showed that the accuracy and precision of R1 maps depend on the phase increment per spoiling pulse, which in case of the FSPGR sequences used in this study was 113°. Furthermore, Preibisch and Deichmann (2009) used a linear calibration function (Equation 6 in Preibisch and Deichmann (2009)) to correct for artefacts due to imperfect spoiling which presumably has a similar effect as the calibration function used to improve the accuracy of R1 measurements in the current study (Equation 4-8). The individual contribution of RF spoiling artefacts to the systematic bias of the R1 measurement could be estimated in phantom experiments after correcting for flip angle artefacts.

This study also explored the possibility of increasing the accuracy of the R1 values by compensating the systematic bias through adjusting the nominal flip angles $\psi_{\{1,2\}}$ configured on the scanner console. Numerical simulations showed that R1 values reconstructed with $\psi_{\{1,2\}} = 2{,}12°$ from SPGR signals (Bernstein *et al.*, 2004) generated with $\tilde{\psi}_{\{1,2\}} = \psi_{\{1,2\}} + \Delta\psi$ with $\Delta\psi = 0.3°$ were affected by a very similar systematic bias as the phantom R1 values in this study. Therefore configuring the dual flip angle FSPGR sequence with $\psi_1 = (2 - 0.3)° = 1.7°$ and $\psi_2 = (12 - 0.3)° = 11.7°$ at the scanner console could possibly calibrate the R1 maps similarly as it was achieved with Equation 4-8 during post processing in this study.

The *in vivo* validation showed that the R1 relaxation rate, but not the transverse relaxation rates R2 and R2*, of the basal ganglia and white matter were within the range of corresponding measurements of previous studies (Aquino *et al.*, 2009; Vymazal *et al.*, 1999). This disparity in the transverse relaxation rates potentially arises from differences in the post-processing methods used since in all studies the scanner field strength was the same and similar sequences were employed to acquire the serial imaging data. In both previous studies mono-exponential models with free baselines were fitted to the serial imaging data where the free baselines accounted for a constant intensity offset due to background noise. However, in this study a three-

parameter model was not sufficiently justified since in an initial investigation fitting such a model to the data yielded less accurate $MnCl_2$ solution relaxation rates and relaxivities than those obtained with the two-parameter model; the variability of the $MnCl_2$ solution relaxation rates per ROI was also higher. Furthermore, a two-parameter model is more likely to produce more accurate results here since the ASSET reconstruction technique of the scanner reduces the background noise in the multi-echo FSE and FSPGR volumes sufficiently well (Graves *et al.*, 2008), thereby eliminating the need of a baseline parameter in the model; a two parameter model is also more robust to image artefacts, such as noise and Gibbs ringing.

This study confirms that the grey matter iron relaxivity $r2*$ is nearly twice as high as $r2$ (Langkammer *et al.*, 2010), hence R2* is twice as sensitive to changes in brain iron in grey matter. Previous studies that relied on T2*-weighted (T2*w) imaging for assessing iron overload, or the distribution of MRI contrast agent in brain tissue, could therefore use R2* maps as these are probably more sensitive to paramagnetic particles. This would have the additional benefit that calibrated R2* measurements can be readily compared across subjects, as well as centres, using scanners with the same field strength (Ropele *et al.*, 2013). Notably, a disadvantage of R2* mapping over T2*w imaging is the prolonged scan time which, however, can be reduced significantly by optimizing the FSPGR sequence parameters or by using multi-echo T2*w EPI sequences.

Contrary to a previous report (Langkammer *et al.*, 2010), the basal ganglia R2 relaxation rates measured in this study correlated better with the estimated iron content than the basal ganglia R2* relaxation rates. This observation might be simply due to the fact that the basal ganglia iron content was estimated and not measured as was done previously. However, this variability could also indicate that smaller iron particles, such as ferritin, seem to accumulate with age at a similar rate in all individuals, whereas larger iron particles, such as haemosiderin or larger iron complexes, seem to accumulate only in certain individuals (Chapter 2). This phenomenon could lead to the higher inter-subject variability in R2*, as found here, since R2* is sensitive to small as well as large iron particles, whereas R2 is more sensitive to small iron particles (Sedlacik *et al.*, 2014). Visual inspection of the T2*w FSPGR serial imaging data, in fact, revealed several focal mineral deposits in the

globus pallidus of older volunteers which were not present in the corresponding T2-weighted FSE serial imaging data, thereby potentially indicating the 'tip of the iceberg' of age-related tissue mineralisation.

The developed relaxation rate mapping method was validated *in vitro* with a custom-built phantom as well as *in vivo* with data from a small group of healthy volunteers. This phantom is stable and cost-effective which could be useful for calibrating relaxation rate mapping methods in multi-centre as well as longitudinal studies. However, a limitation of this method is that a direct comparison of the phantom relaxation rate maps is only possible if the data are acquired at the same temperature (Tofts, 2004), e.g. by keeping the phantom in the scanner room as it was done here. In further studies the $MnCl_2$ solutions of the phantom could be replaced by Ni-DTPA agarose gels which have lower temperature coefficient than $MnCl_2$ solutions (Tofts, 2004), or an MRI compatible temperature probe could be integrated in the phantom to provide accurate temperature measurements. A further limitation of this study is that only 10 young and healthy subjects with narrow age range were analysed. This is sufficient for the initial *in vivo* validation of the developed methods. However, for their application to the study of ageing or neurodegenerative diseases, the methods should be validated in a larger cohort (ideally $N > 30$) of representative subjects to explore, for example, the influence of movement artefacts on the measured relaxation rates (Deoni, 2010).

4.6. Conclusion

This feasibility study successfully implemented and validated R1, R2 and R2* relaxation rate mapping methodology based on readily available FSE and FSPGR MRI sequences. Overall, the $MnCl_2$ phantom solution and average basal ganglia brain iron relaxation rates were precise and the $MnCl_2$ solution and brain iron relaxivities derived from the calibrated relaxation rate maps were in reasonable agreement with those from previous studies. The developed and validated post processing method for reconstructing R2* maps (Section 4.3.4) was subsequently employed in the next study, which investigated the appearance of T2*w hypointensities on R2* maps for estimating the iron content of the underlying mineral deposits (Langkammer *et al.*, 2010).

Chapter 5 A cross-sectional study of focal basal ganglia mineralization on conventional and quantitative MRI

This chapter was partly presented as a poster: Glatz A., Pirpamer L., Langkammer C., Valdés Hernández M.C., Bastin M.E., Wardlaw J.M., Fazekas F., Schmidt R., Ropele S. (2014). An Investigation into the Formation and Histology of Focal Basal Ganglia Mineralization with quantitative MRI. *Proc ISMRM 2014*. Poster #4682.

5.1. Abstract

Background and Purpose: Focal basal ganglia hypointensities on T2*-weighted (T2*w) MRI are a frequent finding in elderly subjects and have been associated with mineralization. Their distribution and development in ageing and their exact composition are largely unknown and are the focus of this investigation.

Materials and Methods: Basal ganglia T2*w hypointensities were segmented and analysed in 250 community-dwelling subjects without history or signs of neurodegenerative diseases. These focal hypointensities were segmented automatically on conventional T2*w and T1-weighted (T1w) MRI, and then characterised using R2* (= 1/T2*) relaxation rate and Larmor frequency shift maps obtained with quantitative MRI sequences.

Results: Focal T2*w hypointensities were found in 93 % of all subjects mostly in the frontomedial globus pallidus and increasingly with age in the posteriolateral putamen. Their R2* relaxation rates, as well as their Larmor frequency shifts, confirmed the presence of paramagnetic trace metal deposits, presumably iron deposits. However, their volume was not associated with age-related iron accumulation in the surrounding normal-appearing basal ganglia tissue suggesting different mechanisms behind the formation of these deposits.

Conclusion: Basal ganglia focal T2*w MRI hypointensities presumably arise from iron-rich mineral deposits, which are possibly caused by an age-related imbalance in the brain iron homeostasis.

5.2. Introduction

Basal ganglia T2*w hypointensities constitute frequent incidental findings in elderly, otherwise healthy subjects (Chapter 2), which are believed to be a consequence of mineral deposits in and around the penetrating arteries (Casanova & Araque, 2003). The results of the multi-modal structural MRI study described in Chapter 2 also confirmed that basal ganglia T2*w hypointensities indeed seem to arise from mineral deposits in form of aggregated trace metals since they typically appear isointense on T2w MRI (Weisskoff *et al.*, 1994). Furthermore, the core regions of these T2*w MRI features, especially of larger focal T2*w hypointensities in the globus pallidus, appeared either slightly or very hypointense on T1w MRI, which indicates an advanced degree of mineralization that is possible consequential to additional calcification (Valdés Hernández *et al.*, 2014; Valdés Hernández *et al.*, 2012). These results are supported by the findings of an earlier histological study of brain mineral deposits by Slager and Wagner (1956), who in fact documented a progression in the basal ganglia mineralization. In the latter study basal ganglia mineral deposits were initially found to consist of iron, whereas at a later stage these deposits also contained other trace metals, such as copper, zinc and calcium.

Although basal ganglia T2*w hypointensities are often seen on T2*w MRI they are typically only considered clinically important if they are very large (Penke *et al.*, 2012; Tsushima & Endo, 2006). However, a few studies have analysed their progression on structural MRI and their associations with other MRI features of ageing. Harder *et al.* (2008) found that focal T2*w hypointensities in the globus pallidus have a wave-like appearance, and that the number of 'waves' and the hypointensity of the putamen is associated with age. Van Es *et al.* (2008) showed that the hypointensity of the caudate is associated with white matter lesions. Lastly, Penke *et al.* (2012) showed that focal T2*w hypointensities in the brain may be associated with a decline in cognitive abilities in normal ageing.

In this study, we analysed focal basal ganglia T2*w hypointensities in community-dwelling subjects of the Austrian Stroke Prevention Study (ASPS-Fam) to provide further information on their extent and pathogenesis in the elderly. In particular, basal ganglia T2*w hypointensities were analysed on R2* (=1/T2*) relaxation rate maps to quantify their iron content (Langkammer *et al.*, 2010), and on

Larmor frequency shift maps to gain a better understanding of the trace metal composition in the underlying tissue (He & Yablonskiy, 2009). To facilitate the segmentation of the basal ganglia T2*w hypointensities and to increase the reproducibility of the results in subsequent studies the basal ganglia T2*w hypointensities of the ASPS-Fam participants were segmented with the fully automated segmentation method presented in Chapter 3.

This study hence aims to confirm the findings of Slager and Wagner (1956) that basal ganglia T2*w hypointensities mainly consist of iron and that subregions of T2*w hypointensities that appear hypointense on T1w MRI are caused by a changed of their underlying trace metal composition. Lastly, this study investigated if the extent of basal ganglia T2*w hypointensities, and hence the underlying mineralization, was associated with age and possibly mediated by age-related iron accumulation in the surrounding normal-appearing brain tissue.

5.3. Materials and Methods

5.3.1. Subjects and MRI protocol

MRI data were obtained from 250 community-dwelling older subjects without signs or history of neurodegenerative disorders (144 females; 68 ± 10 years), who were recruited as part of the ASPS-Fam, a prospective, single-centre study on cerebral effects of vascular risk factors in the normal aged population of the city of Graz, Austria. The ASPS-Fam is an extension of the original Austrian Stroke Prevention Study (ASPS; Schmidt *et al.*, 1994) and includes study participants of the ASPS and their first grade relatives. The subjects were scanned on a Siemens 3T Trio Tim MRI scanner (Siemens, Erlangen, Germany) with the approval of the internal ethics review board and the informed consent of all participants. The MRI data were generated with 12-echo 3D FLASH (TE = 4.9 ms, ΔTE = 4.9 ms, 0.9 x 0.9 x 4 mm voxels, 208 x 256 x 32 acquisition matrix, FA = 15°, rBW = 214Hz/pixel) and MPRAGE (TI = 900 ms, TE = 2.19 ms, TR = 1.9 s, 1 x 1 x 1 mm, 448 x 512 x 176, rBW = 199Hz/pixel) sequences, which both are part of an extended MRI protocol based on that described in an earlier study (Schmidt *et al.*, 2005).

5.3.2. Preprocessing

5.3.2.1. T2*w and T1w MRI

The T2*w and T1w volumes were preprocessed with a previously developed method, which was described in Chapter 2. In short, this preprocessing pipeline segments the brain on T2*w and T1w volumes using FSL BET (Smith, 2002) and sets the intensity of image regions without any brain tissue to 0. Then the T1w volumes are registered to the T2*w volumes using FSL FLIRT (Jenkinson *et al.*, 2002) to avoid distortion of the T2*w volume due to resampling. Low-frequency signal intensity variations due to B1 field inhomogeneities are reduced on the T1w and T2*w volumes using the bias-field correction tool N4 (Tustison *et al.*, 2010).

5.3.2.2. R2* relaxation rate maps

R2* (=1/T2*) relaxation rate maps were calculated by fitting mono-exponential functions

$$S(TE) = S_0 e^{-R2^* TE} \qquad 5\text{-}1$$

voxel-wise to the T2*w magnitude data from the 12-echo gradient echo sequence, where TE is the echo time and S_0 is the T2*w signal at $TE = 0s$. The effective transverse relaxation rate $R2^* \propto c$ is proportional to the concentration c of trace metals in the underlying tissue (Langkammer *et al.*, 2010). Therefore a positive relaxation rate difference $\Delta R2^* = R2^{*MD} - R2^{*Tis}$ between the R2* values associated with basal ganglia T2*w hypointensities and the R2* values of the surrounding tissue potentially indicate mineral deposits that contain additional magnetic trace metals, such as iron, as illustrated in Figure 5-1A. The Levenberg-Marquard-Fletcher algorithm (Fletcher, 1971) was used to fit the mono-exponential functions, which minimized the sum of weighted residuals with the inverse of the image noise at each echo time as weights (Firbank *et al.*, 1999). Lastly, all voxels of a R2* map were then ranked according to the minimized sum of weighted residuals and voxels with residuals above the 90th percentile were considered unreliable and excluded from further analysis.

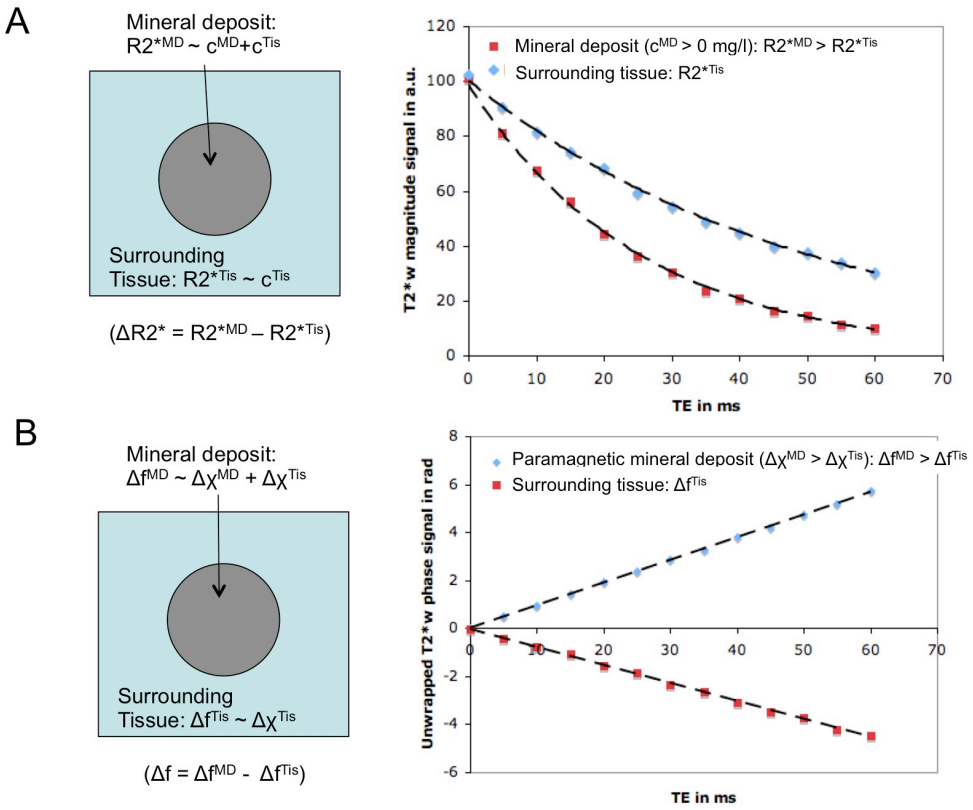

Figure 5-1: Effect of mineral deposits with magnetic trace metals on the T2*w magnitude and phase signals. (A) The T2*w magnitude signal decay over the echo time depends on the concentration of magnetic trace metals in brain tissue. In this study the T2*w magnitude signal decay decay was modelled with mono-exponential functions (dashed lines), where the exponential decay rate $\boldsymbol{R2^*}$ characterises the T2*w signal decay. It has been shown that the relaxation rate $\boldsymbol{R2^* \propto c}$ is proportional to the trace metal concentration c in the underlying tissue (Langkammer *et al.*, 2010). Hence, differences $\boldsymbol{\Delta R2^*}$ between the relaxation rates of the mineral deposit and the surrounding tissue indicate potential differences in the trace metal content of mineral deposit relative to the surrounding tissue. **(B)** The Larmor frequency shift of a voxel i is proportional to the volume magnetic susceptibility of the underlying tissue relative to water $\boldsymbol{\Delta f_i \propto \Delta \chi_i B_0}$. Larmor frequency shift differences between mineral deposits and their surrounding tissue hence indicate volume magnetic susceptibility differences between mineral deposit and the surrounding tissue (He & Yablonskiy, 2009). Larmor frequency shifts are proportional to the rate of change of the unwrapped T2*w phase signal over the echo time $\boldsymbol{\phi \propto \Delta f TE}$, therefore they can be measured by fitting linear regression lines (dashed lines) to the time evolution of the phase signals.

5.3.2.3. Larmor frequency shift maps

Larmor frequency shift Δf maps were calculated by fitting regression lines

$$\phi(TE) = \phi_0 + 2\pi \Delta f TE \qquad 5\text{-}2$$

voxel-wise to the unwrapped phase signal $\phi(TE)$ from the 12-echo gradient-echo sequence, where ϕ_0 is the unwrapped phase signal at $TE = 0s$. The Larmor frequency shifts $\Delta f_i \propto \Delta \chi_i$ of a voxel i, which are then the slope of these regression lines normalized by 2π (He & Yablonskiy, 2009), are proportional to the volume susceptibility differences (relative to water) of the underlying tissue $\Delta \chi_i$. Hence,

positive or negative Larmor frequency shift differences between the Larmor frequency shifts associated with basal ganglia T2*w hypointensities and the surrounding tissue potentially indicate para- or diamagnetic mineral deposits as illustrated in Figure 5-1B. To obtain the unwrapped T2*w phase signals, the T2*w phase volumes of all gradient echoes were first unwrapped with a Laplacian-based phase unwrapping algorithm (Li *et al.*, 2011) and then high-pass filtered with a Gaussian high pass filter with full width at half maximum of 5 mm (Shmueli *et al.*, 2009). The latter reduced low-frequency phase variations across the phase volume due to macroscopic susceptibility variations, which were commonly present at the tissue-air boundaries. The voxel-wise changes of the high pass filtered phase signals over the gradient echo time were modelled with median regression lines (Koenker & Hallock, 2001), whose slopes normalized by 2π represent the Larmor frequency shifts due to mesoscopic field inhomogeneities (He & Yablonskiy, 2009). The Larmor frequency shift map voxels were also ranked according to their minimized sum of residuals and unreliable voxels with residual sums above the 90^{th} percentile were excluded from the further analysis.

5.3.3. Segmentation

5.3.3.1. Brain tissue, basal ganglia and adjacent internal capsule

An experienced rater manually created brain tissue masks on the original T1w volumes, which were used to calculate the brain volume of all subjects. Basal ganglia and internal capsule masks were created automatically, as described in Chapter 3, based on the masks obtained with FSL FIRST (Patenaude *et al.*, 2011) on the original T1w volumes. These masks were then transformed into T2*w space and resampled with nearest neighbour interpolation using FSL FLIRT (Jenkinson *et al.*, 2002) before they were combined in a ROI mask set.

5.3.3.2. Basal ganglia T2*w hypointensities

Focal basal ganglia T2*w hypointensities used as imaging markers of basal ganglia mineralization were segmented with the fully automated and validated method described in Chapter 3. The input of this method consisted of bias-field corrected T1w and T2*w volumes, as well as the ROI masks (Section 5.3.3.1). Here the basal ganglia T2*w hypointensities were segmented on the T2*w volumes

acquired at the third echo time (TE = 14.7 ms) since the contrast-to-noise ratio (CNR) of focal hypointensities was expected to be highest on these volumes as shown in Figure 5-2.

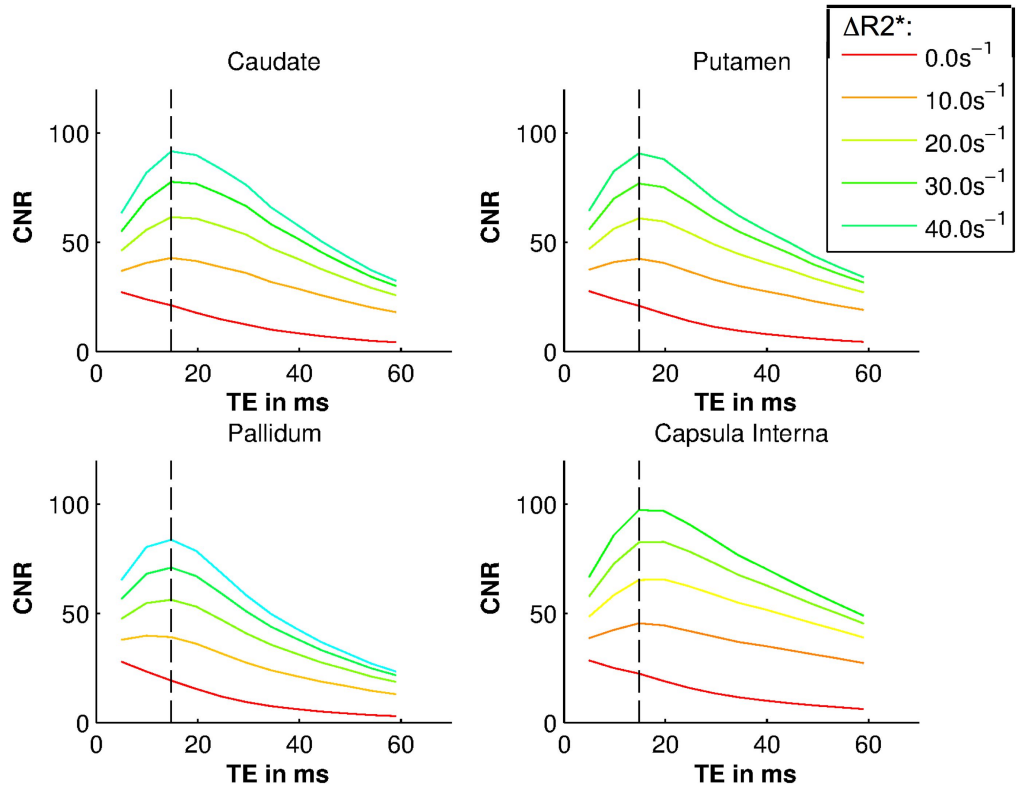

Figure 5-2: Effect of the echo time on the CNR of basal ganglia T2*w hypointensities. Based on the observations of an earlier study (Gregoire *et al.*, 2010), the CNR of basal ganglia T2*w hypointensities was estimated with $\boldsymbol{CNR(TE) = \Delta S(TE, \Delta R2^*) SNR\,(TE)}$. It can be shown that the T2*w signal difference between basal ganglia T2*w hypointensities and the surrounding normal-appearing tissue $\boldsymbol{\Delta S(TE, \Delta R2^*) = (1 - \exp(-\Delta R2^* TE))}$ increases with increasing echo time $\boldsymbol{TE}$ and depends on the difference between the $\boldsymbol{R2^*}$ values of basal ganglia T2*w hypointensities and the surrounding normal-appearing tissue. Conversely, the signal-to-noise ratio $\boldsymbol{SNR(TE)}$ of the normal-appearing tissue was estimated from measurements (Firbank *et al.*, 1999) and decreases with increasing echo time $\boldsymbol{TE}$. Multiplying both factors leads to the CNR curves as shown in this Figure, which exhibit maxima around the third echo time (TE = 14.7 ms; dashed line).

Focal T2*w hypointensities were then segmented in all ROIs with subject specific T2*w thresholds, which were derived from the globus pallidus T2*w/T1w signal intensity distributions. Segmentation artefacts were reduced with a connected components filter that removed connected components of the initial basal ganglia T2*w hypointensity masks with a standardized T2*w variance lower than $q = 0.20 \pm 0.08$, which was optimized with 10-fold cross validation as described in Chapter 3.

Lastly, the connected components of the final masks were assigned unique labels $l \in \{c, p, g, ic\}$ that correspond to their position within the basal ganglia as described in Chapter 2. Lastly, the final mask volumes $V_{T2^*w}^{Hypo}$ and the volumes of all T2*w hypointensities $V_{l,T2^*w}^{Hypo}$ per ROI l were calculated as described in Chapter 2, which were normalized with the corresponding brain volumes to account for differences in brain sizes (Penke *et al.*, 2012).

5.3.3.3. T1w iso- and hypointense subregions of basal ganglia T2*w hypointensities

The regions selected by focal T2*w hypointensity masks were further subdivided into subregions that appeared hypo- and isointense on T1w, which presumably indicate advanced mineralization, such as possibly caused by calcification (Valdés Hernández *et al.*, 2014). These subregions were also segmented with subject and ROI specific T1w thresholds that were derived automatically from the T2*w/T1w intensity distributions of the corresponding ROIs as described in Chapter 3.

5.3.4. Analysis

The segmentation results were analysed in Matlab 2012a (http://www.mathworks.com) with functions of the Statistics Toolbox and in R with the quantreg package (http://cran.r-project.org/web/packages/quantreg/index.html).

5.3.4.1. Trace metal content of basal ganglia mineral deposits

Basal ganglia T2*w hypointensities were characterised on R2* and Larmor frequency shift maps to gain a better understanding of the trace metal content of underlying mineral deposits and to investigate if a change in their trace metal composition, such as caused by calcification (Valdés Hernández *et al.*, 2014), leads to a more hypointense appearance on T1w MRI.

Firstly, the median relaxation rates and Larmor frequency shifts of basal ganglia T2*w hypointensities and their surrounding normal-appearing tissue, i.e. $R2^{*MD}_l$, $R2^{*Tis}_l$, Δf_l^{MD}, and Δf_l^{Tis}, were calculated for each ROI l. Their differences

$$\begin{aligned} \Delta R2_l^* &= R2^{*MD}_l - R2^{*Tis}_l \\ \Delta f_l &= \Delta f_l^{MD} - \Delta f_l^{Tis} \end{aligned} \qquad 5\text{-}3$$

were used as an indicator for the presence of increased trace metals deposition, and if the trace metals were predominantly paramagnetic (Figure 5-1). Then the median

R2* relaxation rates and Larmor frequency shifts of subregions of basal ganglia T2*w hypointensities that appear hypo- and isointense on T1w MRI, i.e. $R2^{*HM}_l$, $R2^{*IM}_l$, Δf_l^{HM}, and $\Delta f_l{}^{IM}$, were calculated for each ROI l. A difference in either the relaxation rates or Larmor frequency shifts

$$\begin{aligned} \Delta R2^{*AM}_l &= R2^{*HM}_l - R2^{*IM}_l \\ \Delta f_l^{AM} &= \Delta f_l^{HM} - \Delta f_l^{IM} \end{aligned} \qquad 5\text{-}4$$

indicates that T1w hypointense subregions of basal ganglia T2*w hypointensities correspond to mineral deposit regions with a different trace metal composition, and hence advanced mineralization. The differences $\Delta R2^*_l, \Delta f_l, \Delta R2^{*AM}_l, \Delta f_l^{AM}$ were calculated for all subjects and their significance was analysed with the independent 2-group Mann-Whitney U Test as implemented in R. The false discovery rate was controlled with the Benjamini–Hochberg method.

5.3.4.2. Iron accumulation and age as a mediator of basal ganglia mineralization

The hypothesis was investigated that the extent of basal ganglia mineral deposits, i.e. the volume of basal ganglia T2*w hypointensities, is associated with age and mediated by age-related brain iron accumulation in the surrounding tissue (Baron & Kenny, 1986). Therefore the associations

$$\begin{aligned} V^{Hypo}_{l,T2*w} &\sim A + 1 \\ R2^{*Tis}_l &\sim A + 1 \\ V^{Hypo}_{l,T2*w} &\sim R2^{*Tis}_l + 1 \end{aligned} \qquad 5\text{-}5$$

between the volume of basal ganglia T2*w hypointensities $V^{Hypo}_{l,T2*w}$, the R2* values of normal-appearing tissue $R2^{*Tis}_l$, and age A were analysed using quantile regression (Koenker & Hallock, 2001). Here, $R2^{*Tis}_l$ estimated the average brain iron content in normal-appearing grey matter tissues (Langkammer *et al.*, 2010). The iron content in the underlying normal-appearing tissue of a ROI was considered a mediator of the basal ganglia T2*w hypointensity volume if all three associations of Equation 5-5 were significant, i.e. the slopes of corresponding median regression lines were significant at $\alpha = 0.05$. If only one or two associations of Equation 5-5 were significant then the respective variables were considered directly associated.

5.4. Results

5.4.1. Segmentation results

Figure 5-3 shows the typical appearance of basal ganglia T2*w hypointensities from this study on T2*w and T1w MRI, where they were segmented.

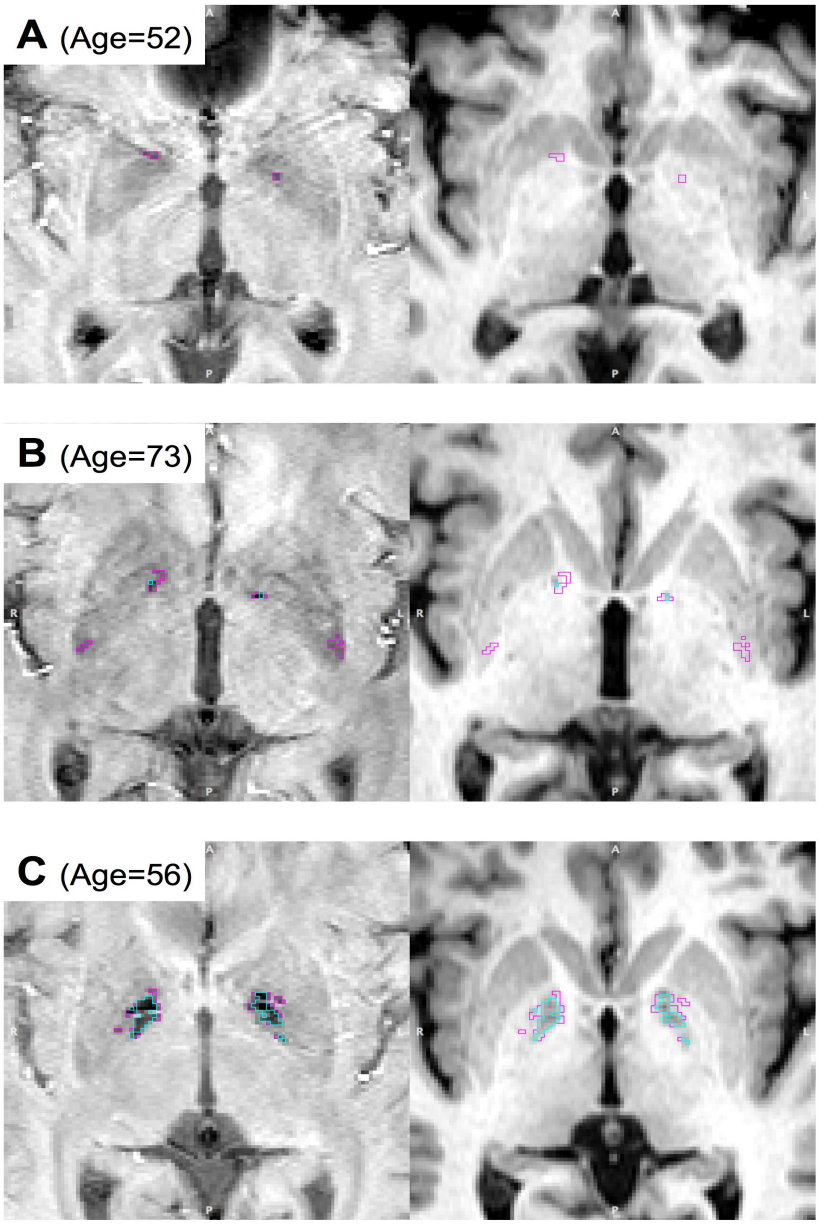

Figure 5-3: Typical appearance of basal ganglia T2*w hypointensities in ageing. These figures show the T2*w and T1w volumes of typical subjects in this study, where the automatically generated basal ganglia T2*w hypointensity masks are indicated in magenta, and the masks of their subregions that appear hypointense on T1w MRI in cyan. Basal ganglia T2*w hypointensities first appear in the globus pallidus (**A**), and with increasing age, also in the genu of the internal capsule, as well as the posterior putamen (**B**). In some subjects (**C**), the basal ganglia T2*w hypointensities can become very large, which tend to have subregions that appear hypointense on T1w MRI.

Overall these features were found in 225 (93 %) of all subjects. Table 5-1 shows that they occurred most frequently in the globus pallidus, followed by the putamen, internal capsule and caudate, where they were present in 81, 47, 32 and 23 % of all subjects. This table also shows that 60 % of all basal ganglia T2*w hypointensities in the globus pallidus exhibited subregions that appeared hypointense on T1w MRI; this figure was 20, 20 and 12 % in case of the putamen, caudate and internal capsule.

5.4.2. Trace metal content of basal ganglia mineral deposits

Table 5-1 shows the differences between the median relaxivity rates and Larmor frequency shifts of basal ganglia mineral deposits and their surrounding normal-appearing tissue. In all investigated structures these differences were significantly positive ($p < 0.05$), which confirms that the basal ganglia T2*w hypointensities mainly arise from an increased amount of paramagnetic trace metals.

The highest $\Delta R2_l^*$ value was found in the internal capsule, while the $\Delta R2_l^*$ values of the putamen, globus pallidus and caudate were very similar. This could indicate that mineral deposits in the internal capsule have a higher trace metal content, or that this difference is due to measurement errors, e.g. caused by increased myelination and the orientation of the myelinated axons (Langkammer *et al.*, 2012). Conversely, in the caudate, putamen and internal capsule Δf_l was similar, whereas in the globus pallidus it was markedly lower, which possibly supports the observation in Chapter 2 that the trace metal content of the globus pallidus mineral deposits is different from the trace metal of mineral deposits in other investigated brain structures.

The differences $\Delta R2_l^{*AM}, \Delta f_l^{AM}$ between the median relaxation rates and Larmor frequency shifts of basal ganglia T2*w hypointensity subregions that appear hypo- and isointense were only significant in the putamen where they both were negative (Table 5-1). These results indicate that only in the putamen T1w hypointense subregions of basal ganglia T2*w hypointensities coincide with a change in the trace metal composition of the underlying regions, whereas in other basal ganglia structures the T1w hypointense subregions are not related to changes in the concentration or magnetic susceptibility of the underlying trace metal deposits.

Table 5-1: Characterisation of basal ganglia T2*w hypointensities on R2* and Δf maps. This table shows the differences of the median R2* and Δf values of basal ganglia T2*w hypointensities and the surrounding normal-appearing tissue, as well as the differences of median R2* and Δf values of basal ganglia T2*w hypointensity subregions that appear hypo- and isointense on T1w MRI. Additionally, the table shows the number of subjects N with basal ganglia T2*w hypointensities and those with basal ganglia T2*w hypointensity subregions that appear hypointense on T1w MRI.

Feature/ Reference	Variables	Caudate	Putamen	Globus pallidus	Internal capsule
T2*w hypointense subregions/ surrounding tissue	N	56	115	197	77
	$\Delta R2_l^*$ [s^{-1}]	20.9 [a]	25.5 [a]	23.2 [a]	37.1 [a]
	p-Value	*1.53e-12*	*1.32e-15*	*1.32e-15*	*1.32e-15*
	Δf_l [Hz]	1.39 [a]	1.29 [a]	0.76 [a]	1.14 [a]
	p-Value	*1.20e-5*	*1.88e-10*	*1.22e-11*	*1.05e-12*
T1w hypointense/ isointense subregions	N^{AM}	11	23	119	9
	$\Delta R2_l^{*AM}$ [s^{-1}]	-2.20	-9.24	1.12	2.55
	p-Value	*0.088*	*0.197*	*0.197*	*0.643*
	Δf_l^{AM} [Hz]	-0.18	-1.38	0.01	-0.58
	p-Value	*0.050*	*0.197*	*0.133*	*0.290*

[a] significant at $\alpha = 0.05$

5.4.3. Iron accumulation and age as a mediator of basal ganglia mineralization

Table 5-2 summarizes the associations between age and volume of basal ganglia T2*w hypointensities, age and R2* of the surrounding normal-appearing tissue as a marker of the iron concentration in this tissue, and R2* and volume of basal ganglia T2*w hypointensities. It shows that of all the investigated associations listed only the volume of basal ganglia T2*w hypointensities in the putamen and the R2* relaxation rates of the normal-appearing caudate tissue are significantly associated with age. Due to the lack of associations between the other investigated variables, basal ganglia T2*w hypointensities are therefore neither directly associated nor mediated by iron concentration in the normal-appearing tissue.

Table 5-2 also shows that the slopes of the of the median regression lines that describe the association of R2* with subject age were not significant, which indicates that the iron accumulation in all investigated structures have reached a plateau

(Aquino *et al.*, 2009). Consequently, the intercepts of the median regression lines then correlate with the iron concentration in these structures and confirm that the normal-appearing globus pallidus tissue contains the highest amounts of iron, followed by the internal capsule, caudate and putamen.

Table 5-2: Associations between the volume of basal ganglia T2*w hypointensities, age and R2* of normal-appearing tissue. The associations between age $\boldsymbol{A}$ and basal ganglia T2*w hypointensity volumes $\boldsymbol{V_{l,T2*w}^{Hypo}}$ and R2* relaxation rates of the surrounding normal-appearing tissues $\boldsymbol{R2_l^{*Tis}}$, as well as those between $\boldsymbol{V_{l,T2*w}^{Hypo}}$ and $\boldsymbol{R2_l^{*Tis}}$, were investigated with median regression lines (Koenker & Hallock, 2001). This table shows the number of subjects N with basal ganglia T2*w hypointensities, as well as the slopes and intercepts of the median regression lines.

Association	Variable	Caudate	Putamen	Globus pallidus	Internal capsule
	N	56	114	196	77
$V_{l,T2*w}^{Hypo} \sim A + 1$	Slope [ppm/year]	0.06	0.32 [a]	0.17	0.05
	p-Value	*0.243*	*0.000*	*0.265*	*0.316*
	Intercept [ppm]	-0.80	-12.77 [a]	1.24	1.14
	p-Value	*0.825*	*0.002*	*0.897*	*0.710*
$R2_l^{*Tis} \sim A + 1$	Slope [s^{-1}/year]	0.15 [b]	0.18 [a]	-0.08	0.00
	p-Value	*0.018*	*0.003*	*0.091*	*0.878*
	Intercept [s^{-1}]	15.67 [a]	15.54 [a]	41.25 [a]	22.08 [a]
	p-Value	*0.001*	*0.000*	0.000	*0.000*
$V_{l,T2*w}^{Hypo} \sim R2_l^{*Tis} + 1$	Slope [ppm/s^{-1}]	0.46 [b]	0.42	0.58	-0.02
	p-Value	*0.009*	*0.082*	*0.123*	*0.927*
	Intercept [ppm]	-8.41	-4.47	-8.62	4.78
	p-Value	*0.063*	*0.470*	*0.532*	*0.426*

[a] significant at $\alpha = 0.01$

[b] significant at $\alpha = 0.05$

5.5. Discussion

Basal ganglia T2*w hypointensities, which are believed to arise from mineralization in and around the penetrating arteries, were a frequent finding in the 250 community-dwelling older subjects. The characterization of basal ganglia T2*w hypointensities on R2* relaxation rate and Larmor frequency shift maps further

confirmed that these features are caused by paramagnetic mineral deposits, presumably consisting mainly of iron. However, basal ganglia T2*w hypointensities were neither directly related to nor mediated by brain iron accumulation in the surrounding tissue, suggesting that these features might be the result of a separate brain iron storage mechanism that protects brain tissue from focal iron overload.

Basal ganglia mineral deposits have long been regarded as a physiological consequence of ageing and are common incidental autopsy findings in elderly subjects where they are described as ferrugination or siderocalinosis to emphasise that predominantly iron salts or calcium are deposited in and around the walls of small vessels in the brain (Haberland, 2007). The mechanisms that cause the formation of these mineral deposits are still unclear. However, some researchers believe that an imbalance in the brain iron homeostasis, i.e. a local iron accumulation due to weakened demand or increased supply of brain iron, might play an important role in their formation (Casanova & Araque, 2003). In the brain, iron supply is tightly controlled by the blood-brain-barrier around penetrating arteries (Rouault, 2013). Furthermore, the basal ganglia are believed to be a major entry point of brain iron, and play an important role in the storage as well in the redistribution of iron inside the brain. Therefore an age-related localised dysfunction of the blood-brain-barrier in the basal ganglia could lead to localised iron accumulation (Popescu *et al.*, 2009), which in the presence of required precursors, such as an organic matrix, could then trigger the formation of focal basal ganglia iron deposits that appear as focal hypointensities on T2*w MRI (Slager & Wagner, 1956). However, this hypothesis still needs further confirmation, which could perhaps be achieved with dynamic susceptibility contrast perfusion MRI as it has the potential to demonstrate a localized leakiness of the blood-brain barrier (Heye *et al.*, 2014).

This study confirmed that basal ganglia T2*w hypointensities are a common finding in community-dwelling subjects without history or signs of neurodegenerative disorders. As in previous studies (Chapter 2; Harder *et al.*, 2008), T2*w hypointensities were most frequently found in the globus pallidus followed by those in the putamen. The previous findings that globus pallidus T2*w hypointensities appeared very hypointense with sharp borders on T2*w MRI (Chapter 2), and were mostly located in the frontomedial globus pallidus, was

confirmed in this study. However, as shown in Figure 5-3, the globus pallidus T2*w hypointensities segmented in this study typically did not have a wave-like appearance as described in Harder *et al.* (2008), which might be due to differences in the study cohorts or reduced iron sensitivity of the T2*w MRI sequence employed here. Furthermore, these results confirm that T2*w hypointensities in the putamen have smoother borders than those in the globus pallidus (Chapter 2), and initially appear in the posterior putamen and then extend in a posterior-anterior direction with age (Aquino *et al.*, 2009; Harder *et al.*, 2008). The differences in appearance of T2*w hypointensities in different basal ganglia structures possibly highlights the fact that these regions are supplied by vessels with different densities, calibres and tortuosities (Marinkovic *et al.*, 1985), which potentially influences the pattern of iron accumulation and mineralization in these regions.

Previous studies have suggested that mineral deposits predominantly consist of iron (Penke *et al.*, 2012; Valdés Hernández *et al.*, 2011). This idea is strengthened by the results obtained from the R2* and Larmor frequency shift maps discussed above. However, the hypothesis that a progressive change in the trace metal composition of mineral deposits (Slager & Wagner, 1956) causes an increasingly hypointense appearance of basal ganglia T2*w hypointensities on T1w MRI (Valdés Hernández *et al.*, 2014) could only be confirmed in the putamen. Furthermore, in the caudate, globus pallidus and internal capsule, T1w hypointense subregions of basal ganglia T2*w hypointensities displayed very similar R2* relaxation rates and Larmor frequency shifts to the corresponding T1w isointense subregions. This suggests that T1w hypointense subregions in these structures possibly arise from changes in the underlying tissue other than calcification, such as a decrease in the solubility of the underlying iron deposits (Vymazal *et al.*, 2000).

The fact that iron accumulation in the underlying tissue of basal ganglia T2*w hypointensities is likely not related with iron accumulation in the surrounding normal-appearing tissue provides further evidence that these deposits might be part of a separate iron storage mechanism (Janaway *et al.*, 2014), possibly of ischemic origin (Dietrich & Bradley, 1988; Morris *et al.*, 1992). This storage mechanism might be more effective in protecting normal tissue in case of severe iron and trace metal overload, such as potentially caused in ageing by an imbalance in brain iron

homeostasis (Casanova & Araque, 2003). This hypothesis is further supported by the observation that basal ganglia T2*w hypointensities progressively appear hypointense on T1w MRI as described above, which suggests a continuous encapsulation of possibly toxic substances, such as iron. However, the exact reasons behind the formation of basal ganglia iron deposits and their effectiveness in protecting the surrounding tissue from the toxic effects of iron are still largely unclear. These questions could be addressed by subsequent clinical studies of ageing, which could investigate the relation between basal ganglia T2*w hypointensities and other features of ageing, such as white matter hyperintensities (Es *et al.*, 2008).

This is one of the first cross-sectional studies of basal ganglia T2*w hypointensities in which these features were segmented with a validated and fully automated method and then analysed using R2* and Larmor frequency shift maps. The automated segmentation of basal ganglia T2*w hypointensities not only facilitated their accurate identification but also helped to reduced the intra-rater variability, and hence increases the reproducibility of the results. The analysis of the segmented basal ganglia T2*w hypointensities on R2* and Larmor frequency shift maps generated quantitative information, which also provides a robust reference for future studies. However, this cross-sectional design has the limitation that all the observed age-related trends in the evolution of T2*w hypointensity volumes and the amount of iron in the surrounding normal-appearing tissue represent average values. More precise information about the subject specific development trajectories of basal ganglia T2*w hypointensities, as well as the cause-and-effect relationships with other MRI markers of ageing, can only be obtained in a longitudinal study design. A further limitation is that MRI is less specific than histological or chemical methods in characterising trace metals deposits. Further insight into the composition of the tissue underlying basal ganglia T2*w hypointensities could therefore be obtained in post-mortem MRI studies (Langkammer *et al.*, 2010), where post-mortem tissue is characterised with histological or chemical methods, as well as MRI.

In conclusion, this study confirmed that focal hypointensities in the basal ganglia are a frequent feature on T2*w MRI in the ASPS-Fam. Their characterisation on quantitative R2* and Larmor frequency shift maps showed that they arise from a focal accumulation of paramagnetic trace metals, presumably iron. As focal T2*w

hypointensities are neither directly associated with nor mediated by iron accumulation in normal-appearing tissue, it seems that they might be part of an iron storage mechanism that protects the tissue from focal iron overload, perhaps due to an imbalance in brain iron homeostasis. Further investigation with advanced imaging techniques, post-mortem samples, as well as in longitudinal studies will help to elucidate the underlying mechanisms that cause basal ganglia mineral deposits.

Chapter 6 Discussion

Basal ganglia mineralization is a frequent feature of ageing in many mammals, including humans, where mineralization was largely considered to be without further consequences unless it affected a very large area of the brain (Martínez *et al.*, 2012; Slager & Wagner, 1956; Wadsworth *et al.*, 1995). Novel clinical imaging techniques, such as computer tomography and MRI have allowed for a more detailed study of basal ganglia mineralization (Casanova & Araque, 2003) with the result that a hypothesis of their potential role in age-related microvascular disease and cognitive decline has emerged (Penke *et al.*, 2012), which this thesis has further investigated using routine, as well as quantitative MRI. A full list of publications relating to this thesis can be found in Appendix F.

6.1. Summary of major findings

Initially very little information was available about the appearance of basal ganglia mineralization on multi-modal routine MRI (Casanova & Araque, 2003; Harder *et al.*, 2008). Therefore the first study (Chapter 2) developed quantitative measures for the characterization of the imaging signatures of basal ganglia T2*w hypointensities of Lothian Birth Cohort 1936 (LBC1936) participants, which included their spatial distribution, morphology, and multi-modal MRI appearance on T2*w, T2w and T1w MRI. The main results of this research shows that the locations of basal ganglia T2*w hypointensities on average coincide with the vascular territories of the lenticulostriate arteries (Donzelli *et al.*, 1998; Feekes *et al.*, 2005), along which brain iron is presumably taken up from the blood serum through the blood-brain-barrier (BBB; Chapter 1). Furthermore, this study showed that basal ganglia T2*w hypointensities are on average very small and occur symmetrical in the left and right hemisphere, which might be a key characteristic that distinguishes basal ganglia mineralization from brain microbleeds as both appear as focal hypointensities on T2*w MRI (Charidimou *et al.*, 2012). Lastly, the multimodal structural MRI imaging signatures of basal ganglia T2*w hypointensities revealed that mineral deposits in the globus pallidus seem to consist of magnetic particles that are more aggregated than those found in other regions of the basal ganglia since

T2*w hypointensities in the globus pallidus appeared on average isointense and hypointense on T2w and T1w MRI, whereas T2*w hypointensities elsewhere in the basal ganglia appeared hypointense and isointense on T2w and T1w MRI.

The next stage of this research project addressed the lack of an automated segmentation method for basal ganglia T2*w hypointensities, since their manual or semi automated segmentation is very time-consuming and associated with a high inter- and intra-rater variability (Valdés Hernández *et al.*, 2011). This method is based on routine T2*w/T1w MRI data, which is used to segment the basal ganglia nuclei and then the basal ganglia T2*w hypointensities within each nucleus. Lastly, it segments sub regions of basal ganglia T2*w hypointensities that appear hypointense on T1w MRI and possibly indicate advanced mineralization, which might involve calcification (Valdés Hernández *et al.*, 2014). Crucially, the developed method, which is described in detail in Chapter 3, considers basal ganglia T2*w hypointensities as outliers of T2*w/T1w signal intensity distributions of basal ganglia nuclei. This comes from the fact that it is very challenging to estimate the intensity distribution of these MRI features, since they are very small and their intensity distribution generally does not resemble a Normal distribution, which was shown in Chapter 2. The developed fully automated segmentation method was first validated on T2*w/T1w MRI of a custom phantom with different mineral deposit models, which showed that the accuracy of the segmentation results depends on the bias-field correction method and that it can be improved by optimizing the connected component filter that reduces segmentation artefacts. The phantom validation also showed that the volume of the segmented T2*w hypointensities is larger than the volume of the underlying mineral deposit models due to blooming artefacts indicating that the volume of the basal ganglia T2*w masks not only reflect the extent of the underlying mineralization but also their magnetic susceptibility. Lastly, the developed method was used to segment a wide range of basal ganglia T2*w hypointensities of 98 LBC1936 study participants, which showed that the method can produce masks that are in substantial agreement with reference mask from an experienced rater. However, the spatial agreement between the generated and reference masks is proportional to the volume of these features, indicating that the segmentation of smaller basal ganglia T2*w hypointensities is especially

challenging. Overall the method, which is freely available for other researchers, provides an objective baseline that can be used to improve it in the future, and it can be used to validate the findings of this study.

In preparation for the third study, a multi-parametric, quantitative MRI relaxometry protocol was developed for the improved characterization of brain iron (Chapter 4). This protocol is based on fast spin-echo and fast spoiled gradient-echo sequences that are readily available on most clinical MRI scanners, which therefore should also increase the applicability of this protocol in future single- and multi-centre studies. Additionally, post-processing methods were developed for the reconstruction of R1, R2 and R2* maps. All calculated relaxation rate maps were first calibrated to reduce systematic measurement errors, which especially affected R1 maps. The validation of the developed multi-parametric relaxation rate mapping methodology showed that the calibrated R1, R2 and R2* relaxation rates of $MnCl_2$ solutions of a custom-built phantom were in good agreement with reference measurements obtained with gold standard methods. Conversely, in volunteers only the calibrated R1 relaxation rates of basal ganglia nuclei were in good agreement with reference values from the literature. However, it was then interesting to find that the r1, r2 an r2* relaxivities of grey matter brain iron (the relaxation rate increase with the concentration of brain iron) were still in good agreement with reference values from the literature. The discrepancy between these findings indicates that the acquisition and post-processing methods can introduce study specific systematic errors that affect the absolute values of the quantitative MRI relaxometry measurements. Therefore it is important, especially in in multi-centre studies, to calibrate the MRI relaxometry methodologies. Furthermore it is advisable to introduce quality assurance methods alongside the actual quantitative measurement methodologies (Tofts, 2004), as it is the case for many other analytical techniques, such as mass spectrometry (Krebs *et al.*, 2014).

In last study of this research project, which is described in Chapter 5, the previously developed methods were used to characterize basal ganglia T2*w hypointensities of Austrian Stroke Prevention Study Family (ASPS-Fam) participants on routine, as well as on quantitative MRI. In this study the basal ganglia T2*w hypointensities of the participants were segmented with the developed fully

automated segmentation method on all T2*w volumes from the multi-echo gradient-echo sequence and the corresponding T1w volumes. This showed that the CNR of the basal ganglia T2*w hypointensities depends on the echo time, and that there is an echo time that maximises the CNR of these features. The basal ganglia T2*w hypointensity masks obtained at the optimal echo time were used to construct spatial distribution maps as in the first study (Chapter 2), which confirmed previous findings that basal ganglia T2*w hypointensities mainly occur in the globus pallidus close to the genu of the internal capsule and in the posterior putamen. In this study basal ganglia T2*w hypointensities were additionally characterized on R2* relaxation rate and Larmor frequency shift maps. This showed that the basal ganglia tissue causing focal T2*w hypointensities predominantly contains paramagnetic particles, which are likely iron or iron compounds since iron is the most abundant paramagnetic trace metal in the human brain (Krebs *et al.*, 2014). Lastly, this study investigated if basal ganglia mineralization was associated with age-related iron accumulation in normal-appearing tissue, which, however, could not be confirmed indicating that basal ganglia mineralization is not merely a consequence of age-related iron accumulation but potentially arises from other age-related changes in the brain.

6.2. Contributions to understanding the role of iron in ageing

The findings of this work contributed to the understanding of three key questions: (i) how does brain iron accumulate in ageing, (ii) how is basal ganglia iron involved in the brain iron homeostasis, and (iii) which factors affect this iron homeostasis.

6.2.1. Brain iron accumulation

Brain iron accumulates in several forms in ageing (Ward *et al.*, 2014), such as ferritin and haemosiderin. Notably, the literature search also produced evidence that brain iron can accumulate in form of lipofuscin (Brunk & Terman, 2002), which is considered a sign of cellular iron overload (Mills *et al.*, 2010). In many of these brain iron storage forms iron is mineralized, as this provides a very efficient means of iron storage (Chasteen & Harrison, 1999). The chemical process that leads to minerals in living organisms is known as biomineralization (Crichton, 2009). The best-known type of mineralization in the human body is calcification, which occurs in the formation of bones and teeth. However, calcification also can also occur as a

response to tissue inflammation (Banks *et al.*, 2005; Stewart *et al.*, 1983) and can be induced by iron present as ferric ATP (Anghileri, 1992; Anghileri & Thouvenot, 2004). In this context the results from the LBC1936 study (Chapter 2) further confirm that these MRI-apparent features possibly arise from vascular mineralization since they coincide with the vascular territories of the penetrating arteries in the basal ganglia, and they appear isointense on T2w MRI, especially in the globus pallidus. The results from the ASPS-Fam study (Chapter 5) confirm that the mineral deposits predominantly consist of paramagnetic particles, presumably iron. Furthermore, this study also showed that especially larger basal ganglia T2*w hypointensities consist of regions that appear hypointense on T1w MRI, which were, however, only potentially associated with calcification in the putamen, whereas in other structures these regions might indicate an decreased solubility of the mineral deposits.

In the brain the highest amounts of iron is present in the nuclei of the extrapyramidal system, where most iron is stored in the substantia nigra and the globus pallidus (Hallgren & Sourander, 1958). In the extrapyramidal nuclei the highest iron accumulation is seen in the first two decades, whereas the rate of iron accumulation decreases on average over the remaining lifespan. However, recent studies with iron-sensitive MRI sequences showed that the trajectories of iron accumulation seem to increase again in old age (Haacke *et al.*, 2010), where these trajectories also exhibit a higher variability (Aquino *et al.*, 2009; Li *et al.*, 2014). The results of this thesis suggest that basal ganglia mineralization, whose appearance and extent vary markedly across subjects (Chapter 2) and presumably contains a significant amount of iron, possibly contributes to the subject-specific rate of iron accumulation in old age, and hence might help to explain the variability of the iron accumulation rate across subjects with similar age.

Overall it is still largely unclear how brain iron accumulation in ‘normal’ ageing influences brain structure and function (Polla *et al.*, 2003). Raz *et al.* (2007) was one of the first researchers to suggest that brain iron accumulation might have an influence on the atrophy of brain regions that are closely correlated with specific cognitive functions, such as the hippocampus that plays a role in memory. In a later study Rodrigue *et al.* (2013) confirmed that brain iron indeed seems to contribute to atrophy of the hippocampus, as well as to deficiencies in memory. This association

between iron accumulation and brain function was explained by the fact that the oxidative stress increases through increased amounts of iron (Chapter 1), which possibly leads to brain cell death and a decline in brain function. Other studies that investigated if brain iron accumulation is associated with age-related declines in cognitive and motor function also found an association between iron and brain function (Ghadery *et al.*, 2014; Li *et al.*, 2015; Penke *et al.*, 2012), which was also attributed to brain iron-mediated increase in oxidative stress. Here this thesis could further confirm the validity of the results in Penke *et al.* (2012) since the underlying tissue of basal ganglia T2*w hypointensities of LBC1936 participants indeed seem to mainly consist of iron, which is derived from the observation that basal ganglia T2*w hypointensities of ASPS-Fam participants segmented with the same methods as those in LBC1936 participants are mainly paramagnetic (Chapter 5).

As brain iron through the link of oxidative stress seems to influence brain function, this study finds that it could be considered another factor in the oxidative stress theory of ageing (Bokov *et al.*, 2004; Harman, 1956; Sohal & Weindruch, 1996)[a]. This theory essentially predicts that sustained changes in oxidative stress in cells may alter the life span in mammals. An increased amount of reactive oxidative species (ROS) in a cell can be caused either through increased ROS production or reduced scavenging of ROS. In ageing and in neurodegenerative diseases free trace metals, such as iron (Fe^{2+}, Fe^{3+}) contribute to an increased amount of ROS mainly through the Fenton reaction (see Introduction). However, healthy cells also have mechanisms that scavenge ROS and control the amount of ROS, which involve Vitamin C, as well as antioxidant enzymes, such as superoxide dismutase. This theory of ageing is still much debated since it could only be proven to some extend in animals (Pérez *et al.*, 2009; Salmon *et al.*, 2010). Overall the results of these studies produced little evidence that the lifespan could be prolonged by deliberately reducing the amount of ROS unless the animals were subjected to acute oxidative stress, e.g. due to disease. However, Salmon *et al.* (2010) suggests that the amount of ROS may rather contribute to the health span, i.e. the period without age-related pathologies, instead of the life span, implying that less ROS could lead to 'successful' ageing. This theory therefore further justifies the role of brain iron as a biomarker for the

[a] Coincidently, Prof. Harman passed away in the year this thesis was completed.

early detection and possibly prevention of disability ageing, which is also supported by theories that imply abnormal iron accumulation in neurodegenerative diseases of ageing (Ward *et al.*, 2014; Zecca *et al.*, 2004), such as Alzheimer's disease.

6.2.2. Brain iron homeostasis

Brain iron is mainly stored in the extrapyramidal nuclei at the centre of the brain, whereas the white matter and the cerebral cortex contain far less iron, although iron is still essentially required in these regions for the myelination of the axons and the neurotransmitter production. This suggests that brain iron is redistributed along this concentration gradient from the centre to the periphery of the brain, which is believed to occur along axons (Dietrich & Bradley, 1988). A decreased demand of iron by the periphery of the brain could therefore lead to increased iron accumulation in the basal ganglia, where iron enters the brain through the BBB. The results of this thesis seem to coincide closely with this theory since basal ganglia T2*w hypointensities of the LBC1936 and ASPS-Fam study participants predominantly are found in the region of the globus pallidus close to the genu of the internal capsule (Chapter 2 and Chapter 5). This spatial distribution of basal ganglia T2*w hypointensities suggests that the redistribution of brain iron possibly occurs along the axons of the corona radiata, which is described as a sheet of ascending and descending axons that pass through the internal capsule adjacent to the basal ganglia and end or start in the cerebral cortex.

6.2.3. Factors affecting the brain iron homeostasis

A dysregulation of the brain iron entry, consumption and redistribution can affect the brain iron homeostasis in the brain, which may result in increased brain iron deposition as a mechanism for protecting the brain from oxidative stress (Brass *et al.*, 2006). An imbalance in the iron homeostasis in the brain potentially followed by vascular mineralization could be caused by chronic conditions, such as hypoxic ischemic brain injury, atrophy and white matter lesions.

Hypoxic ischemic brain injury may lead to hemorrhagic transformation and edema, which are possibly mediated by a breakdown of the BBB (Ballabh *et al.*, 2004; Latour *et al.*, 2004). A deregulation of the BBB consequently may increases the permeability to otherwise tightly controlled substances such as iron, and hence

alter the iron homeostasis by increasing the supply of iron. For example, in Dietrich and Bradley (1988) four children were presented who suffered a severe ischemic-anoxic insult and were resuscitated. This caused T2w hypointensities in the basal ganglia and T2w hyperintensities in the white matter due to gliosis in all four children. Additionally, calcification within T2w hypointensities was found in one of the four children. As this spatial distribution pattern of MRI features resembles that of basal ganglia T2*w hypointensities in healthy elderly subjects very closely (Chapter 2), it suggests that ischemia might also play a role in the formation of basal ganglia mineralization in ageing subjects as also noted in Morris *et al.* (1992) and Janaway *et al.* (2014). Notably, recent research showed that iron might also mediate the opening of the BBB after an ischemic insult (Won *et al.*, 2011), which suggests that higher iron load around the BBB might be a driver, as well as a consequence of BBB breakdown. Furthermore, age-related BBB breakdown is possibly related to cognitive decline (Popescu *et al.*, 2009), which, in light of the previously mentioned findings, provides further clues for explaining how basal ganglia mineral deposits might be associated with age-related cognitive decline (Penke *et al.*, 2012).

Lastly, a decreased peripheral demand of iron, and hence increased proximal iron deposition could be related to atrophy as well as white matter lesions, since under these circumstances less iron is needed for the maintenance of the neurotransmitter balance and myelination of the axons. Recently, Es *et al.* (2008) could partly confirm this relation in non-demented elderly subjects, where an association was found between the iron accumulation in the caudated as seen as hypointensity on T2*w MRI and the volume of white matter T2w hypointensities and atrophy. Notably, both atrophy as well as white matter lesions in ageing could be caused by increased iron-mediated oxidative stress (Rodrigue *et al.*, 2013; Yoshioka *et al.*, 2014), which suggests that peripheral iron accumulation could also contribute to iron accumulation in the basal ganglia.

6.3. Strength and Limitations

This is to the best of knowledge of the author the first study that investigated focal T2*w hypointensities in the basal ganglia on multi-modal routine and quantitative MRI. This study focused on a systematic approach to increase the understanding of

these MRI features, which is also reflected in the chronological order the different sub studies described in this thesis were conducted. This study tried to increase the objectivity of the results by developing robust computational methods, such as the segmentation method for basal ganglia T2*w hypointensities, which were extensively validated with custom-designed phantoms, as well as MRI data from two independent subject cohorts. Furthermore, the developed software was also made publicly available on the Internet as a baseline for future segmentation methods, as a starting point for improving the developed segmentation algorithm, as well as for the use in future studies of basal ganglia T2*w hypointensities. Lastly, this study also explored quantitative methods for detecting and quantifying iron in the brain, such as MRI relaxometry, which due to the recent advancements in this field possibly represent the future standard method in iron research. These quantitative methods were again thoroughly validated *in vitro* as well as *in vivo*.

Notably, this study also has three limitations. Firstly, the hypothesis that basal ganglia T2*w hypointensities as imaging markers of mineralization are closely related with the penetrating arteries of the brain was derived from the literature (Casanova & Araque, 2003; Morris *et al.*, 1992), and then confirmed on spatial distribution maps of basal ganglia T2*w hypointensities (Chapter 2 and Chapter 5). However, further confirmation of this finding is still pending, which could be obtained with images of the microvasculature that are registered to the T2*w MRI images from modalities, such as high-field or black blood MR angiography (Okuchi *et al.*, 2013; Seo *et al.*, 2012). Alternatively, the relation between basal ganglia T2*w hypointensities and the penetrating arteries could also be demonstrated in MR post-mortem studies (Langkammer *et al.*, 2010), where the microvasculature is visualized on histology slices, which are then registered to the MR images.

Secondly, the quantitative MRI methods employed in Chapter 5 helped to improve the understanding the composition of the tissue that causes basal ganglia T2*w hypointensities, however, it does not represent a definitive proof that the aggregated paramagnetic particles are in fact predominantly iron. Such a proof could be obtained by combining MRI findings with the results from chemical analysis of the specific brain tissue. For example, the presence of iron and calcium and their quantity could be shown with histological stains (Sun *et al.*, 2015), with mass

spectrometry (Becker *et al.*, 2010), or X-Ray fluorescence imaging (Zheng *et al.*, 2013). Ideally, unfixed samples should be analysed in such a study since sample preparation with formalin destroys cell structures and potentially changes the composition of the basal ganglia mineralization (Langkammer *et al.*, 2010).

Lastly, potential relations between basal ganglia T2*w hypointensities as markers of basal ganglia mineralization and other MRI markers of ageing, such as white matter lesions, were only derived from the literature and not conclusively investigated. This is related to the fact that at the start of this study only very little information was available in the MRI literature about the interrelations of these features, which was pieced together during the course of this study. This lack of information is also a reason why this study mainly focused on the development and validation of analysis methods for basal ganglia T2*w hypointensities, which are now available to use in future studies.

6.4. Implications for future research

The results of this study further confirm that basal ganglia T2*w hypointensities are potentially a novel MRI marker of ageing and small vessel disease. However this MRI marker is still largely underappreciated although iron deposition in ageing, which presumably causes these MRI features and is associated with the brain function (Ghadery *et al.*, 2014; Li *et al.*, 2015), is already considered as an MRI marker of ageing, as well as a pharmacological target for the prevention of disability caused by neurodegenerative diseases in ageing (Ward *et al.*, 2014). To further promote basal ganglia T2*w hypointensities as a MRI marker of ageing future research has to address the limitations of this study and to demonstrate that basal ganglia T2*w hypointensities are in fact closely related with the microvasculature of the brain, confirm that the underlying mineralization contains iron, and investigate their relation with established features of ageing, such as atrophy and white matter lesions (von Es *et al.*, 2008). The first two points could be confirmed in post-mortem MRI studies (Langkammer *et al.*, 2010), which, however, are difficult to set-up since they require additional Ethics approvals, a close collaboration between pathology and neuroimaging departments, and researchers that are interested in histology, as well as MRI. Conversely, to show how basal ganglia T2*w hypointensities are related to other MRI features of ageing is comparably easier to achieve and could be

replicated in other ageing studies with similar MRI protocols as the LBC1936 and ASPS-Fam and the developed software in this study.

6.5. Conclusions

This study characterised basal ganglia T2*w hypointensities on multi-modal routine and quantitative MRI in two independent ageing cohorts. A fully automated method was developed and validated for the segmentation of these MRI features on routine T2*w/T1w MRI. Furthermore a multi-parameter MRI relaxometry method for the improved characterization of brain iron was developed and validated. With the developed methods it could be further confirmed that basal ganglia T2*w hypointensities arise from iron deposits, which are potentially closely related to the basal ganglia microvasculature. These findings and the literature-derived theory further confirm that basal ganglia T2*w hypointensities represent MRI markers that might help to understand subject-specific rates of cognitive decline in ageing and small vessel disease.

References

Abbott, N., Rönnbäck, L., Hansson, E. (2006). Astrocyte-endothelial interactions at the blood-brain barrier. *Nat Rev Neurosci.* 7, 41-53.

Aja-Fernández, S., Estépar, R. S. J., Alberola-López, C., Westin, C. (2006). Image quality assessment based on local variance. *Conf Proc IEEE Eng Med Biol Soc.* 1, 4815-8.

Andersson, J., Smith, S., Jenkinson, M. (2008). FMRIB's Non-linear Image Registration Tool. *Proc OHBM.* 496.

Anghileri, L. (1992). Soft tissue calcification induced by iron complexes. *Calcif Tissue Int.* 51, 83-4.

Anghileri, L., Thouvenot, P. (2004). Molecular exchange of metal ions and tissular calcium overload. *Biol Trace Elem Res.* 99, 211-7.

Annamraju, R., Venkatesan, R., Vu, A. (2008). T2* Weighted Angiography (SWAN) : T2* weighted non-contrast imaging with multi-echo acquisition & reconstruction. *Proc. ESMRMB.* 482.

Aquino, D., Bizzi, A., Grisoli, M., Garavaglia, B., Bruzzone, M. G., Nardocci, N., Savoiardo, M., Chiapparini, L. (2009). Age-related Iron Deposition in the Basal Ganglia: Quantitative Analysis in Healthy Subjects. *Radiology.* 252, 165-72.

Asano, T., Komatsu, M., Yamaguchi-Iwai, Y., Ishikawa, F., Mizushima, N., Iwai, K. (2011). Distinct mechanisms of ferritin delivery to lysosomes in iron-depleted and iron-replete cells. *Mol Cell Biol.* 31, 2040-52.

Ashburner, J., Friston, K. J. (2005). Unified segmentation. *NeuroImage.* 26, 839-51.

Bagher-Ebadian, H., Jiang, Q., Ewing, J. R. (2008). A modified fourier-based phase unwrapping algorithm with an application to MRI venography. *J Magn Reson Im.* 27, 649-52.

Ballabh, P., Braun, A., Nedergaard, M. (2004). The blood-brain barrier: an overview: structure, regulation, and clinical implications. *Neurobiol Dis.* 16, 1-13.

Banks, K. P., Bui-Mansfield, L. T., Chew, F. S., Collinson, F. (2005). A compartmental approach to the radiographic evaluation of soft-tissue calcifications. 40, 391-407.

Barnes, S. R. S., Haacke, E. M., Ayaz, M., Boikov, A. S., Kirsch, W., Kido, D. (2011). Semiautomated detection of cerebral microbleeds in magnetic resonance images. *Magn Reson Imaging.* 29, 844-52.

Baron, R. M., Kenny, D. A. (1986). The moderator-mediator variable distinction in social psychological research: conceptual, strategic, and statistical considerations. *J Pers Soc Psychol.* 51, 1173-82.

Bartzokis, G., Tishler, T. A., Lu, P. H., Villablanca, P., Altshuler, L. L., Carter, M., Huang, D., Edwards, N., Mintz, J. (2007). Brain ferritin iron may influence age-and gender-related risks of neurodegeneration. *Neurobiol Aging.* 28, 414-23.

Becker, J. S., Matusch, A., Palm, C., Salber, D., Morton, K. A., Becker, J. S. (2010). Bioimaging of metals in brain tissue by laser ablation inductively coupled plasma mass spectrometry (LA-ICP-MS) and metallomics. *Metallomics.* 2, 104-11.

Ben-Gal, I. Outlier Detection. In: Maimon, O., Rokach, L. (2010). Data mining and knowledge discovery handbook. Springer.

Bergstra, J., Bengio, Y. (2012). Random Search for Hyper-parameter Optimization. *J Mach Learn Res.* 13, 281-305.

Bernstein, M., King, K., Zhou, X. (2004). Handbook of MRI pulse sequences. Academic press Inc.

Bhagwandien, R., Van Ee, R., Beersma, R., Bakker, C., Moerland, M., Lagendijk, J. (1992). Numerical analysis of the magnetic field for arbitrary magnetic susceptibility distributions in 2D. *Magn Reson Im.* 10, 299-313.

Bilgic, B., Pfefferbaum, A., Rohlfing, T., Sullivan, E. V., Adalsteinsson, E. (2012). MRI estimates of brain iron concentration in normal aging using quantitative susceptibility mapping. *NeuroImage.* 59, 2625-35.

Birkl, C., Langkammer, C., Haybaeck, J., Ernst, C., Stollberger, R., Fazekas, F., Ropele, S. (2014). Temperature-induced changes of magnetic resonance relaxation times in the human brain: a postmortem study. *Magn Reson Med.* 71, 1575-80.

Bishop, N. A., Lu, T., Yankner, B. A. (2010). Neural mechanisms of ageing and cognitive decline. *Nature.* 464, 529-35.

Bland, J., Altman, D. (1986). Statistical methods for assessing agreement between two methods of clinical measurement. *Lancet.* 1, 307-10.

Bloembergen, N., Morgan, L. (1961). Proton relaxation times in paramagnetic solutions. Effects of electron spin relaxation. *J Chem Phys.* 34, 842.

Boeckh-Behrens, T., Lutz, J., Lummel, N., Burke, M., Wesemann, T., Schöpf, V., Brückmann, H., Linn, J. (2012). Susceptibility-weighted angiography (SWAN) of cerebral veins and arteries compared to TOF-MRA. *Eur J Radiol.* 81, 1238-45.

Bokov, A., Chaudhuri, A., Richardson, A. (2004). The role of oxidative damage and stress in aging. *Mech Ageing Dev.* 125, 811-26.

Bolandzadeh, N., Davis, J. C., Tam, R., Handy, T. C., Liu-Ambrose, T. (2012). The association between cognitive function and white matter lesion location in older adults: a systematic review. *BMC Neurol.* 12, 126.

Bos, C., Viergever, M. A., Bakker, C. J. G. (2003). On the artifact of a subvoxel susceptibility deviation in spoiled gradient-echo imaging. *Magn Reson Med.* 50, 400-4.

Brass, S. D., Chen, N., Mulkern, R. V., Bakshi, R. (2006). Magnetic resonance imaging of iron deposition in neurological disorders. *Top Magn Reson Imaging.* 17, 31-40.

Bribiesca, E. (2008). An easy measure of compactness for 2D and 3D shapes. *Pattern Recogn.* 41, 543-54.

Brooks, R. A., Moiny, F., Gillis, P. (2001). On T2-shortening by weakly magnetized particles: the chemical exchange model. *Magn Reson Med.* 45, 1014-20.

Brooks, R. A., Vymazal, J., Goldfarb, R. B., Bulte, J. W., Aisen, P. (1998). Relaxometry and magnetometry of ferritin. *Magn Reson Med.* 40, 227-35.

Brunk, U. T., Terman, A. (2002). Lipofuscin: mechanisms of age-related accumulation and influence on cell function. *Free Radic Biol Med.* 33, 611-9.

Cao, F., Commowick, O., Bannier, E., Barillot, C. (2014). Simultaneous Estimation of T1, T2 and B1 Maps From Relaxometry MR Sequences. *Proc MICCAI Workshop - IntellMR.*

Casanova, M. F., Araque, J. M. (2003). Mineralization of the basal ganglia: implications for neuropsychiatry, pathology and neuroimaging. *Psychiatry Res.* 121, 59-87.

Caspers, S., Moebus, S., Lux, S., Pundt, N., Schütz, H., Mühleisen, T. W., Gras, V., Eickhoff, S. B., Romanzetti, S., Stöcker, T., Stirnberg, R., Kirlangic, M. E., Minnerop, M., Pieperhoff, P., Mödder, U., Das, S., Evans, A., Jöckel, K.-H.,

Erbel, R., Cichon, S., Nöthen, M. M., Sturma, D., Bauer, A., Shah, J., Zilles, K., Amunts, K. (2014). Studying variability in human brain aging in a population-based German cohort-rationale and design of 1000BRAINS. *Front Aging Neurosci.* 6, 149.

Cass, W., Grondin, R., Andersen, A., Zhang, Z., Hardy, P., Hussey-Andersen, L., Rayens, W., Gerhardt, G., Gash, D. (2007). Iron accumulation in the striatum predicts aging-related decline in motor function in rhesus monkeys. *Neurobiol Aging.* 28, 258-71.

Chan, D. D., Neu, C. P. (2013). Probing articular cartilage damage and disease by quantitative magnetic resonance imaging. *J R Soc Interface.* 10, 20120608.

Charidimou, A., Jäger, H. R., Werring, D. J. (2012). Cerebral microbleed detection and mapping: principles, methodological aspects and rationale in vascular dementia. *Exp Gerontol.* 47, 843-52.

Chasteen, N. D., Harrison, P. M. (1999). Mineralization in ferritin: an efficient means of iron storage. *J Struct Biol.* 126, 182-94.

Chavhan, G. B., Babyn, P. S., Thomas, B., Shroff, M. M., Haacke, E. M. (2009). Principles, techniques, and applications of T2*-based MR imaging and its special applications. *Radiographics.* 29, 1433-49.

Chen, J.-H., Shahnavas, S., Singh, N., Ong, W.-Y., Walczyk, T. (2013). Stable iron isotope tracing reveals significant brain iron uptake in adult rats. *Metallomics.* 5, 167-73.

Cheng, H.-L. M., Stikov, N., Ghugre, N. R., Wright, G. A. (2012). Practical medical applications of quantitative MR relaxometry. *J Magn Reson Imaging.* 36, 805-24.

Cohen, L. A., Gutierrez, L., Weiss, A., Leichtmann-Bardoogo, Y., Zhang, D.-l., Crooks, D. R., Sougrat, R., Morgenstern, A., Galy, B., Hentze, M. W., Lazaro, F. J., Rouault, T. A., Meyron-Holtz, E. G. (2010). Serum ferritin is

derived primarily from macrophages through a nonclassical secretory pathway. *Blood.* 116, 1574-84.

Collingwood, J. F., Chong, R. K. K., Kasama, T., Cervera-Gontard, L., Dunin-Borkowski, R. E., Perry, G., Pósfai, M., Siedlak, S. L., Simpson, E. T., Smith, M. A., others (2008). Three-dimensional tomographic imaging and characterization of iron compounds within Alzheimer's plaque core material. *J Alzheimers Dis.* 14, 235-45.

Conijn, M. M. A., Geerlings, M. I., Luijten, P. R., Zwanenburg, J. J. M., Visser, F., Biessels, G. J., Hendrikse, J. (2010). Visualization of cerebral microbleeds with dual-echo T2*-weighted magnetic resonance imaging at 7.0 T. *J Magn Reson Imaging.* 32, 52-9.

Cordonnier, C. (2010). Brain microbleeds. *Pract Neurol.* 10, 94-100.

Cordonnier, C., Al-Shahi Salman, R., Wardlaw, J. (2007). Spontaneous brain microbleeds: systematic review, subgroup analyses and standards for study design and reporting. *Brain.* 130, 1988-2003.

Cordonnier, C., Potter, G. M., Jackson, C. A., Doubal, F., Keir, S., Sudlow, C. L. M., Wardlaw, J. M., Al-Shahi Salman, R. (2009). improving interrater agreement about brain microbleeds: development of the Brain Observer MicroBleed Scale (BOMBS). *Stroke.* 40, 94-9.

Crichton, R. R. (2009). Iron metabolism: from molecular mechanisms to clinical consequences. John Wiley & Sons Ltd.

Daghighi, M., Rezaei, V., Zarrintan, S., Pourfathi, H. (2007). Intracranial physiological calcifications in adults on computed tomography in Tabriz, Iran. *Folia Morphol (Praha).* 66, 115-9.

De Maesschalck, R., Jouan-Rimbaud, D., Massart, D. L. (2000). The mahalanobis distance. *Chemometr. Intell. Lab.* 50, 1-18.

De Munck, J. C., Bhagwandien, R., Muller, S. H., Verster, F. C., Van Herk, M. B. (1996). The computation of MR image distortions caused by tissue susceptibility using the boundary element method. *IEEE Trans Med Imaging.* 15, 620-7.

De Reuck, J., Auger, F., Cordonnier, C., Deramecourt, V., Durieux, N., Pasquier, F., Bordet, R., Maurage, C. A., Leys, D. (2011). Comparison of 7.0-T T2*-magnetic resonance imaging of cerebral bleeds in post-mortem brain sections of Alzheimer patients with their neuropathological correlates. *Cerebrovasc Dis.* 31, 511-7.

De Rochefort, L., Liu, T., Kressler, B., Liu, J., Spincemaille, P., Lebon, V., Wu, J., Wang, Y. (2010). Quantitative susceptibility map reconstruction from MR phase data using bayesian regularization: validation and application to brain imaging. *Magn Reson Med.* 63, 194-206.

Deary, I. J., Gow, A. J., Pattie, A., Starr, J. M. (2012). Cohort profile: the Lothian Birth Cohorts of 1921 and 1936. *Int J Epidemiol.* 41, 1576-84.

Deary, I. J., Gow, A. J., Taylor, M. D., Corley, J., Brett, C., Wilson, V., Campbell, H., Whalley, L. J., Visscher, P. M., Porteous, D. J., Starr, J. M. (2007). The Lothian Birth Cohort 1936: a study to examine influences on cognitive ageing from age 11 to age 70 and beyond. *BMC Geriatr.* 7, 28.

Deichmann, R., Good, C., Josephs, O., Ashburner, J., Turner, R. (2000). Optimization of 3-D MP-RAGE sequences for structural brain imaging. *Neuroimage.* 12, 112-27.

Deistung, A., Rauscher, A., Sedlacik, J., Witoszynskyj, S., Reichenbach, J. R. (2008). Informatics in Radiology: GUIBOLD: a graphical user interface for image reconstruction and data analysis in susceptibility-weighted MR imaging. *Radiographics.* 28, 639-51.

Deoni, S. C. L. (2010). Quantitative relaxometry of the brain. *Top Magn Reson Imaging.* 21, 101-13.

Deoni, S. C. L. (2007). High-Resolution T1 Mapping of the Brain at 3T with Driven Equilibrium Single Pulse Observation of T1 with High-Speed Incorporation of RF Field Inhomogeneities (DESPOT1-HIFI). *J Magn Reson Im.* 26, 1106-11.

Deoni, S. C. L., Rutt, B. K., Peters, T. M. (2003). Rapid combined T1 and T2 mapping using gradient recalled acquisition in the steady state. *Magn Reson Med.* 49, 515-26.

Dietrich, R. B., Bradley, Jr, W. G. (1988). Iron accumulation in the basal ganglia following severe ischemic-anoxic insults in children. *Radiology.* 168, 203-6.

Donzelli, R., Marinkovic, S., Brigante, L., de Divitiis, O., Nikodijevic, I., Schonauer, C., Maiuri, F. (1998). Territories of the perforating (lenticulostriate) branches of the middle cerebral artery. *Surg Radiol Anat.* 20, 393-8.

Doubal, F. N., MacLullich, A. M. J., Ferguson, K. J., Dennis, M. S., Wardlaw, J. M. (2010). Enlarged perivascular spaces on MRI are a feature of cerebral small vessel disease. *Stroke.* 41, 450-4.

Dowell, N. G., Tofts, P. S. (2007). Fast, accurate, and precise mapping of the RF field in vivo using the 180 degrees signal null. *Magn Reson Med.* 58, 622-30.

Drayer, B., Burger, P., Darwin, R., Riederer, S., Herfkens, R., Johnson, G. (1986). MRI of brain iron. *AJR Am J Roentgenol.* 147, 103-10.

Fazekas, F. (1989). Magnetic resonance signal abnormalities in asymptomatic individuals: their incidence and functional correlates. *Eur Neurol.* 29, 164-8.

Feekes, J. A., Hsu, S. W., Chaloupka, J. C., Cassell, M. D. (2005). Tertiary microvascular territories define lacunar infarcts in the basal ganglia. *Ann Neurol.* 58, 18-30.

Filippini, N., Zsoldos, E., Haapakoski, R., Sexton, C. E., Mahmood, A., Allan, C. L., Topiwala, A., Valkanova, V., Brunner, E. J., Shipley, M. J., Auerbach, E.,

Moeller, S., Uğurbil, K., Xu, J., Yacoub, E., Andersson, J., Bijsterbosch, J., Clare, S., Griffanti, L., Hess, A. T., Jenkinson, M., Miller, K. L., Salimi-Khorshidi, G., Sotiropoulos, S. N., Voets, N. L., Smith, S. M., Geddes, J. R., Singh-Manoux, A., Mackay, C. E., Kivimäki, M., Ebmeier, K. P. (2014). Study protocol: The Whitehall II imaging sub-study. *BMC Psychiatry.* 14, 159.

Filzmoser, P. (2005). Identification of multivariate outliers: a performance study. *Au J Stat.* 34, 127-38.

Filzmoser, P., Garrett, R. G., Reimann, C. (2005). Multivariate outlier detection in exploration geochemistry. *Comput Geosci.* 31, 579-87.

Fineberg, N. A., Haddad, P. M., Carpenter, L., Gannon, B., Sharpe, R., Young, A. H., Joyce, E., Rowe, J., Wellsted, D., Nutt, D. J., Sahakian, B. J. (2013). The size, burden and cost of disorders of the brain in the UK. *J Psychopharmacol.* 27, 761-70.

Firbank, M. J., Coulthard, A., Harrison, R. M., Williams, E. D. (1999). A comparison of two methods for measuring the signal to noise ratio on MR images. *Phys Med Biol.* 44, N261-4.

Fisher, C. M. (1982). Lacunar strokes and infarcts: a review. *Neurology.* 32, 871-6.

Fjell, A. M., Walhovd, K. B., Fennema-Notestine, C., McEvoy, L. K., Hagler, D. J., Holland, D., Brewer, J. B., Dale, A. M. (2009). One-year brain atrophy evident in healthy aging. *J Neurosci.* 29, 15223-31.

Fletcher, R. (1971). Modified Marquardt subroutine for non-linear least squares. *AERE report.* 6799.

Fox, N., Schott, J. (2004). Imaging cerebral atrophy: normal ageing to Alzheimer's disease. *Lancet.* 363, 392-4.

Fraley, C., Raftery, A. E. (2002). Model-based clustering, discriminant analysis, and density estimation. *JASA*. 97, 611-31.

Frisoni, G. B., Fox, N. C., Jack, Jr, C. R., Scheltens, P., Thompson, P. M. (2010). The clinical use of structural MRI in Alzheimer disease. *Nat Rev Neurol.* 6, 67-77.

Gao, G., Chang, Y.-Z. (2014). Mitochondrial ferritin in the regulation of brain iron homeostasis and neurodegenerative diseases. *Front Pharmacol.* 5, 19.

García-Lorenzo, D., Prima, S., Arnold, D. L., Collins, D. L., Barillot, C. (2011). Trimmed-likelihood estimation for focal lesions and tissue segmentation in multisequence MRI for multiple sclerosis. *IEEE Trans Med Imaging.* 30, 1455-67.

Ghadery, C., Pirpamer, L., Hofer, E., Langkammer, C., Petrovic, K., Loitfelder, M., Schwingenschuh, P., Seiler, S., Duering, M., Jouvent, E., Schmidt, H., Fazekas, F., Mangin, J.-F., Chabriat, H., Dichgans, M., Ropele, S., Schmidt, R. (2014). R2* mapping for brain iron: associations with cognition in normal aging. *Neurobiol Aging.* doi: 10.1016/j.neurobiolaging.2014.09.013.

Gillis, P., Roch, A., Brooks, R. A. (1999). Corrected Equations for Susceptibility-Induced T2-Shortening. *J Magn Reson.* 137, 402-7.

Gossuin, Y., Gillis, P., Hocq, A., Vuong, Q. L., Roch, A. (2009). Magnetic resonance relaxation properties of superparamagnetic particles. *Wiley Interdiscip Rev Nanomed Nanobiotechnol.* 1, 299-310.

Gossuin, Y., Gillis, P., Muller, R. N., Hocq, A. (2007). Relaxation by clustered ferritin: a model for ferritin-induced relaxation in vivo. *NMR Biomed.* 20, 749-56.

Gossuin, Y., Roch, A., Muller, R. N., Gillis, P. (2000). Relaxation induced by ferritin and ferritin-like magnetic particles: the role of proton exchange. *Magn Reson Med.* 43, 237-43.

Graves, M. J., Emmens, D., Lejay, H., Hariharan, H., Polzin, J., Lomas, D. J. (2008). T2 and T2* quantification using optimal B1 image reconstruction for multicoil arrays. *J Mag Reson Im.* 28, 278-81.

Graybiel, A. M. (2005). The basal ganglia: learning new tricks and loving it. *Curr Opin Neurobiol.* 15, 638-44.

Gregoire, S. M., Chaudhary, U. J., Brown, M. M., Yousry, T. A., Kallis, C., Jäger, H. R., Werring, D. J. (2009). The Microbleed Anatomical Rating Scale (MARS): reliability of a tool to map brain microbleeds. *Neurology.* 73, 1759-66.

Gregoire, S. M., Werring, D. J., Chaudhary, U. J., Thornton, J. S., Brown, M. M., Yousry, T. A., Jäger, H. R. (2010). Choice of echo time on GRE T2*-weighted MRI influences the classification of brain microbleeds. *Clin Radiol.* 65, 391-4.

Gudbjartsson, H., Patz, S. (1995). The Rician distribution of noisy MRI data. *Mag Reson Med.* 34, 910-14.

Gutteridge, J. (1992). Iron and oxygen radicals in brain. *Ann Neurol.* 32, S16-21.

Guéron, M. (1975). Nuclear relaxation in macromolecules by paramagnetic ions: a novel mechanism. *J Magn Reson.* 19, 58-66.

Haacke, E. M., Brown, R. W., Thompson, M. R., Venkatesan, R. (1999). Magnetic resonance imaging: physical principles and sequence design. John Wiley & Sons New York, NY.

Haacke, E. M., Cheng, N. Y. C., House, M. J., Liu, Q., Neelavalli, J., Ogg, R. J., Khan, A., Ayaz, M., Kirsch, W., Obenaus, A. (2005). Imaging iron stores in the brain using magnetic resonance imaging. *Magn Reson Imaging.* 23, 1-25.

Haacke, E. M., Miao, Y., Liu, M., Habib, C. A., Katkuri, Y., Liu, T., Yang, Z., Lang, Z., Hu, J., Wu, J. (2010). Correlation of putative iron content as represented

by changes in R2* and phase with age in deep gray matter of healthy adults. *J Magn Reson Imaging.* 32, 561-76.

Haacke, E. M., Mittal, S., Wu, Z., Neelavalli, J., Cheng, Y. C. N. (2009). Susceptibility-weighted imaging: technical aspects and clinical applications, part 1. *AJNR Am J Neuroradiol.* 30, 19-30.

Haberland, C. (2007). Clinical Neuropathology: Text and Color Atlas. Demos Medical Publishing.

Hallgren, B., Sourander, P. (1958). The effect of age on the non-haemin iron in the human brain. *J Neurochem.* 3, 41-51.

Haque, T. L., Miki, Y., Kanagaki, M., Takahashi, T., Yamamoto, A., Konishi, J., Nozaki, K., Hashimoto, N., Konishi, J. (2003). MR contrast of ferritin and hemosiderin in the brain: comparison among gradient-echo, conventional spin-echo and fast spin-echo sequences. *Eur J Radiol.* 48, 230-6.

Harder, S. L., Hopp, K. M., Ward, H., Neglio, H., Gitlin, J., Kido, D. (2008). Mineralization of the deep gray matter with age: a retrospective review with susceptibility-weighted MR imaging. *AJNR Am J Neuroradiol.* 29, 176-83.

Hardin, J., Rocke, D. M. (2005). The distribution of robust distances. *J Comput Graph Stat.* 14, 928-46.

Hare, D., Ayton, S., Bush, A., Lei, P. (2013). A delicate balance: Iron metabolism and diseases of the brain. *Front Aging Neurosci.* 5, 34.

Harman, D. (1956). Aging: a theory based on free radical and radiation chemistry. *J Gerontol.* 11, 298-300.

Harper, S. (2014). Economic and social implications of aging societies. *Science.* 346, 587-91.

He, X., Yablonskiy, D. A. (2009). Biophysical mechanisms of phase contrast in gradient echo MRI. *Proc Natl Acad Sci U S A.* 106, 13558-63.

Heier, L. A., Bauer, C. J., Schwartz, L., Zimmerman, R. D., Morgello, S., Deck, M. D. (1989). Large Virchow-Robin spaces: MR-clinical correlation. *AJNR Am J Neuroradiol.* 10, 929-36.

Hellier, P. (2003). Consistent intensity correction of MR images. *Proc IEEE ICIP.* 1, 1109-12.

Henkelman, R., Watts, J., Kucharczyk, W. (1991). High signal intensity in MR images of calcified brain tissue. *Radiology.* 179, 199-206.

Heye, A. K., Culling, R. D., Hernández, M. d. C. V., Thrippleton, M. J., Wardlaw, J. M. (2014). Assessment of blood-brain barrier disruption using dynamic contrast-enhanced MRI. A systematic review. *Neuroimage Clin.* 6, 262-74.

Ho, S., Bullitt, E., Gerig, G. (2002). Level-Set Evolution with Region Competition: Automatic 3-D Segmentation of Brain Tumors. *Proc IEEE ICPR.* 1, 532-35.

Hofman, A., Darwish Murad, S., van Duijn, C. M., Franco, O. H., Goedegebure, A., Ikram, M. A., Klaver, C. C. W., Nijsten, T. E. C., Peeters, R. P., Stricker, B. H. C., Tiemeier, H. W., Uitterlinden, A. G., Vernooij, M. W. (2013). The Rotterdam Study: 2014 objectives and design update. *Eur J Epidemiol.* 28, 889-926.

Huijts, M., Duits, A., Staals, J., Kroon, A. A., de Leeuw, P. W., van Oostenbrugge, R. J. (2014). Basal ganglia enlarged perivascular spaces are linked to cognitive function in patients with cerebral small vessel disease. *Curr Neurovasc Res.* 11, 136-41.

Iadecola, C., Nedergaard, M. (2007). Glial regulation of the cerebral microvasculature. *Nature Neurosci.* 10, 1369-76.

Jager, F., Hornegger, J. (2009). Nonrigid registration of joint histograms for intensity standardization in magnetic resonance imaging. *IEEE Trans Med Imaging.* 28, 137-50.

Janaway, B. M., Simpson, J. E., Hoggard, N., Highley, J. R., Forster, G., Drew, D., Gebril, O. H., Matthews, F. E., Brayne, C., Wharton, S. B., Ince, P. G., Function, M. C., Study, A. N. (2014). Brain haemosiderin in older people: pathological evidence for an ischaemic origin of MRI microbleeds. *Neuropathol Appl Neurobiol.* 3, 258-69.

Jasinschi, R., Ekin, A., van Es, A. C., van der Grond, J., van Buchem, M. A., van Muiswinkel, A. (2006). Automatic Detection and Classification of Hypointensity in MR Images of the Brain. *Proc ISMRM.* 2647.

Jenkinson, M., Bannister, P., Brady, M., Smith, S. (2002). Improved optimization for the robust and accurate linear registration and motion correction of brain images. *NeuroImage.* 17, 825-41.

Jensen, J., Chandra, R. (2002). Theory of nonexponential NMR signal decay in liver with iron overload or superparamagnetic iron oxide particles. *Magn Reson Med.* 47, 1131-8.

Jensen, J. H., Tang, H., Tosti, C. L., Swaminathan, S. V., Nunez, A., Hultman, K., Szulc, K. U., Wu, E. X., Kim, D., Sheth, S., others (2010). Separate MRI quantification of dispersed (ferritin-like) and aggregated (hemosiderin-like) storage iron. *Magn Reson Med.* 63, 1201-9.

Jin, N., Guo, Y., Zhang, Z., Zhang, L., Lu, G., Larson, A. (2013). GESFIDE-PROPELLER approach for simultaneous R2 and R2* measurements in the abdomen. *Magn Reson Imaging.* 31, 1760-5.

Keihaninejad, S., Heckemann, R. A., Fagiolo, G., Symms, M. R., Hajnal, J. V., Hammers, A., Alzheimer's Disease Neuroimaging Initiative (2010). A robust method to estimate the intracranial volume across MRI field strengths (1.5T and 3T). *NeuroImage.* 50, 1427-37.

Keller, S. S., Roberts, N. (2009). Measurement of brain volume using MRI: software, techniques, choices and prerequisites. *J Anthropol Sci.* 87, 127-51.

Kim, K. W., MacFall, J. R., Payne, M. E. (2008). Classification of white matter lesions on magnetic resonance imaging in elderly persons. *Biol Psychiatry.* 64, 273-80.

Kiselev, V., Posse, S. (1999). Analytical model of susceptibility-induced MR signal dephasing: effect of diffusion in a microvascular network. *Magn Reson Med.* 41, 499-509.

Koenker, R., Hallock, K. F. (2001). Quantile Regression. *J Econ Perspect.* 15, 143-56.

Krebs, N., Langkammer, C., Goessler, W., Ropele, S., Fazekas, F., Yen, K., Scheurer, E. (2014). Assessment of trace elements in human brain using inductively coupled plasma mass spectrometry. *J Trace Elem Med Biol.* 28, 1-7.

Kruer, M. C., Boddaert, N., Schneider, S. A., Houlden, H., Bhatia, K. P., Gregory, A., Anderson, J. C., Rooney, W. D., Hogarth, P., Hayflick, S. J. (2012). Neuroimaging features of neurodegeneration with brain iron accumulation. *AJNR Am J Neuroradiol.* 33, 407-14.

Kunimatsu, A., Suzuki, Y., Hagiwara, K., Sasaki, H., Mori, H., Katsura, M., Ohtomo, K. (2012). Clinical Value of 3D T 2*-weighted Imaging with Multi-echo Acquisition: Comparison with Conventional 2D T 2*-weighted Imaging and 3D Phase-sensitive MR Imaging. *Magn Reson Med Sci.* 11, 205-11.

Langkammer, C., Krebs, N., Goessler, W., Scheurer, E., Ebner, F., Yen, K., Fazekas, F., Ropele, S. (2010). Quantitative MR imaging of brain iron: a postmortem validation study. *Radiology.* 257, 455-62.

Langkammer, C., Krebs, N., Goessler, W., Scheurer, E., Yen, K., Fazekas, F., Ropele, S. (2012). Susceptibility induced gray-white matter MRI contrast in the human brain. *NeuroImage.* 59, 1413-9.

Langkammer, C., Schweser, F., Krebs, N., Deistung, A., Goessler, W., Scheurer, E., Sommer, K., Reishofer, G., Yen, K., Fazekas, F., others (2012). Quantitative susceptibility mapping (QSM) as a means to measure brain iron? A post mortem validation study. *NeuroImage.* 62, 1593-9.

Latour, L. L., Kang, D.-W., Ezzeddine, M. A., Chalela, J. A., Warach, S. (2004). Early blood-brain barrier disruption in human focal brain ischemia. *Ann Neurol.* 56, 468-77.

Le Bihan, D. (2003). Looking into the functional architecture of the brain with diffusion MRI. *Nat Rev Neurosci.* 4, 469-80.

Le Bihan, D., Turner, R. (1991). Intravoxel incoherent motion imaging using spin echoes. *Magn Reson Med.* 19, 221-7.

Li, T. Q., Takahashi, A. (2004). Quantitative Assessment of Iron Content in the Body Using Fast Mappings of Relaxation Times. *Proc ISMRM.* 508.

Li, W., Langkammer, C., Chou, Y.-H., Petrovic, K., Schmidt, R., Song, A. W., Madden, D. J., Ropele, S., Liu, C. (2015). Association between Increased Magnetic Susceptibility of Deep Gray Matter Nuclei and Decreased Motor Function in Healthy Adults. *NeuroImage.* 105, 45-52.

Li, W., Wu, B., Batrachenko, A., Bancroft-Wu, V., Morey, R. A., Shashi, V., Langkammer, C., De Bellis, M. D., Ropele, S., Song, A. W., Liu, C. (2014). Differential developmental trajectories of magnetic susceptibility in human brain gray and white matter over the lifespan. *Hum Brain Mapp.* 35, 2698-713.

Li, W., Wu, B., Liu, C. (2011). Quantitative susceptibility mapping of human brain reflects spatial variation in tissue composition. *NeuroImage.* 55, 1645-56.

Lockhart, S. N., DeCarli, C. (2014). Structural imaging measures of brain aging. *Neuropsychol Rev.* 24, 271-89.

Lüdeke, K., Röschmann, P., Tischler, R. (1985). Susceptibility artefacts in NMR imaging. *Magn Reson Im.* 3, 329-43.

Ma, J., Wehrli, F. W. (1996). Method for image-based measurement of the reversible and irreversible contribution to the transverse-relaxation rate. *J Magn Reson B.* 111, 61-9.

Maclullich, A. M. J., Wardlaw, J. M., Ferguson, K. J., Starr, J. M., Seckl, J. R., Deary, I. J. (2004). Enlarged perivascular spaces are associated with cognitive function in healthy elderly men. *J Neurol Neurosurg Psychiatry.* 75, 1519-23.

Marinkovic, S. V., Milisavljevic, M. M., Kovacevic, M. S., Stevic, Z. D. (1985). Perforating branches of the middle cerebral artery. Microanatomy and clinical significance of their intracerebral segments. *Stroke.* 16, 1022-9.

Markl, M., Leupold, J. (2012). Gradient echo imaging. *J Magn Reson Imaging.* 35, 1274-89.

Marques, F., Falcao, A. M., Sousa, J. C., Coppola, G., Geschwind, D., Sousa, N., Correia-Neves, M., Palha, J. A. (2009). Altered iron metabolism is part of the choroid plexus response to peripheral inflammation. *Endocrinology.* 150, 2822-8.

Marques, J., Bowtell, R. (2005). Application of a Fourier-based method for rapid calculation of field inhomogeneity due to spatial variation of magnetic susceptibility. *Concept Magn Reson B.* 25, 65-78.

Martínez, J., Montgomery, D. L., Uzal, F. A. (2012). Vascular mineralization in the brain of horses. *J Vet Diagn Invest.* 24, 612-7.

McAuley, G., Schrag, M., Barnes, S., Obenaus, A., Dickson, A., Holshouser, B., Kirsch, W. (2011). Iron quantification of microbleeds in postmortem brain. *Magn Reson Med.* 65, 1592-601.

McAuliffe, M., Lalonde, F., McGarry, D., Gandler, W., Csaky, K., Trus, B. (2001). Medical Image Processing, Analysis and Visualization in clinical research. *Proc IEEE CBMS.* 381-6.

McRobbie, D., Moore, E., Graves, M. (2003). MRI from Picture to Proton. Cambridge Univ Press.

Messroghli, D. R., Radjenovic, A., Kozerke, S., Higgins, D. M., Sivananthan, M. U., Ridgway, J. P. (2004). Modified Look-Locker inversion recovery (MOLLI) for high-resolution T1 mapping of the heart. *Magn Reson Med.* 52, 141-6.

Messroghli, D. R., Rudolph, A., Abdel-Aty, H., Wassmuth, R., Kühne, T., Dietz, R., Schulz-Menger, J. (2010). An open-source software tool for the generation of relaxation time maps in magnetic resonance imaging. *BMC Med Imaging.* 10, 16.

Mills, E., Dong, X., Wang, F., Xu, H. (2010). Mechanisms of brain iron transport: insight into neurodegeneration and CNS disorders. *Future Med Chem.* 2, 51-64.

Milton, W. J., Atlas, S. W., Lexa, F. J., Mozley, P. D., Gur, R. E. (1991). Deep gray matter hypointensity patterns with aging in healthy adults: MR imaging at 1.5 T. *Radiology.* 181, 715-9.

Mittal, S., Wu, Z., Neelavalli, J., Haacke, E. M. (2009). Susceptibility-weighted imaging: technical aspects and clinical applications, part 2. *American Journal of Neuroradiology.* 30, 232.

Mora, F. (2013). Successful brain aging: plasticity, environmental enrichment, and lifestyle. *Dialogues Clin Neurosci.* 15, 45-52.

Moreau, F., Patel, S., Lauzon, M. L., McCreary, C. R., Goyal, M., Frayne, R., Demchuk, A. M., Coutts, S. B., Smith, E. E. (2012). Cavitation after acute symptomatic lacunar stroke depends on time, location, and MRI sequence. *Stroke.* 43, 1837-42.

Morris, C., Candy, J., Oakley, A., Bloxham, C., Edwardson, J. (1992). Histochemical distribution of non-haem iron in the human brain. *Acta Anat (Basel).* 144, 235-57.

Muckenthaler, M. U., Galy, B., Hentze, M. W. (2008). Systemic iron homeostasis and the iron-responsive element/iron-regulatory protein (IRE/IRP) regulatory network. *Annu Rev Nutr.* 28, 197-213.

Müller-Bierl, B. M., Graf, H., Pereira, P. L., Schick, F. (2006). Numerical simulations of intra-voxel dephasing effects and signal voids in gradient echo MR imaging using different sub-grid sizes. *MAGMA.* 19, 88-95.

Nie, G., Sheftel, A. D., Kim, S. F., Ponka, P. (2005). Overexpression of mitochondrial ferritin causes cytosolic iron depletion and changes cellular iron homeostasis. *Blood.* 105, 2161-7.

Norrving, B. (2008). Lacunar infarcts: no black holes in the brain are benign. *Pract Neurol.* 8, 222-8.

ONS (2014). Population Ageing in the United Kingdom, its Constituent Countries and the European Union. *http://www.ons.gov.uk/ons/dcp171776_258607.pdf* Last checked: 15 Dec 2014.

Ogg, R. J., Steen, R. G. (1998). Age-related changes in brain T1 are correlated with iron concentration. *Magn Reson Med.* 40, 749-53.

Okuchi, S., Okada, T., Ihara, M., Gotoh, K., Kido, A., Fujimoto, K., Yamamoto, A., Kanagaki, M., Tanaka, S., Takahashi, R., Togashi, K. (2013). Visualization of Lenticulostriate Arteries by Flow-Sensitive Black-Blood MR Angiography on a 1.5T MRI System: A Comparative Study between Subjects with and without Stroke. *AJNR Am J Neuroradiol.* 34, 780-4.

Pantoni, L. (2010). Cerebral small vessel disease: from pathogenesis and clinical characteristics to therapeutic challenges. *Lancet Neurol.* 9, 689-701.

Parsey, R. V., Krishnan, K. R. (1997). A new MRI ratio method for in-vivo estimation of signal hypointensity in aging and Alzheimer's disease. *Prog Neuro-Psychoph.* 21, 1257-67.

Patenaude, B., Smith, S. M., Kennedy, D. N., Jenkinson, M. (2011). A Bayesian Model of Shape and Appearance for Subcortical Brain. *NeuroImage.* 56, 907-22.

Pell, G. S., Briellmann, R. S., Waites, A. B., Abbott, D. F., Lewis, D. P., Jackson, G. D. (2006). Optimized clinical T2 relaxometry with a standard CPMG sequence. *J Magn Reson Im.* 23, 248-52.

Penke, L., Valdés Hernandéz, M. C., Maniega, S. M., Gow, A. J., Murray, C., Starr, J. M., Bastin, M. E., Deary, I. J., Wardlaw, J. M. (2012). Brain iron deposits are associated with general cognitive ability and cognitive aging. *Neurobiol Aging.* 33, 510-17.

Pintaske, J., Müller-Bierl, B., Schick, F. (2006). Effect of spatial distribution of magnetic dipoles on Lamor frequency distribution and MR Signal decay--a numerical approach under static dephasing conditions. *MAGMA.* 19, 46-53.

Pintaske, J., Müller-Bierl, B., Schick, F. (2006). Geometry and extension of signal voids in MR images induced by aggregations of magnetically labelled cells. *Phys Med Biol.* 51, 4707-18.

Polla, A. S., Polla, L. L., Polla, B. S. (2003). Iron as the malignant spirit in successful ageing. *Ageing Res Rev.* 2, 25-37.

Popescu, B. O., Toescu, E. C., Popescu, L. M., Bajenaru, O., Muresanu, D. F., Schultzberg, M., Bogdanovic, N. (2009). Blood-brain barrier alterations in ageing and dementia. *J Neurol Sci.* 283, 99-106.

Potter, G. M., Doubal, F. N., Jackson, C. A., Chappell, F. M., Sudlow, C. L., Dennis, M. S., Wardlaw, J. M. (2010). Counting cavitating lacunes underestimates the burden of lacunar infarction. *Stroke.* 41, 267-72.

Preibisch, C., Deichmann, R. (2009). Influence of RF spoiling on the stability and accuracy of T1 mapping based on spoiled FLASH with varying flip angles. *Magn Reson Med.* 61, 125-35.

Pérez, V. I., Bokov, A., Van Remmen, H., Mele, J., Ran, Q., Ikeno, Y., Richardson, A. (2009). Is the oxidative stress theory of aging dead? *Biochim Biophys Acta.* 1790, 1005-14.

Raz, N. Aging of the brain and its impact on cognitive performance: Integration of structural and functional findings. In: Craik, F., TA., S. (2007). The Handbook of Aging and Cognition. Lawrence Erlbaum Associates Inc.

Raz, N., Rodrigue, K. M., Haacke, E. M. (2007). Brain aging and its modifiers: insights from in vivo neuromorphometry and susceptibility weighted imaging. *Ann N Y Acad Sci.* 1097, 84-93.

Rechel, B., Grundy, E., Robine, J.-M., Cylus, J., Mackenbach, J. P., Knai, C., McKee, M. (2013). Ageing in the European Union. *Lancet.* 381, 1312-22.

Reichenbach, J., Venkatesan, R., Schillinger, D., Kido, D., Haacke, E. (1997). Small vessels in the human brain: MR venography with deoxyhemoglobin as an intrinsic contrast agent. *Radiology.* 204, 272.

Reichenbach, J. R., Haacke, E. M. (2001). High-resolution BOLD venographic imaging: a window into brain function. *NMR Biomed.* 14, 453-67.

Rexilius, J., Peitgen, H. O. (2008). Evaluation of accuracy in partial volume analysis of small objects. *Proc SPIE Medical Imaging: Image Processing.* 6914, 169.

Rodrigue, K. M., Daugherty, A. M., Haacke, E. M., Raz, N. (2013). The Role of Hippocampal Iron Concentration and Hippocampal Volume in Age-Related Differences in Memory. *Cereb Cortex.* 23, 1533-41.

Rohrer, M., Bauer, H., Mintorovitch, J., Requardt, M., Weinmann, H. J. (2005). Comparison of magnetic properties of MRI contrast media solutions at different magnetic field strengths. *Investigative radiology.* 40, 715.

Ropele, S., Wattjes, M. P., Langkammer, C., Kilsdonk, I. D., de Graaf, W. L., Frederiksen, J. L., Fuglø, D., Yiannakas, M., Wheeler-Kingshott, C. A. M., Enzinger, C., Rocca, M. A., Sprenger, T., Amman, M., Kappos, L., Filippi, M., Rovira, A., Ciccarelli, O., Barkhof, F., Fazekas, F. (2013). Multicenter R2* mapping in the healthy brain. *Magn Reson Med.* in press, doi: 10.1002/mrm.24772.

Ropele, S., de Graaf, W., Khalil, M., Wattjes, M. P., Langkammer, C., Rocca, M. A., Rovira, A., Palace, J., Barkhof, F., Filippi, M., others (2011). MRI assessment of iron deposition in multiple sclerosis. *J Mag Reson Im.* 34, 13-21.

Rouault, T. A. (2013). Iron metabolism in the CNS: implications for neurodegenerative diseases. *Nat Rev Neurosci.* 14, 551-64.

Rouault, T. A. (2006). The role of iron regulatory proteins in mammalian iron homeostasis and disease. *Nat Chem Biol.* 2, 406-14.

Rouault, T. A., Cooperman, S. (2006). Brain iron metabolism. *Semin Pediatr Neurol.* 13, 142-8.

Rouault, T. A., Zhang, D.-L., Jeong, S. Y. (2009). Brain iron homeostasis, the choroid plexus, and localization of iron transport proteins. *Metab Brain Dis.* 24, 673-84.

Rousseeuw, P. J. (1984). Least median of squares regression. *J Am Statist Assoc.* 79, 871-80.

Rousseeuw, P. J., Driessen, K. V. (1999). A fast algorithm for the minimum covariance determinant estimator. *Technometrics.* 41, 212-23.

Rousseeuw, P. J., Van Zomeren, B. C. (1990). Unmasking multivariate outliers and leverage points. *J Am Statist Assoc.* 85, 633-39.

Rowe, J. W., Kahn, R. L. (1998). Successful aging. *Aging (Milano).* 10, 142-4.

Rudko, D. A., Klassen, L. M., de Chickera, S. N., Gati, J. S., Dekaban, G. A., Menon, R. S. (2014). Origins of R2* orientation dependence in gray and white matter. *Proc Natl Acad Sci U S A.* 111, E159-67.

Runge, V. M., Nitz, W., Schmeets, S. H., Faulkner, W. H., Desai, N. K. (2005). The physics of clinical MR taught through images. Thieme Medical Publishers New York.

Russell, K. H., Bradley, J. R. (2007). Intermediate Physics for Medicine and Biology, 4th Ed. Springer.

Salmon, A. B., Richardson, A., Pérez, V. I. (2010). Update on the oxidative stress theory of aging: does oxidative stress play a role in aging or healthy aging? *Free Radic Biol Med.* 48, 642-55.

Salomir, R., de Senneville, B. D., Moonen, C. T. W. (2003). A fast calculation method for magnetic field inhomogeneity due to an arbitrary distribution of bulk susceptibility. *Concept Magn Reson B.* 19, 26-34.

Schenck, J. F. (2003). Magnetic resonance imaging of brain iron. *J Neurol Sci.* 207, 99-102.

Schenck, J. F., Zimmerman, E. A. (2004). High-field magnetic resonance imaging of brain iron: birth of a biomarker? *NMR Biomed.* 17, 433-45.

Schenker, C., Meier, D., Wichmann, W., Boesiger, P., Valavanis, A. (1993). Age distribution and iron dependency of the T2 relaxation time in the globus pallidus and putamen. *Neuroradiology.* 35, 119-24.

Schmidt, R., Fazekas, F., Kapeller, P., Schmidt, H., Hartung, H. P. (1999). MRI white matter hyperintensities: three-year follow-up of the Austrian Stroke Prevention Study. *Neurology.* 53, 132-9.

Schmidt, R., Lechner, H., Fazekas, F., Niederkorn, K., Reinhart, B., Grieshofer, P., Horner, S., Offenbacher, H., Koch, M., Eber, B. (1994). Assessment of cerebrovascular risk profiles in healthy persons: definition of research goals and the Austrian Stroke Prevention Study (ASPS). *Neuroepidemiology.* 13, 308-13.

Schmidt, R., Ropele, S., Enzinger, C., Petrovic, K., Smith, S., Schmidt, H., Matthews, P. M., Fazekas, F. (2005). White matter lesion progression, brain atrophy, and cognitive decline: the Austrian stroke prevention study. *Ann Neurol.* 58, 610-6.

Schrag, M., McAuley, G., Pomakian, J., Jiffry, A., Tung, S., Mueller, C., Vinters, H. V., Haacke, E. M., Holshouser, B., Kido, D., others (2010). Correlation of hypointensities in susceptibility-weighted images to tissue histology in dementia patients with cerebral amyloid angiopathy: a postmortem MRI study. *Acta Neuropathol.* 119, 291-302.

Schweser, F., Deistung, A., Lehr, B. W., Reichenbach, J. R. (2010). Quantitative imaging of intrinsic magnetic tissue properties using MRI signal phase: An approach to in vivo brain iron metabolism? *Neuroimage.* 54, 2789-807.

Sedlacik, J., Boelmans, K., Löbel, U., Holst, B., Siemonsen, S., Fiehler, J. (2014). Reversible, irreversible and effective transverse relaxation rates in normal aging brain at 3T. *NeuroImage.* 84, 1032-41.

Seghier, M. L., Ramlackhansingh, A., Crinion, J., Leff, A. P., Price, C. J. (2008). Lesion identification using unified segmentation-normalisation models and fuzzy clustering. *Neuroimage.* 41, 1253-66.

Seo, S. W., Kang, C.-K., Kim, S. H., Yoon, D. S., Liao, W., Wörz, S., Rohr, K., Kim, Y.-B., Na, D. L., Cho, Z.-H. (2012). Measurements of lenticulostriate arteries using 7T MRI: new imaging markers for subcortical vascular dementia. *J Neurol Sci.* 322, 200-5.

Sharp, J. C., Saunders, J. K. (1995). Calculation of the static magnetic field in nonuniform media. *J Magn Reson B.* 108, 58-66.

Shattuck, D. W., Prasad, G., Mirza, M., Narr, K. L., Toga, A. W. (2009). Online resource for validation of brain segmentation methods. *NeuroImage.* 45, 431-39.

Shimazaki, H., Shinomoto, S. (2007). A method for selecting the bin size of a time histogram. *Neural Comput.* 19, 1503-27.

Shmueli, K., de Zwart, J. A., van Gelderen, P., Li, T. Q., Dodd, S. J., Duyn, J. H. (2009). Magnetic susceptibility mapping of brain tissue in vivo using MRI phase data. *Mag Reson Med.* 62, 1510-22.

Silvester, P. P., Ferrari, R. L. (1996). Finite elements for electrical engineers. Cambridge university press.

Slager, C. T., Wagner, J. A. (1956). The Incidence, Composition, and Pathological Significance of Intracerebral Vascular Deposits in the Basal Ganglia. *J Neuropathol Exp Neurol.* 15, 417-31.

Smith, S. M. (2002). Fast robust automated brain extraction. *Hum Brain Mapp.* 17, 143-55.

Sohal, R. S., Weindruch, R. (1996). Oxidative stress, caloric restriction, and aging. *Science.* 273, 59-63.

Spatz, H. (1922). Über den eisennachweis im gehirn, besonders in zentren des extrapyramidal-motorischen systems. I. Teil. *Z Gesamte Neurol Psy.* 77, 261-390.

Sprawls, P. (2000). Magnetic Resonance Imaging: Principles, Methods, and Techniques. Madison, Wis: Medical Physics Publishing.

St Pierre, T. G., Clark, P. R., Chua-anusorn, W., Fleming, A. J., Jeffrey, G. P., Olynyk, J. K., Pootrakul, P., Robins, E., Lindeman, R. (2005). Noninvasive measurement and imaging of liver iron concentrations using proton magnetic resonance. *Blood.* 105, 855-61.

Stewart, V. L., Herling, P., Dalinka, M. K. (1983). Calcification in soft tissues. *JAMA.* 250, 78-81.

Stone, M. (1961). The opinion pool. *Ann Math Stat.* 32, 1339-42.

Sun, H., Walsh, A. J., Lebel, R. M., Blevins, G., Catz, I., Lu, J.-Q., Johnson, E. S., Emery, D. J., Warren, K. G., Wilman, A. H. (2015). Validation of quantitative susceptibility mapping with Perls' iron staining for subcortical gray matter. *Neuroimage.* 105, 486-92.

Thompson, C. S., Hakim, A. M. (2009). Living beyond our physiological means: small vessel disease of the brain is an expression of a systemic failure in arteriolar function: a unifying hypothesis. *Stroke.* 40, e322-30.

Tofts, P. (2004). Quantitative MRI of the brain: measuring changes caused by disease. John Wiley & Sons, Ltd.

Tsushima, Y., Endo, K. (2006). Hypointensities in the Brain on T2*-Weighted Gradient-Echo Magnetic Resonance Imaging. *Curr Probl Diagn Radiol.* 35, 140-50.

Tustison, N. J., Avants, B. B., Cook, P. A., Zheng, Y., Egan, A., Yushkevich, P. A., Gee, J. C. (2010). N4ITK: Improved N3 bias correction. *IEEE Trans Med Imaging.* 29, 1310-20.

UN (2014). World Population Prospects: The 2012 Revision. *http://esa.un.org/unpd/wpp/index.htm* Last checked: 15 Dec 2014.

Valdés Hernandéz, M. C., Maconick, L. C., Tan, E. J. M., Wardlaw, J. M. (2012). Identification of mineral deposits in the brain on radiological images. *Eur Radiol.* 22, 2371-81.

Valdés Hernández, M. C., Ferguson, K., Chappell, F., Wardlaw, J. M. (2010). New multispectral MRI data fusion technique for white matter lesion segmentation: method and comparison with thresholding in FLAIR images. *Eur Radiol.* 20, 1684-91.

Valdés Hernández, M. C., Glatz, A., Kiker, A. J., Dickie, D. A., Aribisala, B. S., Royle, N. A., Muñoz Maniega, S., Bastin, M. E., Deary, I. J., Wardlaw, J. M. (2014). Differentiation of calcified regions and iron deposits in the ageing brain on conventional structural MR images. *J Magn Reson Imaging.* 40, 324-33.

Valdés Hernández, M. C., Jeong, T. H., Murray, C., Bastin, M. E., Chappell, F. M., Deary, I. J., Wardlaw, J. M. (2011). Reliability of two techniques for assessing cerebral iron deposits from structural MRI. *J Magn Reson Imaging.* 33, 54-61.

Valdés Hernández, M. C., Maconick, L. C., Tan, E. M. J., Wardlaw, J. M. (2012). Identification of mineral deposits in the brain on radiological images: a systematic review. *Eur Radiol.* 22, 2371-81.

Vanderlinde, J. (2004). Classical electromagnetic theory. Springer Netherlands.

Venkatesan, R., Haacke, E. M. (1997). Role of high resolution in magnetic resonance (MR) imaging: Applications to MR angiography, intracranial T1-weighted imaging, and image interpolation. *Int J Imag Syst Tech.* 8, 529-43.

Verboven, S., Hubert, M. (2005). LIBRA: a Matlab library for robust analysis. *Chemometr Intell Lab.* 75, 127-36.

Vovk, U., Pernus, F., Likar, B. (2007). A review of methods for correction of intensity inhomogeneity in MRI. *IEEE Trans Med Imaging.* 26, 405-21.

Vymazal, J., Righini, A., Brooks, R. A., Canesi, M., Mariani, C., Leonardi, M., Pezzoli, G. (1999). T1 and T2 in the Brain of Healthy Subjects, Patients with Parkinson Disease, and Patients with Multiple System Atrophy: Relation to Iron Content. *Radiology.* 211, 489-95.

Vymazal, J., Urgosik, D., Bulte, J., others (2000). Differentiation between hemosiderin-and ferritin-bound brain iron using nuclear magnetic resonance and magnetic resonance imaging. *Cell Mol Biol (Noisy-le-grand).* 46, 835-42.

Vymazal, J., Zak, O., Bulte, J. W., Aisen, P., Brooks, R. A. (1996). T1 and T2 of ferritin solutions: effect of loading factor. *Magn Reson Med.* 36, 61-5.

WHO/Europe (2012). Healthy Ageing. *http://www.euro.who.int/en/health-topics/Life-stages/healthy-ageing* Last checked: 15 Dec 2014.

WHO/US-NIA (2011). Global health and aging. *http://www.who.int/ageing/publications/global_health/en/* Last checked: 15 Dec 2014.

Wadell, H. (1932). Volume, shape, and roundness of rock particles. *J Geol.* 40, 443-51.

Wadsworth, P. F., Jones, H. B., Cavanagh, J. B. (1995). The topography, structure and incidence of mineralized bodies in the basal ganglia of the brain of cynomolgus monkeys (Macaca fascicularis). *Lab Anim.* 29, 276-81.

Wang, J., Mao, W., Qiu, M., Smith, M. B., Constable, R. T. (2006). Factors influencing flip angle mapping in MRI: RF pulse shape, slice-select gradients, off-resonance excitation, and B0 inhomogeneities. *Magn Reson Med.* 56, 463-8.

Ward, R. J., Zucca, F. A., Duyn, J. H., Crichton, R. R., Zecca, L. (2014). The role of iron in brain ageing and neurodegenerative disorders. *Lancet Neurol.* 13, 1045-60.

Wardlaw, J. M., Bastin, M. E., Valdés Hernández, M. C., Maniega, S. M., Royle, N. A., Morris, Z., Clayden, J. D., Sandeman, E. M., Eadie, E., Murray, C., Starr, J. M., Deary, I. J. (2011). Brain aging, cognition in youth and old age and vascular disease in the Lothian Birth Cohort 1936: rationale, design and methodology of the imaging protocol. *Int J Stroke.* 6, 547-59.

Wardlaw, J. M., Smith, E. E., Biessels, G. J., Cordonnier, C., Fazekas, F., Frayne, R., Lindley, R. I., O'Brien, J. T., Barkhof, F., Benavente, O. R., Black, S. E., Brayne, C., Breteler, M., Chabriat, H., Decarli, C., de Leeuw, F.-E., Doubal, F., Duering, M., Fox, N. C., Greenberg, S., Hachinski, V., Kilimann, I., Mok, V., Oostenbrugge, R. v., Pantoni, L., Speck, O., Stephan, B. C. M., Teipel, S., Viswanathan, A., Werring, D., Chen, C., Smith, C., van Buchem, M., Norrving, B., Gorelick, P. B., Dichgans, M., STandards for ReportIng Vascular changes on nEuroimaging (STRIVE v1) (2013). Neuroimaging standards for research into small vessel disease and its contribution to ageing and neurodegeneration. *Lancet Neurol.* 12, 822-38.

Wehrli, F. W. (2013). Magnetic resonance of calcified tissues. *J Magn Reson.* 229, 35-48.

Weiskopf, N., Suckling, J., Williams, G., Correia, M. M., Inkster, B., Tait, R., Ooi, C., Bullmore, E. T., Lutti, A. (2013). Quantitative multi-parameter mapping of R1, PD*, MT and R2* at 3T: a multi-center validation. *Front Neurosci.* 7, doi: 10.3389/fnins.2013.00095.

Weisskoff, R. M., Zuo, C. S., Boxerman, J. L., Rosen, B. R. (1994). Microscopic susceptibility variation and transverse relaxation: theory and experiment. *Magn Reson Med.* 31, 601-10.

Witoszynskyj, S., Rauscher, A., Reichenbach, J. R., Barth, M. (2009). Phase unwrapping of MR images using [Phi] UN-A fast and robust region growing algorithm. *Med Image Anal.* 13, 257-68.

Won, S. M., Lee, J. H., Park, U. J., Gwag, J., Gwag, B. J., Lee, Y. B. (2011). Iron mediates endothelial cell damage and blood-brain barrier opening in the hippocampus after transient forebrain ischemia in rats. *Exp Mol Med.* 43, 121-8.

Wycliffe, N. D., Choe, J., Holshouser, B., Oyoyo, U. E., Haacke, E. M., Kido, D. K. (2004). Reliability in detection of hemorrhage in acute stroke by a new three-dimensional gradient recalled echo susceptibility-weighted imaging technique compared to computed tomography: A retrospective study. *J Magn Reson Im.* 20, 372-7.

Xie, M., Olderøy, M. Ø., Andreassen, J. P., Selbach, S. M., Strand, B. L., Sikorski, P. (2010). Alginate-controlled formation of nanoscale calcium carbonate and hydroxyapatite mineral phase within hydrogel networks. *Acta Biomater.* 6, 3665-75.

Yablonskiy, D. A. (1998). Quantitation of intrinsic magnetic susceptibility-related effects in a tissue matrix. Phantom study. *Magn Reson Med.* 39, 417-28.

Yablonskiy, D. A., Haacke, E. M. (1994). Theory of NMR signal behavior in magnetically inhomogeneous tissues: the static dephasing regime. *Magn Reson Med.* 32, 749-63.

Yamada, N., Imakita, S., Sakuma, T., Takamiya, M. (1996). Intracranial calcification on gradient-echo phase image: depiction of diamagnetic susceptibility. *Radiology.* 198, 171-8.

Yoshioka, H., Wakai, T., Kinouchi, H., Chan, P. H. Oxidative Stress in White Matter Injury. In: Baltan, S., Carmichael, S. T., Matute, C., Xi, G., Zhang, J. H. (2014). White Matter Injury in Stroke and CNS Disease. Springer.

Yung, K.-T. (2003). Empirical models of transverse relaxation for spherical magnetic perturbers. *Magn Reson Im.* 21, 451-63.

Zecca, L., Youdim, M. B. H., Riederer, P., Connor, J. R., Crichton, R. R. (2004). Iron, brain ageing and neurodegenerative disorders. *Nat Rev Neurosci.* 5, 863-73.

Zhang, Y., Brady, M., Smith, S. (2001). Segmentation of brain MR images through a hidden Markov random field model and the expectation-maximization algorithm. *IEEE Trans Med Imaging.* 20, 45-57.

Zheng, J. (2013). Assessment of myocardial oxygenation with MRI. *Quant Imaging Med Surg.* 3, 67-72.

Zheng, W., Aschner, M., Ghersi-Egea, J.-F. (2003). Brain barrier systems: a new frontier in metal neurotoxicological research. *Toxicol Appl Pharmacol.* 192, 1-11.

Zheng, W., Nichol, H., Liu, S., Cheng, Y.-C. N., Haacke, E. M. (2013). Measuring iron in the brain using quantitative susceptibility mapping and X-ray fluorescence imaging. *NeuroImage.* 78, 68-74.

Zhu, Y.-C., Tzourio, C., Soumaré, A., Mazoyer, B., Dufouil, C., Chabriat, H. (2010). Severity of dilated Virchow-Robin spaces is associated with age, blood pressure, and MRI markers of small vessel disease: a population-based study. *Stroke.* 41, 2483-90.

de Pasquale, F., Cherubini, A., Péran, P., Caltagirone, C., Sabatini, U. (2013). Influence of white matter fiber orientation on R2* revealed by MRI segmentation. *J Magn Reson Imaging.* 37, 85-91.

van Es, A. C. G. M., van der Grond, J., de Craen, A. J. M., Admiraal-Behloul, F., Blauw, G. J., van Buchem, M. A. (2008). Caudate nucleus hypointensity in the elderly is associated with markers of neurodegeneration on MRI. *Neurobiol Aging*. 29, 1839-46.

Appendix A Introduction to Magnetic Resonance Imaging

A.1. The physics of MRI

A more detailed introduction to the physics of MRI can be found, for example, in Russell and Bradley (2007).

A.1.1. Nuclear magnetic moment

Similarly as electrons, the nuclei of atoms are associated with a nuclear angular momentum, which is commonly denoted by the symbol $\boldsymbol{I}$. Quantum mechanics demonstrates that the magnitude of the nuclear spin angular momentum is $|\boldsymbol{I}| = \hbar\sqrt{i(i+1)}$, where $i \in \{1/2, 1, 3/2, ...\}$ is the spin quantum number of a nucleus and $\hbar$ is the reduced Planck's constant. This spin quantum number i denotes an important quantity of an atom since it determines the number of states of a nucleus and hence shows that an atomic nucleus possesses discrete states. In case of atoms the spin quantum number can be determined from the number of unpaired protons or neutrons. An atom with even number of protons and neutrons has no nuclear spin. Nuclear particles with a spin angular momentum also possesses a magnetic moment

$$\boldsymbol{\mu} = g\frac{\mu_N}{\hbar}\boldsymbol{I}, \qquad \text{A-1}$$

where g is the g-factor and μ_N is the nuclear magneton. This equation shows that the nuclear magnetic moment is perfectly aligned with the nuclear angular momentum.

A.1.2. Nuclear spin polarization

A strong external magnetic field $\boldsymbol{B_0}$ interacts with the nuclear magnetic moment $\boldsymbol{\mu}$ and polarizes the nuclei of a sample. Although the nuclear magnetic moment $\boldsymbol{\mu}$ is a three-dimensional vector the uncertainty principle states that only one of these vector components can be measured in an experiment. This observable vector component is denoted $\mu_z = g\mu_N i_z$ with $i_z \epsilon \{-i, -i+1, \dots, i\}$, which is the projection of $\boldsymbol{\mu}$ on the z-axis aligned with the main direction of the external magnetic field.

A proton, for example, has a spin quantum number of $i = 1/2$ and hence two observable nuclear magnetic moments, a so-called 'up' and a 'down' magnetic moment since $\mu_z = \pm g\mu_N/2$. These observable nuclear magnetic moments $\boldsymbol{\mu}$,

which are not perfectly aligned with the external magnetic field since $|\boldsymbol{\mu}| \neq \mu_z$, also correspond to the minimum and maximum energy of a proton. In thermodynamic equilibrium proton energies of a sample follow a Boltzmann distribution and the number of protons with an 'up' and 'down' magnetic moment, i.e. the nuclear spin excess, at 37 °C caused by an external magnetic field of 1 T is 3.29 ppm of the total number of protons. This shows that the proton spin polarization enhances the external magnetic field by a small amount, which can be measured.

A.1.3. Nuclear spin precession

A homogenous magnetic field $\boldsymbol{B_0} = B_0\boldsymbol{e_z}$ causes an angular momentum $\boldsymbol{D_\mu} = \boldsymbol{\mu}\times\boldsymbol{B_0}$ on the nuclei due to their nuclear magnetic moment $\boldsymbol{\mu}$, and hence aligns the magnetic moments of the nuclei in direction of the external magnetic field $\boldsymbol{e_z}$. As the nuclear magnetic moments never aligns perfectly along the field $\boldsymbol{B_0}$ since $|\boldsymbol{\mu}| \neq \mu_z$ a residual angular momentum remains and causes a rotational motion of the magnetic moment μ, which is called Larmor precession. It can be shown that the Larmor precession frequency ω_0 is proportional to B_0 according to

$$\omega_0 = \gamma B_0, \qquad \text{A-2}$$

where γ is the gyromagnetic ratio. This ratio is specific for atomic nuclei, and in case of protons it is $\gamma/2\pi = 42.576 MHz/T$.

A.1.4. Nuclear spin excitation and relaxation

To simplify further calculations, nuclear spins that experience the same magnetic field B_0 are typically combined and treated as a unit, a so-called spin packet or isochromat. A spin packet is associated with a magnetization vector $\boldsymbol{M}$, which represents the vector sum of all nuclear magnetic moments $\boldsymbol{\mu}$ from individual nuclei per volume. This magnetization vector is oriented perfectly parallel to the external magnetic field $\boldsymbol{B_0}$ unlike the nuclear magnetic moments from individual nuclei. In case of protons the magnitude of the magnetization vector is proportional to the excess amount of protons in the 'up' state per volume.

Nuclear spin excitation occurs if an additional external radio-frequency (RF) field $\boldsymbol{B_1}$ that is tuned to the Larmor frequency interacts with the magnetic moment of polarized nuclei $\boldsymbol{\mu}$. This RF field exerts an angular momentum $\boldsymbol{M}\times\gamma\boldsymbol{B_1}$ on the bulk magnetization, which can flip it completely into the plane perpendicular to the

direction of the main magnetic field. The calculation of this angular momentum can be simplified by transforming the latter equation into a coordinate system that rotates with the Larmor frequency ω_0, i.e. the rotating frame, where the magnetization vector is denoted $\boldsymbol{M}' = \left(M'_x, M'_y, M'_z\right)^T$. Nuclear relaxation occurs after an external RF field is turned off, which causes the excited atomic nuclei to return to their initial equilibrium state. Formally, this is described by the Bloch equations

$$\begin{aligned} \frac{dM'_x}{dt} &= -R2M'_x \\ \frac{dM'_y}{dt} &= -R2M'_y + \gamma B_1 M'_z \quad , \\ \frac{dM'_z}{dt} &= -\gamma B_1 M'_z - R1\left(M_z - M_{z,0}\right) \end{aligned} \qquad \text{A-3}$$

where R1 (=1/T1) and R2 (=1/T2) are the spin-lattice and spin-spin relaxation rates and $M_{z,0}$ is the initial magnetization in thermodynamic equilibrium. In case of nuclear relaxation after an excitation pulse B_1 the solutions of these equations are

$$\begin{aligned} M'_{xy} &= M'_{xy,0} e^{-R2t} \\ M'_z &= M_{z,0}(1 - e^{-R1t})' \end{aligned} \qquad \text{A-4}$$

which show that after removing the RF field both the transverse as well as the longitudinal magnetizations decay mono-exponentially with the R1 and R2 relaxation rates as also illustrated in Figure A-1.

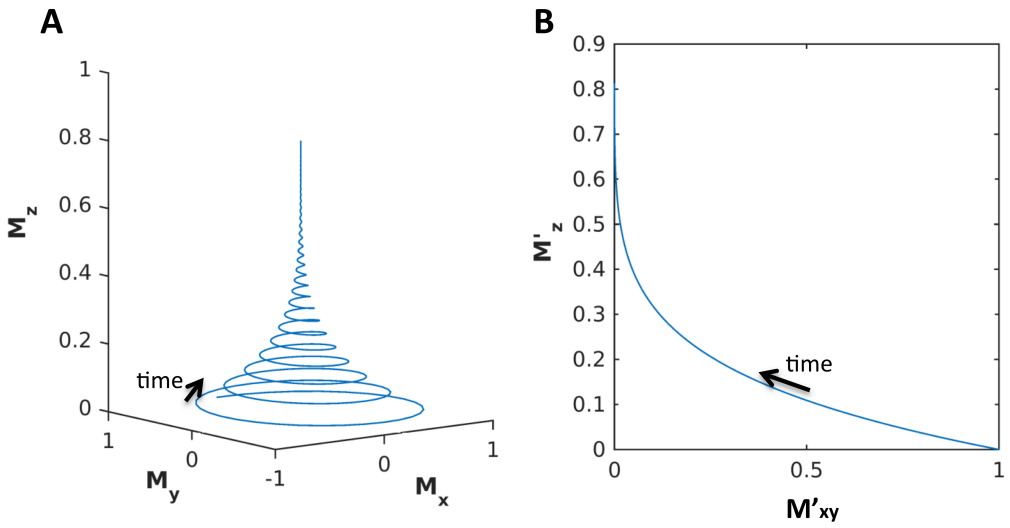

Figure A-1: Magnetic resonance relaxation in the fixed and rotating coordinate system. The solutions of the Block equations (Equation **A-3**) after excitation of the magnetization vector with a RF pulse were plotted in the fixed coordinate system (**A**) and a coordinate system that rotates with the Larmor frequency (**B**). The plots show that over time the magnetization vector aligns itself parallel to the z-axis, the direction of the external magnetic field.

A.2. Principles of MRI signal formation

More detailed information about the MRI signal formation can be found, for example, in Haacke *et al.* (1999) and McRobbie *et al.* (2003).

A.2.1. Components of a clinical MRI scanner

An MRI typically consists of a cylindrical, superconducting coil generating a very homogenous magnetic field B_0 that is typically oriented along the main axis of a subject. Gradient coils generate magnetic gradient fields for selecting which regions of the body should be excited by a RF field. This RF field is emitted by an RF coil or coil array, which is placed around the head of a subject in case of neurological applications. This RF coil array typically emits or receives a RF field tuned to the Larmor frequency of water protons ^{1}H since approximately 65 % of the human body consists of water.

A.2.2. Free induction decay (FID)

The free induction decay (FID) is observed after exciting water protons of a sample volume V with a RF pulse oscillating with the proton Larmor frequency ω_0, which rotates the magnetization $\boldsymbol{M} = \boldsymbol{M}(\boldsymbol{r}, t)$ into the transverse plane. Immediately after this so-called 90° RF pulse the magnetization continues precessing with the proton Larmor frequency ω_0 around the static field B_0 (Section A.1.4). Faraday's law states that a rotating magnetization induces an electromotoric force in a static receiver coil

$$\mathcal{E} = -\frac{d}{dt}\int_V \boldsymbol{M}(\boldsymbol{r}, t)\boldsymbol{B_1}(\boldsymbol{r})dV, \qquad \text{A-5}$$

where $\boldsymbol{B_1} = \boldsymbol{B_1}(\boldsymbol{r})$ denotes the receiver coil sensitivity field. After removing the Larmor frequency component ω_0 of the received proton RF signal with a quadrature demodulator the demodulated FID signal can be described in complex notation since only the transverse components of $\boldsymbol{M}, \boldsymbol{B_1}$ contribute to this signal. The FID signal is

$$s(t) \propto \omega_0 \int_V \underline{M_{xy}}(r, t)\left(\underline{B_{1,xy}}(r)\right)^* , \qquad \text{A-6}$$

where

$$\underline{M_{xy}}(\boldsymbol{r}, t) = \underline{M_{xy}}(\boldsymbol{r}, 0)\exp\left(-R2^*(\boldsymbol{r})t + i2\pi\Delta f(\boldsymbol{r})t\right), \qquad \text{A-7}$$

is the the complex magnetization and $\underline{B_{1,xy}}(\boldsymbol{r})$ the complex coil sensitivity.

Notably, Equation A-7 shows that the magnitude of the FID signal decays with the effective transverse relaxation rate R2* and the phase of the FID signal changes linearly with the Larmor frequency shift Δf. In a perfectly homogenous main magnetic field the effective transverse relaxation rate is equal to the transverse relaxation rate R2* = R2 and the Larmor frequency shift is $\Delta f = 0Hz$. However, typically the effective relaxation rate R2* > R2 and the Larmor frequency shift $\Delta f \neq 0Hz$ since the main magnetic field always exhibits either local or global field inhomogeneities.

A.2.3. Spin-echo

After excitation of the proton spins of a volume with a 90° RF pulse all proton spins initially precess with the Larmor frequency. However, over time the spins loose their coherence due to spin-spin interaction, which causes the transverse component of the magnetization, and hence the received signal to decay with R2. This dephasing is accelerated by local and global main field inhomogeneities, which causes a more rapid decay of the received signal with the relaxation rate R2* > R2. This dephasing of the proton spins can partly be reversed by applying a 180° RF field pulse. After this 180° RF pulse the proton spins start rephasing and partially regain their coherence, which causes another signal maximum at the receiver

$$s(t) \propto \exp(-R2TE) \qquad \text{A-8}$$

after the echo time TE, which is called spin-echo. Notably, the spin echo signal depends on R2 and not R2* unlike the FID signal.

A.2.4. Gradient-echo

In a gradient-echo experiment the spins are exited with only a single RF pulse that flips the magnetisation vector by a flip-angle α, which is typically much smaller than 90°. After the initial dephasing of the proton spins of a voxel a phase-reversal pulse is applied that rephases the spins similar to the 180° pulse of a spin-echo sequence. This then generates a gradient-echo signal, whose signal maximum is determined by the R2* rate of a tissue

$$s(t) \propto \exp(-R2^{*}TE). \qquad \text{A-9}$$

As reviewed by Markl and Leupold (2012), gradient-echo sequences that are commonly available on conventional MRI scanners can be classed into slow (TR >> 1/R2) and fast sequences (TR ~ 1/R2), where TR is the repetition time of the sequence. The fast sequences can be further sub classified in unbalanced gradient-echo sequences (e.g. GRASS), spoiled gradient-echo sequences (e.g. SPGR) and fully balanced gradient-echo sequences (e.g. FIESTA). These fast gradient-echo sequences differ how the residual transversal magnetization is kept in a steady state. In case of the slow and spoiled gradient echo sequences the signal at the receiver can be maximised for a given tissue by setting the RF flip angle equal to the Ernst-angle

$$\alpha = \arccos\left(e^{-R1TR}\right), \qquad \text{A-10}$$

which depends on the tissue-specific R1 relaxation rate.

A.2.5. Inversion recovery FID and spin-echo

In an inversion recovery experiment the magnetization vector $\boldsymbol{M}$ is inverted with a 180° RF pulse at the inversion time TI before it is rotated with a 90° RF pulse into the transverse plane. Due to this RF pulse sequence the FIDs or spin-echo signals then also depend on the longitudinal relaxation rate R1

$$s(t) \propto |1 - 2\exp(-R1TI)| \begin{cases} \exp\left(-R2^*(t - TI)\right) & FID \\ \exp(-R2TE) & spin - echo \end{cases} \qquad \text{A-11}$$

An inversion recovery FID and spin-echo experiment can therefore be used to measure the longitudinal relaxation rate R1 of a sample.

A.3. Introduction to clinical MRI sequences

MRI sequences are used to automated MRI experiments and hence make it possible to reconstruct images of a sample in a clinically acceptable time. The smallest unit of an image series obtained with a MRI sequence is called a voxel (volume element). The MRI image series is either obtained by scanning a sample volume with 2D MRI sequences slice-by-slice or with 3D MRI sequences, which acquire more than one slices of a sample volume at once. More detailed information about the MRI sequences can be found, for example, in Haacke *et al.* (1999), McRobbie *et al.* (2003) and Bernstein *et al.* (2004). A good overview of sequences and their parameters for the application in clinical protocols can be found, for example, in Runge *et al.* (2005).

A.3.1. Building blocks of a MRI sequence

MRI sequences typically consist of RF and gradient-field pulses that excite protons spins of a specific sample volume that are then followed by gradient-field pulses that encode information about the spatial location of proton spins. Finally, in case of gradient-echo sequences gradient-field readout pulses are used to form FIDs, or in case of spin-echo sequences RF pulses in combination with gradient-field pulses are used to form spin-echoes. The generated proton RF signals are received, demodulated, and recorded. The final images are then typically reconstructed with the k-space formalism, which involves the Fourier transformation of the measured data. For example, in a 2D spin-echo sequence the 90° RF pulse is combined with a slice select pulse for exiting just one slice of a volume. Then a 180° RF pulse reverses the transverse dephasing at TE/2 and a gradient pulse encodes the spatial information. During the readout of the spin-echo signal a readout gradient-field pulse encodes the spatial locations. Each line of an image slice is acquired in the repetition time TR, which is the time between the 90° RF pulses.

A.3.2. MRI contrast

An important parameter of an MRI image is the image contrast, which is influence by the proton density (PD), as well as the relaxation rates R1 (=1/T1), R2 (=1/T2), and R2* (=1/T2*). MRI images are classified according to the tissue parameter that mostly influences the contrast. A 2D spin-echo sequence, for example, can produce T1-, T2- and PD-weighted images depending on TE and TR as illustrated in Figure A-2 a short TE and TR creates a T1-weighted (T1w) image, a short TE and long TR creates a PD-weighted (PDw) image, and a long TE and TE creates a T2-weighted (T2w) image. The specific MRI image contrast is quantified with the contrast-to-noise ratio

$$CNR = \frac{\left|s_1^{\mu} - s_2^{\mu}\right|}{s^{Noise}}, \qquad \text{A-12}$$

where s_1^{μ}, s_2^{μ} are the mean signal intensities of two regions in an image, and s^{Noise} is the image noise, which can be measured as described in Firbank *et al.* (1999). The CNR of two regions in a specific image type is mainly influenced by a difference in corresponding underlying tissue parameters. For example, the CNR between white

and grey matter in T2w images depends on the difference between the T2 relaxation rates of the white and grey matter. Combining Equations A-8 and A-12 gives

$$CNR_{WM,GM} = \frac{|s^{\mu}_{WM} - s^{\mu}_{GM}|}{s^{Noise}} = SNR_{WM}|1 - ke^{-\Delta R2TE}|, \qquad \text{A-13}$$

which shows that the CNR between white and grey matter depends on the signal-to-noise ratio of the white matter, a factor k that describes the proton density difference between white and grey matter, as well as the difference between the T2 relaxation rates of the white and grey matter $\Delta R2 = R2_{GM} - R2_{WM}$.

The CNR as well as the image resolution determine the visibility of features in MRI. As further described in (Venkatesan & Haacke, 1997) the visibility of a feature in an MRI image is proportional to $CNR\sqrt{n}$, where n is the number of voxels that form a part of the specific feature (Venkatesan & Haacke, 1997). Hence, the higher the CNR and image resolution the more features become visible on MRI images. However, if the image resolution is increased the image noise increases as well, which decreases the CNR. Therefore the maximum amount of features that can be made visible on MRI images is essentially limited by the image noise.

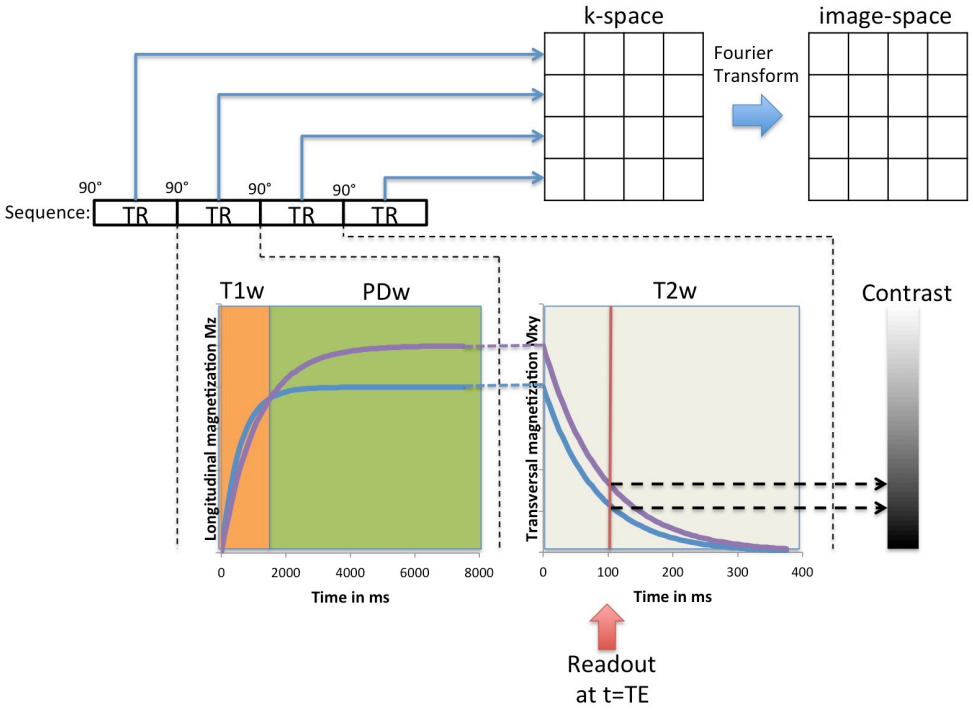

Figure A-2: Formation of the image contrast from a 2D spin-echo sequence. This simple spin-echo sequence acquires a single image slice with 4 line, and 4 voxels per line. During the repetition time TR the longitudinal magnetization recovers and the transverse magnetization decays. Both the repetition- and echo-times are used to influence the contrast in the image. This image was adapted from a figure in Sprawls (2000).

Appendix B MRI cohort studies of ageing

The structural and functional changes in the ageing brain of community-dwelling individuals are the research interest of many large cohort studies of ageing. The following summary shows that the MRI protocols commonly include routine T1w, FLAIR, T2w and T2*w sequences. A few MRI protocols also include qMRI sequences for assessing the relaxation rates R1, R2, R2* of brain tissue directly. Furthermore, most MRI protocols also include diffusion MRI (dMRI) sequences mainly for assessing white matter microstructure properties and the gross axonal connections in the brain, and magnetization transfer (MT) sequences mainly for assessing white matter structural integrity. Some MRI protocols also included functional MRI (fMRI) sequences for assessing the spatial brain activation patterns when performing specific tasks. The latter three sequence types are not the topic of this thesis and hence are not discussed further. However, more information on these sequences can be found in, e.g. McRobbie *et al.* (2003).

B.1. Lothian Birth Cohort 1936 (LBC1936)

The Lothian Birth Cohort 1936 Study (Deary *et al.*, 2012; Deary *et al.*, 2007) is an observational, longitudinal study and includes community-dwelling subjects without dementia that were all born in 1936 in the Lothian area of Scotland, and are hence now in their 70s. In particular, this study aims to gain further insights into the biological basis of cognitive decline to further devise strategies of early prevention of disability in older age. MRI is an important part of this cohort study (Wardlaw *et al.*, 2011) since it provides a sensitive means to detect age-related biological changes in the brain non-invasively. The MRI protocol includes several structural sequences as shown in Table B-1, which allow for the detection and characterization of many features of the ageing brain. In parallel, the genetic and lifestyle information of the participants were assessed, and the participants also underwent a range of cognitive tests, such as a version of the Moray House Intelligence Test No. 12. This particular cognitive test was, in fact, taken twice by the participants of this study; once during the Scottish Mental Survey of 1947, when they were 11 years old, as well as when they were around 70 years old. The results from the latter test, in particular, provide a

life-long measure of cognitive ability, and an unparalleled opportunity to study the correlation between biological and cognitive changes in the ageing brain.

B.2. Austrian Stroke Prevention Study Family (ASPS-Fam)

The Austrian Stroke Prevention Study Family (ASPS-Fam) is a prospective cohort study of the cerebral effects of vascular risk factors in community-dwelling subjects without signs or history of stroke and neurodegenerative diseases from the city of Graz. The ASPS-Fam represents a follow-up study of the ASPS (Schmidt *et al.*, 1999; Schmidt *et al.*, 1994), which recruited ASPS participants, as well as their first grade relatives. In total, the cohort has 381 participants from 169 families, where the number of family members ranged from 2 to 6. The study records include the clinical history of the participants, blood test data, results from cognitive testing, as well as results from an extended vascular risk factor assessment. The ASPS-Fam MRI protocol includes several structural sequences as well as quantitative MRI sequences that measure R2 and R2* as shown in Table B-1. Notably, the quantitative MRI sequences were included in the MRI protocol since they provide a more sensitive measure of brain iron (Langkammer *et al.*, 2010), which was presumed to be associated with age-related vascular injury, as well as age-related cognitive decline (Penke *et al.*, 2012).

B.3. Whitehall II imaging study

The Whitehall II imaging study (Filippini *et al.*, 2014) is a sub-study of the Whitehall II study, comprising a total of 10308 British civil servants, which investigates factors that affect brain health and cognitive ageing. The Whitehall II imaging study randomly recruited 800 participants from the Whitehall II, phase 11 study, who subsequently underwent a detailed clinical and cognitive assessment, followed by a MRI protocol that included structural and functional MRI sequences as shown in Table B-1. The structural sequences also included a novel multi-echo MRRAGE sequence for producing subject motion corrected T1w volumes. The Whitehall II imaging study aims to integrate biological, psychological and socio-economic markers for a better understanding of (i) the development and impact of age-related conditions, such as cognitive decline and depression, (ii) their impact for

employment and work in later life, and (iii) the neural compensation mechanisms that are related with cognitive decline and age-related stress.

B.4. Cam-CAN

The Cambridge Centre for Ageing and Neuroscience (Cam-CAN) project assesses neuroimaging and cognitive measures across the whole adult lifespan and aims to identify factors that (i) contribute to 'successful' ageing, (ii) lead to targeted interventions, and (iii) differentiate normal ageing from neurodegenerative diseases. In phase 1 of this project, 3000 healthy volunteers were recruited with a wide age range who underwent a detailed assessment of their health and lifestyle, a cognitive assessment, and lifetime experiences and physical activities. Seven hundred participants were then selected for phase 2, and 280 participants for phase 3. In phase 2 and 3, the participants underwent a structural and functional MRI protocol, a magneto encephalogram (MEG), blood tests, as well as detailed cognitive tests, which included tests for assessing several cognitive domains, such as attention, language, motor & learning, memory and emotion. The structural MRI protocol only contained two routine sequences, as shown in Table B-1, as well as diffusion weighted and magnetization transfer MRI sequences.

B.5. Rotterdam scan study

The Rotterdam study (Hofman *et al.*, 2013) is a large, prospective cohort study of people who are 45 years of age and over living in Rotterdam, The Netherlands. The study aims to find causes and strategies for the prevention of diseases that occur frequently in the elderly, such as cardiovascular diseases, stroke, dementia and cancer. The Rotterdam scan study is a major component of the Rotterdam study, which aims to assess imaging markers of ageing and disease in their pre-symptomatic phases using computer tomography and MRI. Since 2005 all participants of the Rotterdam study were scanned with the structural MRI sequences shown in Table B-1, as well as with additional dMRI and fMRI sequences. An important emphasis of the imaging study is the development of (fully) automated image analysis tools, which aid researchers in the effective analysis and management of the vast amount of information obtained from the imaging study. So far automated image processing methods have been developed for quantifying several imaging

features of the ageing brain, such as atrophy, white matter hyperintensities, hippocampal volume, cerebellar volume, as well as cerebral microbleeds.

B.6. 1000Brains

The 1000Brains study (Caspers *et al.*, 2014) aims to identify the factors that influence the structural and functional variability of the ageing brain. The participants of this study are recruited from the Heinz Nixdorf (HNR) Recall and HNR MultiGeneration study, which are studies that investigate cardiovascular risk factors in participants aged 45-75 years from the Ruhr area, Germany. At the end of 2013, a total of 653 subjects have been scanned with the 1000Brains study protocol, which includes structural, as well as functional MRI sequences as shown in Table B-1. This study pursues a multimodal approach by combining the results from neuroimaging, behavioural and cognitive tests, genetics and blood tests, with the longitudinal study results from HNR studies of cardiovascular risk factors. It aims to broaden the understanding of the role of genes, as well as cardiovascular and lifestyle factors in the ageing process of the brain.

Table B-1: On-going MRI cohort studies of ageing. This table summarizes the MRI protocols of current cohort studies of ageing. See main text for references.

General cohort characteristics						
Name	LBC 1936	ASPS-Fam	White-hall II	Cam-CAN	Rotterdam Study	1000 Brains
Cohort origin	Lothian region, Scotland	Graz, Austria	British Civil Servants	Cambridge, England	Rotterdam, Netherlands	Ruhr region, Germany
N *	1091	355	800	700	>5000	653
Ages [years]	70s	38-86	60-85	18-87	>45	45-75
Structural MRI protocol						
B_0 [T]	1.5	3	3	3	1.5	3
Type **	G	S	S	S	G	S
T1w	✔	✔	✔	✔	✔	✔
T2w	✔	✔		✔		✔
T2*w	✔	✔	✔		✔	
FLAIR	✔	✔	✔		✔	✔
PDw		✔				
R1	✔					
R2		✔				
R2*		✔				
Others	✔	✔	✔	✔	✔	✔

G = General Electric (Milwaukee, WI, USA); S = Siemens (Erlangen, Germany)

Appendix C Unsupervised outlier detection method for bivariate data

The unsupervised outlier detection method (Filzmoser *et al.*, 2005) that was applied in this study was originally developed for exploration geochemistry. Figure C-1 shows an overview of this method that in this study was adapted for MRI data, where the input are co-registered T2*w/T1w intensities from a ROI. The method involves two steps. First it estimates the tolerance ellipse from the T2*w/T1w intensity distribution for classifying these T2*w/T1w intensities into outlier and normal-appearing tissue intensities. Secondly, T2*w/T1w thresholds are derived from the obtained tolerance ellipse for the segmentation of T2*w hypointensities and their subregions that appear hypointense on T1w MRI.

C.1. Tolerance ellipse of a T2*w/T1w intensity distribution

As shown in Figure C-1 the bivariate T2*w/T1w intensity distribution are first transformed into a univariate robust distance distribution from which a critical robust distance is derived, which represents the tolerance ellipse in the bivariate intensity distribution space.

C.1.1. Transformation into the univariate robust distance space

Given the T2*w/T1w intensity tuples of all voxels $i \in M$

$$\boldsymbol{s_i} = \begin{pmatrix} s_{i,T2*w} \\ s_{i,T1w} \end{pmatrix} \quad \text{C-1}$$

the mean of all ROI tuples $i \in M_l^{ROI}$ is denoted by

$$\boldsymbol{s_l^{\mu}} = \begin{pmatrix} s_{l,T2*w}^{\mu} \\ s_{l,T1w}^{\mu} \end{pmatrix} \quad \text{C-2}$$

and their covariance is denoted by

$$\boldsymbol{S_l^{\Sigma}} = \begin{pmatrix} \left(s_{l,T2*w}^{\sigma}\right)^2 & r_l \; s_{l,T2*w}^{\sigma} s_{l,T1w}^{\sigma} \\ r_l \; s_{l,T2*w}^{\sigma} s_{l,T1w}^{\sigma} & \left(s_{l,T1w}^{\sigma}\right)^2 \end{pmatrix}, \quad \text{C-3}$$

where $s_{l,T2*w}^{\sigma}, s_{l,T1w}^{\sigma}$ are the respective standard deviations and r_l is Pearson's correlation coefficient. In this study, the mean and covariance were estimated with the Minimum Covariance Determinant (MCD) estimator (Rousseeuw, 1984), which

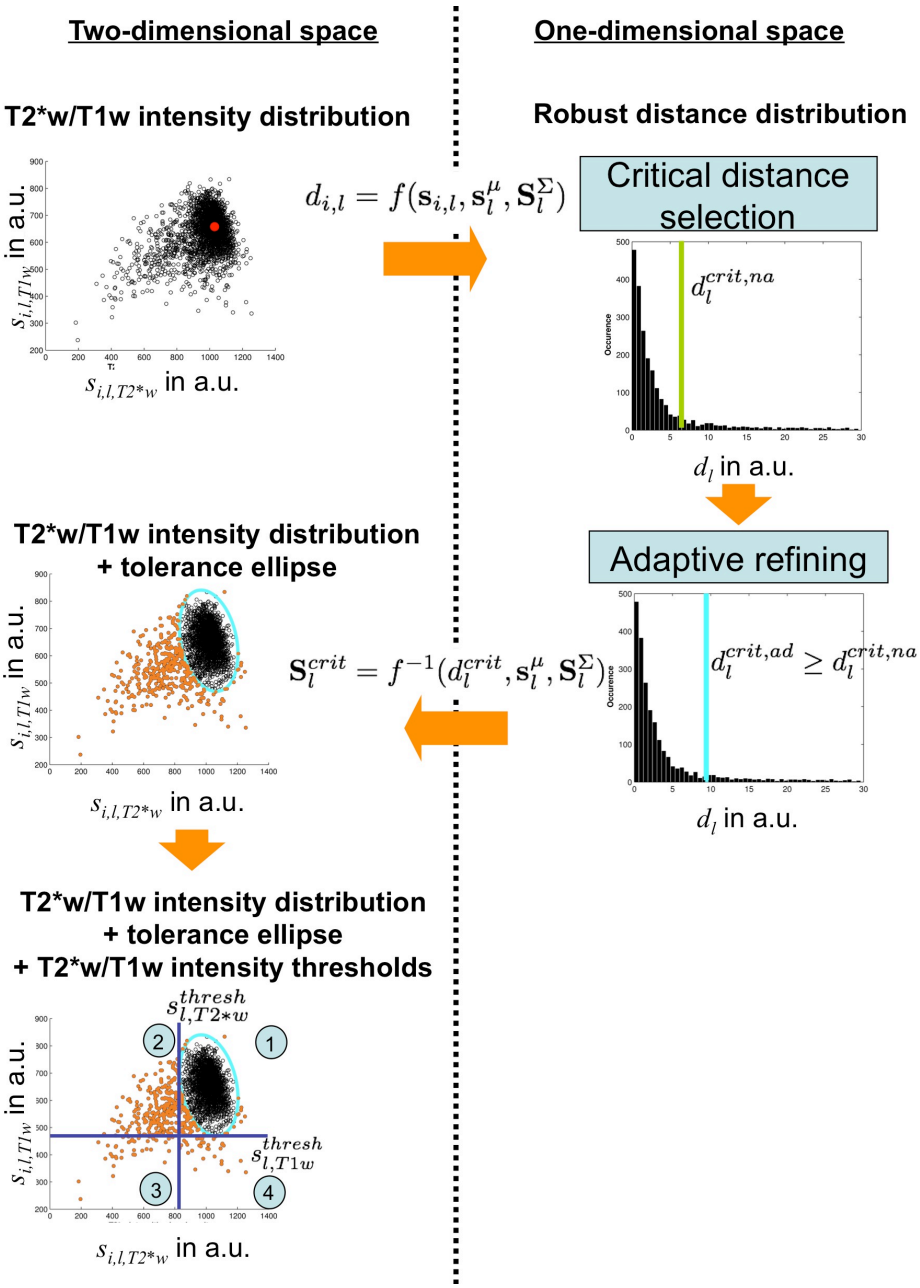

Figure C-1: Automatic T2*w and T1w intensity threshold selection based on the T2*w/T1w intensity distribution outliers of a ROI. The T2*w/T1w intensity distribution of a ROI is mapped from the two-dimensional intensity distribution space to the one-dimensional robust distance space by calculating the robust distance (Hardin & Rocke, 2005) between each T2*w/T1w intensity pair and the centre of the distribution (red dot). An initial critical robust distance $\boldsymbol{d_l^{crit}}$ is then estimated from a χ^2 distribution (degrees of freedom = 2). In the case of the adaptive variant of the outlier detection method this distance is further refined (Filzmoser *et al.*, 2005). The final critical distance is mapped back to the two-dimensional intensity distribution space where it represents a tolerance ellipse (cyan). T2*w/T1w intensity tuples on and outside this tolerance ellipse (orange dots) are considered to be associated with focal features, such as basal ganglia T2*w hypointensities, whereas those inside the ellipse are considered to be associated with normal-appearing tissue. T2*w and T1w thresholds (purple) are derived from the tolerance ellipse to achieve segmentation results similar to an experienced rater using a semi-automated thresholding method (Valdés Hernández *et al.*, 2011). These thresholds define four quadrants (1-4), where T2*w hypointensies are located in quadrants 2-3.

provides robust estimates of these parameters and resists up to 50% outliers. The robust mean and covariance were then used to calculate the robust distances (Rousseeuw & Van Zomeren, 1990)

$$d_i(\boldsymbol{s_i}) = \left(\boldsymbol{s_i} - \boldsymbol{s_l^{\mu}}\right)^T (\boldsymbol{S_l^{\Sigma}})^{-1}\left(\boldsymbol{s_i} - \boldsymbol{s_l^{\mu}}\right), \qquad \text{C-4}$$

which represent the distances between the T2*w/T1w intensity distribution centre and each T2*w/T1w intensity tuple $i \in M_l^{ROI}$.

C.1.2. Critical robust distance of a robust distance distribution

The unsupervised outlier detection method is based on the assumption that the T2*w/T1w intensities follow a bivariate normal distribution, which is sufficiently satisfied in ROIs with signal-to-noise ratios (SNRs) larger than 2 (Gudbjartsson & Patz, 1995). The robust distances (Equation A.4) then follow a non-central chi-square distribution $\chi^2(p, df = 2)$ with two degrees of freedom (Hardin & Rocke, 2005). Signal intensity outliers have the highest robust distances and hence are found in the right tail of the χ^2 distributions above a critical distance

$$d_l^{crit,na} = \chi^2(p = 0.975, df = 2). \qquad \text{C-5}$$

The selection of the critical distance is crucial for separating extreme values of distributions and outliers, while Filzmoser (2005) showed that a refinement of the critical distance with an adaptive method is more robust and leads to better results. This adaptive outlier detection method uses the critical distance of the non-adaptive method $d_l^{crit,na}$ as an initial estimate, which is then refined by considering the sample size n_l of the T2*w/T1w intensity distribution. Firstly, the difference in the tails of the cumulative distribution function G of a chi-square distribution $\chi^2(df = 2)$ and the empirical distribution G_{n_l} of the robust distances d_i of ROI l is calculated. If no outliers are present then this difference denoted by

$$\Delta G_{n_l}^{tail} = \sup_{d \geq d_l^{crit,na}} \left(G(d) - G_{n_l}(d)\right)^+. \qquad \text{C-6}$$

is expected to be lower than a critical difference $\Delta G_{n_l}^{tail,crit}$. Filzmoser *et al.* (2005) derived the relationship between the sample size and the critical difference $\Delta G_{n_l}^{tail,crit}$ for normal distributions in computer simulations. For bivariate normal distributions this relationship is

$$\Delta G_{n_l}^{tail,crit} = \frac{0.234}{\sqrt{n_l}}. \quad \text{C-7}$$

The refined critical robust distance is then

$$d_l^{crit,ad} = G_n^{-1}(1 - a_{n_l}^{tail}). \quad \text{C-8}$$

with

$$a_{n_l}^{tail} = \begin{cases} 0 & \Delta G_{n_l}^{tail} \leq \Delta G_{n_l}^{tail,crit} \\ \Delta G_{n_l}^{tail} & \Delta G_{n_l}^{tail} > \Delta G_{n_l}^{tail,crit} \end{cases}. \quad \text{C-9}$$

In case of a bivariate normal distribution the critical robust distance $d_l^{crit,ad}$ is equal to the robust distance of the sample point that is furthest away from the distribution centre. In the latter case this is the desired behaviour since a normal distribution does not have outliers but only extreme values, i.e. sample points from the same distribution should not be declared outliers.

C.2. Estimating T2*w and T1w thresholds from a tolerance ellipse

T2*w/T1w thresholds were specifically chosen to achieve segmentation results that are most similar to the ones obtained by an experienced rater using a semi-automated thresholding method (Valdés Hernández *et al.*, 2011). As illustrated in Figure C-1, these T2*w/T1w thresholds represent the minimum of all points of the estimated tolerance ellipse of the T2*w/T1w intensity distribution. Given the previously estimated critical robust distance $d_l^{crit,m}$ with $m \in \{na, ad\}$, they can be calculated by solving Equation C-4 for $\boldsymbol{s_i}$ and finding the minimum of each dimension of $\boldsymbol{s_i}$. Figure C-1 shows that the obtained thresholds

$$\begin{aligned} s_{l,T2*w}^{thresh,m} &= s_{l,T2*w}^{\mu} - s_{l,T2*w}^{\sigma} \check{d}_l^{crit,m} \\ s_{l,T1w}^{thresh,m} &= s_{l,T1w}^{\mu} - s_{l,T1w}^{\sigma} \check{d}_l^{crit,m} \end{aligned}, \quad \text{C-10}$$

where $\check{d}_l^{crit,m} = \sqrt{d_l^{crit,m}}$ represents the z-score associated with the critical distance, partitions the T2*w/T1w intensity space into four quadrants, where the first quadrant contains most of the normal appearing T2*w/T1w intensities, the second quadrant contains T2*w hypointensities that appear isointense on T1w MRI, the third quadrant contains T2*w hypointensities that appear hypointense on T1w MRI, and the fourth quadrant contains artefacts (e.g. from the co-registration) that appear isointense on T2*w MRI and hypointense on T1w MRI.

Appendix D Segmentation of T2*w hypointensities in the basal ganglia

Initial basal ganglia T2*w hypointensity masks were generated by thresholding the T2*w intensities of all ROIs with the lowest T2*w threshold, i.e. that of the globus pallidus. The connected components of these masks were then identified and filtered based on their T2*w intensity variance, which reduces segmentation artefacts, mostly due to image noise. Subregions of the final masks that appear hypointense on T1w MRI were also segmented since they possibly indicate advanced mineralization, such as calcification (Valdés Hernández *et al.*, 2014).

Initial basal ganglia T2*w hypointensity masks

$$\mathcal{M}_{T2*w}^{hypo,init} = \left\{ i \in \mathcal{M}^{ROI} | s_{i,T2*w} < s_{gp,T2*w}^{thresh,m} \right\}, \quad \text{D-1}$$

were obtained with the globus pallidus T2*w threshold $s_{gp,T2*w}^{thresh,m}$ (Equation C-10). Then the connected components (six-connected neighbourhood) of these masks, with the unique labels $h \in \{1,2,\dots,h^{max}\}$ and the masks $\mathcal{M}_{h,T2*w}^{hypo,init} \subset \mathcal{M}_{T2*w}^{hypo,init}$, were identified with the Matlab function 'bwlabeln()'. The locations of these connected components within the basal ganglia were determined with the ROI mask set $\mathcal{M}^{ROI}$ as described in Chapter 2. This yielded sets $\mathcal{H}_l^{init}$ that contained the indices of all connected components located within each ROI l.

The standardized T2*w intensity variance of a connected component was defined with $h \in \mathcal{H}_l^{init}$ as

$$q_{l,h} = \frac{\left(s_{h,T2*w}^{hypo,\sigma}\right)^2}{\left(s_{l,T2*w}^{norm,\sigma^{loc}}\right)^2}. \quad \text{D-2}$$

The nominator represents the T2*w intensity variance of a connected component and the denominator represents the local T2*w intensity variance of the surrounding normal-appearing tissue. The latter was defined as

$$s_{l,T2*w}^{norm,\sigma^{loc}} = \left(S_{T2*w}^{norm,\sigma^{loc}}\right)_{0.5} \quad \text{D-3}$$

with $S_{T2*w}^{norm,\sigma^{loc}} = \left\{ s_{i,T2*w}^{norm,\sigma^{loc}} | i \in \mathcal{M}_l^{norm} \right\}$, where the local T2*w intensity variances of each voxel $s_{i,T2*w}^{norm,\sigma^{loc}}$ were obtained with the Matlab function 'stdfilt()' and the normal-appearing tissue mask

$$\mathcal{M}_l^{norm} = \left\{ i \in \mathcal{M}_l^{ROI} | d_i < d_l^{crit,m} \right\} \quad \text{D-4}$$

The standardized T2*w intensity variance $q_{l,h}$ therefore represents a measure of how inhomogeneous a connected component appears on T2*w MRI relative to the surrounding normal-appearing tissue.

To reduce segmentation artefacts the connected component filter of the method removed connected components of the initial basal ganglia T2*w hypointensity masks that appeared too homogenous on T2*w MRI, i.e. connected components with a standardized T2*w intensity variance below a threshold q. This yielded the final basal ganglia T2*w hypointensity masks for each ROI l

$$\mathcal{M}_{l,T2*w}^{hypo} = \bigcup_{h \in \mathcal{H}_l} \mathcal{M}_{h,T2*w}^{hypo,init} \quad \text{D-5}$$

with $\mathcal{H}_l = \left\{ h \in \mathcal{H}_l^{init} \middle| q_{l,h} \geq q \right\}$.

Lastly, basal ganglia T2*w/T1w hypointensity masks

$$\mathcal{M}_{T1w}^{hypo} = \bigcup_{\forall l} \{ i \in \mathcal{M}_{l,T2*w}^{hypo} | s_{i,T1w} < s_{l,T1w}^{thresh,m} \}, \quad \text{D-6}$$

which select subregions of the final basal ganglia T2*w hypointensity masks that appear hypointense on T1w MRI, were segmented by thresholding the T1w intensities selected by $\mathcal{M}_{l,T2*w}^{hypo}$ with the respective thresholds $s_{l,T1w}^{thresh,m}$ (Equation C-10).

Appendix E Ten fold cross-validation method for estimating the optimal connected components filter parameter q

Figure E-1 illustrates the method for estimating the optimal connected component filter parameter q^{opt} for a given subject sample. Firstly, the subject sample was randomized and split into 10 approximately equally sized subsamples. Each subsample was used as a validation set, whereas the remaining nine subsamples were combined into a training set. The optimal filter parameter of a given training set was then estimated with a grid search (Bergstra & Bengio, 2012), where masks $\mathcal{M}_{T2*w,\mathcal{k}}^{hypo}(q)$ for the basal ganglia T2*w hypointensities of the training set subjects with index $\mathcal{k}$ were generated with the connected components filter parameters $q = 0{,}0.1, \dots, 1.5$. The average spatial agreement between the generated and corresponding reference masks was quantified with the median Jaccard index

$$J^{med}(q) = \left(J_{\mathcal{k}}(q)\right)_{0.5} \qquad \text{E-1}$$

with

$$J_k(q) = \left|\frac{\mathcal{M}_{T2*w,\mathcal{k}}^{hypo}(q) \cap M_{T2*w,k}^{hypo,ref}}{\mathcal{M}_{T2*w,\mathcal{k}}^{hypo}(q) \cup M_{T2*w,k}^{hypo,ref}}\right|, \qquad \text{E-2}$$

where $\mathcal{M}_{T2*w,\mathcal{k}}^{hypo,ref}$ denote the manually created reference masks. The filter parameter that was associated with the highest median Jaccard index

$$q^{opt} = \underset{\forall q}{\operatorname{argmax}} J^{med}(q), \qquad \text{E-3}$$

was selected as the optimal filter parameter for the corresponding validation set and subsequently used to create the basal ganglia T2*w hypointensity masks $\mathcal{M}_{T2*w,\mathcal{k}}^{hypo,opt} \coloneqq \mathcal{M}_{T2*w,\mathcal{k}}^{hypo}(q = q^{opt})$ of the corresponding validation set subjects, as well as the T2*w/T1w hypointensity masks $\mathcal{M}_{T1w,\mathcal{k}}^{hypo,opt} \coloneqq \mathcal{M}_{T1w,\mathcal{k}}^{hypo}(q = q^{opt})$.

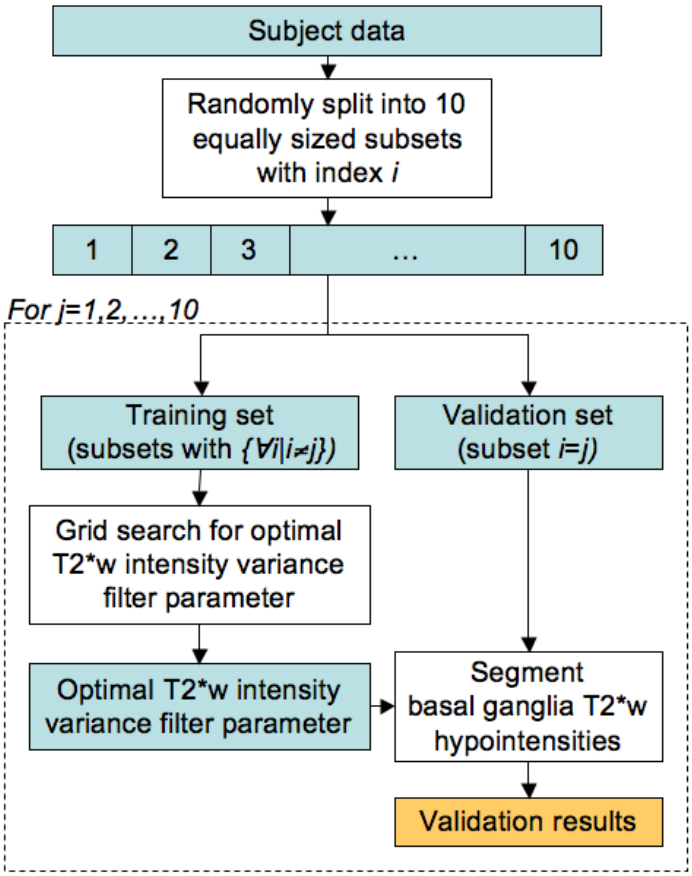

Figure E-1: Optimal selection of the connected component filter parameter q with 10-fold cross-validation. This flow diagram illustrates how the subject data was split into training and validation sets in the 10-fold cross-validation. The optimal connected component filter parameter $\boldsymbol{q}^{\boldsymbol{opt}}$ was then estimated in a grid search for each training set. This parameter represents the connected component filter parameter $\boldsymbol{q}$ that maximises the Jaccard index $\boldsymbol{J}^{\boldsymbol{med}}(\boldsymbol{q})$ (Equation **E-1**), and hence maximises the spatial agreement between the automatically generated masks for the training set subjects and the corresponding reference masks from the rater. The estimated parameters $\boldsymbol{q}^{\boldsymbol{opt}}$ were subsequently used to segment the basal ganglia T2*w hypointensities of the subjects in the corresponding validation sets.

Appendix F List of Publications

Journal publications

1. **Glatz A.**, Bastin M.E., Kiker A.J., Deary I.J., Wardlaw J.M., Valdés Hernández M.C. (2015) Automated segmentation of multifocal basal ganglia T2*-weighted MRI hypointensities. *NeuroImage* 105:332-46.
2. Valdés Hernández M.C., Allan J.L., **Glatz A.**, Kyle J., Corley J., Brett C.E., Muñoz Maniega S., Royle N.A., Bastin M.E., Starr J.M., Deary I.J., Wardlaw J.M. (2014) Exploratory analysis of dietary intake and brain iron accumulation detected using Magnetic Resonance Imaging in older individuals: the Lothian Birth Cohort 1936. *J Nutr Health Aging* doi:10.1007/s12603-014-0523-3.
3. Valdés Hernandéz M.C., **Glatz A.**, Kiker A.J., Dickie D.A., Aribisala B.S., Royle N.A., Muñoz Maniega S., Bastin M.E., Deary I.J., Wardlaw J.M. (2014) Differentiation of Calcified Regions and Iron Deposits in the Ageing Brain on Conventional Structural MR Images. *J Magn Res Im* 40(2):324-33.
4. **Glatz A.**, Valdés Hernández M.C., Kiker A.J., Bastin M.E., Deary I.J., Wardlaw J.M. (2013) Characterisation of multifocal T2*-weighted MRI hypointensities in the basal ganglia of elderly, community-dwelling subjects. *NeuroImage* 82:470-80.

Journal publications (in press)

1. Valdés Hernández M.C., **Glatz A.**, Allerhand M., Muñoz Maniega S., Gow A.J., Royle N.A., Morris Z., Bastin M.E., Starr J.M., Deary I.J., Wardlaw J.M. (in press) Neuroanatomical correlates of regional brain iron deposits, cognitive abilities and white matter hyperintensities in the elderly. *Neurobiol. Aging* Submitted.
2. **Glatz A.**, Valdés Hernández M.C., Wardlaw J.M., Bastin M.E. (in press) Combined R1, R2 and R2* relaxation rate mapping methodology for the improved characterisation of brain iron on clinical MRI scanners. *J Magn Res Im* Submitted.

Conference Proceedings

1. **Glatz A.**, Pirpamer L., Langkammer C., Valdés Hernández M.C., Bastin M.E., Wardlaw J.M., Fazekas F., Schmidt R., Ropele S. (2014) An investigation into the formation and histology of focal basal ganglia mineralization with quantitative MRI. *Proc ISMRM 2014* Poster #4682.
2. **Glatz A.**, Pirpamer L., Langkammer C., Li W., Liu C., Valdés Hernández M.C., Bastin M.E., Wardlaw J.M., Fazekas F., Schmidt R., Ropele S. (2014) Basal ganglia iron deposits in the Austrian Stroke Prevention study: Validation of Lothian Birth Cohort 1936 findings and further insights into their chemical composition. *Proc ASM 2013* (Talk).
3. **Glatz A.**, Valdés Hernández M.C., Kiker A.J., Bastin M.E., Muñoz Maniega S., Royle N.A., Deary I.J., Wardlaw J.M. (2013) Automated segmentation of basal ganglia iron deposits on clinical T1- and T2*-weighted MRI volumes *Proc ECR 2013* doi: 10.1594/ecr2013/C-2293.
4. **Glatz A.**, Valdés Hernández M.C., Kiker A.J., Bastin M.E., Muñoz Maniega S., Deary I.J., Wardlaw J.M. (2012) Characteristic appearance of basal ganglia iron deposits of healthy, elderly subjects on clinical MRI volumes. *Proc. ESMRMB 2012* doi: 10.1007/s10334-012-0324-9.
5. **Glatz A.**, Buchanan C.R., Valdés Hernández M.C., Bastin M.E., Wardlaw J.M. (2012) Intuitive and efficient deployment of neuroimaging pipelines in clinical research with BRICpipe. *Proc. Neuroinformatics 2012* doi: 10.3389/conf.fninf.2014.08.00014.
6. **Glatz A.**, Valdés Hernández M.C., Bastin M.E., Wardlaw J.M. (2012) Validation of quantitative MR sequences for improved diagnosis in microvascular stroke and ageing. *Proc. ASM 2012* (Poster).
7. **Glatz A.**, Valdés Hernandéz M.C., Kiker A.J., Bastin M.E., Muñoz Maniega S., Royle N.A., Deary I.J., Wardlaw J.M. (2011) Towards quantization of basal ganglia iron deposits: automated segmentation with co-registered T1- and T2*-weighted MRI volumes. *Proc. ESMRMB 2011* doi: 10.1007/s10334-011-0268-5

8. **Glatz A.**, Valdés Hernandéz M.C., Kiker A.J., Bastin M.E., Muñoz Maniega S., Royle N.A., Deary I.J., Wardlaw J.M. (2011) Automatic segmentation of basal ganglia iron deposits from structural MRI. *Proc. ASM 2011* (Poster).
9. **Glatz A.**, Valdés Hernandéz M.C., Kiker A.J., Bastin M.E., Muñoz Maniega S., Royle N.A., Deary I.J., Wardlaw J.M. (2011) Automatic segmentation of basal ganglia iron deposits from structural MRI. *Proc. MIUA 2011* http://www.biomedical-image-analysis.co.uk/index.php/on-line-proceedings.